Detection and Characterisation of Young Planetary-Mass Objects: Novel Techniques and Optimised Survey Strategies

Sophie Charlotte Dubber

Doctor of Philosophy
The University of Edinburgh
February 2022

For Granny and Papa

Abstract

Young, low-mass brown dwarfs can be similar in size and composition to young, giant exoplanets. Many exist without host stars and are uncontaminated by starlight, making them useful analogues for studying planets in solar systems. Increasing the population of well-studied brown dwarfs and exoplanets will improve our understanding of the underlying distribution of planets, and of which formation scenarios are viable. Young star-forming regions, such as Serpens and Taurus, are ideal targets when looking for populations of planetary-mass brown dwarfs, as they are relatively nearby, young and active in star formation.

In this thesis, I present surveys, past and future, of nearby star-forming regions, conducted in the hope of finding new, very low-mass brown dwarf and planetary-mass members. I also focus on the characterisation of newly-identified individual objects, and of populations as a whole. I aim to demonstrate how custom-designed narrowband photometric filters can be incredibly effective at selecting brown dwarf members of young regions for spectroscopic follow-up.

In Chapter 2, I present a survey of the Serpens star-forming region using the novel W-band technique. I obtain photometry using the Wide-field Infrared Camera (WIRCAM) on the Canada-France-Hawaii Telescope (CFHT), and the custom-designed W-band filter, which is centred on the 1.45 μm absorption feature present in brown dwarf atmospheres. I then describe a spectroscopic follow-up campaign, covering $J-$, $H-$ and $K-$bands. Finally, I describe a subset of observations using the Hubble Space Telescope (HST), obtained to identify possible low-mass companions or binary components. Using this photometric, spectroscopic, and high-resolution imaging data, I identify five likely-members of Serpens Core and Serpens South, four of which are consistent with having spectral types of M5 or later.

In Chapter 3, I describe a future direct imaging survey, optimised to detect young, giant planets using a custom filter and a target list informed by our current understanding of the underlying planet distribution. The survey will use the Near Infrared Camera System (NIX), a high-contrast imager, part of the Enhanced Resolution Imager and Spectrograph (ERIS) instrument that has recently been installed at the Very Large Telescope (VLT). I present the 'spectral shape' technique, which uses the custom-designed $K-$peak filter to efficiently identify promising targets for follow-up observations. I discuss possible targets for such a survey, and conclude that a nearby, young star-forming region is an ideal target to maximise the yield of planet and brown dwarf detections.

Finally, in Chapter 4 I use an additional W-band data set to investigate the the form of the initial mass function (IMF) in the Taurus star-forming region, and the question of the possible environmental dependence of the IMF. I combine CFHT and Gaia photometry to isolate likely Taurus members from field contaminants. Using the isolated cluster population, I run multiple Monte Carlo Markov Chain simulations to assess the likely form of the IMF. I use different IMF functional forms (broken power law and log-normal) and Taurus star-formation histories, and find evidence for a spread of stellar ages in Taurus from 1–10 Myr. I also find that both functional forms provide a reasonable fit to the data (with a slight preference for the broken power law), and that the best-fit IMF parameters extracted are consistent with literature values for other clusters and the general Galactic population, supporting the theory of a universal IMF.

Lay Summary

There are billions upon billions of stars in the universe, the nuclei of solar systems containing billions upon billions of planets. Brown dwarfs bridge the gap between these objects: they are loosely defined as less massive than stars but more massive than planets. Unlike stars, brown dwarfs do not burn enough fuel to remain stable and bright - they get fainter and colder as they age. We have discovered $\sim$5000 exoplanets (planets beyond our own solar system) to date, and thousands of brown dwarfs. This thesis focuses on the continued hunt for planets and brown dwarfs in our Galaxy. The lowest-mass brown dwarfs can be comparable to some of the largest exoplanets (e.g. Jupiter-sized), and are thought to be made of similar materials. As a result, studying brown dwarfs can improve our knowledge of giant exoplanets.

Many observational techniques can be used to detect planets and brown dwarfs, all of which require powerful telescopes and state-of-the-art instruments. Planets that range from a few Earth masses to many Jupiter masses in size have been found using indirect techniques. This means their presence is inferred by an effect that they have on their host star. For example, a planet may pass in front of its host star and block its light - we can measure this dimming effect. It could also affect the motion of its host star via its gravity - we can measure this change. To directly measure a planet or brown dwarf, however, we need to image it. This can be straightforward for brown dwarfs, but challenging for planets: planets are much, much fainter than the stars they orbit, and can be completely obscured by starlight. It is possible to use sophisticated instrumentation and observational methods to block the light from a star, and directly measure the emission from a hot young planet. Contrastingly, many brown dwarfs exist in isolation, without bright host stars to contend with, meaning we can image them with more basic instruments and smaller telescopes.

Directly imaging giant planets and brown dwarfs is just one observational approach: there are many more techniques that provide unique information. Photometry is the process of measuring light emitted by an object, using a filter that only transmits certain wavelengths. When we obtain photometry of an object, we can also measure astrometry, which describes the position of an object on the sky. By combining photometry and astrometry, we can organise the stars and brown dwarfs that we observe into groups, and determine how old and distant they are. We can also observe an object spectroscopically, collecting lots of light over a wide range of wavelengths, and measuring how it varies. Spectra of brown dwarfs and giant planets are crucial when trying to characterise them: we can use them to assess temperature and composition, which give hints of atmospheric conditions and even possible weather patterns on other worlds.

In this thesis, I will describe a number of surveys that make use of photometry, astrometry, spectroscopy and direct imaging to detect and characterise new brown dwarfs and giant exoplanets. Of particular importance is the use of custom filters for photometry, which are designed to look for specific molecules in brown dwarf and giant planet atmospheres, e.g. water or methane. I aim to show the importance of using optimised techniques such as custom filters when trying to maximise the number of new discoveries from a survey.

In Chapter 2, I present the results from a survey of the Serpens star-forming region, a compact region of the Milky Way galaxy that contains many young stars. I obtained data from ground- and space-based telescopes to detect and characterise five new low-mass brown dwarfs. In Chapter 3, I discuss the design of a new direct imaging survey. ERIS/NIX is a new imaging instrument that will soon be installed on the Very Large Telescope in Chile. In this chapter I present a variety of possible survey designs, considering different target regions that are likely to contain many brown dwarfs and giant exoplanets. In Chapter 4, I use a catalogue of photometry from another star-forming region, Taurus, and investigate the properties of its stellar members. I analyse the masses of the stars and brown dwarfs that it contains, and compare the results to other compact regions, and to the Milky Way as a whole.

Declaration

I declare that this thesis was composed by myself, that the work contained herein is my own except where explicitly stated otherwise in the text, and that this work has not been submitted for any other degree or professional qualification except as specified.

Chapter 2 is based on work published in Dubber et al. (2021). Chapter 3 is based on work that has been submitted to Monthly Notices of the Royal Astronomical Society, and is currently under review. In these chapters, I use ‘we’ to acknowledge the help of my collaborators in producing this work.

(*Sophie Charlotte Dubber, February 2022*)

Acknowledgements

It is hard to know where to begin with all of the thanks I want to express. So many people have made my time in Edinburgh and at the Royal Observatory the most incredible few years. Firstly, my supervisor Beth, who has given me so much encouragement and so many opportunities - I feel confident as a researcher in a way I would never have anticipated as a nervous first year, and I have you to thank for that. I have to mention Annelies, my Masters supervisor, and all of the people I met in Leiden and Sydney, who encouraged me to pursue a PhD and gave me my first invaluable research experiences.

Next, the Discord gang, Rohit, Sarah, Dylan and Nicole, who kept me sane during the many, many days spent working from home - the world was scary and unfamiliar, but your cheery voices and live-streams of your dogs are some of my best memories. Thanks also to Niall, for the chats about reality TV and thesis woes, and a place to stay on future New York trips.

Every single PhD student that I have met during my time at the observatory has added a little bit of light to my life here: Rokas, Phil, James, Massi, Lea, Harry, Manika, Abbie, Andrea, Ryan and all the rest (especially the new first years bringing back some energy and enthusiasm to the department post-pandemic). Edinburgh is a really special astronomy department, where you are all but guaranteed to meet Good Eggs (shout out to the PhD recruiters).

My amazing family have supported me as consistently through my PhD as they have done my whole life. Thanks to Auntie Frances, Uncle Nick and Auntie Carrie, Jack, Jem and Jamie, and to my Granny, Nanny and Grandad. Being so far away and unable to see you can be really hard, so thank you for making the trek up to visit me whenever you could, and for always taking me out to dinner.

Friends from different eras of my life: Annie, Tara, Katie, Niamh, Emma and Emma; Sally, Loui, Ellen, Sophie and Sian - I don't think I truly comprehended the importance of having good, kind people in your life until 2020 happened. You helped me keep a (mostly) healthy work-life balance, and dragged me back into the light when I got consumed by brown dwarfs. My wonderful friend Sarah, my day-1 PhD buddy, you are a bundle of joy and I'll miss working next to you. Special thanks to Angus, for always being there for me and being a constant source of levity and comfort when I needed it the most.

Finally, to my Mum and Dad: I am where I am because of you, because of your constant, gentle encouragement and never-ending support. Thank you for being the best parents.

Contents

4 The IMF in Taurus 145

List of Figures

List of Tables

1

Introduction

1.1 Brown Dwarfs and Giant Exoplanets

1.1.1 A General Introduction

To experience the sheer number of stars in our Galaxy, you need only look up at the night sky. Humanity has been doing this for millennia, from the ancient Greeks to Copernicus. It is no large stretch to imagine to a population of planets out there around those stars, inspired by the multiple planets in our Solar System. Long before the discovery of the Galactic exoplanet population, astronomers attempted to understand these two seemingly separate types of celestial objects: should stars and planets be considered fundamentally different? Or should they be described as two parts of some mysterious spectrum, occupying opposite ends of an unknown scale? The discovery of the first brown dwarfs began to answer this question.

In the mid-1990s, astronomers observed brown dwarfs for the first time. They estimated their masses, and found them to be tens of times more massive than Jupiter, but far less massive than the sun (Rebolo et al., 1995; Nakajima et al., 1995; Basri et al., 1996). Based on these observations, we began to understand that planets and brown dwarfs occupy different areas of the same substellar parameter space. If we attempt to categorise them solely by their masses, planets have masses below the deuterium burning limit, ≈13 M_J (Jupiter mass), and brown dwarfs have masses in the range ≈13–72 M_J, below the limit for hydrogen fusion - thus clearly distinguishing them from stars.

Over the decades since these first observations of brown dwarfs, our understanding of them has grown enormously, but the ability to fully classify planets, brown dwarfs and stars into entirely separate populations remains elusive. There are three factors that must be considered in tandem when in determining if an object is a giant planet or a low-mass brown dwarf: mass, formation mechanism and composition. For example, in star-forming regions (parts of the Galaxy where large numbers of stars are born), many brown dwarfs have been discovered. These objects are classified as brown dwarfs due to the likely formation mechanisms active in these environments (see Section 1.1.2.1). However, many of these objects have been detected with masses of 10–20 M_J (e.g. Luhman et al., 2003; Bayo et al., 2011; Esplin & Luhman, 2017), straddling the fine line between the planetary and brown dwarf regimes. Should these objects be classified as low-mass brown dwarfs, giant exoplanets, or an entirely new category of object? The answer is still unclear.

Whilst overlapping properties is an issue for nomenclature, it can be advantageous observationally. Similarities between classification categories mean that the lowest mass brown dwarfs can be used as analogues for giant exoplanets. About half of all known planets are classified as giants, with masses > 0.5 M_J: the majority of these orbit stars. Observing such a planet is very challenging, as the much brighter host star can fully obscure any planetary signal. Complex techniques such as coronagraphy (blocking the light that comes from the star, see Section 1.3.3) must be implemented to overcome this challenge. Brown dwarfs, however, tend to exist in isolation, with no bright host stars to contend with, and can often be observed with relative ease. By discovering a multitude of brown dwarfs with masses comparable to giant planets, we can study their atmospheres and compositions to increase our understanding of giant planets, without the increased observational challenges.

1.1.2 Brown Dwarfs

1.1.2.1 Formation

Stars form via the gravitational collapse of dense molecular cores, which are embedded in molecular clouds. Using this most basic model of star formation, one can hypothesise that brown dwarf form in isolation via an identical process. The brown dwarfs formed as a result of such a process are described as free-floating, as they are not companions to any stellar objects. There is a major issue with this explanation of brown dwarf formation. Brown dwarfs are below the Jean's mass in most molecular clouds, the critical mass above which gravity dominates. In order to form free-floating brown dwarfs in the same way as stars, there must be a mechanism that either halts accretion or lowers the Jean's mass of the cloud, otherwise cores with brown dwarf masses would simply continue to accrete material and become stars.

Numerical simulations that model clouds of hundreds of stellar masses have led to additional brown dwarf formation theories, that pose solutions to the fundamental challenge described above. One example, the ejection mechanism (Watkins et al., 1998; Reipurth & Clarke, 2001; Bate et al., 2002; Bate, 2012), begins with disk fragmentation, and suggests that the resulting objects formed will undergo N-body interactions, and ultimately eject some of their number from the disk. The ejected objects will stop accreting mass, while the objects still forming in the fragmented disk will continue to grow. If the ejected objects have masses below the minimum mass for stable hydrogen fusion, they will form a population of free-floating brown dwarfs.

Removing the need for a mysterious mechanism that can reconcile the mismatch between brown dwarf masses and the typical Jean's mass of a cloud, there are multiple schools of thought that consider brown dwarf formation distinct from star formation. One such example is the fragmentation of massive disks (e.g. Whitworth & Stamatellos, 2006; Matzner & Levin, 2005) - this process could explain the formation of brown dwarfs found to be companions to stars. Fragmentation occurs when a massive disk collapses due to its own gravity and splits into 'clumps'. These over-dense clumps can then accrete matter from the surrounding disk, and grow to brown-dwarf masses. Fragmentation is thought to occur beyond a specific radius, which depends on the disk mass, but is generally tens of astronomical units (AU, the distance from the Earth to the Sun). Many other mechanisms (e.g. formation in dense filaments, see Whitworth (2018) for a comprehensive review) have also been proposed and explored.

Whilst the argument concerning the need for separate formation mechanisms for stars and brown dwarfs continues, the ever-growing population of detected free-floating brown dwarfs, and other observed properties of stellar and sub-stellar populations, seem to suggest that most brown dwarfs form in isolation in a similar way to stars. For example, the initial mass function (IMF; the distribution of stellar masses at the point of formation - see Section 1.4) seems to be one continuous function across the Hydrogen burning limit ($\sim$ 72 M_J), suggesting that a single mechanism is responsible for forming both stars and brown dwarfs.

1.1.2.2 Evolution

As discussed in Section 1.1.1, using a mass-based definition, brown dwarfs are described as objects with masses above the deuterium burning limit, but below the limit for stable hydrogen fusion ($\approx$13–72 M_J). Those that do burn deuterium only do so for a very short fraction of their total lifetime. A lack of stable element burning means that they dim over time, as they cool from their hottest temperature at the point of formation. Unlike stars, which remain at a constant luminosity and temperature for a large chunk of their total lifetime (the main-sequence), the observable properties of brown dwarfs evolve as they cool. The consequences of this evolution are clear: the older a brown dwarf gets, the dimmer it becomes and the harder it is to detect. As a result, surveys attempting to discover new brown dwarfs, especially low-mass brown dwarfs, tend to target the youngest possible regions of the Galaxy, where it is likely that the stars have just formed.

The evolution of brown dwarfs after formation also brings challenges for classification. Generally, the more massive an object, the brighter it is. But

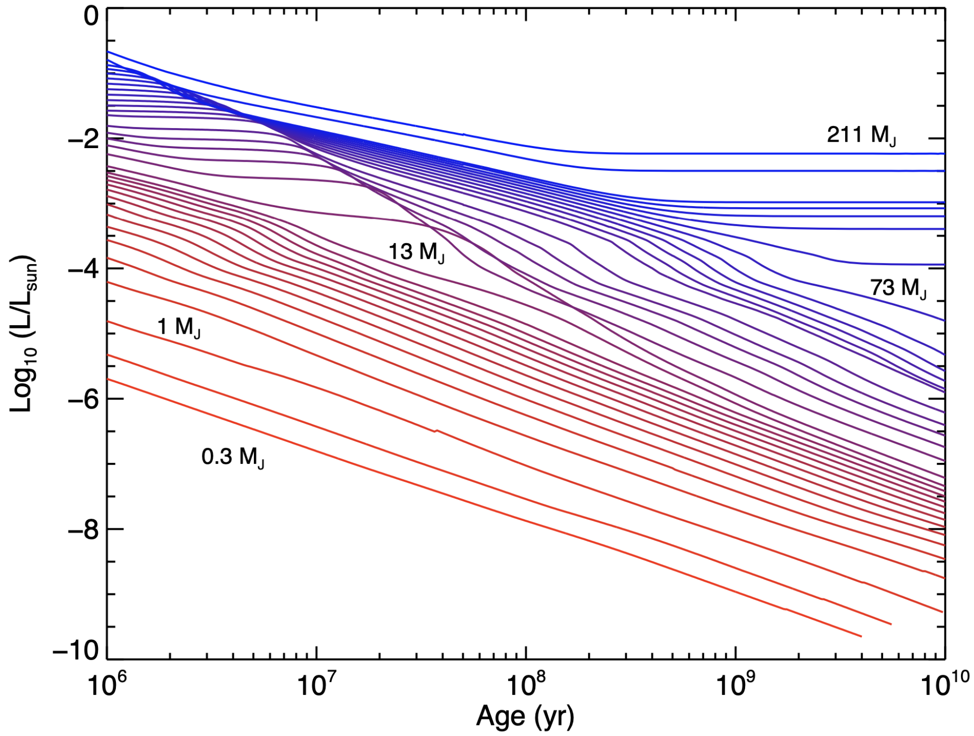

Figure 1.1 *Model curves showing the evolution of luminosity over time for M-dwarf stars (blue), brown dwarfs (purple) and planetary-mass (red) objects, taken from Burrows et al. (1997).*

consider as an example a very low-mass brown dwarf just after formation, and an intermediate mass brown dwarf that is millions of years old. If we were to measure how bright these two objects are, we might find that they appear very similar. As we are (usually) unable to directly measure an object's mass (and instead must infer it using models), we would be forgiven for assuming that these objects had similar overall properties. However, if we were also able to obtain age estimates, we would see that they are actually at very different points in their evolution. Estimating ages is challenging - generally it is only possible to assign an accurate age to a brown dwarf if it is a confirmed member of a stellar association. This degeneracy between luminosity, age and mass is demonstrated visually in Figure 1.1, taken from Burrows et al. (1997).

1.1.2.3 The Spectral Sequence

Brown dwarfs are intrinsically dimmer than stars, meaning that for more than 20 years after they were hypothesised (Kumar, 1963; Hayashi & Nakano, 1963), none were detected. The first confirmed brown dwarfs were reported in the mid 1990s: two young objects in nearby clusters (Rebolo et al., 1995; Basri et al., 1996) and an older companion to a nearby star (Nakajima et al., 1995). These detections were all higher mass brown dwarfs, in the range ~20-80 M_J. The advent of deep, wide field surveys subsequently led to other discoveries. Many objects had spectra that varied significantly from the standard M-dwarf definition (which describes the lowest mass stars), warranting the creation of new spectral types, L and T (Kirkpatrick, 2005). In Figure 1.2, I show a series of example spectra, which demonstrate how the emitted flux of early-M to T-type objects varies with wavelength. The infrared spectra shown are taken from the SpeX Prism Spectral Libraries[1]. L- and T-type objects are defined by absorption features at optical and near-infrared (IR) wavelengths. L dwarfs show strong H_2O, FeH and CO absorption bands in the near-IR, whilst T dwarfs also exhibit strong CH_4 bands (Cushing et al., 2005). Another identifying feature of these objects is the shape of the continuum in certain IR bands. The shape of the H-band (~ 1.4-1.8 μm, see Figure 1.2) has a noticeably 'triangular' shape for late-M and L types when compared with early-Ms, due to the lower gravity of the stellar photosphere (Lucas & Roche, 2000; Allers et al., 2007, e.g.). A further spectral category of Y was suggested to extend the classification system to account for cooler objects, the first of which were discovered in 2011 (Cushing et al., 2011). With extremely cool temperatures ranging from 300-500K, these objects highlight the difficulty in defining a firm dividing line between planets and brown dwarfs.

As discussed above, classification beyond spectral types for brown dwarfs can be challenging. They cool over time after formation, passing through the full range of M-L-T-Y spectral types as they age. Without an independent measurement of mass, there is no simple way of mapping the observable luminosity to age. Furthermore, there is evidence to suggest that the low surface gravity of young, low-mass objects can affect spectral shape, and the transition temperature between spectral types (Barman et al., 2011), further complicating the classification effort.

---

[1] Maintained by A.Burgasser, http://pono.ucsd.edu/ adam/browndwarfs/spexprism.

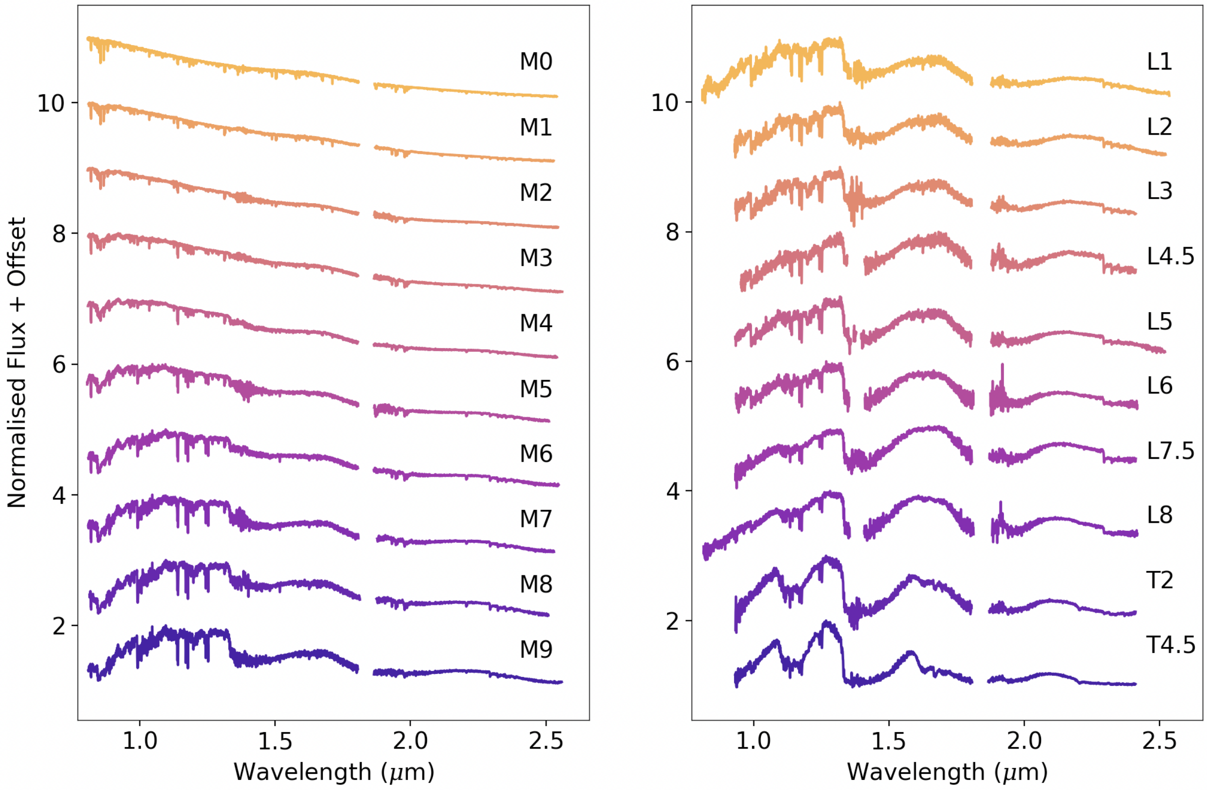

Figure 1.2 *The spectral sequence for brown dwarfs from M–T spectral types, in the near-infrared ($\sim 1-2.5\mu m$). Spectra are normalised to peak flux, and are taken from the SpeX Prism Spectral Libraries.*

1.1.2.4 Characterisation using Spectral Templates

There is a long-established method for determining the spectral types of objects from their observed spectra. The Morgan-Keenan system (Morgan et al., 1943) involves visually comparing the observed spectra to a set of spectral templates with well-determined spectral types. These are considered standard stars. This visual approach works reasonably well, as often human judgement is key in picking out specific spectral features. Conversely, it can be insufficient as cool brown dwarf spectra are very heterogeneous at IR wavelengths. As a result, despite quantitative systems for optical classification being long-established (Boeshaar & Tyson, 1985; Kirkpatrick et al., 1999), an equivalent system using IR data from young brown dwarfs has only recently been proposed.

Allers & Liu (2013) were the first to implement such a system in the infrared, and also include determination of the age of an object, via examination of its surface gravity (again, previously only applicable to optical data, Cruz et al., 2009). By combining the standard visual inspection technique with a spectral index-based approach (a ratio of fluxes that is used to describe the strength of a particular absorption feature in a spectrum), they establish a set of infrared spectral standards from M5–L6. Other authors, such as Zhang et al. (2018), have since built on this classification technique, using the indicies first defined in Allers & Liu (2013).

The combination of visual inspection and index-based classification is now a standard technique in the field. Despite this, there is still no definitive catalogue of standard stars in the IR: different authors have used different libraries, depending on the types of objects being classified. The spectra discussed in Allers & Liu (2013) are proposed as a set of low-gravity IR standards, and have been used in much work since (e.g. Bonavita et al., 2017; Chauvin et al., 2017; Claudi et al., 2019). Luhman et al. (2017) also present a library of standard spectra for young objects (< 10 Myr) in the near-IR, which are the mean spectra of multiple objects with the same spectral type. The lack of a singular accepted system can result in difficulties when attempting to compare the results of studies that use different sets of standards to classify the same spectra. Conversely, it can also act as a good test of consistency, to check that results are unchanged when a different set of standards is used.

An important additional consideration when attempting to characterise young brown dwarfs using spectral data is the presence of spectral features caused by disks or accretion. A disk-hosting brown dwarf will have an infrared excess, which can be measured and identified using spectral data, due to the high infrared emission of disk material. When characterising a brown dwarf, it is useful to know if it is disk-hosting, so that one can factor this additional source of flux into the analysis of spectra. Various surveys have specifically looked for young, disk-hosting brown dwarfs, often using infrared excess as an observational indicator (e.g. Kaas, 1999; Povich et al., 2013; Dunham et al., 2015). If a young brown dwarf is actively accreting material, this is also detectable via spectral data. Accretion causes peaks in flux at specific wavelengths, and can alter the observed properties of a target - signs of ongoing accretion can be used to confirm the youth of a brown dwarf (e.g. Jose et al., 2020).

1.1.2.5 Brown Dwarf Modelling

There are certain physical properties of brown dwarfs that are very difficult, if not currently impossible, to directly or indirectly measure. It is possible to model the atmospheres of brown dwarfs (in a way that is consistent with their interior structure) to reproduce their observed properties. These models then allow us to probe physical properties that we are unable to investigate observationally. Using atmospheric models, we can reproduce the evolution of brown dwarfs as they cool over time. Evolutionary models track the changes in luminosity of an object of a specific mass as it ages. From a computed set of evolutionary models, one can also extract isochrones, which track how the luminosities of objects of different masses vary at a singular point in their evolution.

There are two components of brown dwarf evolutionary models: the first, interior structure modelling, has been well understood for decades, and the basic physical processes and equations used have changed very little in this time. The second, atmosphere modelling, is in a state of constant evolution, with our understanding of molecular line lists (studies of specific molecules that accurately describe the positions of each of their characteristic absorption and emission features) improving with every passing year.

Research groups have spent decades attempting to use atmospheric models of brown dwarfs to replicate the observed brown dwarf population. The accuracy of evolutionary models and isochrones is tested by comparing colour-magnitude diagrams (or mass-luminosity relations) of the generated model populations to data from real objects. The BHAC98 evolutionary models (Baraffe et al., 1998) were a benchmark in the field for a long time, and are based on the atmospheric models of Hauschildt et al. (1999). They can be used for stars and substellar objects with $m = 0.02 - 1.4$ $M_{\odot}$, spanning 1 Myr–1 Gyr. However, there are known flaws with these models, including their ability to reproduce observed colours. The Dusty and COND models, based on the AMES molecular line lists, are updated versions of the BHAC98 models, (Chabrier et al., 2000; Allard et al., 2001; Baraffe et al., 2003). They give the user flexibility in including optional clouds and varying dust opacity in the brown dwarf atmospheres. The Dusty models can effectively reproduce the spectra of L-dwarfs, as they assume uniform mixing of dust in atmospheres. The COND models treat the dust as entirely settled, and can be used to study the evolution of T-dwarfs. This group has published multiple iterations of updated models (e.g. Baraffe et al., 2015; Phillips et al., 2020), covering a wide range of stellar masses and ages, based on the BT-Settl atmosphere models (Allard et al., 2012b,a; Rajpurohit et al., 2013). Another set of regularly-used models are the MIST stellar evolutionary tracks (Dotter, 2016; Choi et al., 2016), based on the MESA stellar evolution package (Paxton et al., 2011, 2013, 2015), althought these currently reach a minimum mass of $0.1M_{\odot}$.

How can we use this wealth of model data to characterise observed objects? Evolutionary models and isochrones are usually computed in a range of filters, and provide magnitudes for objects of different ages and masses. At a basic level, one can match the observed magnitudes of an object to the closest values in the model (after correcting for extinction and distance), and obtain an estimate for mass and age (and radius, chemical abundances etc). A more complex approach involves using the measured magnitudes to map to a luminosity and temperature (using additional models e.g. Herczeg & Hillenbrand, 2014), and plotting these along with the tracks and isochrones on a Hertzsprung-Russell (HR) diagram. One can then extract physical properties based on the positions of the objects in this diagram when compared to the models.

The choice of evolutionary model can have a large impact on the results of an analysis of sub-stellar object properties. Different suites of models can have widely varying assumptions or treatments of the underlying physics. It is crucial to understand the impact that the use of a singular modelling system will have on a set of results. Additionally, different models also offer different coverage of mass, effective temperature, age and other properties. As discussed previously, the Dusty and COND models, produced by the same group, themselves make different assumptions about dust mixing in brown dwarf atmospheres, resulting in different predicted properties in many cases. Comparing these to the Sonora evolutionary models (Marley et al., 2021), a much more recent example, further variations are present. They offer similar mass coverages, both reaching ~ 0.5 $\mathrm{M_J}$, but Sonora uses updated opacities and atmospheric chemistry modelling, and provides modelled data for cloud-free atmospheres in chemical equilibrium. As a result, they predict slightly different values for the same object: for a 10 Myr, 0.01 $\mathrm{M_\odot}$ object, COND predicts T_{eff} = 1731 K and $\log(L/\mathrm{L_\odot})$ = -3.704, whereas Sonora predicts T_{eff} = 1706 K and $\log(L/\mathrm{L_\odot})$ of -3.746. These differences are small, but non-negligible, and should be considered when discussing the results of an analysis. Other examples of stellar models, such as MIST (currently covering $0.1 < m < 300$ $\mathrm{M_\odot}$) and the PARSEC models ($0.1 < m < 12$ $\mathrm{M_\odot}$) do not focus specifically on the sub-stellar regime, and offer a wide scope of higher mass models. They have many small differences in their input parameters, assumptions, and range of chemical elements included. The difference in coverage and input physics of these four sets of models highlights the need to understand and account for the impact that the choice of model has on results, and the need to be consistent with model choices when conducting multiple analyses for comparison purposes.

1.1.3 Giant Exoplanets

The definition of a planet is surprisingly controversial - one doesn't even need to leave the solar system for an example of this (Pluto is now officially considered a 'dwarf-planet'). The definition adopted by the International Astronomical Union is: 'a planet is a celestial body that (a) is in orbit around the Sun, (b) has sufficient mass for its self-gravity to overcome rigid body forces so that it assumes a hydrostatic equilibrium (nearly round) shape and (c) has cleared the neighbourhood around its orbit'. An exoplanet is a planetary body beyond our solar system. Current detection techniques are limited to finding exoplanets within our own Galaxy (a possible notable exception: Di Stefano et al., 2021). At the time of writing, there are 4,933 confirmed exoplanets[2], a figure that has been exponentially increasing since the early 2000s.

1.1.3.1 Formation and Evolution

Our historic understanding of planet formation is naturally informed by the structure of the Solar System. The Solar System planets were born in a protoplanetary disk that surrounded the Sun, and was composed primarily of hydrogen and helium, with a small amount of heavier elements (collectively referred to as dust). The material in this disk coagulated into larger clumps, which grew in size to form rocky planetesimals (e.g. Hayashi et al., 1977). Depending on their size, these collided with other objects to form the rocky planets, or accreted an atmosphere to become the gas giants. The specifics of how these processes occurred are hotly-debated aspects of planet formation research. In particular, exactly how giant planets form in protoplanetary disks remains unknown (see e.g. D'Angelo & Lissauer, 2018).

The observed properties of stars can indicate the presence of a disk (e.g. if an infrared excess is observed) - and protoplanetary disks have been directly detected around hundreds of stars in our Galaxy[3]. In fact, in recent years, we have imaged planets actively forming in a handful of young disks (e.g. Keppler et al., 2018; Haffert et al., 2019). Such observations shed light on some of the most important questions in planet formation, including the question of how giant planets initially form: the two most popular theories are the core accretion theory, and the gravitational instability theory.

In the core accretion scenario, giant planets form in a similar way to smaller, rocky planets - by slowly accreting material from the disk. Specifically, in this model the protostellar disk (i.e. the disk present prior to the formation of a star) contains micron-sized grains of material, which stick together via collisions, and then sink towards the mid-plane of the disk due to their increased mass (see e.g. Lissauer, 1993). This results in the formation of a layer of material containing particles a few cm in size. Such particles can ultimately form kilometer-sized planetesimals

---

[2] https://exoplanetarchive.ipac.caltech.edu

[3] https://www.circumstellardisks.org/index.php

(Goldreich & Ward, 1973), which can then accrete gaseous material from the disk to become giant planets.

In the gravitational stability scenario, fragmentation of protoplanetary disks is the process that gives birth to giant planets (Boss, 1997). This is very similar to the brown dwarf fragmentation theory discussed in Section 1.1.2.1. In the early stages of disk evolution, when a protoplanetary disk is still relatively massive, density waves can create gravitational instabilities that become dense clumps of material with masses ∼1 M_J (Boss, 2000).

Both formation theories face a number of obstacles, in both the timescales required for successful planet formation and conflicts with some observational results. Further detection of giant planets will continue to prove crucial in establishing which formation scenario is most viable - large surveys of hundreds of stars are allowing us to begin to compare models to observations (e.g. Nielsen et al., 2019; Vigan et al., 2021).

1.1.3.2 Detections

Wolszczan & Frail (1992) discovered the first confirmed exoplanets orbiting a pulsar. The first detection of an exoplanet orbiting a main-sequence star followed shortly after in 1995, with the discovery of the giant planet 51 Peg b (Mayor & Queloz, 1995). The fields of exoplanets and brown dwarfs grew simultaneously through the late 1990s and 2000s, with indirect detection techniques such as transit photometry and radial velocity proving very effective at finding planets.

The radial velocity (RV) technique was used by Mayor & Queloz (1995) to detect 51 Peg b. This technique involves measuring the gravitational interaction between a star and an orbiting planet (see Wright, 2018, for a review). If we continuously monitor a star, and a planet is present in the system, we can often detect evidence of this planet in the form of a ‘wobble’ in the data. This is caused by the star orbiting the common centre of mass of the system, which causes a Doppler shift in the light we detect (a change in frequency, demonstrated in the upper-left panel of Figure 1.3). Using the radial velocity technique, we can measure a minimum mass of the planet (or an actual mass if the inclination of the system is known) and the eccentricity of its orbit, as well as its orbital period. Nearly a thousand

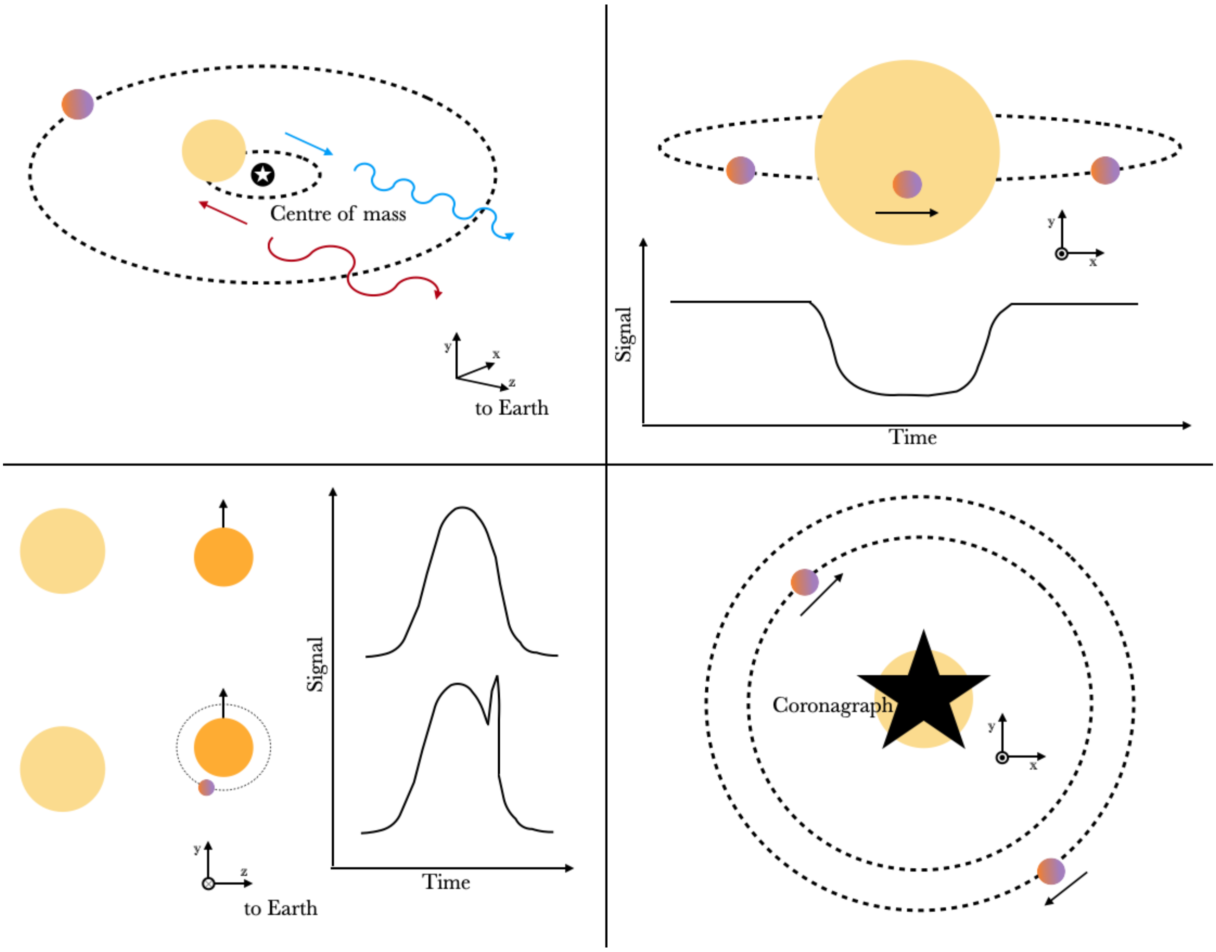

Figure 1.3 *A summary of the exoplanet detection techniques discussed in this Chapter. Top left: a schematic of the radial velocity technique, showing the Doppler motion of a host star. Top right: the photometric transit technique, demonstrating the drop in flux due to a transiting planet. Bottom left: demonstration of the microlensing technique, showing the effect of a planet in the lensing signal. Bottom right: direct imaging of a planetary system, using a coronagraphic mask. In each panel is a 3D axis, with the z-axis pointing to the direction of Earth from each system.*

planets have been detected using the RV technique to date [4], a large fraction of which are giant planets. RV observations are more likely to detect giant planets, because they cause a larger Doppler ‘wobble’.

Transit photometry is another extremely successful method of exoplanet detection (see Deeg & Alonso, 2018, for a review). Unlike RV, there have been multiple space telescope missions dedicated solely to detecting planets via transits. A transit is the movement of a planet in front of a host star: during the transit, the planet will block out some of the light that the star emits. This requires a specific orientation of the system, as demonstrated in the upper-right panel of Figure 1.3. Plotting light collected as a function of time, one can detect a signature dip that is indicative of the presence of a transiting planet in the system. Such dips can be caused by other phenomena (e.g. grazing binaries or unresolved multiple systems, e.g. Poleski et al., 2010), but planet transits have a characteristic shape that can usually be identified by eye. The Kepler mission (Borucki et al., 2010) was a space telescope designed to discover planets via transit photometry. It monitored 150,000 stars during its lifetime, and found over 2500 transiting planets. The science output of Kepler is ongoing - such a wealth of data was collected that astronomers are continuing to find new planets, using novel techniques such as deep learning (e.g. Pearson et al., 2018; Shallue & Vanderburg, 2018; Dattilo et al., 2019). The Transiting Exoplanet Survey Satellite (TESS; Ricker et al., 2015), another NASA mission designed to observe transits, is currently in the process of scanning and monitoring the entire sky. It is continuing the legacy of Kepler, and has so far proven incredibly successful, enabling the discovery of many interesting planetary systems (recent examples include: Newton et al., 2021; Lam et al., 2021; Grunblatt et al., 2022).

Radial velocity and transit photometry are both biased towards planets on short orbits close to their host stars, and also detect higher mass planets more frequently (as these produce a larger, more easily detectable signal). A number of additional exoplanet detection techniques have yielded fewer total detections than radial velocity or transit, but cover a different area of mass-separation parameter space.

Gravitational microlensing is one example - lensing occurs when the gravitational field of a star acts like a lens, magnifying the signal of a distant background star. If the lensing star has an orbiting planet, the gravitational field of the planet can

---

[4] exoplanet.eu

have a measureable effect on the lensing signal - as shown in the lower-left panel of Figure 1.3 (see Gaudi, 2012; Tsapras, 2018, for reviews). The drawback of this technique is that lensing requires perfect alignment that will never happen again after the event - follow-up observations of the planet are essentially impossible. However, despite the rarity of lensing events, we now have the telescope sensitivity to be able to detect and characterise small rocky planets using this technique (e.g. Mróz et al., 2020; Zang et al., 2021). To date, microlensing has been used to detect ≈ 150 planets - this number will likely sharply increase with the launch of the Nancy Grace Roman Space Telescope (likely within the next decade), which will include a dedicated microlensing survey (Penny et al., 2019; Johnson et al., 2020; Sajadian, 2021).

Every technique I have discussed so far is indirect: the presence of a planet in a system is inferred by an effect on a stellar signal (either the system star or a distant background star). Direct detection enables imaging of exoplanets, and hence measurements of properties using their emitted light. Marois et al. (2008, 2010) and Lagrange et al. (2009, 2010) discovered the first directly imaged planets, in the HR8799 and β Pictoris systems. The direct imaging technique can be as simple as pointing at and imaging an object, but for most exoplanet observations it is far more complex. Planets are much fainter than their host stars, requiring high-contrast direct imaging. This involves blocking out the stellar signal using coronagraphy - a complex mask is positioned in front of the star, improving our ability to disentangle the planetary signal from starlight. To date, direct imaging has been very successful at detecting young giant exoplanets far from their host stars, as these emit a significant signal in the infrared and are minimally contaminated by starlight. Tens of giant exoplanets have been discovered to date using direct imaging, both stand-alone detections (e.g. Lagrange et al., 2009) and as part of large imaging surveys (e.g. Marois et al., 2008; Macintosh et al., 2015; Chauvin et al., 2017).

1.1.3.3 Characterisation of Giant Planets

When discussing characterisation of giant planets, the methods of detections and follow-up observations are crucial - different methods allow us to measure different properties of a planet. Using radial velocity data, one can determine a (minimum) planet mass, an orbital eccentricity and an orbital period, as has been done

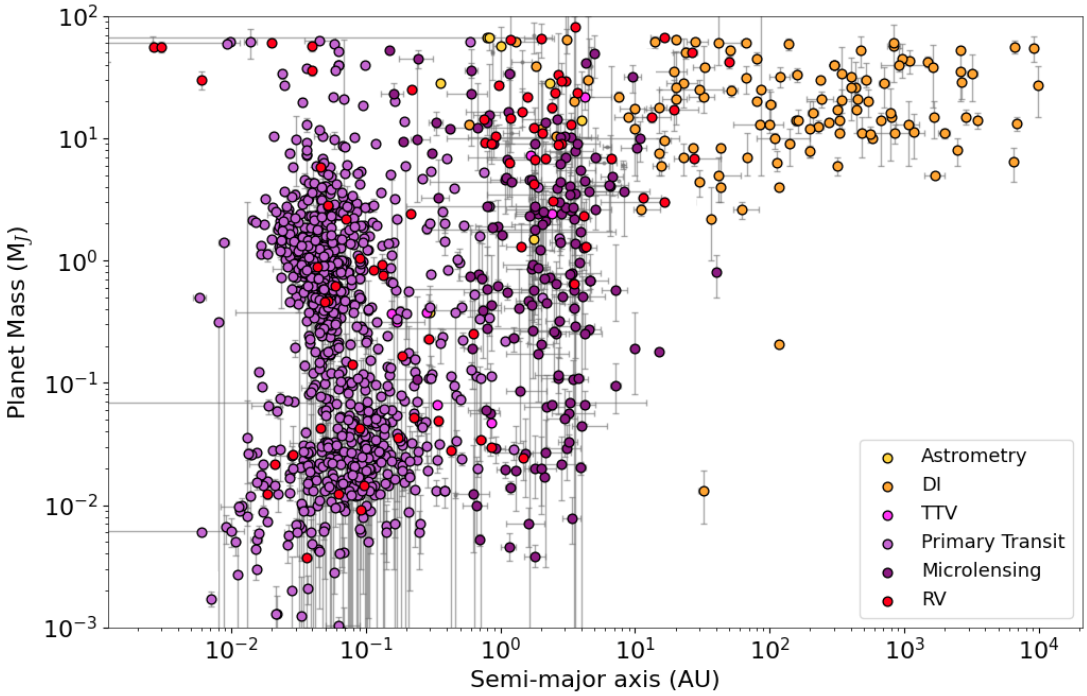

Figure 1.4 *Semi-major axis/planetary mass parameter space, showing the current state of the exoplanet population (as of January 2022, exoplanet.eu). Different colours indicate different detection methods.*

for hundreds of hot Jupiters (Jupiter-mass planets orbiting very close to their stars). Radial velocity measurements are spectral data, but any planetary signal is entangled with stellar light, making it difficult to extract information about the composition of the planet. Radial velocity and photometric transit observations are often combined. If one has observed a planet using both methods, a radius and an inclination can be added to the pool of measurements. An inclination estimate can be used to derive the true mass of the planet, which can then be used in combination with the radius to estimate the density and speculate on the composition. These indirect detection methods suffer from the pitfalls of requiring a detailed understanding of the properties of the host star to extract any planetary parameters.

If characterising the atmosphere of a giant planet is the main goal, one must obtain observations that either directly detect planetary light, or where the planet signal can be accurately disentangled from the stellar signal. Direct imaging is an excellent technique for atmospheric characterisation - the standard for current instruments is to perform simultaneous high-contrast imaging and spectroscopy. This allows for a direct detection of a planetary atmosphere, by providing a (typically) low-resolution spectrum. Even low-resolution spectroscopy can provide a huge amount of information about the temperature and composition of a planetary atmosphere - many species have now been detected in the atmospheres of hot Jupiters, including methane in 51 Eri b (Macintosh et al., 2015), and CO and H20 in β Pic b (Hoeijmakers et al., 2018b). In additional to general atmospheric composition, it is possible to monitor the variability of giant exoplanets using high-contrast imaging and spectroscopy (e.g. Biller et al., 2021).

Transit spectroscopy is another method that can be used to characterise the atmosphere of a planet. Spectroscopic observations during a transit primarily detect starlight, but also a small component of planetary light. This is light that has travelled through the thin atmosphere around the edge of the planet silhouette. To disentangle it from the starlight, it is necessary to compare data from the star in and out of transit. In this way it is possible to measure absorption features caused by the planet's upper atmosphere, and determine the elements present - the first example of this was the detection of sodium in the atmosphere of HD 209458b using the Hubble Space Telescope (Charbonneau et al., 2002). This technique has continued to progress, with an ever-growing list of elements detected during planetary transits (e.g. iron and titanium in Kelt-9b, Hoeijmakers et al., 2018a).

1.1.3.4 Planet population models

Compared to the billions of known, characterised stars, the total size of the entire known exoplanet population is ~5000. This population is then spread across a widely-varying parameter space: planets at 0.1 AU separation from their host stars have very different properties to those at 50 AU. Furthermore, these detections are not uniformly distributed across the full range of separations, masses, densities etc - we have detected far more close-in planets than widely-separated, as Figure 1.4 shows. The result of this imbalance is that there are large areas of parameter space where we cannot perform general assessments of the overarching properties of the population. A prime example of this is the uncertainty surrounding the underlying planet population at wide separations - i.e. how the frequency of planets changes at increasing distances from the star.

In the decade after the discoveries of the first exoplanets, the majority of detections were made using the radial velocity technique. A few hundred planets were found, and studies into the underlying distributions of all planets were based on this small sample, with most objects detected using a technique with strong observational biases. The first studies of the RV population, such as Cumming et al. (2008), found a rising power law for planet frequency in both mass and orbital period (i.e. m^{α}), predicting that many giant planets were likely to be found at large distances from their stars. In this work, they fit a power law to a sample containing 585 stars and 48 planets, covering masses from 0.3 $\mathrm{M_J}$–10 $\mathrm{M_J}$, and periods $<$ 2000 days. This ground-breaking study was used to inform many future surveys, predicting high yields of giant planets at wide separations. Ultimately, this was not confirmed observationally - many direct imaging surveys planned using these model populations (e.g. Lafrenière et al., 2007a; Beuzit et al., 2008; Heinze et al., 2010; Macintosh et al., 2014) reported far lower yields than expected. These results confirmed a long-standing suspicion - simply extending the planet population (predicted by solely RV planets) to higher masses and wider separations did not correctly describe the underlying exoplanet population.

Meyer et al. (2018) attempted to improve on the work published by Cumming et al. (2008), by including more detection techniques in the sample of fitted planets. This enabled them to include planets at much wider separations. They found that a log-normal function best fit the data they included (from RV, transit photometry, microlensing and direct imaging detections), agreeing with observations that planet frequency decreases at wide separations ($>$ 30 AU Bowler, 2016; Galicher et al., 2016). Other studies agreed that the frequency appeared to decline, for separations $> 3 - 10$ AU (Bryan et al., 2016). Fernandes et al. (2019) made use of a large sample of transit photometry and RV data, and used occurrence rates corrected for survey completeness (an important step to deal with observational biases). They also found a turnover in planet frequency at $\sim 2 - 3$ AU - the location of the snowline in the solar system, the point beyond which solid ices can form.

The approximate location of the turn-over in giant planet frequency with respect to semi-major axis can be explained using the physical processes at work in a protoplanetary disk. Referring back to the formation mechanisms discussed in Section 1.1.3.1, we can recall that the core accretion scenario requires the accretion of rocky material to first form a giant planet core, which will then accrete an atmosphere. The solid materials needed to form a large planetary core are abundant at distances beyond the snow line, as temperatures are cool enough for water vapour to condense into ice. Hence, the semi-major axis distribution for giant planets is expected to be low for distances far inside the snow line (due to a lack of materials), and reach a peak at its location. The drop in frequency of giant planets at distances far beyond the snow line can be explained by the long timescales involved - less material is available (due to the distance from the star), meaning it would take longer for a core to reach giant planet masses, often longer than the overall lifetime of the disk. This is an issue for the core accretion theory, as we do see some wide, massive planets, which this theory cannot properly account for. The width of the peak in the semi-major axis distribution may be due to the non-static nature of the snow line - studies have found the location to vary significantly depending on the age or mass of the star - in some cases being located at the distance of Pluto in the solar system (Cieza et al., 2016).

The above discussion is applicable to the core accretion model of giant planet formation. If we consider instead gravitational instability as the dominant process, we can still explain the location of the peak in giant planet frequency at the snow line. Disk fragmentation preferentially occurs in the cool outer regions of a disk, resulting in a lack of giant planets at close separations, as the planet frequency distribution shows. However, gravitational instability forms few close in planets, thus this mechanism of planet formation alone is insufficient at replicating the observed semi-major axis distribution.

Fulton et al. (2021) recently published a study that uses RV data from over 700 stars that were observed for 3 decades by the California Legacy Survey (CLS; Rosenthal et al., 2021). The dataset approximates a random sample of nearby stars, with 177 planets present across all systems. Fulton et al. (2021) find a similar result to Fernandes et al. (2019) for the overall shape of the planet frequency distribution, but with a peak at ∼3.6 AU. The distribution decreases beyond this separation, extending out to 10 AU, and is valid for planets with $M = 0.09 - 3.1$ $\mathrm{M_J}$. Figure 1.5 is taken from Fulton et al. (2021), and shows these results, also comparing them to other older models. Their findings are consistent with the newest results from large direct imaging surveys (e.g. Nielsen et al., 2019; Vigan et al., 2021; Desidera et al., 2021; Langlois et al., 2021), suggesting that their planet population model can effectively replicate the overall observed distribution of directly imaged planets.

Thus, recent studies have shed light on a turnover in planet frequency, resulting in fewer giant planets at wide separations, but the specifics of where this peak lies and the occurrence rates of planets beyond $\sim$ 10 AU are still relatively uncertain. Reducing this uncertainty requires more detections at these large separations, an area of parameter space covered by direct imaging.

Nielsen et al. (2019) investigate planet frequency as a function of stellar mass, based on results from the Gemini Planet Imager Exoplanet Survey (Gemini-GPIES). Using the planet detections from this direct imaging survey (6 planets out of a sample of 300 stars), they find a clear dependence of planet frequency on stellar mass, with higher mass stars more likely to host widely separated giant planets than low-mass stars. They also fitted a power law to their planet frequency distribution, but as this is derived from only 6 planets, it is unlikely to be robust. Vigan et al. (2021) perform a similar analysis, using the first 150 stars from the SPHERE infrared survey for exoplanets (SPHERE-SHINE Vigan et al., 2021; Langlois et al., 2021; Desidera et al., 2021). They find qualitative agreement with the results of Nielsen et al. (2019), but again note that this is based on a small sample. They also compare their results with the two dominant planet formation scenarios (core accretion and gravitational instability, see Section 1.1.3.1), comparing synthetic populations from models to real data. They find that both mechanisms are needed to explain the observations, with a slightly larger component drawn from the core accretion population. They again note that this needs to be confirmed using the full SPHERE-SHINE sample.

Another example of the ongoing reconciliation of observations and models is the planet mass distribution. This describes how many planets of each mass have so far been detected (or more fundamentally, how many of each mass are predicted to have formed). The observed distribution can loosely be described as 'double-peaked', with Jupiter-mass and 'super-Earth' mass planets ($\sim$10 $M_{\oplus}$) dominating the current census. Compared to the distribution of planet masses in our solar system, the current observed exoplanet mass distribution is very top-heavy - although this is likely in part due to the limitations of our current observational techniques. The *giant* planet mass distribution has been modelled using both the core accretion and gravitational instability formation models, which have been used to predict a rising power law distribution (which varies with stellar mass, e.g. Adams et al., 2021) and a top-heavy distribution with most planets $\gtrsim$ 5 M_J (e.g. Forgan et al., 2015), respectively. Many additional giant planets must

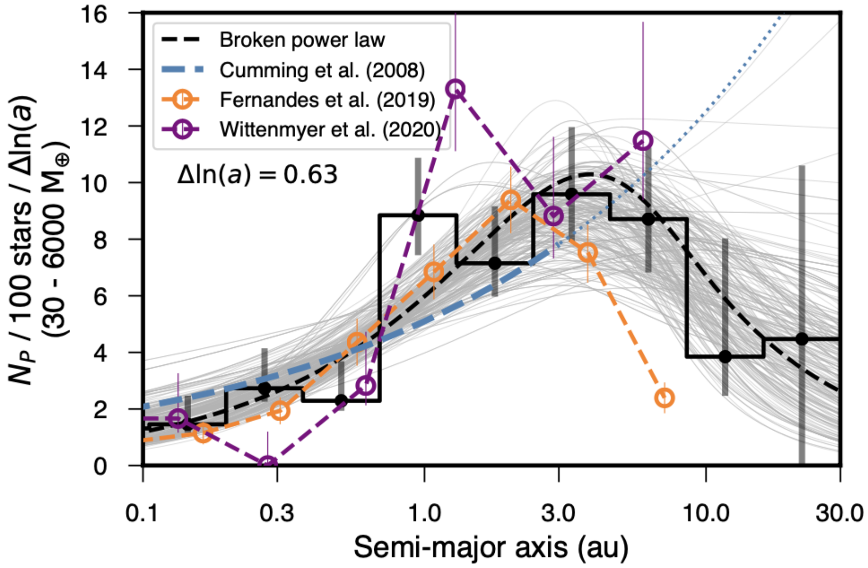

Figure 1.5 *Planet occurrence distributions, taken from Fulton et al. (2021), comparing the latest results with the original RV planet predictions. Fulton et al. (2021) find a turnover in frequency at* ~ 3.6 *AU (black dashed line).*

be detected and characterised before we can begin to understand which singular formation model, or which combination of models, best fits the observed giant planet mass distribution.

1.1.4 What is a YPMO?

Young planetary-mass objects (YPMOs) are young objects that have masses in the planetary regime. This includes both giant exoplanets and very low-mass brown dwarfs, with masses that are comparable to the largest planets - for the sake of definition, objects with masses $\lesssim 20$ M_J.

1.2 Star-forming Regions and Moving Groups

1.2.1 What are they?

Young stars rarely exist in isolation - the process of star-formation (the collapse of a molecular cloud causing local over-densities that become stars) results in groups or associations of stars, which share certain properties (such as metallicity). Star-forming regions and moving groups are two types of stellar grouping, with differing ages.

Star-forming regions are parts of the Galaxy where star formation is either ongoing or has recently happened, meaning there are many very young stars in a compact area of sky. These stars have a common age and chemical composition, and a single star-forming region will likely contain stars with a wide range of masses, including very low-mass brown dwarfs and potential planet-hosting stars. They are often very dusty and obscured: the dust and gas from the star-formation process will eventually be blown away, but at very young ages, it is still a dominant component of the environment.

As the name suggests, stars in moving groups have common motion through the Galaxy and move as a group. Members are identified using their on-sky motion - they are all roughly the same distance from the Earth, moving at the same speed and in the same direction. They also have similar chemistry and ages: since they also formed together, and have spread out spatially over time. The main distinction between star-forming regions and moving groups is that moving groups tend to be older - the gas and dust from star-formation has essentially dispersed, and the component stars are less tightly clustered on-sky.

There is often cross-over in these definitions - some regions can be described as both a star-forming region and a moving group, due to the transition between the two classifications. Nearby young star-forming regions and the youngest moving groups with many member objects and low levels of dust obscuration are often the targets of YPMO surveys. This is due to the fact that star-formation has either occurred recently or is ongoing, and YPMOs will be close to the point of formation and therefore at their brightest, making them significantly easier to detect.

1.2.2 Local Examples

1.2.2.1 Star-forming Regions

Scorpius-Centaurus is the nearest OB Association (a region containing many young O- and B-type stars), and the nearest region of recent massive star-formation. It contains three prominent sub-clusters: Upper Scorpius (US), Upper Centaurus Lupus (UCL) and Lower Centaurus Crux (LCC). Upper Scorpius is at a distance of $\approx$ 145pc (De Bruijne et al., 1997), and has an age of $\approx$ 5–10 Myr (Pecaut et al., 2012; Pecaut & Mamajek, 2016; David et al., 2019). With a large stellar population (>1000 stars, Preibisch & Mamajek, 2008), it has been the subject of many wide field imaging surveys (e.g. Cook et al., 2017; Wilkinson et al., 2018). It is the most-studied of the three sub-clusters, and has also been the target of many YPMO surveys (e.g. Slesnick et al., 2006; Kraus et al., 2008; Biller et al., 2011; Lodieu et al., 2013; Miret-Roig et al., 2021), that have used a variety of techniques (including photometry and direct imaging) to search for new US members, and companions to known objects. Upper Centaurus Lupus is an older sub-cluster ($\sim$ 17 Myr), and is significantly less studied than US. In part this is due to age, and also because it is not as compact on sky and more of its members lie along the Galactic plane line of sight (Preibisch & Mamajek, 2008), an extremely crowded, extincted field. Lower Centaurus-Crux is the final sub-cluster, and is the closest of the Sco-Cen sub-clusters (110-120 pc) but also contains an older population (12-17 Myr). It has substructure between its northern (110 pc, 12 Myr) and southern regions (120 pc, 17 Myr), with the north older and more distant. It is the least studied of the three sub-clusters.

In the northern sky lies the Perseus Molecular Cloud, a 10^4 $M_\odot$ cloud (Bally et al., 2008) that contains a multitude of regions and groups with different properties. Generally it is thought to be within 300 pc of the sun, less than 6 Myr in age and active in star formation. A notable star-forming region within Perseus is IC 348, a $<$ 5 Myr cluster containing many young stars (several hundred total members Muench et al., 2007)), at a distance of 293–321 pc (Ortiz-León et al., 2018a). Being small, compact, nearby and young ($\sim$2 Myr), it has been surveyed at many wavelengths (see Herbst, 2008, for a review) and many low-mass members have been detected (e.g. Luhman, 1999; Alves de Oliveira et al., 2013; Luhman et al., 2016)

Orion is the nearest region of ongoing high-mass star-formation with a multitude of both high- and low-mass stars (Bally, 2008). It is vast - containing tens of thousands of stars, it is the best studied region of star-formation in the sky. Located at a distance of $\sim$400 pc, it contains various sub-groups: including OB1a (8–12 Myr), OB1b (1.7 – 8 Myr) and the Orion Nebular Cluster (ONC). The ONC is located in the Orion A molecular cloud, and is < 2 Myr in age (Muench et al., 2008). This young age has made it a target of many YPMO surveys (e.g. Hillenbrand & Carpenter, 2000; Slesnick et al., 2004; Robberto et al., 2020).

The Serpens star-forming region is located in the Northern sky, at a distance of $\approx$436 pc (Ortiz-León et al., 2017, 2018b). Due to its distance, it is compact on the sky, covering a total area of few square degrees (Eiroa et al., 2008). Within this small area are three main subclusters: Serpens South, Serpens Main and W40. Serpens Main contains Serpens Core, the densely-populated centre of the star-forming region. Serpens Core has been the subject of many surveys, and contains a few hundred candidate members (Herczeg et al., 2019). 3° south of Serpens Main lie W40 and Serpens South. Serpens South was discovered by Gutermuth et al. (2008), and contains a plethora of young stellar objects (YSOs), many of which have circumstellar disks (Povich et al., 2013; Dunham et al., 2015; Getman et al., 2017). Serpens South has been generally less targeted by surveys, in large part due to its higher average visual extinction (Herczeg et al., 2019).

Taurus is one of the most intensely studied star-forming regions, and is part of the Taurus-Auriga association. It is favoured due to its proximity to the sun ($\sim$130–160 pc), low visual extinction and youth - with an age of 1–2 Myr, it is one of the youngest known regions. The literature studies of Taurus are extensive, ranging from studies of massive protoplanetary disks (e.g. Manara et al., 2019; Long et al., 2018), and cloud structure and chemistry (e.g. Seo et al., 2015; Tokuda et al., 2018), to surveys for the lowest mass members. The current number of detected Taurus members is around 500-600 objects (Esplin & Luhman, 2019), with spectral types ranging from late-B to early-L. Initial surveys of Taurus around the start of the millennium were complete down to $\sim$0.01 $M_\odot$ (e.g. Briceño et al., 1998; Luhman et al., 2000; Briceño et al., 2002). Over the next decade, instrumentation improved dramatically, and large surveys of Taurus improved in sensitivity, probing lower masses than ever before (e.g. Luhman, 2004; Todorov et al., 2010, 2014; Esplin & Luhman, 2017; Best et al., 2017; Esplin & Luhman, 2019). Currently, the lowest known Taurus members

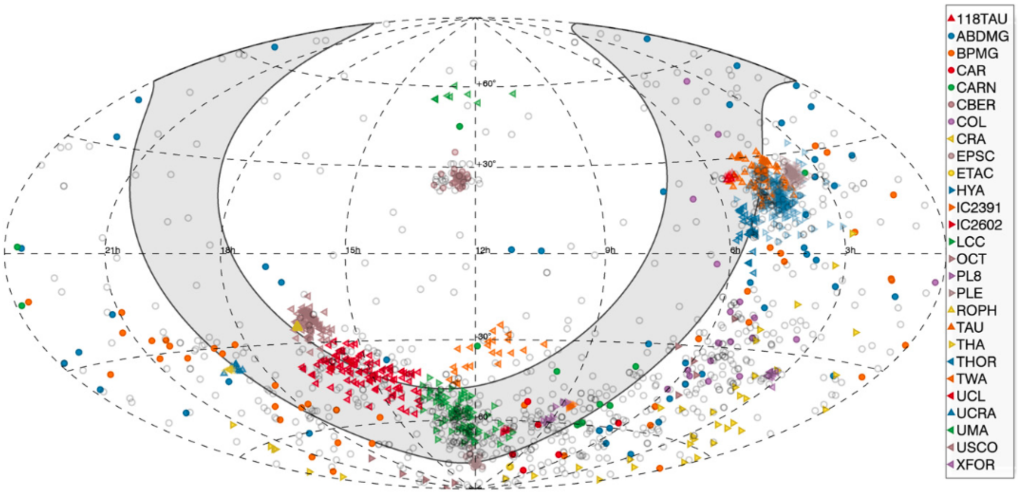

Figure 1.6 *Sky positions of known moving group members, taken from Gagné & Faherty (2018). The Galactic plane (±15°) is highlighted in grey. See Gagné & Faherty (2018) for full moving group names.*

have estimated masses of just a few Jupiter masses (e.g. Luhman et al., 2009; Best et al., 2017; Zhang et al., 2018; Esplin & Luhman, 2019).

1.2.2.2 Moving Groups

Compared to some of the star-forming regions mentioned above, moving groups by nature have less internal structure and fewer sub-associations. They are older than star-forming regions, but are generally closer to the sun.

Ursa Major is one of the best known moving groups, first discovered in 1869. At a distance of 25 pc, it is extremely close (in astronomical terms) to the sun, which would make it a prime target for high contrast imaging studies and YPMO surveys. However, it has an age of 414 Myr (Jones et al., 2015), so despite its proximity, any member YPMOs are likely now too faint to robustly detect. AB Doradus is another of the closest moving groups to the sun, at 20-30 pc, and has a much younger age of 50-100 Myr (Ortega et al., 2007; Barenfeld et al., 2013), meaning it has been well-studied and surveyed (e.g. Zuckerman et al., 2004; Schlieder et al., 2012; Gagné et al., 2015).

The β Pictoris moving group is also nearby (d = 35 pc) and has an age of ~ 23 Myr (Mamajek & Bell, 2014). The name-sake star β Pictoris has a directly imaged planetary companion (Lagrange et al., 2009), and PS0-J318 (a free-floating planet) is also a member of this group (Liu et al., 2013). Due to these previous detections of YPMOs, β Pictoris moving group stars are regularly chosen as prime targets for direct imaging surveys.

The TW Hydrae associtaion is the youngest association within 100 pc of the Sun. It is located at a distance of 60 ± 10 pc and is $\sim$ 10 Myr old (Bell et al., 2015). Tens of members have been confirmed (Gagné et al., 2017), and are generally low-mass. It also contains the name-sake star TW Hydrae, which has a well-studied protostellar-disk with much internal structure (e.g. Calvet et al., 2002; Andrews et al., 2012, 2016).

Finally, the Columba moving group is a well-known example, primarily because it is thought to include the famous HR 8799 system, in which four planets have so far been detected (Marois et al., 2008, 2010). It is approximately 50 pc away, and $\sim$ 40 Myr old. (Bell et al., 2015).

For a very thorough, recent compilation of nearby moving groups, their properties and compendiums of members, see Gagné & Faherty (2018). Figure 1.6 is taken from this work, and shows the on-sky distribution of members of the moving groups described above, as well as many others.

1.3 YPMO Surveys

Astronomical surveys are wide-ranging and varying in scope - from all-sky surveys such as 2MASS (Skrutskie et al., 2006), PanSTARRS-1 (Chambers et al., 2016) and Gaia (Gaia Collaboration et al., 2016b,a, 2018, 2021), to focused surveys of specific compact regions of the Galaxy (Zhang et al., 2018; Robberto et al., 2020; Dubber et al., 2021, e.g.). A large-scale survey is an incredibly efficient way of obtaining astronomical data for a large number of targets simultaneously. Through a strategic choice of technique and filters, one can investigate and characterise both individual objects and entire populations using the same survey dataset.

1.3.1 Photometry

Photometric surveys involve using state-of-the-art telescopes and cameras to take an image of the sky with a specific filter applied, and calculating the magnitude of every object detected in that image. In this way, minimal observing time is needed to measure the properties of large populations. We can build catalogues of regions of the sky by imaging them many times with different filters, each time measuring a different magnitude.

The choice of filter is informed by the science goals of an observation. A broadband filter will have a wide bandwidth (range of wavelengths covered), and therefore enables the collection of lots of light from an object. Broadband filters are standard options for most instruments. The most common set of broadband filters in the optical is the Johnson-Cousins $UBVRI$ system, which have bandwidths of 1000Å. It extends to the $JHKLM$ system in the infrared, which each have a bandwidth of $\sim 1\mu$m. Narrowband filters are logically narrower in bandwidth, and can be used to measure specific spectral features of an object. They are narrow in design so that only this chosen feature is transmitted by the filter, and described by the resulting magnitude. For example (as mentioned in Section 1.1.2.3), brown dwarfs have distinct absorption features, including CO and CH_4 in the infrared. Certain narrowband filters be used to measure this absorption, and allow for comparison and characterisation of different objects based on these particular features.

In an astronomical context, a colour is the difference in magnitude of an object in two different filters. Colours can provide incredibly useful diagnostic information about the object that has been observed.

1.3.1.1 Interstellar Extinction

When we measure the light emitted by an astronomical object, it has likely encountered material in the interstellar medium on its way to us - a major component of this material is interstellar dust. The shorter the wavelength of light, the more affected it is by dust interactions. The consequence of these interactions is that we will measure an artificially reduced intensity at shorter wavelengths, making objects appear ‘redder’ (i.e. as if they have more flux at longer wavelengths) - hence the process of dust extinction being known as ‘reddening’. If we wish to use the spectrum of an object to characterise it, we need to understand the amount of reddening that the light has experienced, in order to ‘undo’ the effect of dust extinction and retrieve the true spectral shape of the object.

To quantify how strongly the extinction varies with wavelength, one can calculate the slope of the extinction law, usually expressed with in terms of visual wavelength R_V:

$$R_V = \frac{A_V}{E_{B-V}} \tag{1.1}$$

where $E(B-V)$ is the colour excess, the difference between the intrinsic and reddened $B-V$ colour. A smaller value of R_V corresponds to a steeper extinction law slope, meaning that shorter wavelengths are more affected and the overall impact is higher reddening. Various studies of the extinction law slope, and the relation between extinction at different wavelengths, have been performed over the last few decades, often focusing on a specific part of the Galaxy or local universe: for example, in the Milky Way (e.g. Cardelli et al., 1989; Fitzpatrick, 1999), the Large Magellanic Cloud (e.g. Fitzpatrick, 1986) and the Small Magellanic Cloud (e.g. Prevot et al., 1984).

The variation in extinction law slopes along different lines of sight is primarily caused by differing dust properties in the local environment. For a typical low-density interstellar medium (ISM) line-of-sight, which contains diffuse dust grains, the value of R_V is approximately 3.1 (Cardelli et al., 1989). This is a standard value used for measurements across the Milky Way, when the intervening material between the observer and the target is thought to be typical of the diffuse ISM. I use this standard value for the analysis presented in this thesis. For lines-of-sight that look through dense clouds, the value of R_V can be significantly larger (e.g. Cardelli et al., 1989), due to the high concentration of dust.

The distribution of interstellar dust varies dramatically across the Milky Way. Figure 1.7 shows the cumulative reddening across the Galaxy within 500pc, calculated by Green et al. (2019). Objects in different parts of the sky, and at different distances, will experience different amounts of extinction, depending on

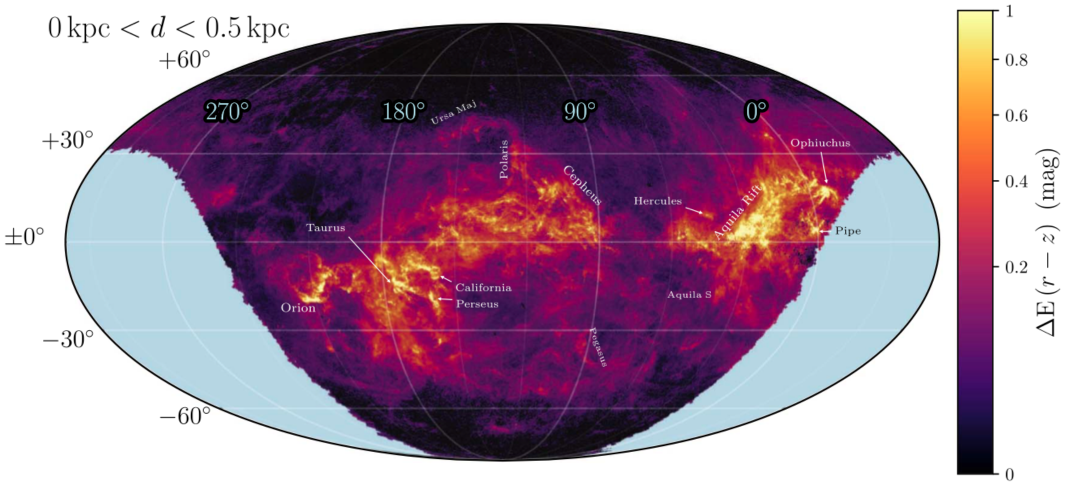

Figure 1.7 *Map of total reddening within 500 pc, taken from Green et al. (2019). In this projection, the Galactic centre is offset to the right, and some major star-forming regions are labelled. Colour map shows the reddening calculated using Gaia, Pan-STARRS 1 and 2MASS (see Green et al., 2019, for more details).*

the intervening Galactic structure. Dust is highly concentrated in the Galactic plane and bulge, and in other localised regions where large, dense clouds are present - in images taken at visual wavelengths, these regions appear as empty dark areas, as very little light from the background stars is transmitted.

1.3.1.2 Photometric Surveys for YPMOs

Studying low-mass objects is a numbers game: the initial discovery of YPMOs is recent (compared to high mass stars), and they are intrinsically hard to detect, a combination of factors causing the size of the YPMO population to remain relatively small. When statements are made about the properties of these objects, they are based on this small sample, which makes them inherently uncertain. A higher degree of confidence in our knowledge of these objects requires a large population of them to study. As a result, surveys intending to discover new YPMOs tend to start from photometric data: efficiency is key.

Photometric surveys target specific parts of the sky where many YPMOs are likely to exist in a compact region, aiming for a high yield of low-mass objects from a small number of images. Such regions include star-formation regions and moving groups (see Section 1.2). Others make use of all-sky survey data that is open-access, focusing on one or multiple regions for their analysis, using photometry that is already available. The former can ultimately be a longer process, but allows for customisation that can lead to high success rates, including custom narrowband filters (see Section 1.3.1.4).

A photometric catalogue will contain a multitude of objects, from the lowest-mass brown dwarfs to distant, faint galaxies, so distant that they appear as point sources. Sorting through the wealth of data in a catalogue to find the intended targets of a survey is no trivial task: identification of YPMOs is a difficult, time-consuming process. Typically, a photometric catalogue is the starting point for selecting targets appropriate for further investigation (i.e. that appear to be young and low-mass). However, a significant proportion of these objects can turn out to be false positives. Late-type field brown dwarfs that have the expected YPMO spectral features, but are actually far older than members of star-forming regions, can be erroneously selected using photometric colours. In regions of high extinction, background stars can be reddened such that their broadband colours look very similar to those of real young cluster members. Consequently, relying solely on standard photometric data for candidate identification can lead to wasted follow-up observations. It is important to employ other techniques to better understand the properties of candidate objects prior to further observations.

1.3.1.3 Combining Photometry and Astrometry

Astrometry involves precise measurement of the positions and motions of objects on the sky. At a fundamental level, it gives astronomers a frame of reference for observations. Beyond this, it allows us to look for anomalies in the motion of objects, to group objects into co-moving clusters and to track the orbits of imaged exoplanets, to name but a few applications. Astrometry and photometry are often calculated simultaneously, as photometric detections of objects are used to determine their astrometric positions.

The HIgh Precision PARallax COllecting Satellite (HIPPARCOS) mission (ESA, 1997; Perryman et al., 1997) was the first space telescope dedicated to precision astrometry. It measured the brightness, positions and distances of millions of stars. Distance is calculated using parallax, the change in position of an object due to the motion of the observer i.e. the orbit of the Earth around the sun. Another parameter provided by HIPPARCOS is proper motion, which describes the overall motion of a star on the sky, compared to more distant, approximately stationary objects. Data from the HIPPARCOS satellite was revolutionary, with precise stellar positions and distances allowing for dramatic progression in many fields, including studies of nearby stellar associations (e.g. De Zeeuw et al., 1999), the structure and kinematics of the Milky Way (e.g. Dehnen & Binney, 1998; Fuhrmann, 1998) and Cepheid variables (e.g. Feast & Catchpole, 1997; Feast & Whitelock, 1997).

Data from the Gaia satellite, the successor to HIPPARCOS, was first released in 2016 (Gaia Collaboration et al., 2016b,a). Gaia DR1 contains magnitudes for a billion stars, and parallaxes, proper motions and positions for millions of these, dramatically surpassing the coverage of HIPPARCOS, and offering far superior precision. Gaia DR2 (Gaia Collaboration et al., 2018) was released 2 years later, and contains more parallaxes, proper motions and positions, as well as greater general precision. Gaia eDR3 is detailed in Gaia Collaboration et al. (2021), and contains further improvements to previous measurements. The implications of the Gaia dataset have been vast, and have enabled us to map our Galaxy at an unprecedented resolution (e.g. Bailer-Jones et al., 2018; Cantat-Gaudin et al., 2018; Green et al., 2019).

Gaia has also proven incredibly useful in characterising YPMOs, namely in allowing estimations of age based on membership of specific groups. Membership confirmation of previously ambiguous objects can be achieved by looking at proper motion relative to other known group members. Gagné et al. (2018) and Gagné & Faherty (2018) used Gaia data to discover hundreds of new, highly-likely members of nearby young associations. Esplin & Luhman (2017) used Gaia in combination with other instruments to identify 18 new members of the Taurus star-forming region, with spectral types ranging from mid-M to early-L.

1.3.1.4 Custom Filters

There are a multitude of ‘standard’ filters used to measure magnitudes, defined in a uniform way across different telescopes and facilities. These cover the full range of the electromagnetic spectrum. Often, standard filters are sufficient for a survey

- i.e. they can accurately target the spectral features of interest. However, if the desired spectral feature is not well-covered by the standard filters, it is possible to create a custom photometric filter at the desired wavelength, designed to measure a specific property of an object.

Using custom filters for photometric detection of brown dwarfs was first pioneered as a technique by Najita et al. (2000). They made use of water absorption in the photospheres of brown dwarfs (with spectral types late-M or later). They used three narrow-band filters on the Hubble Space Telescope/NICMOS imager, with one centred on the water absorption feature at 1.9μm, and the first and third measuring continuum flux either side. After imaging the IC 348 cluster, which has typical extinction values of $A_{\mathrm{v}} = 5-10$, they were able to effectively separate low-mass members from the field population. Similarly, Mainzer & McLean (2003) used FLITECAM (Mainzer et al., 2003), a camera equipped with a range of filters, some designed for the detection of water and methane. They used two of these filters, positioned at 1.495 and 1.6 μm, respectively, with widths of 0.1 μm, and a H-Band continuum filter. They also surveyed IC 348, and used a colour-colour diagram to identify YPMO targets, finding 18 candidate brown dwarfs.

The W-band survey (Allers & Liu, 2020; Jose et al., 2020; Dubber et al., 2021) operates using similar principles to these two examples. A custom medium-width infrared filter is used, centred at 1.45 μm, the location of a deep water absorption feature in the spectra of young brown dwarfs. In this instance, a reddening-insensitive index, Q, is calculated, which can be used to distinguish between high- and low-mass objects. To date, the W-band technique has been used to survey the Serpens (Jose et al., 2020; Dubber et al., 2021) and Taurus (Biller et al, in prep) star-forming regions.

1.3.2 Spectroscopic Follow-up

Spectroscopy involves using broad wavelength ranges to maximise the information returned by an observation. Collected light is dispersed using a prism or grating (or a grism, a combination of the two) into a spectrum. As discussed in Section 1.1.2.3, spectra can contain absorption and emission features at specific wavelengths. One can use knowledge of which elements cause which of these spectral features to examine the composition of objects.

The above description is the basic motivation for obtaining follow-up spectroscopic observations of objects, after they have been identified photometrically. Photometric surveys are great for obtaining a small amount of information on a huge number of objects. For example, one could obtain a catalogue containing 5 different magnitudes for every observed object. These magnitudes can then be used to loosely characterise a property of the object - i.e. is it likely a brown dwarf? Or a higher mass star? However, as discussed above, using photometry alone for characterisation can be insufficient. As a result, it is common practice to obtain a spectrum of an object to fully confirm its nature.

This is the approach typically used when searching for YPMOs (e.g. Luhman et al., 2017; Zhang et al., 2018; Jose et al., 2020; Dubber et al., 2021). It would be fair to question why spectroscopy is not obtained for all objects in a catalogue as standard. This is possible (using an instrument called an Integral Field Spectrograph), but is very observationally intensive, requiring a large amount of telescope time. Consequently, most studies do not rely on this technique, instead being selective with their choice of targets.

1.3.3 Direct imaging

If the science goals of a survey are to obtain as much information as possible about every target, direct imaging is an excellent option. As a technique, it is ideally suited for detecting and characterising wide-orbit planets and brown dwarf companions ($>$ 10 AU, 10 M_J, see Figure 1.4). With long enough temporal baselines, we can also learn about the orbital motion of these objects, and which formation scenarios are viable.

Conducting a direct imaging survey is a challenging task - the difference in brightness of a star and planet can be on the order of 10^{-10}, for an Earth-like planet (Trauger & Traub, 2007). It is less dramatic for a Jupiter-like planet: but still $\sim 10^{-9}$ for a 1 M_J planet at a distance of 10 pc, $\sim$ 0.5 arcseconds from its host star. To reach these extreme contrasts, in addition to the complex coronagraphs discussed in Section 1.1.3.2, ground-based instruments use Adaptive Optics (AO) systems to remove atmospheric distortion and speckle patterns (bright spots in the image which can vary over both short and long timescales, Marois et al., 2006). Current direct imaging instruments that combine AO and coronagraphs can achieve contrasts of 10^{-5}–10^{-6}, and resolve separations of 0.5” (e.g. Macintosh et al., 2014).

1.3.3.1 A History of Surveys

At the start of the 21st century, the first instruments designed specifically to detect giant exoplanets via direct imaging came online. This first generation of instruments used innovative AO systems to suppress speckle noise. These instruments were used for surveys that targeted tens of nearby host stars, and did not detect any planetary companions (e.g. Masciadri et al., 2005), but achieved a typical contrasts of Δ(mag)$\sim$ 8 at 0.5” (meaning planets could be detected that were approximately 8 magnitudes fainter than their host star, and at separations of approximately 0.5 arcseconds). Such surveys were able to place observationally-derived constraints on the frequency of giant planets for the first time. The next generation of instruments made use of advancements in speckle suppression techniques, and were used for slightly larger surveys ($\sim$50-100 stars, e.g. Biller et al., 2007; Lafrenière et al., 2007a). Coronagraphs were implemented on the subsequent generation of instruments, including the Near-Infrared Coronagraphic Imager (NICI; Chun et al., 2008) at Gemini South. Direct imaging surveys that used these instruments typically observed $>$ 100 stars, and achieved typical contrasts of Δ(mag)$\sim$ 12 at 0.5”. Many new brown dwarf companions (e.g. Bowler et al., 2013; Brandt et al., 2014) and a handful of planetary-mass companions (e.g. Rameau et al., 2013b) were found as a result, demonstrating how crucial coronagraphy is for successful high-contrast imaging.

Progression in the design and implementation of coronagraphs played a large part in the improvement between these first generations of instruments, but was by no means the only technical advancement that aided instrumental progress. AO systems make use of densely packed actuators, that each move a small section of a deformable mirror in order to mimic small wavefront variations (Beckers, 1993). These systems have evolved dramatically since their initial deployment on telescopes, in both the number of actuators or deformable mirror segments, and the speed with which the system can respond to wavefront changes (e.g. Close et al., 2012). Other progress has been made in the challenging task of removing speckles that vary on very long timescales (caused by aberrations in instrument optics). These techniques are applied either during data acquisition, or in postprocessing: for example, the Angular Differential Imaging technique (ADI; Marois et al., 2006), Locally Optimised Combination of Images for PSF-subtraction (LOCI; Lafrenière et al., 2007a), and the KL Image Projection algorithm (KLIP; Soummer et al., 2012), which uses principle component analysis.

The current generation of high-contrast imaging instruments contain custom-built, extreme AO systems, and have spectroscopic capabilities. Two key examples are the Gemini Planet Imager (GPI; Macintosh et al., 2014) and SPHERE (Beuzit et al., 2019), both of which have been used for the largest direct imaging surveys ever conducted, observing hundreds of target stars each. The first results of these surveys have now been published, achieving typical contrasts of Δ(mag)$\sim 13 - 14$ at 0.5”. The GPIES survey, which uses GPI and targeted 100 Myr – 1 Gyr old stars within 70pc, reported 3 brown dwarf detections, 1 new planet and 5 re-detections from a sample of 300, and used these to investigate planet occurrence rates (see Section 1.1.3.4). Analysis from the first 150 stars of the SHINE survey (most of which are moving group members), which uses the SPHERE imager on the VLT, has now been released, detailing 16 detections or re-detections of planet and brown dwarf companions (Langlois et al., 2021; Desidera et al., 2021; Vigan et al., 2021). The sheer quantity of observed stars in these surveys is proving incredibly enlightening for analysis of the overall properties of giant planet and brown dwarf populations.

1.3.3.2 Future Surveys

The overall lack of exoplanet detections by ongoing and historical surveys suggests that, despite the major improvements in instrumentation and data reduction techniques over the last two decades, there is still progress to be made in the field of high-contrast imaging. Funding bodies appear to agree, and backing has been given to many planned instruments, as well as some coming on line in the very near future.

The James Webb Space Telescope (JWST) is a state-of-the-art instrument due to begin observing in 2022, which has coronagraphic capabilities. The Near-InfraRed Camera (NIRCam Rieke et al., 2005) contains multiple coronagraphic masks, and will make use of the high levels of infrared flux (0.6–5 μm) emitted by young giant planets. The likely performance of JWST has been modelled by

Carter et al. (2021), who find that JWST will be able to measure companions with $m \approx 0.1$ $\mathrm{M_J}$ beyond ∼100 AU - a considerable improvement over the sensitivity of current ground-based instruments. Beyond JWST, the Nancy Grace Roman Space Telscope (formerly WFIRST) is scheduled for launch in 2027, and will contain the Coronagraphic Instrument (CGI; Noecker et al., 2016). The CGI will provide visible-light imaging capabilities and low-resolution spectroscopy, allowing characterisation of giant planets in a relatively unexplored wavelength range (e.g. Lacy et al., 2019; Lacy & Burrows, 2020).

The prospects for ground-based instruments are just as bright. Future upgrades to both GPI (Chilcote et al., 2018, 2020) and SPHERE (Boccaletti et al., 2020) will enable these existing instruments to achieve better contrasts and detect even lower-mass objects. Multiple Extremely Large Telescopes (ELTs) are currently being built (namely the ELT, the Giant Magellan Telescope (GMT), the Thirty Meter Telescope (TMT)), with first light planned for the end of this decade. The ELT (previously the E-ELT) contains the METIS instrument, a mid-infrared imager and spectrograph operating from 3–14 μm (Brandl et al., 2010, 2014), which will likely be able to directly-image radial velocity planets for the first time (Quanz et al., 2015).

Considering much longer timescales, in the next 20 years development will begin for a number of space missions specifically designed to improve our high contrast imaging capabilities. With concept studies such as HabEx (Mennesson et al., 2016; Gaudi et al., 2020) and LUVOIR (Roberge & Moustakas, 2018; The LUVOIR Team, 2019) providing the groundwork, we may be able to image super-earths and even earth-mass planets for the very first time.

1.4 The Initial Mass Function

1.4.1 An Overview of Previous Studies

The initial mass function (IMF) is an empirical function that describes the distribution of stellar masses at the point of formation. Distinct from the present day mass function, which is affected by stellar evolution and the deaths of high mass stars, the IMF is a direct consequence of the star formation process.

The initial mass of a star determines its luminosity, lifetime and colour. In general, the IMF has a declining power-law shape for masses above a characteristic peak (with an approximate slope of -1.35, Bastian et al., 2010), and a flatter slope for masses below this peak, down to some minimum mass value. The peak of the initial mass function (i.e the most prevalent stellar mass at the point of formation) is thought to be dictated by the thermodynamic behaviour of the star-forming interstellar gas, but the exact mechanisms that affect this value are still being investigated (reviewed recently by Colman & Teyssier, 2020). It has typically been found to range from 0.2 $M_{\odot}$ to 0.3 $M_{\odot}$. The highest stellar mass often adopted in IMF parameterisations is $\sim$150 $M_{\odot}$, as derived by Zinnecker & Yorke (2007), who found this to be upper mass limit of stars in massive clusters within the Milky Way and LMC. The form of the low-mass end of the IMF, and the minimum mass value, are highly debated topics (see Bastian et al., 2010, for a review), due to the ongoing uncertainty surrounding brown dwarf formation, and the dividing line between the lowest-mass brown dwarfs and the highest-mass planets.

Salpeter (1955) was the first to quantify the 'rate of star creation as a function of stellar mass', in a truly ground-breaking work that made use of the observed Galactic luminosity function. The initial mass function derived predicted that the number of stars in a mass bin would decrease rapidly with increasing mass. Salpeter (1955) found that this relation was consistent with a power law, valid between $\sim$0.4 $M_{\odot}$ and $\sim$10 $M_{\odot}$. Miller & Scalo (1979) built on this work by studying the form of the initial mass function for objects with < 1 $M_{\odot}$, and suggested that it flattened for masses below this transition value. This can be seen in Figure 1.8, which shows some of the most commonly used IMF parameterisations.

Since these initial studies, observational and theoretical studies of the IMF have progressed in tandem, but some key questions persist: what is the functional form of the IMF across a wide range of stellar masses? Is the IMF universal, or does it vary in different environments within the universe? Two landmark studies into the functional form of the initial mass distribution were conducted by Kroupa (2001) and Chabrier (2003).

Kroupa (2001) present a power law IMF function, with distinct slopes separated by transition masses. These masses define the stellar/substellar boundary, and the boundary between low-mass and high-mass stars (Kroupa, 2001). They find that number of stars, $\xi(m)$, varies with mass according to:

$$\xi(m) \;\propto\; m^{\alpha_i}, \tag{1.2}$$

where:

$$\begin{aligned}
&\alpha_0 = -0.3 \pm 0.4,\; 0.01 \leq m/M_{\odot} < 0.08,\\
&\alpha_1 = -1.3 \pm 0.5,\; 0.08 \leq m/M_{\odot} < 0.5,\\
&\alpha_2 = -2.3 \pm 0.3,\; 0.5 \leq m/M_{\odot} < 1.00,\\
&\alpha_3 = -2.3 \pm 0.7,\; 1.00 \leq m/M_{\odot}
\end{aligned} \tag{1.3}$$

Chabrier (2003) present a log-normal form of the IMF, a combination of an exponential function and power law, again with a specific transition mass. For disks and young clusters:

$$\begin{aligned}
\xi(\log m) \;&= m^{\alpha_H},\; m > m_H\\
&\quad k\, e^{\frac{-(\log m - \log m_c)^{\,2}}{2\sigma^2}},\; m \leq m_H
\end{aligned} \tag{1.4}$$

where:

$$\begin{aligned}
&m_H = 1.0\\
&\alpha_H = -1.3\\
&k = 0.158^{+0.051}_{-0.046}\\
&m_c = 0.079^{0.021}_{-0.016}\\
&\sigma = 0.69^{0.05}_{0.01}
\end{aligned} \tag{1.5}$$

These two functional forms have been the basis for many subsequent studies of the IMF, which often compare newly derived results to these original parameter values (e.g. Alves de Oliveira et al., 2013; Gennaro & Robberto, 2020).

The IMF is an outcome of star formation, and describes the state of a population at the moment when it first formed - how do we measure such a precise epoch? The answer is to observe both direct and indirect consequences of the IMF,

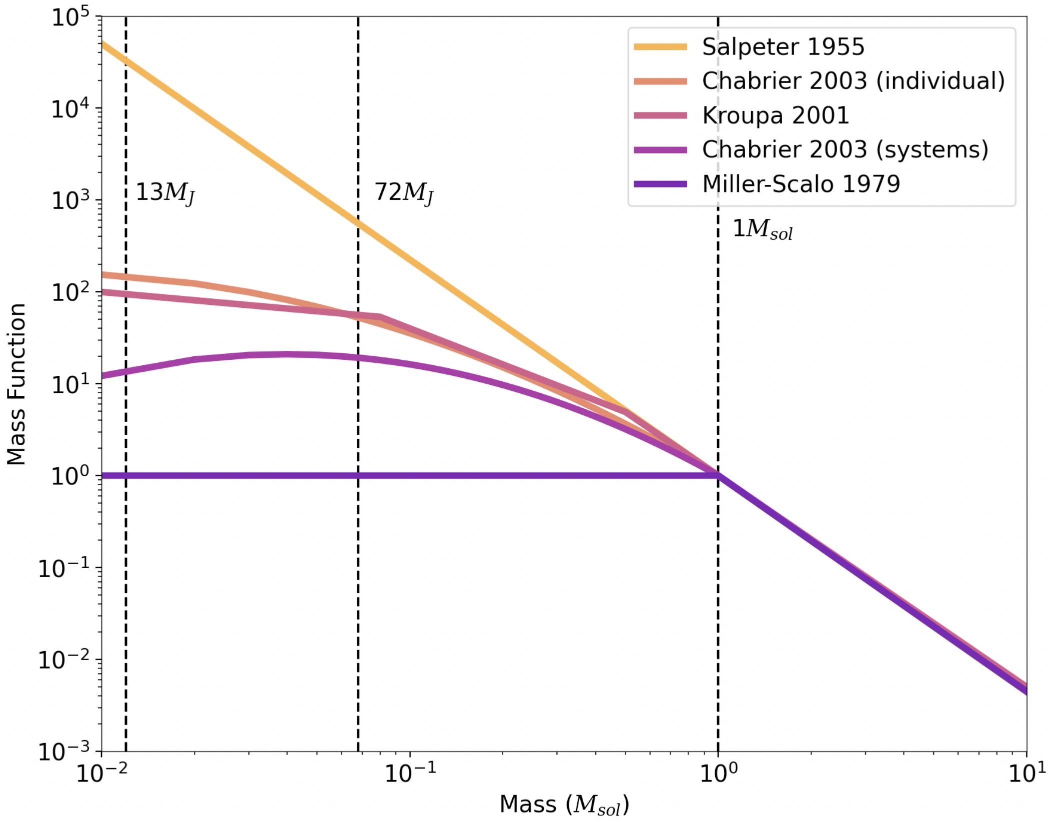

Figure 1.8 *Commonly-used IMF functional forms. Salpeter (1955),Miller & Scalo (1979),Kroupa (2001) and Chabrier (2003) initial mass functions are shown, over a 0.01-10* $M_\odot$ *range. The approximate brown dwarf mass range, 13–72* M_J*, is indicated by the vertical lines.*

and subsequently infer its properties: for example, using stellar kinematics (e.g. Cappellari et al., 2012; Guo et al., 2020), gravitational lensing (e.g. Treu et al., 2010; Sonnenfeld et al., 2012) or chemical abundance constraints (e.g. Audouze & Tinsley, 1976; Lucatello et al., 2005; Komiya et al., 2007). Hopkins (2018) presents a thorough summary of different observational techniques, as well as a general overview of IMF research.

The multitude of different techniques that can be used to measure the IMF has led to an abundance of seemingly conflicting results - e.g. 'top-heavy' or 'bottom-heavy' IMFs, with an over-abundance of either high-mass or low-mass stars compared to the 'universal' form. However, different techniques often measure different properties, covering different timescales of star formation and different spatial scales - because of this, it is possible that 'conflicting' results aren't actually conflicting. It is difficult, if not currently impossible, to measure the full range of the IMF in one cluster (a quandry highlighted by Elmegreen, 2009): to detect the highest mass stars, one needs to observe a very massive cluster - these are rare, and the closest is too distant to detect the lowest mass stars. However, to cover the full mass range, these low-mass stars need be detected in large numbers - we can only do this in nearby clusters that don't contain the highest mass stars! A solution to this problem may be afforded by the next generation of instruments (e.g.ELTs, JWST), which will provide better sensitivity in distant clusters - but this is currently beyond our observational capabilities.

1.4.2 Environmental Dependence and Local variation

The discussion of the possible environmental dependence of the IMF has been a fiercely debated topic for decades.

If one considers the process of a star-formation event, the collapse of a molecular cloud that forms local high-density clumps that accrete matter, one can see where physical properties of the cloud could affect the mass distribution of the objects that form. Taking two hypothetical clouds, one with a higher temperature and pressure than the other, you would fundamentally expect the higher temperature cloud to produce a distribution of stars with higher average stellar masses (Larson, 1998). The temperature of a cloud is dictated by its surroundings, and could be increased by variety of local events, including the deaths of massive stars, flares and solar winds. Additionally, the low-mass stars could have their formation affected by the strong UV winds of OB stars, which can destroy their accretion envelopes (Kroupa, 2001). This basic physical interpretation of environmentally-impacted star formation is what motivates the question of a universal vs environmentally-dependent IMF.

The default historical assumption when considering IMF variation tends to be universality i.e. a constant IMF regardless of environment or moment in cosmic history. This is often the default stance because it is the simplest, and there is a lack of strong, consistent evidence supporting environmental dependence. The 'universal' assumption allows for easy comparison between different Galactic populations, and the calculation of quantities such as stellar mass and star-formation rate (Hopkins, 2018). However, there are various observational anomalies that could point to a possible environmental dependence of the IMF. The G-dwarf problem, the phenomenon that fewer metal-poor G-type stars are observed in the solar neighbourhood than models predict (e.g. Rocha-Pinto & Maciel, 1996; Nordström et al., 2004; Caimmi, 2008), is one such example. It has been observed in other high-mass spiral galaxies (e.g. Worthey et al., 1996; Greener et al., 2021), and could potentially be explained by a 'top-heavy' IMF. Other observational anomalies have been seen, in particular when looking further afield to distant galaxies. The spectra of massive early-type galaxies have been found to vary from predictions based on a Milky Way-like IMF, and suggest a bottom-heavy IMF (e.g. Van Dokkum & Conroy, 2010; Ferreras et al., 2013).

When considering only the low-mass end of the IMF, studies searching for environmental dependence tend to focus on compact, young regions. Star-forming regions and moving groups are excellent targets for such studies, as they contain populations of objects that formed simultaneously, and, in the youngest regions, are all still present. They also present some challenges: as discussed above, the closest groups are not massive enough to contain higher mass stars, and the youngest groups may still be actively star-forming, so may not yet contain a full range of masses. Regardless, many studies have aimed to obtain full compilations of low-mass members of specific regions. Notable examples include: Esplin & Luhman (2019), who provide an up-to-date membership list of the Taurus star-forming region and assess the local IMF; Da Rio et al. (2012), who assign masses and ages of objects down to 0.02 $M_\odot$ in the ONC; Gennaro & Robberto (2020), who present a HST survey of the ONC and derive an IMF consistent with both

Kroupa (2001) and Chabrier (2003).

Using a photometric catalogue of a compact, well-defined region, it is possible model the local form of the IMF and extract the best-fit parameters. To do this, one must first isolate the likely members of a cluster from any contaminant objects that may be present in the photometric catalogue. After obtaining a sample of objects that likely belong to a cluster, and were thus formed at the same time/during the same burst of star-formation, one can derive the mass function that describes this population.

1.5 Thesis Outline

The work presented in this thesis uses a variety of observational techniques, with the aim of detecting new YPMOs and characterising populations in different regions of the Galaxy.

In Chapter 2, I present the results from a survey of the Serpens star-forming region, conducted using the W-band custom filter that can be used to identify low-mass brown dwarfs via water absorption features in their spectra. I describe new detections of likely low-mass Serpens members, and the discovery of a brown dwarf binary system using high-resolution imaging data.

In Chapter 3, I describe the process and conclusions of an investigation into an optimal survey strategy using a custom filter on the new ERIS/NIX instrument. I consider a variety of possible targets for such a survey, and describe the design and useful properties of the custom K-peak filter.

In Chapter 4, I use photometric data to investigate the form of the IMF in the Taurus star-forming region. By combining W-band and Gaia photometry, I identify likely members of Taurus, and use an MCMC model to find the best-fit IMF parameters and functional form. I then compare this outcome to results from other studies, to investigate the universality of the IMF.

2

Searching for very low-mass brown dwarfs in Serpens South and Serpens Core

2.1 Introduction

Nearby young star-forming regions, such as Perseus (Bally et al., 2008), Taurus-Auriga (Kenyon et al., 2008), Serpens South (Gutermuth et al., 2008) & Chamaeleon (Luhman, 2008), have been extensively surveyed with the goal of discovering low-mass members. A key motivating factor for such a survey is to improve the understanding of the statistical properties of stellar populations.

The initial mass function (IMF) is an empirical function that describes the distribution of stellar masses at formation. Discovering low-mass members of star-forming regions constrains the substellar IMF in such clusters, which can then be directly compared to the substellar IMF in the local solar neighbourhood (Kirkpatrick et al., 2019). The IMF may be environmentally dependent (e.g. Van Dokkum & Conroy, 2010; Lu et al., 2013; Gennaro et al., 2018; Hosek et al., 2019), meaning investigations of its form in specific regions are crucial. Furthermore, different theories predict different values of the minimum mass (e.g. Larson, 1992; Whitworth et al., 2007), highlighting the importance of finding the lowest-mass members in every region.

There are other motivations to push detection thresholds into the planetary-mass regime in young star-forming regions. Planetary-mass brown dwarfs are often targets of atmospheric investigations (e.g. Knapp et al., 2004; Saumon et al., 2006; Cushing et al., 2008). They can be studied as analogues of directly-imaged planets, and increase our understanding of a different part of the temperature-surface gravity grid. Investigating the full range of possible atmospheric parameters is key in understanding how planets and brown dwarfs form and evolve. Doing so again requires a large sample of such objects.

Surveys of star-forming regions have predominantly used optical and infrared (IR) photometry to identify young, very low-mass members. Wide-field surveys such as 2MASS (Skrutskie et al., 2006), PanSTARRS (Chambers et al., 2016), and WISE (Wright et al., 2010) play a crucial role in initial photometric identification. Typically, survey objects are placed on colour-magnitude diagrams, with the parameter space chosen such that late- and early-type populations lie in (somewhat) distinct regions (e.g. Briceño et al., 2002; Luhman, 1999; Rebull et al., 2010). Spectroscopic follow-up is then used to confirm the spectral type of suspected late objects, and to constrain their physical properties. This method is challenging as interstellar reddening by dust changes the observed properties of objects. This can cause the spectra of older, background stars in the field to be reddened to the extent that they have extremely similar colours to young brown dwarfs that are bonafide members of the star-forming region. As a result, spectroscopic follow-up can often reveal that objects chosen photometrically are in fact contaminants - and surveys identifying candidates in this way can suffer from low confirmation rates. In cases where photometry can be combined with proper motion information or additional photometric bands, confirmation rates can be much higher (e.g. Zapatero Osorio et al., 2017; Lodieu et al., 2018, $\approx 80\%$,) The W-band technique uses standard *J*- and *H*-bands in combination with a custom medium-band (6%) IR filter centred at 1.45 μm (Allers & Liu, 2020), the W-band. The filter is located at a wavelength that is sensitive to the depth of the H_2O absorption feature present in objects with spectral types of M6 or later, the approximate stellar/substellar boundary in typical star-forming regions (Alves de Oliveira et al., 2010). Photometry from these three bands can be combined to calculate a reddening-insensitive index, Q, which can be used to distinguish between early- and late-type objects. The calculated Q-values are used to identify candidates for spectroscopic follow-up, greatly improving the success rate of detecting brown dwarfs (Allers & Liu, 2020; Jose et al., 2020).

This Chapter forms part of the W-band series. In the first W-band paper, Allers & Liu (2020) present the initial proof-of-concept results, and report a confirmation rate of 84% for the initial W-band survey - comparable to other surveys that use many more photometric bands. In the second, Jose et al. (2020) present the first results from the W-band survey of Serpens South. In this work, we present full results from the W-band survey of Serpens South and Serpens Core. The Serpens star-forming region is more distant than other frequently-observed nearby regions ($d = 436.0 \pm 9.2$ pc, Ortiz-León et al. (2017, 2018b)) and highly attenuated by dust (generally Av = 10–30 mag, see Section 2.2). However, it is also young ($\sim$0.5 Myr), compact and active in star-formation. The first candidate L-type dwarf member was reported in 2002 (Lodieu et al., 2002), and further deep IR photometric surveys (e.g. Klotz et al., 2004; Spezzi et al., 2012) have each reported candidate low-mass objects in Serpens Core. Winston et al. (2018) detail a recent survey dedicated to finding the lowest mass members of Serpens South, reaching a lower mass limit of ≈ 0.1 $M_\odot$. In the second W-band paper, Jose et al. (2020) present the first survey dedicated to finding ultracool dwarfs (the very lowest mass stars, brown dwarfs and planetary-mass objects) in Serpens South. As such, the four discoveries presented in Jose et al. (2020) are the coolest and lowest mass candidate members of Serpens South identified to date. In this work, we use the same photometric catalogue of Serpens South as Jose et al. (2020), and present follow-up of new targets.

We describe the properties of Serpens South and Serpens Core in Section 2.2, and explain the Q-index in Section 2.3. We present the observations undertaken in Section 2.4, which include: photometry obtained using the W-band filter on the Canada-France-Hawaii Telescope (CFHT), follow-up spectroscopy using SpeX on

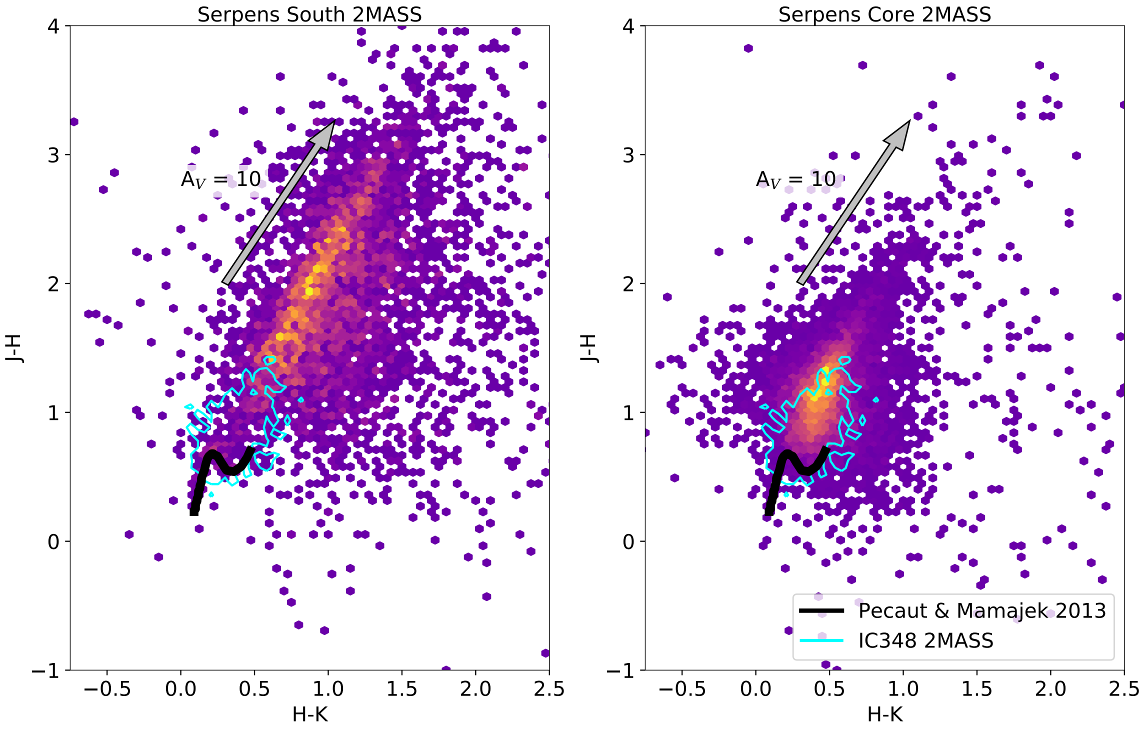

Figure 2.1 *2MASS* $J - H$ *vs* $H - K$ *colour-colour diagrams for Serpens South (left) and Serpens Core (right). Binned colour-colour number density distributions of objects in each region detected by 2MASS are shown, with yellow indicating the highest density of sources. Also shown in each panel is the* $A_V = 10$ *extinction vector (grey arrow). The black (thick) line is the intrinsic colour sequence of G-M stars from Pecaut & Mamajek (2013), and plotted in cyan (thin) is a 1*σ *contour of objects in the IC348 star-forming region, again obtained using 2MASS.*

the NASA Infrared Telescope Facility (IRTF), and imaging of a subsample of objects obtaining using the Hubble Space Telescope (HST). In Section 2.5, we consider the effects of dust attenuation on our survey results. In Section 2.6, we discuss the late-type candidate members of Serpens South and Serpens Core discovered in this work, as well as their physical properties. Finally, we present the results for a newly discovered binary system, identified using our HST data.

2.2 The Serpens star-forming Region

Serpens is a highly compact, highly dust-attenuated region containing at least 2000 stars (Herczeg et al., 2019). The physical properties of the cluster vary significantly across its extent. Furthermore, the region has low proper motion, and is located near the Galactic plane. Both factors present significant challenges when searching for young, low-mass objects in this region. Proper motion selection of candidates is nearly impossible, and there are more background contaminant objects compared to other areas of sky.

The Serpens Core subcluster is part of Serpens Main, historically the best studied part of the complex (see Eiroa et al., 2008, for a detailed review of Serpens Core). Serpens Main is actively star-forming, with a few hundred known candidate members. Herczeg et al. (2019) report optical counterparts for many of these members. The Serpens South subcluster, discovered by Gutermuth et al. (2008) in a *Spitzer* survey, lies approximately 3 deg south of Serpens Main in a separate cloud (Herczeg et al., 2019). It contains a large fraction of protostars (77%, Gutermuth et al., 2008), and Herczeg et al. (2019) find that few of these have optical counterparts, suggesting this region may be younger than the other Serpens subclusters. The distance to Serpens remains a topic of debate, with accepted values ranging from $\approx 260 - 460$ pc (see Winston et al., 2018, for a detailed review of recent distance estimates to Serpens South and Serpens Core). Whilst the two regions are known to be spatially distinct, various works have shown that the radial extent of the Serpens cloud is small, and as such we adopt the same distance for both subclusters, $d = 436.0 \pm 9.2$ pc (Ortiz-León et al., 2017, 2018b).

Stars in the Serpens star-forming region are affected by high levels of dust extinction (Herczeg et al., 2019). To quantify this, and to investigate any differences between the two subclusters, we compared their 2MASS (Skrutskie et al., 2006) colour-colour diagrams. Using the same survey areas as our CFHT photometric observations (see Section 2.4), we found 2MASS $J - H$ and $H - K$ colours for all objects detected in these fields. Figure 2.1 shows colour-colour number density plots for Serpens South (left) and Serpens Core (right) (where the brightest areas indicate the highest density of objects). Also shown is the intrinsic colour sequence for G-M stars given in Pecaut & Mamajek (2013). A_{V}

= 10 extinction vectors are plotted, along with the 1σ contour of objects from a 2MASS query of the IC348 star-forming region, which has comparatively low extinction ($A_{\rm V} \approx 1 - 7$; Herbst, 2008).

When examining the colour-colour diagrams in conjunction with this additional information, the high extinction of both subclusters is clear. Both 2MASS distributions extend well above the low extinction contour of IC348 and the intrinsic G-M colour sequence, suggesting high values of extinction for many objects. We can quantify the approximate peak extinction values by comparing to the average intrinsic $J - H$ colour of the Pecaut & Mamajek (2013) sequence, $J - H \approx 0.5$. We can see from Figure 2.1 that the maximum value of $J - H$ for sources in Serpens South is ≈ 3.25 (not including a scattering of bins populated by just one object that are above this value), and is similarly ≈ 2.5 for Serpens Core. This is equivalent to a colour excess $E(J - H) = 2.75$ mag and $E(J - H)$ = 2.0 mag for Serpens South and Serpens Core respectively, when compared to the intrinsic colours from Pecaut & Mamajek (2013). Using the extinction law of Fitzpatrick (1999) we can convert these colour excesses to approximate upper limits on the extinction in each region: $A_{\rm V,max} \approx 33$ for Serpens South, and $A_{\rm V,max} \approx 24$ for Serpens Core. This is comparable to the results obtained from analysis of our own photometric catalogue, discussed in Section 2.5 (extinction maps shown in Figure 4.6).

2.3 The Reddening Insensitive Index (Q)

2.3.1 CFHT Photometry

For the W-band photometric survey of Serpens, we used the WIRCam instrument on CFHT (Puget et al., 2004). We imaged the Serpens South and Serpens Core fields across 5 nights in 2016-2017. The W-band method uses a custom filter at 1.45 μm combined with standard CFHT J and H photometry to build a reddening insensitive index, Q. Our custom filter is centred on the 1.45 μm H_2O absorption feature, the depth of which is an indicator of spectral type (SpT). The construction of the Q-index is explained in detail in Allers & Liu (2020). For each

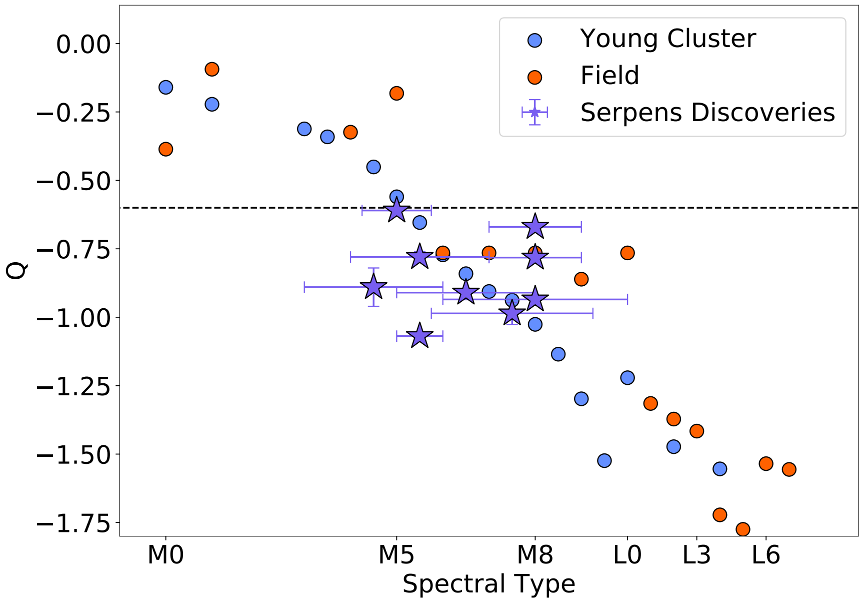

Figure 2.2 *Q vs SpT for field objects and young cluster members. Orange shows the synthetic Q values of field-age standards of varying spectral types, taken from the SpeX spectral library (Cushing et al., 2005; Rayner et al., 2009). Pink shows the synthetic Q values of young, low surface gravity standards (Luhman et al., 2017), modelled at the distance of Serpens. Purple stars show our young, late type candidate Serpens members.*

object, we calculate Q:

$$Q = (J - W) + e(H - W) \tag{2.1}$$

where J,H, and W are the magnitudes of the object observed in these photometric bands, and e is a ratio of extinction in said bands:

$$e = (A_{\mathrm{J}} - A_{\mathrm{W}})/(A_{\mathrm{H}} - A_{\mathrm{W}}) \tag{2.2}$$

A value of e must be adopted based on the type of contaminant that is most common. This value was determined for the entire W-band survey, not specifically for observations of Serpens. The most common background contaminants in the survey are M0 stars, so the Q scale was fixed such that a star with SpT = M0 corresponds to $Q = 0$. Consequently, increasingly negative values of Q correspond to objects with increasingly later spectral types. This is demonstrated in Figure 2.2. Here we show Q vs SpT for field and young cluster objects (calculated from synthetic photometry of standard targets), as well as for the new Serpens candidate members discovered in Jose et al. (2020) and in this work.

To fix the value of e, we used synthetic photometry of an M0 standard spectrum from Kirkpatrick et al. (2010), reddened by $A_{\mathrm{V}} = 10$ mag (an average value along all lines of sight observed in the W-band survey) using the $R_{\mathrm{V}} = 3.1$ reddening law of Fitzpatrick (1999). We compared reddened synthetic photometry for this object to unreddened values, and used this to determine the selective extinctions. These were then used to calculate e, resulting in $e = 1.85$. This value was used in all W-band Q calculations.

Based on this Q-scale, we can estimate which values should correspond to the spectral types of interest for this survey. Using synthetic photometry in J,H and W of young objects (Allers & Liu, 2013; Muench et al., 2007) and field standards (Cushing et al., 2005), we calculated that objects with spectral types later than M6 (the approximate stellar/substellar boundary, Alves de Oliveira et al., 2010) should have values of $Q < -0.6$.

2.3.2 HST Photometry

We obtained HST WFC3 photometry for a subsample of our Serpens South objects. Due to the different filter set available with HST WFC3, we required a second version of the reddening insensitive index, Q_{HST}. We use a combination of filters: F139M (1.34-1.43 μm) gives information on the H_2O absorption feature, and is used in conjunction with F127M (1.22-1.32 μm) and F850LP (0.82-1.09 μm) fluxes to build Q_{HST}:

$$Q_{\mathrm{HST}} = -2.5\log\left(\frac{F_{\mathrm{F850LP}}}{F_{\mathrm{F127M}}}\right) + e \times 2.5\log\left(\frac{F_{\mathrm{F127M}}}{F_{\mathrm{F139M}}}\right) \tag{2.3}$$

where F_{F850LP}, F_{F127M} and F_{F139M} are the filter fluxes, and e is calculated as in Eq. 2.2, but using this HST filter set. Using Q_{HST}, objects with late-M, L & T spectral types will have $Q_{\mathrm{HST}} > 1$, while background stars will have $Q_{\mathrm{HST}} \approx 0$.

2.4 Observations

2.4.1 Photometric survey observations

Photometry for both Serpens South and Serpens Core was obtained using WIRCam on CFHT (Puget et al., 2004). The WIRCam field of view is $\sim 20' \times 20'$, with a sampling of 0.3 arcseconds per pixel. The Serpens South photometric catalogue was first discussed in Jose et al. (2020). The Serpens Core catalogue is presented for the first time in this work. Both were processed and calibrated according to the methods described in Jose et al. (2020).

A single pointing was used to image all of Serpens South, centred on RA = 277.5125°, Dec = -2.0327°. We used a 21-point dithering pattern to fill the gaps between the four detectors of WIRCam and to accurately subtract the sky background. This photometry was obtained during 14-15th July 2016. In addition to J- and H-bands, we also obtained photometry using our custom 1.45μm (W-band) filter. The integration times used were 1890, 1920, and 12285s for J, H and W respectively.

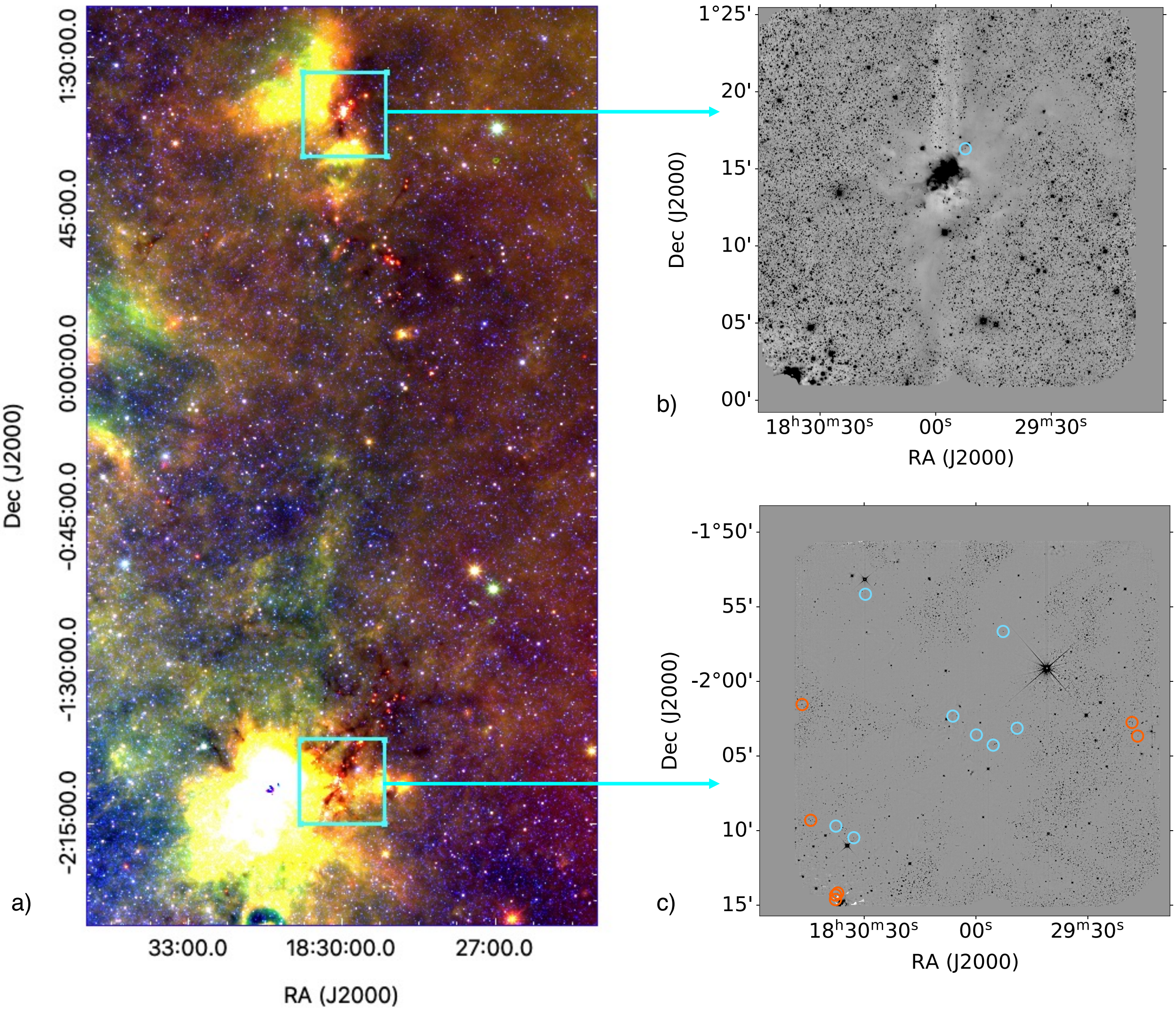

Figure 2.3 *a) Colour-composite image of Serpens Core, Serpens South and the surrounding regions, obtained using WISE 22 μm (red), 12 μm (green) and 3.4 μm (blue) images. The cyan boxes show the areas covered by the WIRCam observations of Serpens Core (a) and Serpens South (b). Both contain the dark filament structures that run through each subcluster. The nebulosity that contributes to the high visual extinctions of both regions is also visible. b) J-Band WIRCam image of Serpens Core. The blue circle indicates the Serpens Core object, SC182952+011618, followed up spectroscopically in this work. c) J-Band WIRCam image of Serpens South. The orange circles show objects followed up spectroscopically in Jose et al. (2020). The blue circles show the 8 Serpens South objects with spectroscopic follow-up reported in this work.*

A single pointing was also used to image all of Serpens Core, centred on RA = 277.4729°, Dec = 1.2055°. We again used a 21-point dithering pattern and obtained photometry using the J,H and W filters. The integration times used were 1350, 1650, and 14625s for J,H and W respectively, with the images taken on 12th, 13th and 15th April 2017.

The stacked J-band exposures of Serpens Core and Serpens south are shown in panels b) and c) of Figure 2.3. Figure 2.3 also shows a WISE colour-composite image (22μm (red), 12μm (green) and 3.4μm (blue)) covering $\sim 2.5° \times 4.5°$, along with the WIRCam imaging areas for each subcluster (cyan boxes). Comparing these imaging areas to Figure 4 of Herczeg et al. (2019) - which shows the spatial extent of both Serpens South and Serpens Core, based on Gaia DR2 data (Gaia Collaboration et al., 2018) - it is clear that they cover the dense central regions of each subcluster, but are likely not large enough in size to encompass all known members.

2.4.2 Photometric criteria for candidate member selection

2.4.2.1 Serpens South

Figure 2.4 shows the J-H colour vs H magnitude for all objects in Serpens South with photometric uncertainty < 0.1 mag, extracted from our CFHT images (a total of 15,276 objects, grey points without error bars in Figures 2.4 and 2.5). Also shown in Figure 2.4 are young stellar objects (YSOs) found to be likely members of Serpens South by Winston et al. (2018) (yellow squares).

As discussed in Section 2.3, objects with $Q < -0.6$ are likely to have spectral types $\geq$ M6. Figures 2.4 and 2.5 show all objects, in black, that satisfy the criteria $H < 18$ and $Q \leq -(0.6 + Q_{\rm err})$ or $H > 18$ and $Q \leq -(0.6 + 3 \times Q_{\rm err})$ (where $Q_{\rm err}$ is calculated using the standard propagation of errors). A more stringent cut on $Q_{\rm err}$ is required for fainter objects, as their photometric errors are significantly larger, as is the likelihood of contamination by reddened background sources. This is effectively a $1\sigma/3\sigma$ cut on the sample, and gives a total of 69 objects.

To identify targets for spectroscopic follow, we further examined the $Q <$

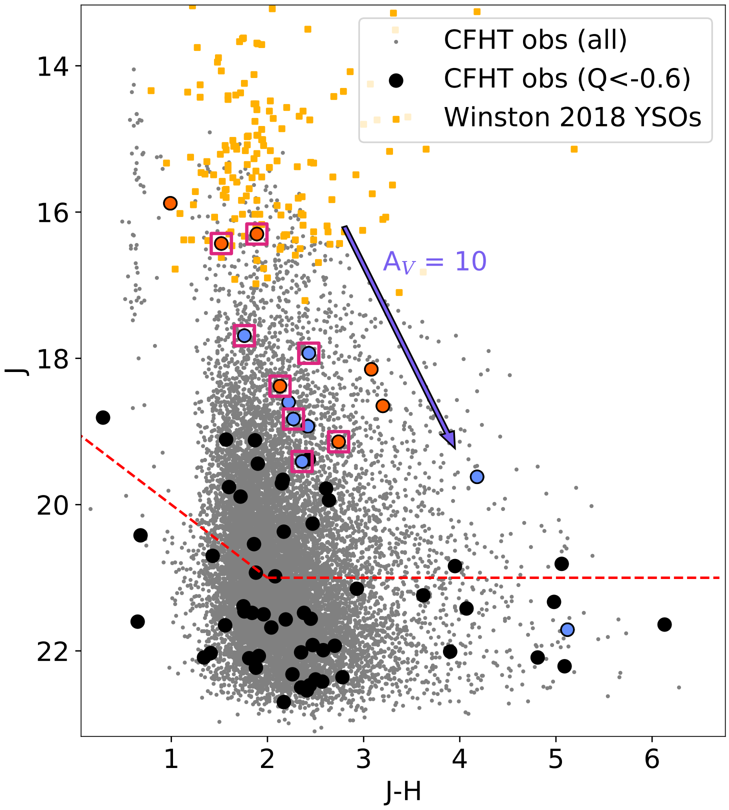

Figure 2.4 *J-H vs J colour-magnitude diagram for Serpens South objects with magnitude errors* < 0.1 *mag (grey). The black points show all of the objects that satisfy the photometric criteria* $Q \leq -(0.6 + Q_{err})$ *if* $H < 18$ *or* $Q \leq -(0.6 + 3 \times Q_{err})$ *if* $H > 18$ *(69 targets). The large orange circles show objects followed up spectroscopically in Jose et al. (2020); large blue circles are objects followed up spectroscopically in this work. Pink boxes indicate confirmed young, low-mass Serpens South candidates. Likely YSO members of Serpens South from Winston et al. (2018) are shown as yellow squares. The dashed red line indicates the completeness limit for the CFHT photometric survey, and the purple arrow shows the* $A_V = 10$ *extinction vector.*

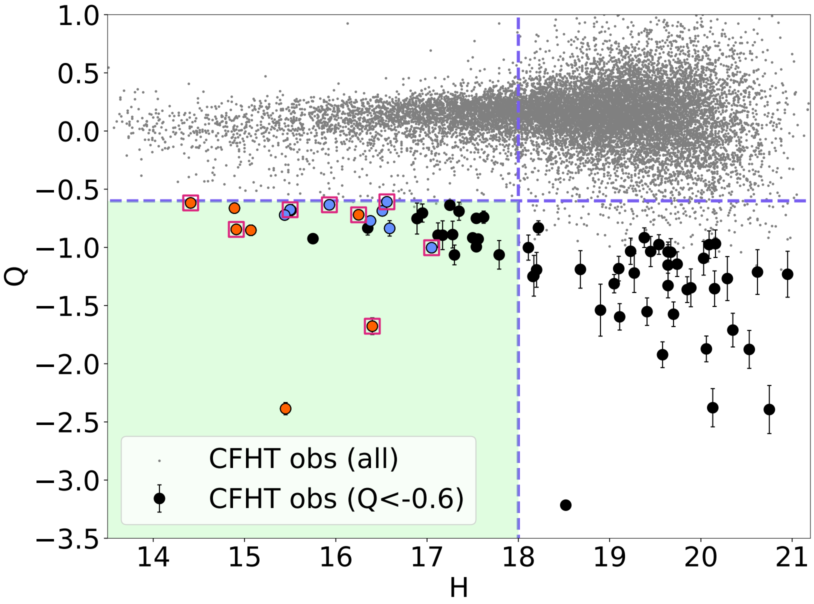

Figure 2.5 *H mag vs Q for all objects in our Serpens South catalogue with photometric precision* < 0.1 *mag (grey). The black points show all of the objects that satisfy the photometric criteria* $Q \leq -(0.6+Q_{err})$ *if* $H < 18$ *or* $Q \leq -(0.6 + 3 \times Q_{err})$ *if* $H > 18$ *(69 targets). The orange points show objects followed up spectroscopically in Jose et al. (2020); blue shows objects followed up spectroscopically in this work. Pink boxes indicate confirmed young, low-mass Serpens South candidates. The green box shows the region of parameter space suitable for spectroscopic follow-up with 4-m class telescopes.*

-0.6 sample. We additionally required objects to be sufficiently bright for spectroscopic follow-up with a 4-m class telescope ($H < 18$) - this was a total of 32 objects, highlighted by the green quadrant of Figure 2.5. We then cross-matched these with the ALLWISE catalogue (Cutri et al., 2013). We expect targets with spectral types $\geq$ M6 to have intrinsic $W1 - W2 > 0.1$ (Kirkpatrick et al., 2011), and thus required this condition to be met by all candidates. We also noted that any target with a very bright $W1$ magnitude is unlikely to be substellar at the distance of Serpens. We used evolutionary models from Baraffe et al. (2015) to quantify this brightness cutoff (approximately equating the L' band with $W1$, thus assuming solely photospheric flux). Considering an upper limit of 0.2 $\mathrm{M}_{\odot}$, and an object at the age (0.5 Myr) and distance (436 pc) of Serpens, we find that objects with masses above this limit will have a W1 magnitude brighter than $\approx$ 11 mag. This is considering objects without visual extinction - which is clearly unlikely for objects in Serpens (see Section 2.5). Considering instead $A_{\mathrm{V}} = 5$, we find that objects with masses 0.2 $\mathrm{M}_{\odot}$ will have a $W1$ magnitude brighter than $\approx$ 12 mag. Consequently, we remove targets with $W1 < 12$, or $W1 - W2 < 0.1$ from our final sample. We also cross-matched with PS1 (Chambers et al., 2016) to remove objects with bright optical counterparts (e.g. $z_{\mathrm{PS1}} - J_{\mathrm{CFHT}} \leq 2$). Combining these photometric criteria, we obtain a final sample of 29 objects suitable for spectroscopic follow-up. CFHT and ALLWISE photometry for the 29 photometric candidates is reported in Tables 2.1 and 2.2.

We chose to follow-up the brightest objects ($H < 17$) spectroscopically. Seven bright targets were reported and discussed in Jose et al. (2020), highlighted as orange points in Figures 2.3, 2.4 and 2.5. We report spectroscopic follow-up of eight additional bright targets (blue in Figures 2.3, 2.4 and 2.5). The pink squares highlight which of these targets were later confirmed as late-types. The remaining targets from Table 2.1 are strong candidates for further spectroscopic follow-up.

2.4.2.2 Serpens Core

Objects with photometric uncertainty < 0.1 mag in Serpens Core are shown in grey in Figures 2.6 and 2.7, a total of 34,835 objects. The high density of sources in the core is seen in Figure 2.3, and leads to a larger quantity of objects in the full photometric sample. As a result, we used a more stringent cut on Q_{err} to create a subsample of objects considered for follow-up. We selected objects satisfying

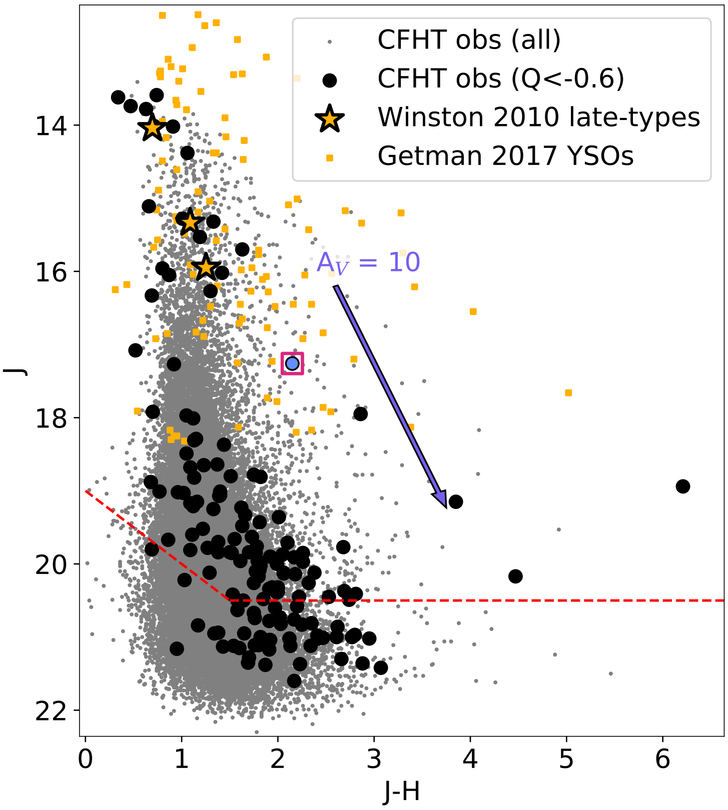

Figure 2.6 *J-H vs J colour-magnitude diagram for Serpens Core objects with magnitude errors* < 0.1 *mag (grey). The black points show all of the objects that satisfy the photometric criterion* $Q \leq -(0.6 + 5 \times Q_{err})$ *(151 targets). The blue point shows the target followed up spectroscopically in this work, SC182952+011618 - with a pink box indicating it was confirmed as a young, low-mass Serpens Core candidate member. Likely YSO members of Serpens South from Getman et al. (2017) are shown as yellow squares. Also shown are three late-type spectroscopically confirmed objects from Winston et al. (2010), discussed in Section 2.4.1. The dashed red line indicates the completeness limit for the CFHT photometric survey, and the purple arrow shows the* $A_V = 10$ *extinction vector.*

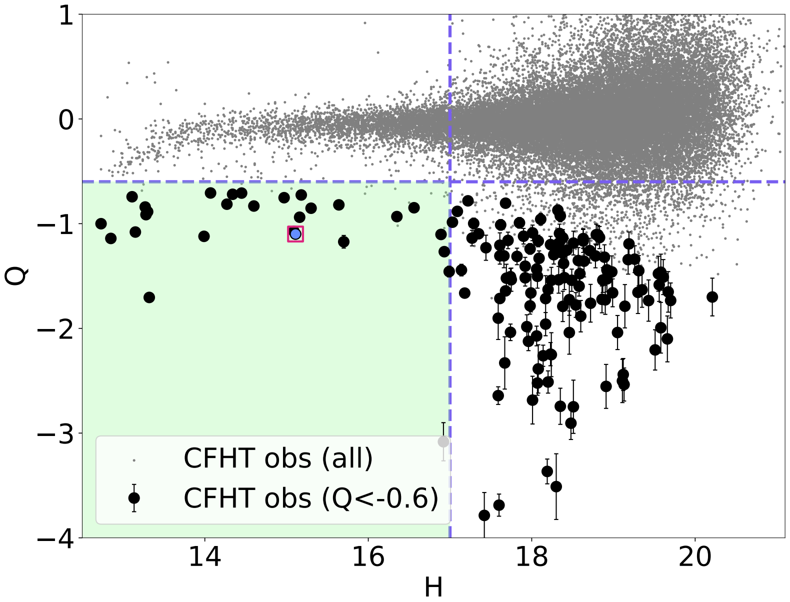

Figure 2.7 *H mag vs Q for all objects in our Serpens Core catalogue with photometric precision* < 0.1 *mag (grey). The black points show all of the objects that satisfy the photometric criterion* $Q \leq -(0.6 + 5 \times Q_{err})$ *(151 targets). The blue point shows the target followed up spectroscopically in this work - with a pink box indicating it was confirmed as a young, low-mass Serpens Core candidate. The green box shows the region of parameter space suitable for spectroscopic follow-up with 4-m class telescopes.*

$Q \leq -(0.6 + 5 \times Q_{\mathrm{err}})$, effectively a 5σ cut. These are shown as the black points in Figures 2.6 and 2.7, a total of 151 objects. Also shown in Figure 2.4 are likely YSO members of Serpens Core from Getman et al. (2017).

To select targets for spectroscopic follow-up, we retain objects observable with a 4-m class telescope ($H = 17$ for Serpens Core). We also removed objects with $Q < -2.0$ here, as previous experience showed that the majority of these objects with extremely low Q values (in this magnitude range) would be contaminant objects with spurious photometry. More specifically, we expect H vs Q to follow a trend for a given cluster (i.e. objects at the same distance with similar extinctions) - a brighter object should have a higher mass and more positive value of Q than a lower mass object. This can be seen in Figure 2.5: the object with $H = 15.55$, $Q = -2.39$ lies well below the general trend. Spectroscopic follow-up for this target was reported in Jose et al. (2020) (SS183038-021437 in Table 2.1) - and it was found to be a clear contaminant. After imposing this additional photometric cut, we retain a sample of 27 objects, shown in the green shaded quadrant of Figure 2.7.

As in Serpens South, we applied WISE-based selection criteria. In addition to the criteria discussed above ($W1 > 12$ and $W1 - W2 > 0.1$), we also required Serpens Core candidates to have WISE detections - i.e. WISE dropouts were removed from the sample. This gave us a sample of 7 candidates suitable for spectroscopic follow-up - 26% of the targets that meet all other photometric criteria also have WISE detections. CFHT and ALLWISE photometry for these candidates is reported in Tables 2.1 and 2.2. We obtained spectroscopic follow-up of one of these objects, which is highlighted in pink in Figures 2.6 and 2.7.
SC182955+011034, SC182956+011218 and SC183005+011235, three of the six candidates we have not yet followed up, are spectroscopically characterised in Winston et al. (2010). These targets have spectral types of M5, M8.5 and M9, respectively. They are shown for comparison to the W-band sample in Figure 2.6 as yellow stars.

Table 2.1 *Magnitudes in W (1.45μm), J and H from CHFT for Serpens South and Serpens Core objects that meet the criteria from Sections 2.4.2.1 & 2.4.2.2. Q-value calculated from these, as detailed in Section 2.3.*

Object ID	RA deg	Dec deg	[1.45] mag	J_{CFHT} mag	H_{CFHT} mag	Q_{CFHT}
Serpens South candidates with spectroscopic follow-up:						
SS182917-020340†	277.3193	-2.0610	17.25 ± 0.01	18.38 ± 0.01	16.25 ± 0.01	-0.72± 0.02
SS182918-020245†	277.3256	-2.0458	15.47 ± 0.01	16.43 ± 0.01	14.91 ± 0.01	-0.85 ± 0.01
SS182949-020308	277.4540	-2.0522	17.43 ± 0.01	18.60 ± 0.01	16.38 ± 0.01	-0.77 ± 0.01
SS182953-015639	277.4696	-1.9442	16.59 ± 0.01	17.93 ± 0.01	15.50 ± 0.01	-0.68 ± 0.01
SS182955-020416	277.4807	-2.0712	17.57 ± 0.01	18.83 ± 0.01	16.56 ± 0.01	-0.61 ± 0.01
SS182959-020335	277.4995	-2.0598	18.23 ± 0.01	19.41 ± 0.02	17.05 ± 0.01	-1.00 ± 0.04
SS183006-020219	277.5258	-2.0387	18.68 ± 0.01	21.71 ± 0.06	16.59 ± 0.01	-0.84 ± 0.07
SS183029-015409	277.6235	-1.9026	17.16 ± 0.01	19.62 ± 0.02	15.44 ± 0.01	-0.72 ± 0.02
SS183032-021028	277.6365	-2.1745	16.77 ± 0.01	17.69 ± 0.01	15.93 ± 0.01	-0.63 ± 0.01
SS183037-021411†	277.6545	-2.2363	16.45 ± 0.01	18.15 ± 0.03	15.07 ± 0.01	-0.85 ± 0.05
SS183037-020941	277.6566	-2.1616	17.60 ± 0.01	18.93 ± 0.01	16.51 ± 0.01	-0.69 ± 0.01
SS183038-021419†	277.6568	-2.2386	17.95 ± 0.01	19.14 ± 0.04	16.40 ± 0.01	-1.68 ± 0.07
SS183038-021437†	277.6570	-2.2437	17.41 ± 0.01	18.65 ± 0.04	15.45 ± 0.01	-2.39 ± 0.05
SS183044-020918†	277.6847	-2.1551	15.29 ± 0.01	16.30 ± 0.01	14.41 ± 0.01	-0.62 ± 0.01
SS183047-020133†	277.6943	-2.0258	15.47 ± 0.01	15.88 ± 0.01	14.89 ± 0.01	-0.66 ± 0.01

continued...

continued...

Other Serpens South photometric candidates:						
SS182912-021300	277.3011	-2.2167	18.40 ± 0.03	19.78 ± 0.05	17.17 ± 0.04	-0.90 ± 0.12
SS182917-020923	277.3217	-2.1564	18.58 ± 0.01	19.66 ± 0.02	17.50 ± 0.01	-0.92 ± 0.04
SS182938-015935	277.4112	-1.9930	18.47 ± 0.00	19.44 ± 0.01	17.54 ± 0.01	-0.75 ± 0.02
SS182942-015935	277.4275	-1.9931	18.44 ± 0.00	19.11 ± 0.01	17.54 ± 0.01	-1.00 ± 0.02
SS182949-020558	277.4557	-2.0995	18.13 ± 0.00	19.12 ± 0.01	17.25 ± 0.01	-0.64 ± 0.02
SS182957-015409	277.4891	-1.9027	19.02 ± 0.01	21.42 ± 0.07	17.35 ± 0.01	-0.69 ± 0.08
SS182959-020917	277.4978	-2.1547	19.28 ± 0.01	22.09 ± 0.11	17.28 ± 0.01	-0.89 ± 0.12
SS183016-015728	277.5683	-1.9578	19.15 ± 0.01	21.24 ± 0.04	17.62 ± 0.01	-0.74 ± 0.05
SS183019-020130	277.5824	-2.0251	18.64 ± 0.01	19.71 ± 0.01	17.56 ± 0.01	-0.93 ± 0.04
SS183022-015315	277.5929	-1.8875	19.22 ± 0.01	22.21 ± 0.10	17.12 ± 0.01	-0.89 ± 0.11
SS183042-021334	277.6751	-2.2263	18.05 ± 0.02	19.38 ± 0.05	16.95 ± 0.01	-0.71 ± 0.08
SS183046-021202	277.6947	-2.2007	18.54 ± 0.03	20.84 ± 0.10	16.89 ± 0.01	-0.75 ± 0.13
SS183046-015651	277.6954	-1.9476	18.60 ± 0.02	19.94 ± 0.06	17.30 ± 0.01	-1.07 ± 0.08
SS183047-015834	277.6974	-1.9761	19.03 ± 0.03	20.26 ± 0.08	17.79 ± 0.02	-1.06 ± 0.12
Serpens Core candidates with spectroscopic follow-up:						
SC182952+011618	277.4679	1.2717	16.25 ± 0.01	17.26 ± 0.01	15.11 ± 0.01	-1.10 ± 0.02

continued...

continued...

Other Serpens Core photometric candidates:						
SC182955+011034⋆	277.4806	1.1761	13.86 ± 0.00	14.01 ± 0.00	13.30 ± 0.01	-0.89 ± 0.02
SC182956+010940	277.4837	1.1612	14.89 ± 0.00	15.70 ± 0.00	14.07 ± 0.01	-0.71 ± 0.02
SC182956+011218⋆	277.4848	1.2050	14.91 ± 0.00	15.28 ± 0.00	14.27 ± 0.01	-0.81 ± 0.02
SC183005+011235⋆	277.5209	1.2099	15.39 ± 0.00	16.02 ± 0.00	14.60 ± 0.01	-0.83 ± 0.02
SC183008+010830	277.5364	1.1418	14.85 ± 0.00	15.32 ± 0.00	13.99 ± 0.01	-1.12 ± 0.02
SC183016+013307	277.5708	1.2187	15.69 ± 0.00	16.27 ± 0.01	14.97 ± 0.01	-0.75 ± 0.02

† Objects first reported in Jose et al. (2020).

⋆ Spectroscopically characterised in Winston et al. (2010).

2.4.3 Spectroscopic Follow-up

We obtained spectra of each of the objects identified in Section 2.4.2. Spectroscopy can confirm water absorption, and be used to characterise the spectral type and age of a target. The full sample of 9 spectra obtained is shown in Figure 2.8. Each is normalised to the peak of the $K-$band flux.

We observed 8 targets in Serpens South and 1 target in Serpens Core using the SpeX spectrograph on the IRTF (Rayner et al., 2003), on 5 nights between July 2017 and June 2018. These targets, and those presented in Jose et al. (2020), are named in Table 2.3. For each observation, a standard ABBA nodding pattern was used to obtain sky and target spectra, with total integration times ranging from 1430 - 3820s. The observations were undertaken in prism mode using either the 0.5" or 0.8" slit, depending on the observing conditions, corresponding to an average resolving power R $\sim$ 100. When observing the objects, flat field frames were taken before each set of observations. Wavelength calibration was achieved using Argon lines, determined by observing an argon lamp, again prior to each set of observations. We used `Spextool` (V4.1 Cushing et al., 2004), an IDL-based data reduction package, to extract the spectra of the target object from the data, and to combine the individual frames for each target into one spectrum. Bad pixels and other variable effects were pruned from the spectra, which were then scaled to a common median flux level. After visual inspection, the spectra were median combined into a single file. Additionally, an A0 standard star was observed within an hour either before or after each science observation. We used one of four standard stars for each of the target observations: either HD174240, HD172792, HD182299 or HD167163. The median combined spectra of the standard star was then used for telluric correction of the science targets. By comparing this modelled spectra to the A0 V spectra and modifying it for any observed differences, the intrinsic and observed spectra of the standard can be used to determine the function necessary for correcting the target spectra (Vacca et al., 2003).

Table 2.2 *ALLWISE magnitudes for detected Serpens South and Serpens Core sources (Cutri et al., 2013).*

Object ID	RA deg	Dec deg	$W1$ mag	$W2$ mag
SS182918-020245[†]	277.3256	-2.0458	12.39 ± 0.03	11.84 ± 0.03
SS182949-020308	277.4540	-2.0522	14.58 ± 0.04	14.34 ± 0.07
SS182953-015639	277.4696	-1.9442	13.40 ± 0.03	12.73 ± 0.03
SS183029-015409	277.6235	-1.9026	12.18 ± 0.03	11.40 ± 0.02
SS183032-021028	277.6365	-2.1745	13.75 ± 0.05	13.61 ± 0.08
SS183037-021411[†]	277.6545	-2.2363	12.54 ± 0.03	12.25 ± 0.02
SS183038-021419[†]	277.6568	-2.2386	12.86 ± 0.03	11.86 ± 0.02
SS183038-021437[†]	277.6570	-2.2437	12.00 ± 0.03	11.70 ± 0.02
SS183044-020918[†]	277.6847	-2.1551	12.28 ± 0.05	11.42 ± 0.04
SS183047-020133[†]	277.6943	-2.0258	13.73 ± 0.11	15.15 ± 0.38
SS182949-020558	277.4557	-2.0995	13.88 ± 0.03	13.48 ± 0.05
SS182957-015409	277.4891	-1.9027	13.96 ± 0.03	13.32 ± 0.03
SS182959-020917	277.4978	-2.1547	13.47 ± 0.03	12.37 ± 0.03
SS183016-015728	277.5683	-1.9578	15.36 ± 0.06	14.41 ± 0.07
SS183022-015315	277.5929	-1.8875	13.37 ± 0.04	12.41 ± 0.03
SS183046-015651	277.6954	-1.9476	13.49 ± 0.04	11.74 ± 0.04
SC182952+011618	277.4679	1.2717	13.13 ± 0.03	12.56 ± 0.03
SC182955+011034[⋆]	277.4806	1.1761	12.62 ± 0.03	12.44 ± 0.03
SC182956+010940	277.4837	1.1612	12.72 ± 0.03	12.36 ± 0.02
SC182956+011218[⋆]	277.4848	1.2050	13.11 ± 0.03	12.62 ± 0.03
SC183005+011235[⋆]	277.5209	1.2099	12.74 ± 0.05	12.14 ± 0.05
SC183008+010830	277.5364	1.1418	12.85 ± 0.03	12.43 ± 0.03
SC183016+013307	277.5708	1.2187	13.41 ± 0.03	13.03 ± 0.03

[†] Objects first reported in Jose et al. (2020).

[⋆] Spectroscopically characterised in Winston et al. (2010).

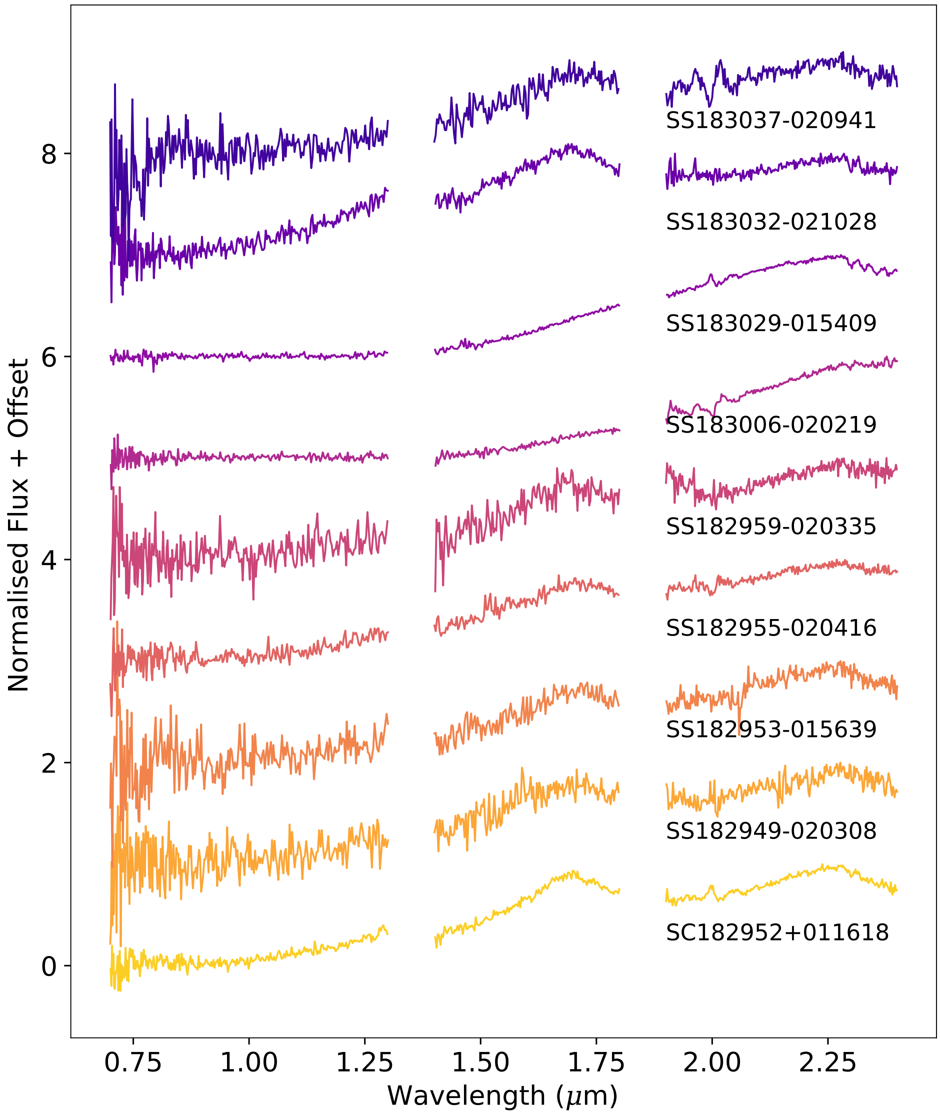

Figure 2.8 *IRTF SpeX spectra of Serpens South and Serpens Core objects (J−, H− and K−bands) reported in this Chapter (before dereddening), normalised to the K-band peak.*

2.4.4 High Resolution Follow-up Observations

We obtained HST WFC3 optical and near-IR imaging (GO 15628, PI Biller) for 6 objects identified as candidate members of Serpens South (three from this work, three from Jose et al., 2020) in order to search for low-mass companions to these objects. These are identified in Table 2.3 where we present their HST fluxes and Q_{HST}-values. Through spectral fitting analysis (see Section 2.6.1), we have confirmed 5 of these as bonafide late-type candidate Serpens members, and classified one as a late-M field-age contaminant.

We observed each object using the IR detector with the F127M and F139M filters, and using the UVIS detector with the F850LP filter. IR imaging was obtained using a 3-point dither pattern with exposure times of 197s. UVIS imaging was obtained using a 3-point dither pattern with 275s exposures, as well as the 2K2C sub-aperture and a 10s flash to correct for charge transfer inefficiency. The combination of F127M and F139M is analogous to the W-band technique - we expect to see objects showing water-absorption to be visible in F127M and drop out significantly in F139M. The reddening insensitive index, Q_{HST}, is also used here, calculated specifically for this combination of HST filters using Eq. 2.3. As discussed in Section 2.3.2, objects with late-M, L & T spectral types will have $Q_{\mathrm{HST}} > 1$, while background stars will have $Q_{\mathrm{HST}} \approx 0$. Two targets were not detected in F850LP, and as a result no Q_{HST} value is reported.

Table 2.3 *W-band Serpens survey objects that were followed-up spectroscopically, and subsequently characterised. HST filter magnitudes and fluxes are given for objects that were imaged and detected, as well as the HST Q-value. We report a spectral type, if one was determined from spectral fitting (C = contaminant), and highlight the objects that were confirmed as late-type brown dwarfs in this work and in Jose et al. (2020) (Y in 'Conf.?' column).*

Object ID	F_{F850LP} erg cm^{-2} s^{-1} Å^{-1}	F_{F127M} erg cm^{-2} s^{-1} Å^{-1}	F_{F139M} erg cm^{-2} s^{-1} Å^{-1}	Q_{HST}	SpT	Conf.?
Serpens South (this work):						
SS182949-020308	-	$(1.24 \pm 0.01)\times10^{-17}$	$(1.46 \pm 0.01)\times10^{-17}$	-	C (late-M)	N
SS182953-015639	-	$(2.22 \pm 0.01)\times10^{-17}$	$(2.90 \pm 0.01)\times10^{-17}$	-	M7-LO	Y
SS182955-020416	-	-	-	-	M4-M6.5	Y
SS182959-020335	-	-	-	-	M5-LO	Y
SS183006-020219	-	-	-	-	C (early-M)	N
SS183029-015409	-	-	-	-	C (early-M)	N
SS183032-021028	$(5.44 \pm 0.30)\times10^{-18}$	$(2.69 \pm 0.06)\times10^{-17}$	$(2.74 \pm 0.02)\times10^{-17}$	1.62	M5-M6.5	Y
SS183037-020941	-	-	-	-	C (early-M)	N
Serpens Core (this work):						
SC182952+011618	-	-	-	-	M7-M9	Y
Serpens South (Jose et al., 2020):						
SS182917-020340	$(1.17 \pm 0.11)\times10^{-18}$	$(1.39 \pm 0.01)\times10^{-17}$	$(1.54 \pm 0.01)\times10^{-17}$	2.04	M4-M7	Y

continued...

continued...

SS182918-020245	$(1.06 \pm 0.01)\times10^{-17}$	$(7.95 \pm 0.02)\times10^{-17}$	$(7.46 \pm 0.02)\times10^{-17}$	2.58	M5-M8	Y
SS183037-021411	-	-	-	-	C (early-M)	N
SS183038-021419	-	-	-	-	M3-M6	Y
SS183038-021437	-	-	-	-	C (early-M)	N
SS183044-020918	$(6.46 \pm 0.13)\times10^{-18}$	$(9.43 \pm 0.02)\times10^{-18}$	$(1.01 \pm 0.00)\times10^{-16}$	2.51	M7-M9	Y
SS183047-020133	-	-	-	-	C(early-M)	N

2.5 Effects of Extinction

The visual extinction ($A_{\rm V}$) along the Serpens line of sight is generally high. We used our CFHT photometric catalogues of Serpens Core and Serpens South to produce extinction maps of both regions, shown in Figure 2.9. A spectral energy distribution (SED) fit is performed for each detected object in the field, using photometry from the three observed bands and any available in literature catalogues (e.g. 2MASS, PanSTARRS), with visual extinction as an additional fitting parameter. The best-fit $A_{\rm V}$ is stored for every object. To create Figure 2.9, we used nearest-neighbour interpolation[1] to find an estimate of the spatial distribution of the dust attenuation across both full fields. We found an average value of $A_{\rm V,mean} = 21.3$, and a range of $A_{\rm V} = 0 - 31$ (the maximum value of extinction considered) for Serpens South. As can be seen from the map in Figure 2.9, high extinction dominates, but localised, lower-extinction regions are distributed uniformly across the area of sky that we imaged. We also found an average value of $A_{\rm V,mean} = 6.3$ and a range of $A_{\rm V} = 0 - 31$ for Serpens Core. However, here the spatial distribution of high and low values is not uniform - extinction in the centre of the imaged region (where the Core is located) is very high, and drops rapidly to lower values elsewhere. These values are comparable to those found in the 2MASS extinction analysis of the region, discussed in Section 2.2. Both analyses show higher average and maximum values for Serpens South, and consistently high values across both subclusters.

As described in Allers & Liu (2020), the W-band method was originally designed and optimised for star-forming regions with far lower interstellar extinction levels (e.g. Taurus). Consequently, we investigated the effect that the significantly higher extinctions of the two Serpens regions would have on the effectiveness of our technique. Starting from our photometric observations of Serpens South, we examined the location of true and false positives on the H vs Q diagram.

First, we considered the population of objects that the W-band filter was designed to find: young, late-type members of nearby star-forming regions. Luhman et al. (2017) (henceforth L17) propose a set of near-IR spectral standards for young, late-type objects, which we adopted here as suitable template spectra. We calculated synthetic photometry in J, H and W, as well as Q, for the standards

---

[1] using the `scipy NearestNDInterpolator` function.

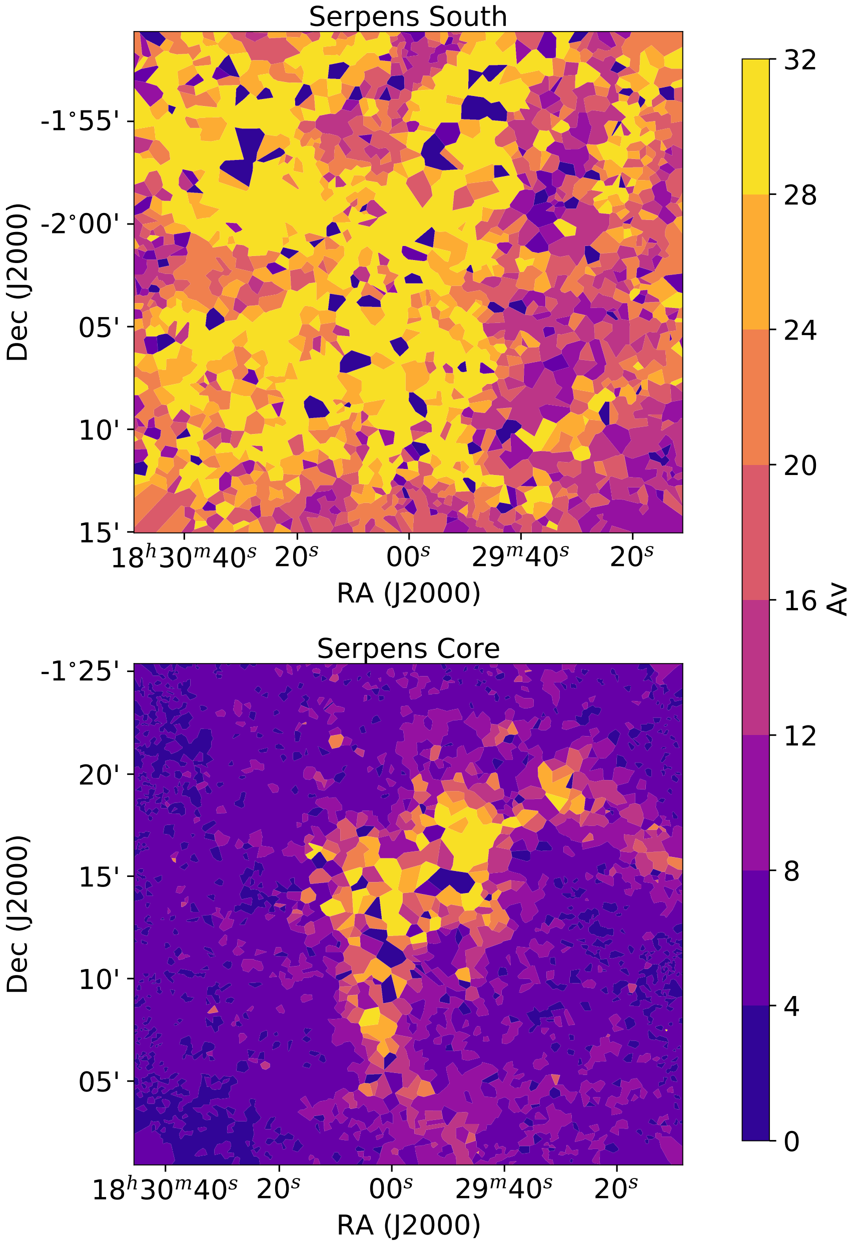

Figure 2.9 *Visual extinction (A_V) maps for Serpens South and Serpens Core, generated using the photometric catalogues from CFHT WIRCam. Nearest neighbour interpolation is used to fill the parameter space between coordinates with observed values of A_V.*

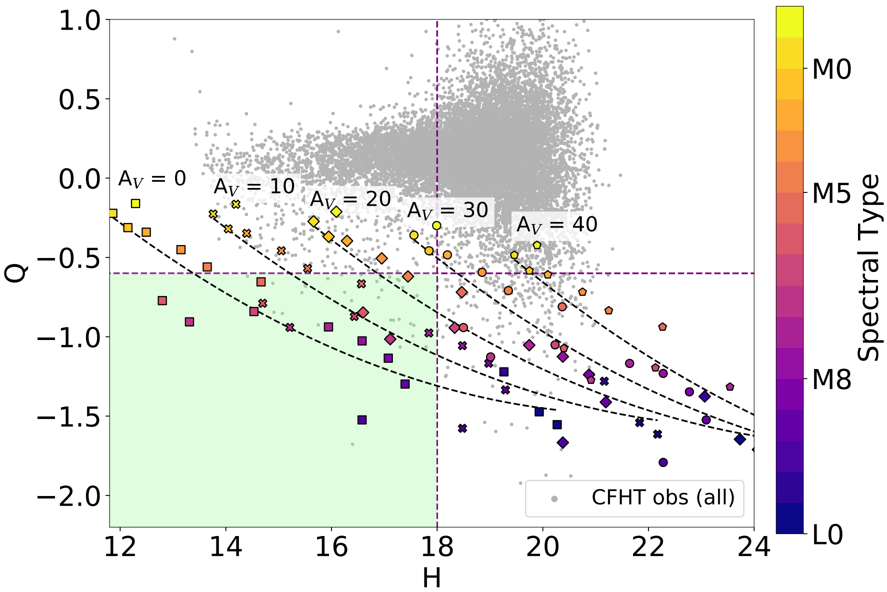

Figure 2.10 *H mag vs Q for objects used to construct the spectral standards described in Luhman et al. (2017). Sequences of objects with SpT = M0–L4 are reddened by varying amounts between A_V = 0–40. SpT is indicated by colour. The green box shows the region of parameter space suitable for spectroscopic follow-up with 4-m class telescopes.*

with SpT = M0–L4. We repeated this calculation multiple times for each object, placing them in Serpens South each time (d = 436 pc) and reddening them by $A_{\rm V}$ = 0, 10, 20, 30 and 40. These sequences are shown as the coloured markers in Figure 2.10. This analysis demonstrates that using the W-band filter to look at Serpens truly pushes the Q-index to its limits. When considering the highest extinction levels, we see that Q can no longer be considered ‘reddening-insensitive’ - it is significantly altered from the low-$A_{\rm V}$ levels. However, Figure 2.10 does show that we largely avoid early-M contaminants in the green shaded quadrant (which shows the area of parameter space suitable for spectroscopic follow-up with 4-m class telescopes in Serpens South). When considering fainter magnitudes ($H > 18$), we find that highly-reddened early-mid Ms may have $Q < -0.6$, which will be an important consideration for further follow-up with larger telescopes. Additionally, late Ms and early Ls can be pushed into the $H > 18$ regime if highly attenuated by dust, meaning many may have been missed in this portion of follow-up.

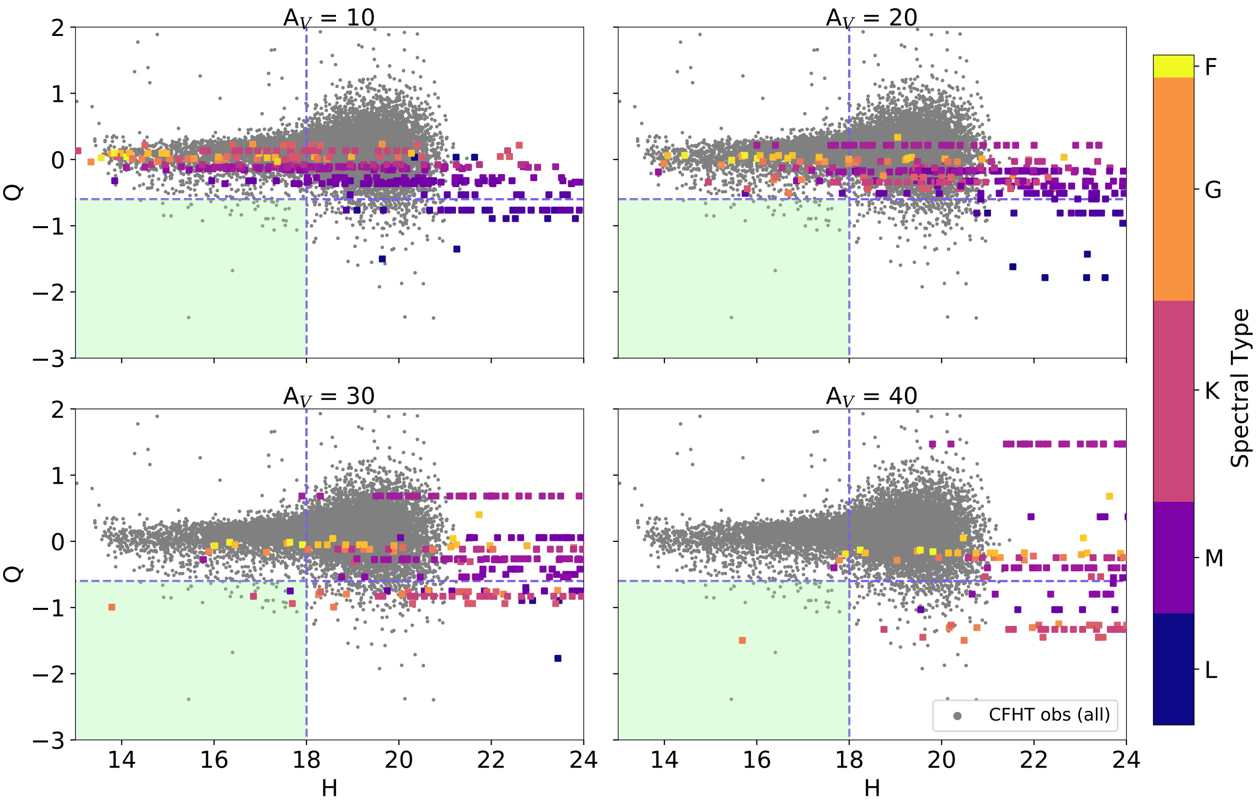

Figure 2.11 *H vs Q for objects generated using the Trilegal Galactic model (Girardi et al., 2012) centred on Serpens South (RA = 277.5,Dec = -2.25). Spectral type is indicated by colour. The grey points are all objects in our Serpens South CFHT catalogue with photometric precision* < 0.1 *mag. The green boxes shows the region of parameter space suitable for spectroscopic follow-up with 4-m class telescopes.*

We also explored the effect of reddened field objects along the cluster line-of-sight on the success of our technique. As discussed, the W-band method and Q-index are optimised for separating late-type brown dwarfs from earlier spectral type objects. However, we cannot always distinguish between young late-type members of star-forming regions and older, field brown dwarfs, with simple photometry alone. Consequently, it is likely a lack of low surface gravity (youthful) features in follow-up spectra will indicate that some selected objects are actually field-age brown dwarfs.

We used the Trilegal Galactic model (Girardi et al., 2012) to obtain a population of objects along the Serpens South line-of-sight. We simulated a field of view of 0.1225 sq. deg, centred on RA = 277.5°, Dec = -2.25°. The CFHT

MegaCam+WIRCam system was chosen for output magnitudes, and we used the Kroupa IMF (Kroupa, 2001), including binaries. This resulted in a population of 1,543 objects along the Serpens South line-of-sight. Each object generated by the Trilegal model has an associated effective temperature. To convert these to spectral types, we used Mamajek's 'Modern Mean Dwarf Stellar Color and Effective Temperature Sequence' [2] (described in part in Pecaut & Mamajek (2013)). We associated each object with the appropriate spectral type from the IRTF spectral library to obtain a template spectrum (Rayner et al., 2009), and then used CFHT filter information to calculate the Q-index and associated apparent magnitudes for each member of the population. We calculated synthetic photometry for a range of visual extinction values, again $A_{\mathrm{V}} = 10$, 20, 30 and 40, and plotted each resulting population on the H-mag vs Q diagram, as shown in Figure 2.11.

Figure 2.11 demonstrates that the majority of field objects with $H < 18$ retain $Q > -0.6$, despite extreme reddening, and as such would not be false positives in our survey. However, there are a handful of objects with $A_{\mathrm{V}} = 30$ that fall into the $Q < -0.6$, $H < 18$ region, and as such would be considered for follow-up. On closer inspection, these objects are M, K, and G stars with extinction-altered colours. As a result, there is a possibility of including a small numbers of significantly earlier-type stars in a spectroscopic follow-up sample (as well as field-age brown dwarfs with M or later spectral types). Therefore, it is important to check for signs of youth when characterising our late-type discoveries spectroscopically, and determine whether they are young, candidate cluster members, or field-age background contaminants.

A final possible source of contamination, that we do not quantify here, but regardless should be considered, are extincted extragalactic objects. Whilst significantly rarer than the other contaminants described in this Chapter, it is possible that the spectra of AGN and distant, dusty galaxies could be reshifted or extincted in such a way that would scatter them into our Q-index selection criteria. This could affect the success rate of photometric selection, but these objects are also easily-identifiable due to their strikingly non-stellar infrared spectra, and so could not be incorrectly spectroscopically characterised as brown dwarf detections.

---

[2] https: //www.pas.rochester.edu/ emamajek/EEM_dwarf_UBVIJHK_colors_Teff.txt, accessed April 2020

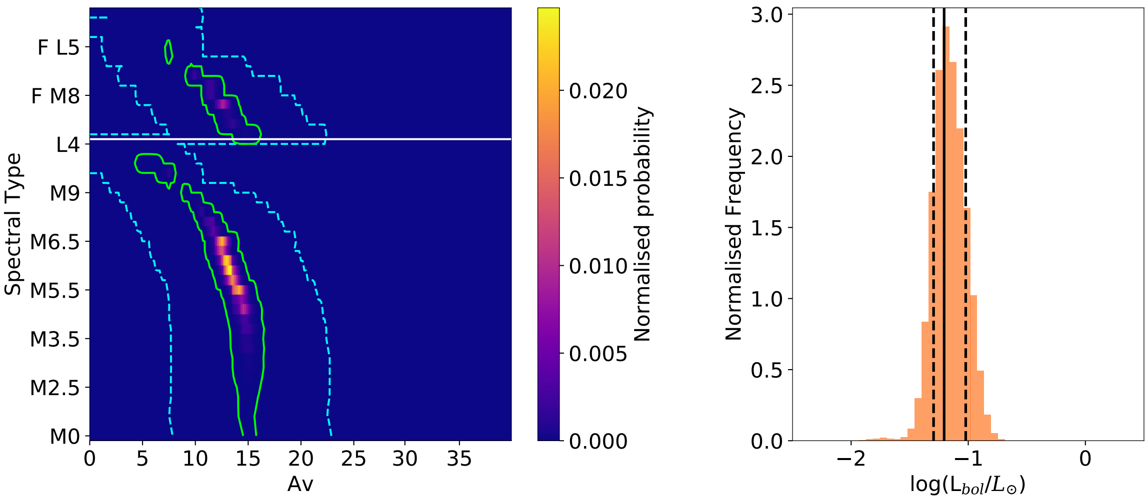

Figure 2.12 *Left: Normalised probability map for SS183032-021028. Contours show 1σ (blue, dashed) and 2σ (green, solid) levels, respectively. Field and young standard solutions are separated by the white line (field denoted by F). Right: Histogram of log($L_{bol}/L_{\odot}$) solutions for SS183032-021028, derived from the probability map. Also shown is the peak value (solid line), and the 68% (or 1σ) Bayesian credible intervals (dashed lines), which reflect the asymmetry of the distribution.*

2.6 Characterisation

2.6.1 Spectral Fitting

As discussed in Section 2.1, one must consider the spectral type, visual extinction and age in combination to be able to accurately characterise an object. The procedure used for characterising targets in the W-band survey is explained in detail in Jose et al. (2020) and Biller et al. (in preparation). We used a grid-based approach to compare the Serpens spectra with spectral standards. We used a library of standards compiled from two different sources: spectra of field brown dwarfs from the SpeX spectral library (Cushing et al., 2005; Rayner et al., 2009), and spectra of young brown dwarfs from L17. Each standard belongs to one of three age groups: VL-G (very low gravity, ≈ 1 Myr), INT-G (intermediate gravity, ≈ 10 Myr) and FLD-G (field gravity, for much older field stars). These age classifications are based on the work of Allers & Liu (2013). For each standard

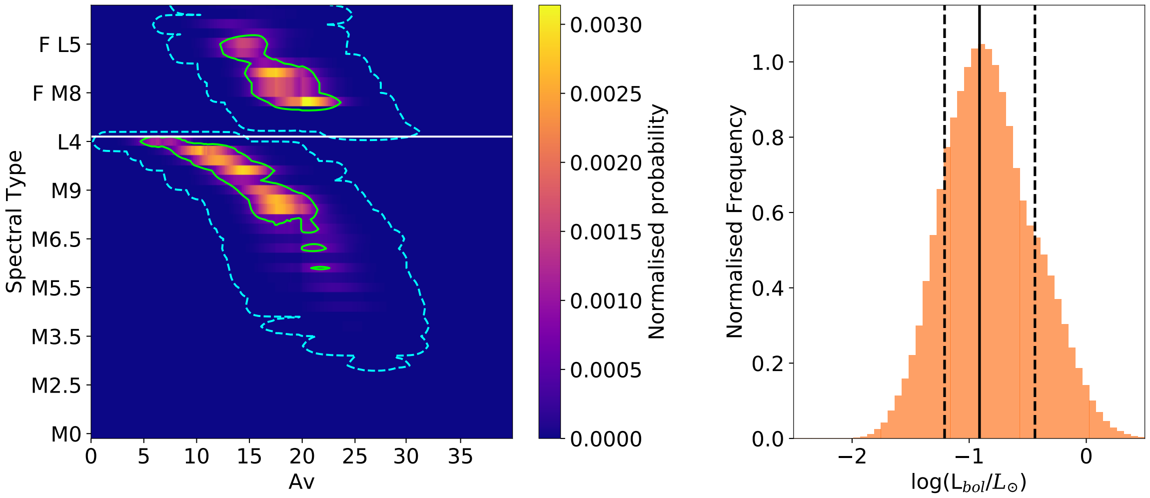

Figure 2.13 *Left: Normalised probability map for SS182953-015639. Right: Histogram of log($L_{bol}/L_{\odot}$) solutions for SS182953-015639, derived from the normalised probability map.*

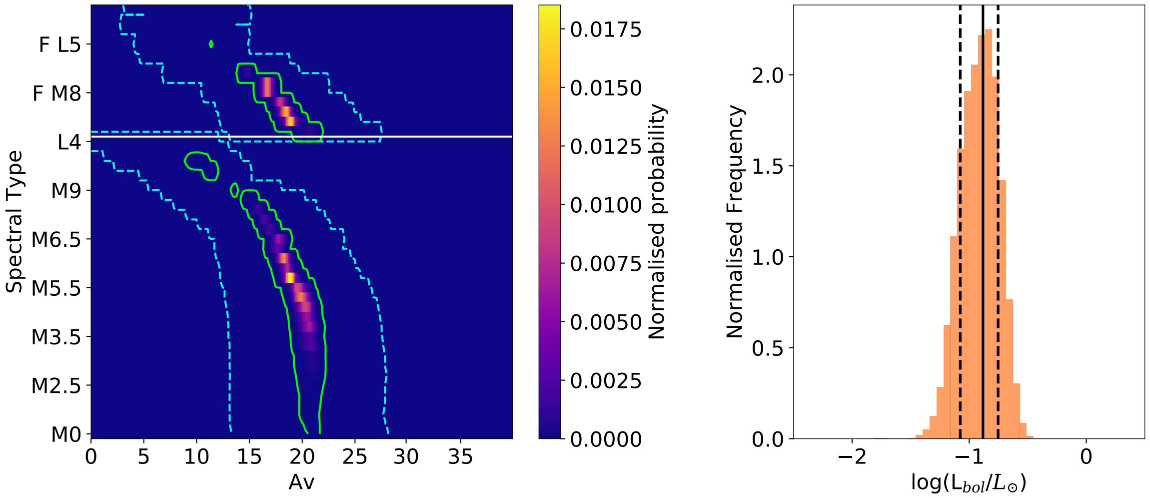

Figure 2.14 *Left: Normalised probability map for SS182955-020416. Right: Histogram of log($L_{bol}/L_{\odot}$) solutions for SS182955-020416, derived from the normalised probability map.*

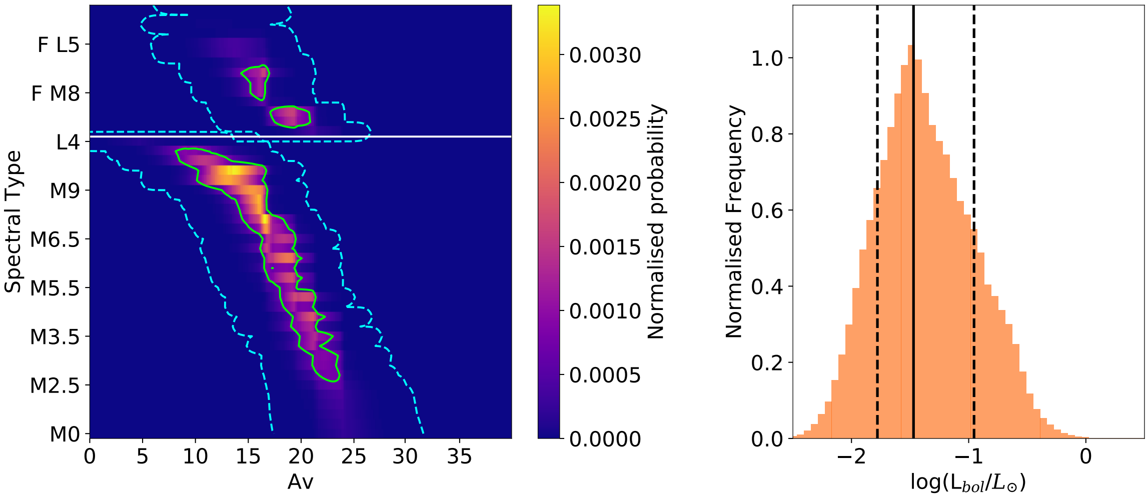

Figure 2.15 *Left: Normalised probability map for SS182959-020335. Right: Histogram of log($L_{bol}/L_\odot$) solutions for SS182959-020335, derived from the normalised probability map.*

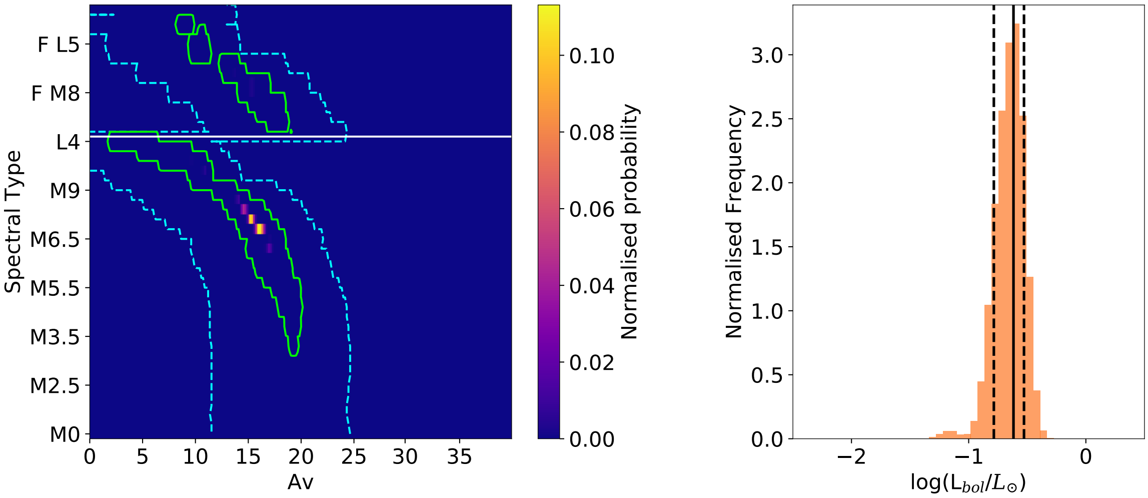

Figure 2.16 *Left: Normalised probability map for SC182952+011618. Right: Histogram of log($L_{bol}/L_\odot$) solutions for SC182952+011618, derived from the normalised probability map.*

we evaluated a χ^2 'goodness-of-fit', with the data reddened by A_v values from 0–40 using the reddening law from Fitzpatrick (1999). We investigated the effect of the choice of extinction law on our best-fit parameters in Jose et al. (2020), and found it to have a minimal effect on our results.
The signal-to-noise (S/N) in the *J*-band portion of some of the spectra (1.07-1.4 μm) was not sufficient for a reliable fit, due to the high extinction of the region. As a result, some of the spectral types presented here were determined using a fit to the *H*- (1.4 - 1.8 μm) and *K*- (1.9 - 2.3 μm) bands only. Having obtained a χ^2 value for each grid point of A_v vs SpT, we plotted normalised probability maps of the parameter space, in order to evaluate the best-fit parameter combination. One such map is shown in Figure 2.12, for SS183032-021028. Results for the younger and field age standards are distinguished by the horizontal white line. We used the 1σ contour in A_v-SpT space to inform the best-fit spectral type and extinction combination. A_v vs SpT probability maps for SS182953-015639, S182955-020416, SS182959-020335 and SC182952+011618 (the other low-mass candidate Serpens members reported in this work, see below) are given in Figures 2.13, 2.14, 2.15 & 2.16. The spectral types (if constrained) for each Serpens object are given in Table 2.3, along with spectral types of the seven targets discussed in Jose et al. (2020). Extinctions and ages for late-type discoveries are given in Table 2.4. Of the 9 objects in this portion of spectroscopic follow-up of Serpens South and Serpens Core, we report spectral types for five objects (discussed further in Section 2.6.2). From rest of the sample reported in this work, three objects (SS183029-015409, SS183037-020941 and SS183006-020219) are classified as clear early-M contaminants. We also find one late-M, field age object, SS182949-020308. We used visual inspection of the spectra to confirm by eye whether our classifications from this analysis were reasonable. The spectral features of young and field age late M and L type objects differ. Low surface gravity (i.e. young) objects have a distinctly 'peaky' *H*-band shape (Lucas & Roche, 2000; Allers et al., 2007; Allers & Liu, 2013). We see this feature (to varying degrees) in each of our late-type detections. Additional indicators of low surface gravity are present in the $J-$,$H-$ and $K-$ bands, but we have insufficient S/N to use these for classification. Similarly, we do not see any features that can be used to distinguish between early-M (M0–M4) objects. As a result, the targets classified as early M objects could have spectral types ranging from M0–M4.

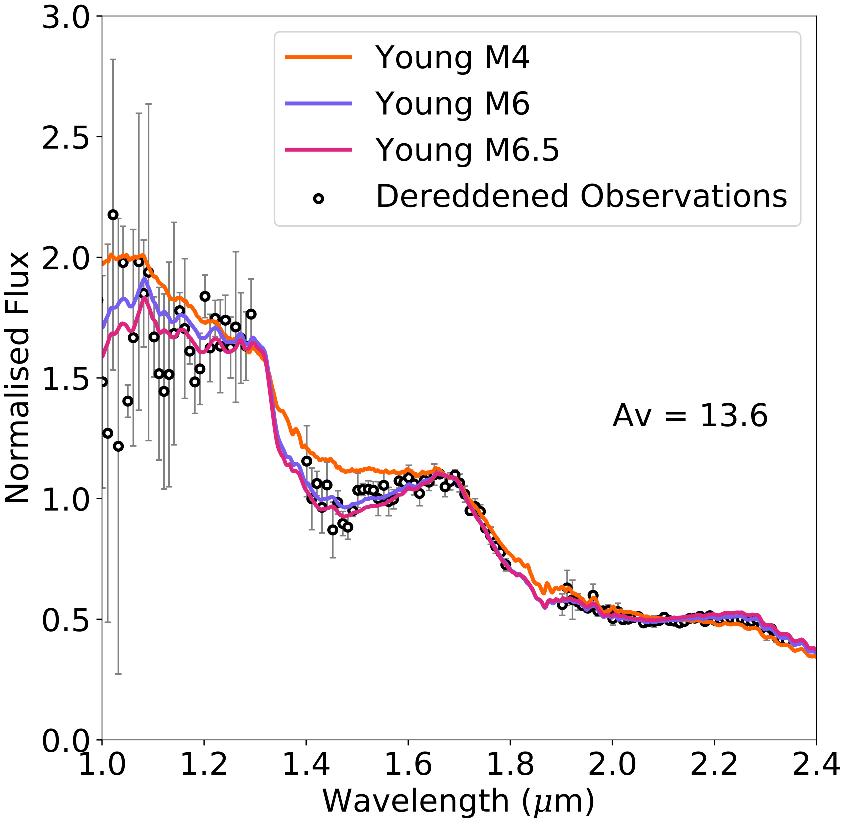

Figure 2.17 *Spectrum of SS183032-021028, dereddened by the best-fit* A_V *(black open circles). Spectral data is compared to best-fit M6 spectral template from L17 (purple), and the earliest (M4, orange) and latest (M6.5, pink) templates as informed by 1*σ *errors.*

2.6.2 New Detections

We find five new candidate Serpens members: four in Serpens South and one in Serpens Core. SC182952+011626 and SS182959-020335 are found to have best-fit spectral types of M8 and M7.5 respectively, and are discussed further below. SS183032-021028 (spectrum shown in Figure 2.17) is found to be best fit by a young, M6 standard, placing it at the boundary of substellar objects in Serpens South. SS182953-015639 (spectrum shown in Figure 2.18) is best fit by an M7 standard spectrum, but we see clear bimodality between young and field age templates. This can be seen in the normalised probability map shown in Figure 2.13. We are confident in the late spectral type of this object, but cannot report a confident age as the spectral fitting results do not strongly favour one population.

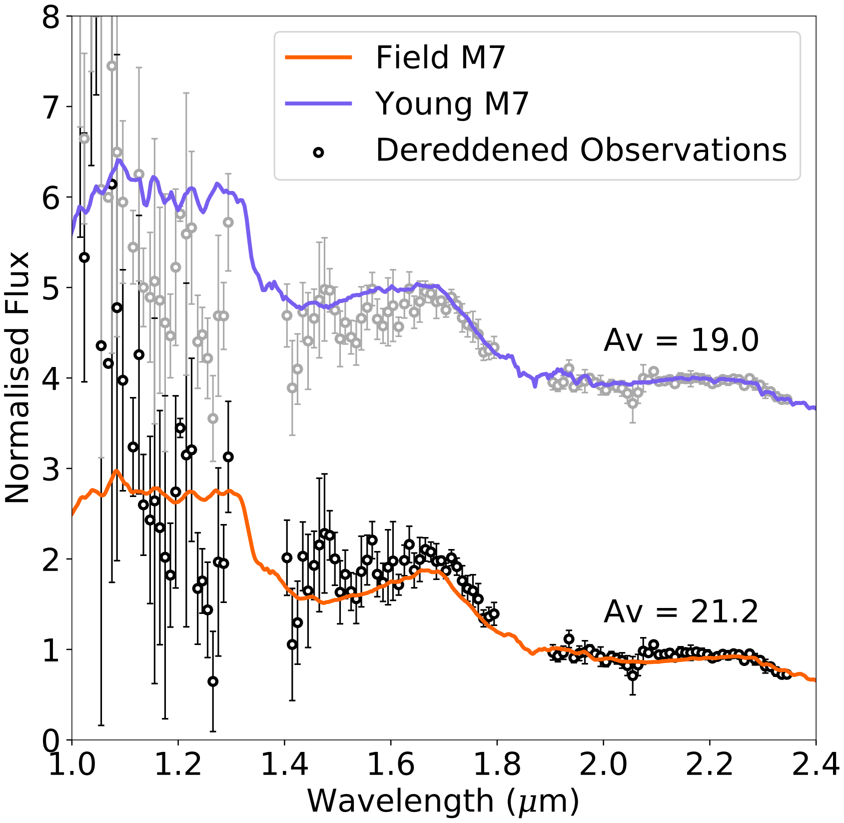

Figure 2.18 *Spectrum of SS182953-015639, dereddened by the best-fit A_V (black open circles), compared to a young M7 template fit (upper) and a field M7 template fit (lower).*

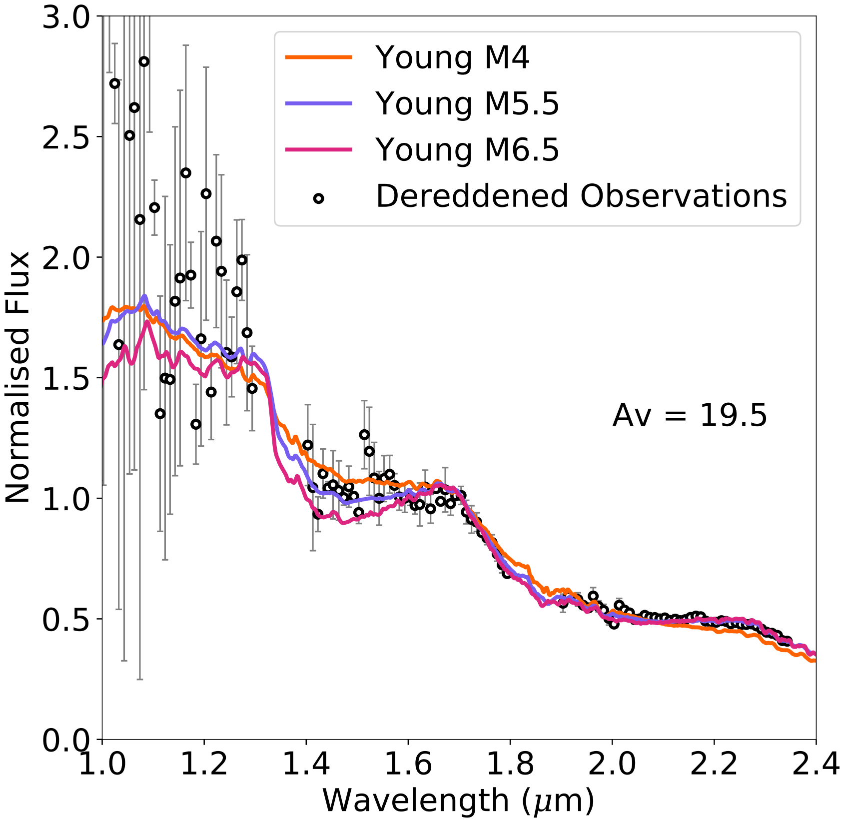

Figure 2.19 *Spectrum of SS182955-020416, dereddened by the best-fit* A_V *(black open circles). Spectral data is compared to best-fit M5.5 spectral template from L17 (purple), and the earliest (M4, orange) and latest (M6.5, pink) templates as informed by* 1σ *errors.*

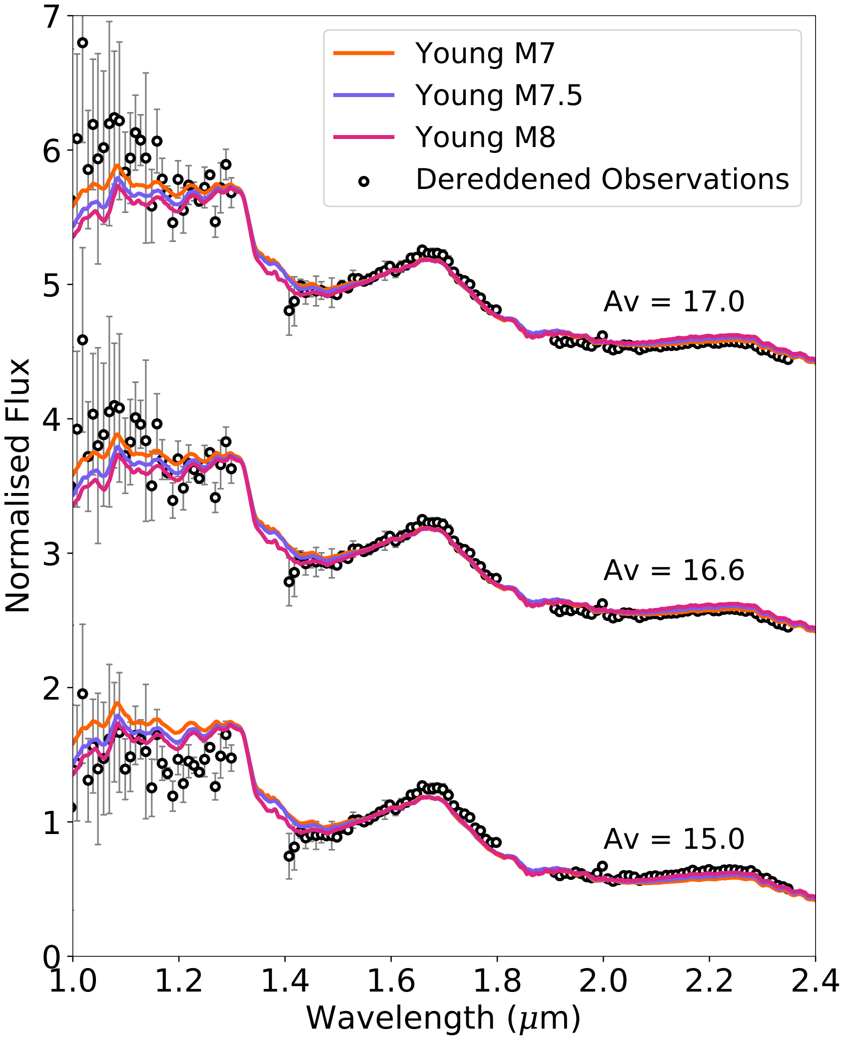

Figure 2.20 *Spectrum of SC182952+011618 (black open circles). Middle: data dereddened by the best-fit* A_v*, compared to the* 1σ *range of L17 spectral templates determined from the probability maps (best-fit = M7.5). Upper and lower plots show the same template spectra, with the minimum and maximum bounds of* A_v*, compared with the dereddened data.*

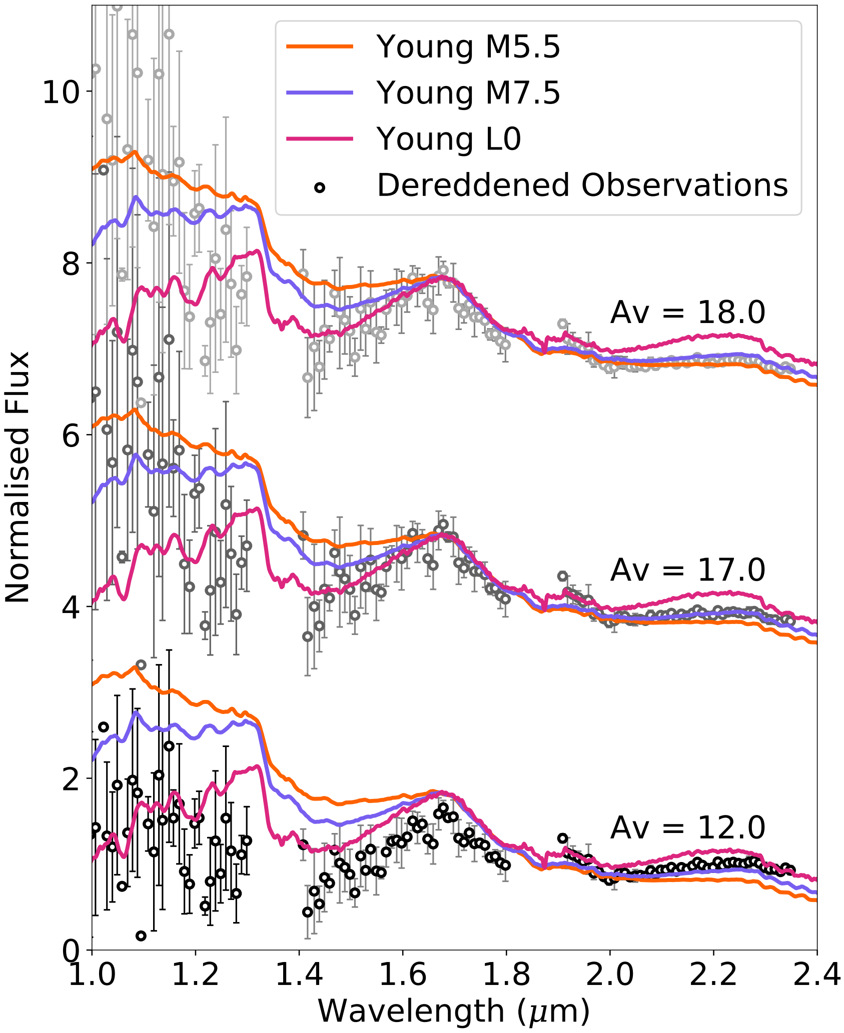

Figure 2.21 *Spectrum of SS182959-020335 (black open circles). Middle: data dereddened by the best-fit* A_v*, compared to the* 1σ *range of L17 spectral templates determined from the probability maps (best-fit = M7.5). Upper and lower plots show the same template spectra, with the minimum and maximum bounds of* A_v*, compared with the dereddened data.*

Constraining the age of this object, and whether it is a likely Serpens South member, will require additional spectroscopy to improve the S/N of possible youthful features. The final likely young Serpens South candidate member, SS182955-020416, has a best-fit spectral type of M5, in the range M4.5-M6, likely above the boundary of substellar objects in Serpens South (spectrum shown in Figure 2.19). We classify this target as a young object (despite bimodality in age from spectral fitting, it appears in multiple YSO catalogues - see Section 2.6.3), and as a result report this target as a Serpens South candidate member.

2.6.2.1 SC182952+011618

SC182952+011618 (Serpens Core) has a best-fit spectral type of M7.5, in the range M7-M8, with a best-fit $A_{\rm v}$ of 16.6, in the range of 15-17. We quote a range in $A_{\rm v}$ as we found that our errors were often asymmetric. The spectral type was determined by fitting standard templates to the full spectrum (J-,H- and K-bands). The spectrum of SC182952+011618 is shown in Figure 2.20: the peaky H-band feature is clear, as we would expect to see for a young, late-type object. In this figure, we also demonstrate the spread in spectral types and extinctions that fit well to this data, informed by the parameter ranges given in Table 2.4.

2.6.2.2 SS182959-020335

SS182959-020335 (Serpens South) has a best-fit spectral type of M7.5, in the range M5-L0, and best-fit $A_{\rm v}$ of 20.2, with a range of 12-18. Again, we can see that the best-fit young templates in Figure 2.21 reproduce the shape of the H-band well. However, the clear spread in the H-band data demonstrates the need for a wider range of possible spectral type fits for this object, compared to SC182952+011618. Additionally, the spectral type for this object was determined only using the H- and K- bands, as the J-band suffers from significantly lower S/N. Constraining the spectral type range further will require additional observation of the J- and H- bands.

Table 2.4 *Parameters derived from spectral fitting for the new candidate Serpens members discovered in the W-band Serpens surveys. Adopted spectral types and extinctions are given, as well as the population according to the near-IR gravity classification in Allers & Liu (2013) (VLG = very low gravity, INTG-G = intermediate gravity).*

Target No.	Object ID	SpT	$A_{V,best}$	$A_{V,range}$	Age
Serpens South (this work):					
1	SS182953-015639	M6–L0	-	10–23	-
2	SS182955-020416	M4–M6.5	19.5	17–21	INT-G
3	SS182959-020335	M5–LO	17.0	12–18	VL-G
4	SS183032-021028	M5–M6.5	13.6	12–15	INT-G
Serpens Core (this work):					
5	SC182952+011618	M7–M8	16.6	15–17	VL-G
Serpens South (Jose et al., 2020):					
6	SS182917-020340	M4–M7	20.0	17–22	VL-G
7	SS182918-020245	M5–M8	11.9	10–13	VL-G
8	SS183038-021419	M3–M6	21.9	18–24	VL-G
9	SS183044-020918	M7–M9	13.6	12–15	VL-G

Table 2.5 *Physical properties of the new candidate Serpens members discovered in the W-band Serpens surveys. The bolometric correction needed to calculate log($L_{bol}/L_{\odot}$) is taken from either Filippazzo et al. (2015) or Herczeg & Hillenbrand (2015), depending on the spectral type of the object. Mass estimates shown are approximate values derived from the positions of targets in Figure 2.22. Objects that appear in YSO catalogues are indicated: G = appears as YSO in Getman et al. (2017), D = appears as YSO in Dunham et al. (2015), P = appears as YSO in Povich et al. (2013), G-NOD = listed as 'No disk' in Getman et al. (2017).*

Target No.	Object ID	log($L_{\mathrm{bol}}/L_{\odot}$)	T_{eff} (K)	Mass (M$_{\odot}$)	YSO?
Serpens South (this work):					
1	SS182953-015639	$-0.91^{+0.47}_{-0.30}$	2720 ± 200	0.07–0.1	...
2	SS182955-020416	$-0.88^{+0.13}_{-0.19}$	2920 ± 165	0.1–0.15	G,D,P
3	SS182959-020335	$-1.47^{+0.52}_{-0.31}$	2770 ± 200	0.05–0.09	G,P
4	SS183032-021028	$-1.21^{+0.18}_{-0.09}$	2860 ± 120	0.07–0.1	...
Serpens Core (this work):					
5	SC182952+011618	$-0.61^{+0.08}_{-0.17}$	2720 ± 50	0.07–0.12	G-NOD
Serpens South (Jose et al., 2020):					
6	SS182917-020340	-0.78 ± 0.28	2980 ± 210	∼0.1	G,D,P
7	SS182918-020245	-0.91 ± 0.17	2825 ± 155	0.05–0.08	G,D,P
8	SS183038-021419	-0.89 ± 0.34	3135 ± 275	∼0.1	G,D,P
9	SS183044-020918	-0.67 ± 0.09	2670 ± 100	0.05–0.08	G,D,P

2.6.3 YSO Catalogues

Jose et al. (2020) use the presence of a Serpens candidate member in catalogues of young stellar objects (YSOs) as an independent indication of youth and Serpens membership. In all cases in Jose et al. (2020), the late-type objects identified spectroscopically appeared in the MYStIX IR-Excess Source Catalogue (Povich et al., 2013, hereafter P13), SFiNCs Xray-Infrared Catalogue (Getman et al., 2017, hereafter G17) and the Gould Belt Survey (Dunham et al., 2015, hereafter D15). This was used as strong evidence to break the population degeneracy found in the χ^2 maps for some of these objects, and classify them as young. However, for the objects discussed in this work, the evidence is less conclusive. In Table 2.5, the column labelled 'YSO?' indicates whether an object is identified as a YSO in these surveys. SS182953-015639 and SS183032-021028 do not appear in any of the catalogues. SS182959-020335 is listed as a young stellar object in both G17 and P13, and SS182955-020416 appears in both of these and in D15. SC182952+011618 does not appear in D15, and is flagged as 'NO-DISK' in G17, meaning this object is identified as diskless by this survey (P13 does not cover Serpens Core). This classification is based on the shape of the IR SED, as well as other properties of IR and X-Ray photometry (see Getman et al., 2017). This is not conclusive proof against the youth of this object, but does strongly indicate that the object does not host an accreting disk. Winston et al. (2018) report a sub-sample of 18 diskless objects in Serpens South. They argue that whilst they clearly lack disks, other indicators of youth imply these objects are likely young cluster members, that may have rapidly lost their disks due to external environmental factors (e.g. stripping by nearby massive stars, tidal disruption). They report that 30-53% of X-ray sources discovered in Serpens South are diskless (comparable to 48±11% for Serpens Core, Winston et al., 2007) - consequently, we consider it likely that SC182952+011618 is one of these diskless, young cluster members.

In general, the information gathered about these objects from YSO catalogues is somewhat inconclusive. For SS182959-020335, SS183032-021028 and SC182952+011618, spectral type fitting unambiguously classifies these objects as young, based on their spectral features. However, this is not the case for SS182953-015639 and SS182955-020416, where we see bimodality in the SpT-A_V χ^2 maps. The latter appears in all 3 YSO surveys considered here, demonstrating additional evidence of youth and supporting the young spectral solution for this target, which we henceforth adopt. The lack of information in YSO catalogues for SS182953-015639 means we are unable to break the degeneracy between the young and field solutions, and we cannot confidently assign SS182953-015639 to a population.

2.6.4 Physical Parameters

We used our CFHT photometry and SpT-A_V probability maps to calculate the bolometric magnitude and luminosity of each candidate Serpens member in our sample. We performed a Monte Carlo analysis, using 500,000 model objects distributed proportionally across the SpT-A_V grid. For each simulated object in each SpT-A_V probability bin, we calculated a bolometric magnitude (Eq. 2.4) by sampling Gaussian distributions of distance modulus, d_mod and apparent magnitude, m_J.

$$M_\mathrm{bol} = m_\mathrm{J} - d_\mathrm{mod} - A_\mathrm{J} + BC_\mathrm{J} \tag{2.4}$$

The Gaussian distribution of m_J is constructed using the CFHT apparent magnitude and error, as listed in Table 2.1. The Gaussian distribution of d_mod is constructed using the assumed value of 8.2 ± 0.18 mag, calculated using the Serpens distance given in Ortiz-León et al. (2017). In Eq. 2.4 we also use the conversion factor from A_V to A_J, taken to be 0.282 (Cardelli et al., 1989), and the bolometric correction, BC_J. The bolometric correction is taken from two sources: for spectral type M7 or later, the relevant polynomial described in Filippazzo et al. (2015) is used; if the spectral type is earlier than M7, the bolometric corrections given in Herczeg & Hillenbrand (2015) are used. To convert from bolometric magnitude to bolometric luminosity, we use Eq. 2.5, where the solar bolometric magnitude is taken to be 4.73 mags:

$$\log_{10}(L_\mathrm{bol}/L_\odot) = -(M_\mathrm{bol} - M_{\mathrm{bol},\odot})/2.5 \tag{2.5}$$

Having obtained a bolometric luminosity ($L_\mathrm{bol}/L_\odot$) for each model object in each bin, we use this data to plot a histogram of $\log(L_\mathrm{bol}/L_\odot)$ values. The values given in Table 2.5 are the peak positions of these histograms, with errors derived from the 68% Bayesian credible intervals of the distribution, which reflect the asymmetry seen for every object. Log($L_{\mathrm{bol}}/L_{\odot}$) histograms are shown in Figures 2.12, 2.13, 2.14, 2.15 & 2.16 for the Serpens candidate members reported in this work. In some cases, we saw bimodal distributions in log($L_{\mathrm{bol}}/L_{\odot}$): the parameter values in these cases are taken from the most prominent peak in the distribution. We made one key assumption when modelling the luminosity distribution across the full range of Av and SpT: we only included the section of the parameter space corresponding to young template fits. This is due to the inclusion of the distance modulus in the bolometric magnitude calculation, as the adopted distance modulus is only valid for actual members of Serpens. As a result, we assume that all 5 objects are young (with strong evidence of this being true for all targets except SS182953-015639), and calculate a luminosity range that would be valid in this case. Figure 2.22 shows the 5 new detections presented in this Chapter plotted on a HR-diagram (numbering from Table 2.5), also showing age and mass isochrones (taken from Baraffe et al., 2015) to give context for other objects of these masses and ages. The effective temperatures (T_{eff}) plotted here and given in Table 2.5 are estimated using our derived spectral types and the relations given in Table 5 of Herczeg & Hillenbrand (2014). The 4 young, late-type candidate Serpens members presented in Jose et al. (2020) are also shown, with physical parameters given in Table 2.5.

2.6.5 HST Imaging

As discussed in Section 2.4.4, to search for low-mass companions to our new Serpens candidate members, we obtained IR and UVIS (UV and visible) imaging of 6 targets in Serpens South, using Wide Field Camera 3 (WFC3) on the Hubble Space Telescope (HST).

2.6.5.1 New Binary Detection: SS183044-020918

The F850LP image of target SS183044-020918 appears notably elongated compared to other objects in the field. The components appear marginally resolved in the F850LP data, shown in Figure 2.23, along with the unresolved components in the IR filter F127M - the IR channel of has a much coarser pixel scale than

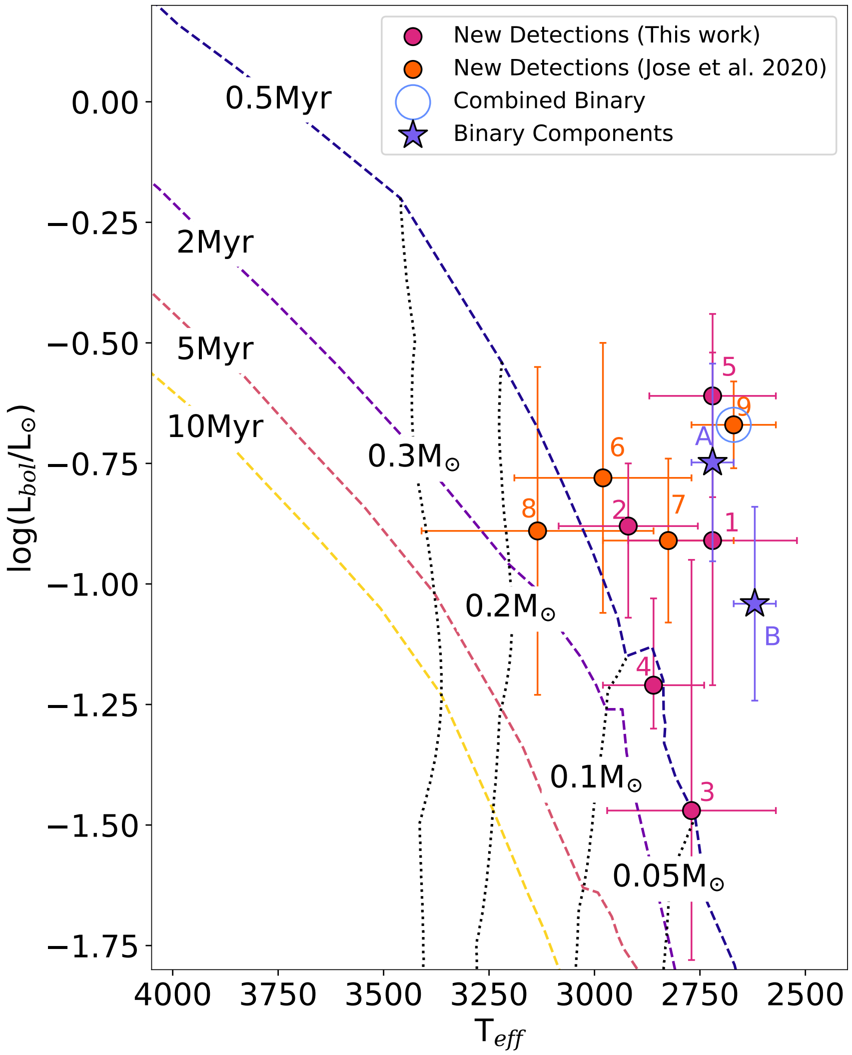

Figure 2.22 *H-R diagram for the five candidate Serpens members identified in this Chapter (pink points), 4 in Serpens South (1,2,3,4) and 1 in Serpens Core (5). Also shown are the four low-mass candidate members presented in Jose et al. (2020) (orange points, 6,7,8,9). Object 9 is the newly discovered binary system (blue circle): purple stars show the binary components (A and B). Isochrones (dashed lines) and evolutionary tracks (dotted lines) shown are taken from Baraffe et al. (2015).*

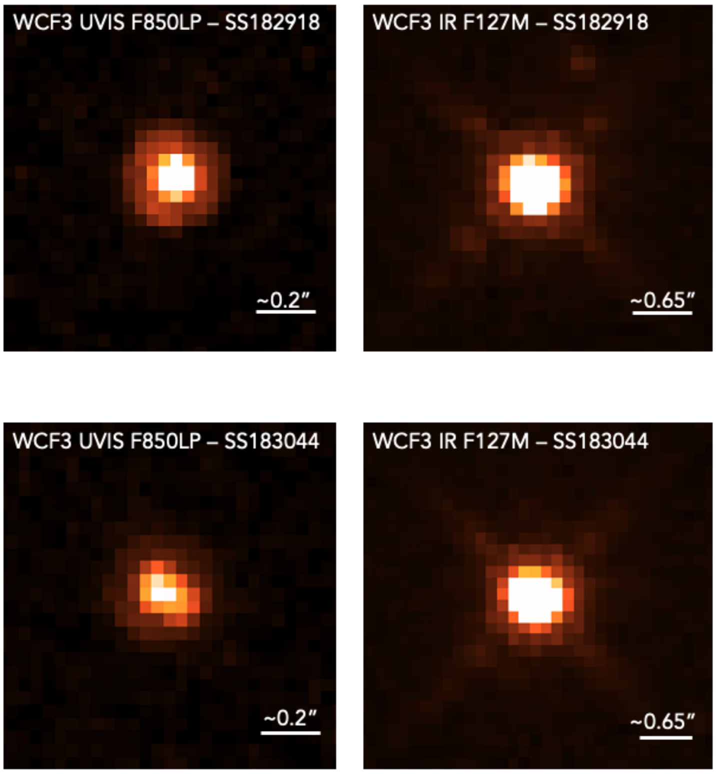

Figure 2.23 *Upper panels: for comparison, F850LP (upper left) and F127M (upper right) images of SS182918-020245, a non-binary target from the Serpens HST program. Lower panels: the newly discovered low-mass binary, SS183044-020918. The binary components are resolved in F850LP (lower left), and unresolved in F127M (lower right), due to the larger pixel scale of the HST IR channel.*

the UVIS. We also show the F127M and F850LP images for SS182918-020245, to highlight the elliptical appearance of SS183044-020918 in F850LP. This elongation is clearly caused by two distinct components: best explained by a binary system, as we show below.

To determine the separation and the relative flux contributions of each binary component, we built an effective point spread function (ePSF) using the other target stars from the HST survey. After removing some stars due to contamination or bright pixels, we retained a sample of 28 stars to build the ePSF. These were centred and scaled by the `EPSFBuilder` algorithm available in the python package `photutils`, and combined into a single ePSF. We then ran a Markov chain Monte Carlo (MCMC) analysis for parameter estimation, using

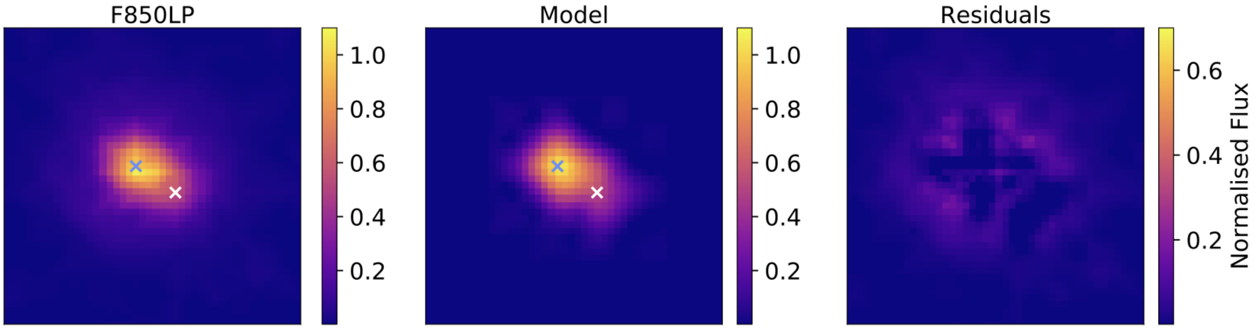

Figure 2.24 *Best-fit PSF subtraction model for both components of SS183044-020918, using ePSF method. Coloured crosses indicate the best-fit component positions. Left panel shows raw F850LP data. Centre panel shows model imaged constructed using best-fit parameters from MCMC analysis. Right panel shows residuals from model fit.*

the python package `emcee` (Foreman-Mackey et al., 2013). At each step of the MCMC chain, an artificial image is constructed using two scaled ePSFs, with the coordinates of both components as model parameters, as well as the relative flux ratio. We minimise over χ^2 to obtain a best-fit model image and binary component parameters, as well as associated errors. The best-fit model and fit residuals are shown in Figure 2.24.

We calculated the binary separation using the best-fit component positions from this analysis, and calculated the magnitude difference of the two components from the best-fit flux ratio. We find that the components are not equal magnitude: SS183044-020918B is 0.76±0.06 magnitudes fainter than SS183044-020918A in the F850LP filter. All data calculated using this model fitting is given in Table 2.6, including errors for each fit parameter. The secondary is at a separation of 0.092±0.008" from the primary, which corresponds to 41.9±3.6 AU in Serpens South. This distance was calculated using the F850LP images only, as it is less than the pixel scale of the IR channel detector (0.13"), and thus the two components are unresolved in F127M and F139M.

Jose et al. (2020) present a combined spectrum of SS183044-020918, which was best fit with a young standard of spectral type M7-M9, and an A_V in the range 12-15 mag. We explored whether a combination of multiple spectral type templates (one for each binary component) provides a better fit than a single component template. We again used the young spectral templates from L17, combined in pairs and fitted to the observed spectrum, whilst varying the A_V between

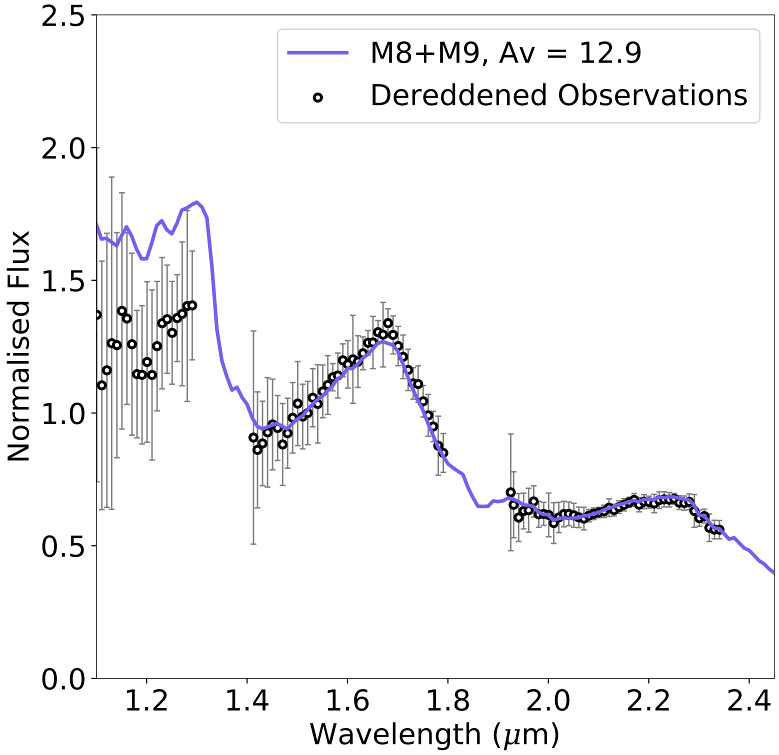

Figure 2.25 *Spectrum of SS183044-020918, first reported in Jose et al. (2020). Data is shown in black open circles, and is dereddened by the best-fit A_V = 12.9. The best-fit combined template spectrum, M8+M9, is shown in purple.*

the previously-found best-fit range. For the primary, we considered M7-M9 as reasonable spectral types, and for the secondary, we used the broader range of M7-L2. We only considered solutions where the secondary was of a later spectral type than the primary - informed by the flux ratio in F850LP. The resulting best-fit spectral types for each component are given in Table 2.6. We again give a range of spectral types - as we saw that different combinations of templates gave similarly good answers, with slightly varying $A_{\rm V}$ values. We find that SS183044-020918A has a best-fit spectral type of M7-M8, and SS183044-020918B has a best-fit spectral type of M8-M9. Figure 2.25 shows the overall best fit of M8+M9 with an $A_{\rm V}$ of 12.9±0.3, slightly lower than the previously reported value of 13.6 (Jose et al., 2020).

We used the flux ratio of the components, and the photometry and spectroscopy obtained from both the W-band and HST surveys, to determine physical properties. These are detailed in Table 2.6. The J and H mags were calculated using $\Delta(\text{mag}) = 0.76$, derived from the best fit to the F850LP image and the CFHT photometry for the combined components. As the binary is only resolved in F850LP, we must assume that the flux ratio between the two components is similar in every filter, and calculate properties based on this assumption. The similar spectral types of both components support this assumption, indicating that Δ(mag) will likely be similar in different filters. As in Section 2.6.4, to calculate the bolometric luminosity of each component, the bolometric correction BC_{J} was taken from Filippazzo et al. (2015). We use the extinction determined from our combined standard best-fit, $A_{\text{V}} = 12.9$. T_{eff} for each component is estimated using Table 5 of Herczeg & Hillenbrand (2015). If we plot the two binary on Figure 2.22 (purple stars), we find that SS183044+020918A is consistent with a mass of ~0.08-0.1 $\text{M}_{\odot}$, and SS183044+020918B is consistent with a lower mass of ~0.05-0.07 $\text{M}_{\odot}$, truly pushing into the substellar regime. As seen with the other reported discoveries in Section 2.6, the two binary components lie above the 0.5 Myr isochrone, and as such the masses determined by extended the evolutionary models beyond this age have large associated errors.

2.6.5.2 Likelihood of Binarity

At a distance of > 400 pc, the motion of objects in Serpens South is too low to allow common proper motion confirmation of this candidate on a timescale < 10 years. Instead, we estimate the likelihood that SS183044-020918B is a background object using the 2MASS survey and Eq. 1 from Brandner et al. (2000):

$$P(\Theta, m) = 1 - e^{-\pi\rho(m)\Theta^2} \qquad (2.6)$$

where Θ is defined as the angular distance from the target considered, and ρ(m) is defined as 'the cumulative surface density of background sources down to a limiting magnitude m' (Brandner et al., 2000). A 2MASS query within a 1° radius of the primary returns 102,537 sources with J magnitudes of 16.5 or brighter. We use this as the surface density of background sources ρ(m), with an angular distance Θ equal to the binary separation. This returns a probability of $P(\Theta, m) \approx 2.1 \times 10^{-4}$ of finding a background source with a brightness at least that of the secondary within 0.096" of the primary. This calculation does not

Table 2.6 *Properties of the binary system, SS183044-020918.*

Property	Primary	Secondary
Distance	436.0 ± 9.2 pc[a]	
Age	0.5 Myr[b]	
Separation	0.092 ± 0.008" (41.9 ± 3.6 AU)	
Δ(mag) (F850LP)	0.76 ± 0.06	
$z^{\dagger}$	21.46	22.22
$J^{\dagger}$	16.74	17.50
$H^{\dagger}$	14.85	15.61
A_{V}	12.9 ± 0.3	
Spectral Type	M7-M8	M8-M9
$\log(L/L_{\odot})^{\dagger}$	-0.748 ± 0.205	-1.041 ± 0.210
T_{eff}	2720 ± 50 K	2620 ± 50 K
Estimated mass[†]	0.08–0.1 $\mathrm{M}_{\odot}$	0.05–0.07 $\mathrm{M}_{\odot}$

[a] Distance from Ortiz-León et al. (2017, 2018b).

[b] Age from Gutermuth et al. (2008).

[†] Assuming F850LP Δ(mag) is true for all wavelengths

account for the size of the survey, or the colour information of the sources, both of which give us additional insight into the nature of the secondary. Thus, we are confident that the binary we report is indeed a binary, and not a Serpens South member aligned with an unrelated background star.

Further evidence of the binarity of this system can be found in the spectral data. As detailed above, our combined spectrum is best fit by a young M8+M9 combined template. This strongly implies the secondary has a similar or later spectral type to the primary, as does the F850LP flux ratio. When considering this in conjunction with the calculation of the likelihood of the secondary being an unrelated foreground/background object, the probability of a similarly late and young background object in chance alignment with the primary is, as stated above, very small.

2.6.6 Other Serpens South HST observations

We examined the 6 Serpens South HST datasets for binary systems, close-in and wide companions, and do not report any additional candidate companions. To perform this examination, we used a two-fold approach. We visually inspected each image for close companions, looking for obvious elongation or close neighbouring sources. This initial inspection led to the identification of SS183044+020918 as a binary, but of no other candidates. Next, we performed PSF subtraction on each of the images, using two parallel techniques.

The first method uses an ePSF constructed from other target stars in the survey, as detailed above for the binary analysis. We used this ePSF in conjunction with the PSF subtraction algorithms available in `photutils`. More specifically, the `IterativelySubtractedPSFPhotometry` function was used to subtract the target-constructed ePSF from each of the objects, leaving a residual image with the starlight removed. If there were any close in companions around the targets objects, previously obscured by the objects themselves, these should be visible in the ePSF-subtracted residuals.

To confirm the results of the aforementioned method to detect possible Serpens companions, we made use of tools from the Vortex Image Processing package (VIP; Gomez Gonzalez et al., 2017) to perform a PSF subtraction. VIP has an implementation of the Reference Differential Imaging method (RDI; Lagrange et al., 2009; Lafrenière et al., 2009; Soummer et al., 2012) where a reference PSF is constructed using similar but distinct PSFs to subtract from the science PSF. This is combined with an implementation of Principal Component Analysis (Soummer et al., 2012) to reduce the dimensionality of the data. We build our reference library by using other stellar PSFs in the Serpens cluster data in addition to previously observed data from the Ophiuchus and Taurus associations, all observed with HST in the F850LP filter. We then divide this into nine separate 'sublibraries' based on which subpixel the PSF peak position falls on: where the subpixels are each pixel divided into nine equal squares. To determine the peak of the science PSF, a Gaussian fit is made to the Serpens target PSF. This peak defines which sublibrary will be used for the PSF subtraction, as the reference sublibrary will be made up only of PSFs whose peak falls in the same subpixel as the target's peak. Using this method with 5 principal components, we made a redetection for the binary companion to SS183044+020918. We also performed this analysis on the other Serpens objects, for which we made no further detections, agreeing with the results of the method above.

We also examined the images for wide companions, and investigated the nature of other objects nearby in the field. We examined each object with 3 criteria in mind: 1) were there any nearby (within $\sim$ 20”) sources with similar or larger Q_{HST} values than the target, 2) were there any nearby sources (within $\sim$ 3”) with blue F127M - F139M colours and 3) were there any nearby F139M dropouts (i.e. $< 10\sigma$ detection in F127M and no detection in F139M). For all of the Serpens images, there were no nearby sources that satisfied these criteria, ruling out finding any wide-companions with these diagnostics.

2.6.7 Contrast Curves

We present contrast curves for our HST observations in Figure 2.26. To generate contrast curves, we added a simulated planet (the ePSF used in Section 2.6.5.1, scaled and cropped) into the F127M images of the five datasets with no detections, at a specified position and magnitude difference (relative to the primary star). We varied the planet-star separation and magnitude difference to cover a grid ranging from 0.13 - 2.0” in separation and from $\Delta\mathrm{mag} = 0 - 8$. To obtain the contrast value plotted for each separation, we performed PSF subtraction (as in Section 2.6.5.1) on the image containing the injected planet. We then calculated the signal in an ePSF-sized aperture placed over the location of the injected planet in the PSF-subtracted image. To calculate the noise level, we used the same aperture at the position of the injected planet, but in a PSF-subtracted image where no planet was added. For each separation, the magnitude difference that yielded a signal-to-noise ratio (S/N) > 5 was adopted as the contrast at that radius.

The achieved contrast is similar for all targets at separations $\lesssim$ 0.6” from the primary star. The contrasts diverge at separations greater than this, and reach differing levels at separations $\gtrsim$ 1.0” (corresponding to $\approx$ 10 pixels in the F127M images). In Figure 2.26, we also present the minimum detectable apparent magnitude of a planet around each target, to account for the variation in contrast caused by the differing intrinsic brightness of each target. From this, we can see that the performance for each target is actually quite similar, with a mean value reaching $\sim m = 23$ at a separation of $\sim$1.0” from the primary. We present contrast curves in F127M, as two targets were not detected in F850LP. We also used VIP and the technique discussed previously to calculate contrast curves, and find good agreement between the two methods for all targets.

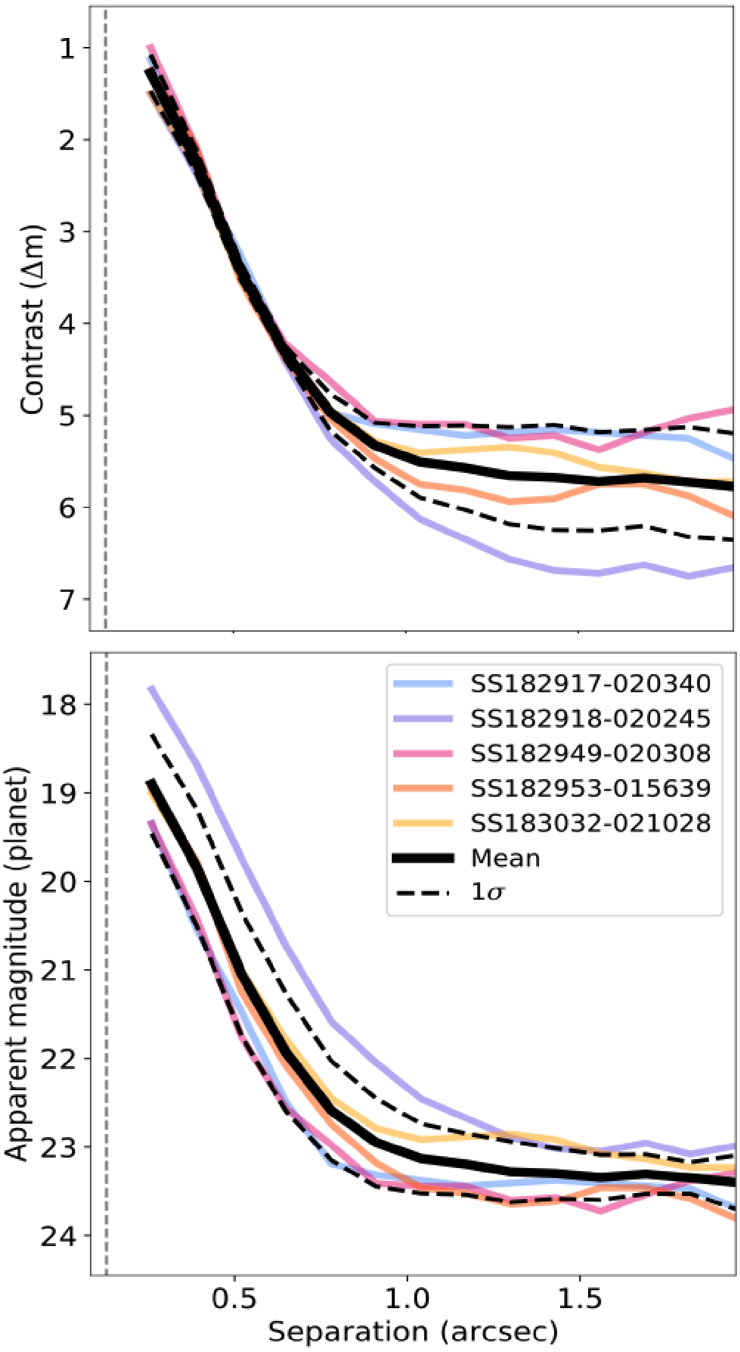

Figure 2.26 *Left: Contrast curves in F127M for the five Serpens objects with no detected companions. Contrast values were calculated by injecting synthetic planets into the images and checking the magnitude at which these are no longer detectable. Dashed line indicates the pixel scale of the F127M HST images (0.13"). Right: Minimum detectable apparent magnitude for planets around each target (coloured dashed lines). Solid black line shows the mean value for all 5 targets at each separation, dashed lines show 1σ error on this value.*

2.7 Discussion

The W-band technique has proven highly effective in identifying ultracool dwarfs in nearby star-forming regions. By looking at Serpens South and Serpens Core, we have pushed its effectiveness to its limits, yet still demonstrated its usefulness by finding more low-mass, likely members of these subclusters. The number of new detections presented in this Chapter is small, but adds to the growing number of objects creating a statistically significant low-mass sample. We cannot provide additional constrains on the form of the low-mass end of the IMF with just the small sample presented in this work. However as further low-mass members of Serpens are discovered, the possibility for a meaningful, focused investigation of the IMF in this region increases.

2.7.1 Mass estimates of new detections

In Section 2.6.4, we calculated physical properties of the 5 mid-late M, candidate Serpens members reported in this portion of the W-band Serpens survey. Figure 2.22 shows these objects on a HR diagram, as well as the four candidates reported in Jose et al. (2020), and isochrones and evolutionary tracks from Baraffe et al. (2015).

SS183032-021028 (target 4, numbering given in Table 2.5) lies effectively on the 0.5 Myr isochrone (the approximate age of Serpens South, Gutermuth et al., 2008), and has an effective temperature consistent with a mass of approximately 0.07–0.1 $M_{\odot}$. SS182955-020416 (target 2) lies close the 0.5 Myr isochrone, but likely has a higher mass, approximately 0.1–0.15 $M_{\odot}$.

Similarly, SS182959-020335 (target 3) also sits on the 0.5 Myr isochrone, and likely has the lowest mass of the 5 Serpens candidate members. We report a mass interval of 0.05–0.09 $M_{\odot}$ for this object based on its position in Figure 2.22 - although the mass range encompassed by the error bars indicates that this target could be consistent with a mass lower than this. However, the evolutionary tracks shown here do not extend below 0.05 $M_{\odot}$, and so we cannot confidently report a lower limit that goes beyond the coverage of the models used for characterisation.

SS182953-015639 (target 1) lies above the youngest available isochrone (0.5 Myr).

Again, since this is beyond the range of the evolutionary models, estimating a mass requires extending the model trends to the position of SS182953-015639 - leading to a mass of 0.07–0.1 $M_{\odot}$, which should be treated as very approximate. In previous sections, we discussed the likely age of SS182953-015639, and were unable to constrain it to either a young or field-age population. The calculation of $L_{\mathrm{bol}}/L_{\odot}$ used here assumes that the best solution is a young template - field-age solutions are not considered. Thus, we cannot use Figure 2.22 as strong proof of a young age for SS182953-015639, as the assumption of youth is used in the calculations of the parameters plotted.

One of the objects reported in Jose et al. (2020), SS183044-020918 (target 9), sits high above the 0.5 Myr isochrone. As discussed above in Section 2.6, we report that this object is actually an unresolved binary system, confirmed using multi-filter HST imaging. This explains the anomalously high luminosity seen in this analysis, as we are actually measuring the combined properties of two unresolved objects. Similar to SS183044-020918, SC182952+010116 (target 5) also sits high above the 0.5 Myr isochrone. It is consistent with a mass of $\approx$ 0.07–0.12 $M_{\odot}$, although again, extending the evolutionary tracks beyond the provided values creates a large margin of error. The similarity in physical properties between this target and the newly-discovered binary system suggest that binarity could also explain the anomalously high $L_{\mathrm{bol}}/L_{\odot}$ of SC182952-010116.

SS182918-020245 (target 7) also sits above the youngest isochrone in Figure 2.22. Jose et al. (2020) found signatures of ongoing accretion in the spectrum of this object. The models shown in Figure 2.22 (Baraffe et al., 2015) assume photospheric emission as the primary contributing factor to luminosity - consequently, if an object is also actively accreting, these models are not best suited for characterising its properties. The positioning of many of the Serpens discoveries above the 0.5 Myr isochrone is discussed in further detail in Jose et al. (2020). Ongoing accretion could explain the properties of the two targets from this work that are inconsistent with the 0.5 Myr isochrone, SS182953-015639 (target 1) and SC182952+010116 (target 5). However, the IRTF SpeX spectra obtained for these objects have insufficient resolution to look for the accretion signatures discussed in Jose et al. (2020), and as such we cannot identify accretion as the driving factor for their high luminosities.

The five late-type candidate Serpens members discussed in this work all have masses consistent with 0.05–0.15 $M_\odot$ (using isochrones from Baraffe et al. (2015)). Mass estimates are given in Table 2.5, including objects from Jose et al. (2020). If the boundary between low-mass stellar objects and substellar brown dwarfs is taken to be ∼0.075 $M_\odot$ (Reid et al., 1999), SS182953-015639, SS182959-020335, SS183032-021028 and SC182952+011618 could all be characterised as substellar, although the large error bars on their derived masses mean that this characterisation remains uncertain. It should be noted that the mass estimates given in Jose et al. (2020) (and in Table 2.5) are derived using solely the $T_{\rm eff}$ of each object, which differs slightly from the method used in this work (where luminosities and effective temperatures are used in combination).

2.7.2 New binary discovery

In Section 2.6.5.1, we present the properties of SS183044-020918, derived from analysis of IR and UVIS HST images. As discussed here, the mass estimate of 0.05–0.07 $M_\odot$ derived for SS183044-020918B makes it the lowest mass object discovered in the W-band/HST survey of Serpens, and also the most likely substellar candidate member. With a primary mass of 0.08–0.10 $M_\odot$, the more massive component of this binary is likely a very low-mass star, with a mass lying just above the hydrogen-burning limit. Such component masses, with a measured projected separation of ∼40 AU, are not unusual for late-type M dwarfs, which tend to have more similar component masses and tighter binary separations compared to more massive stars (Bergfors et al., 2010).

Although low-mass stars and brown dwarfs are preferentially seen in compact binaries, a number of wide low-mass systems have been discovered with separations of several tens to hundreds of AU, both in young associations and in the field population. For example, the young Taurus binaries CFHT-Tau-7 (with masses of 0.07 and 0.06 $M_\odot$), CFHT-Tau-17 (0.10 and 0.06 $M_\odot$) and CFHT-Tau-18 (0.10 and 0.06 $M_\odot$) have orbital separations of 32, 82 and 31 AU, respectively (Konopacky et al., 2007). In the field, systems in similar configurations include DENIS J220002.05−303832.9AB (Burgasser & McElwain, 2006), a 0.085+0.083 $M_\odot$ binary with a 38-AU separation, or 2MASS J15500845+1455180AB (Burgasser et al., 2009), which consists of 0.070 and 0.067-$M_\odot$ L dwarfs separated by 30 AU. While not very common, such wide systems are thus known to exist at various evolutionary stages. In fact, systems with comparable masses to SS183044-020918 are even known with separations larger than 100 AU, such as the 2–4 Gyr old 2MASS J0130−4445 binary (0.083+0.070 $M_{\odot}$, 130 AU; Dhital et al., 2011). We thus consider that SS183044-020918 is not abnormally wide for a binary with a very low-mass stellar host.

An alternative way to compare binary properties is in terms of gravitational binding energy. We calculate upper and lower limits on the binding energy of the SS183044-020918 binary system, based on the ranges of mass and separation given in Table 2.6. Using masses of 0.1M $_{\odot}$ and 0.07 $M_{\odot}$ ($m_{\mathrm{T,upper}} \approx 178$ M_{J}), and the minimum derived separation of 38.3 AU, we obtain an upper limit on binding energy, $E_{\mathrm{b,upper}} = 3.2 \times 10^{42}$ ergs. Alternatively, using masses of 0.08 $M_{\odot}$ and 0.05 $M_{\odot}$ ($m_{\mathrm{T,lower}} \approx 136$ M_{J}), and the maximum derived separation of 45.5 AU, we obtain a lower limit on binding, $E_{\mathrm{b,lower}} = 1.8 \times 10^{42}$ ergs. Fontanive et al. (2020) present an up-to-date summary of binding energy vs total mass in their Figure 4, showing low-mass binaries in the field and in young associations (see Faherty et al., 2020 for a full compilation). Considering the limits on binding energy and total mass of SS183044-020918 derived here, this new binary system agrees well with previous measurements of both field and young association systems, consistent with our conclusions above. Given that systems with similar architectures are observed from young star-forming regions to the old field population, our newly-discovered Serpens binary is likely to be stable to dynamical evolutionary processes and to survive to field ages.

2.8 Conclusions

We present results from a multi-technique survey of Serpens South and Serpens Core, using photometric, spectroscopic and high-resolution imaging data to hunt for the lowest mass, youngest members of these regions. We have identified five likely-young low-mass candidate members of Serpens South and Serpens Core, adding to the four detections reported in Jose et al. (2020). We find that four of these objects have spectral types later than ∼M5, and have effective temperatures and luminosities consistent with $\lesssim 0.12$ $M_{\odot}$. Additional evidence suggests that three of these objects are highly likely to be Serpens members, but this cannot be confirmed with proper motion follow-up on reasonable timescales for the Serpens region. We also provide an update on one of the detections from Jose et al. (2020), SS183044-020918, which we have found through a HST imaging program to be a binary system, resolved in visible light. We cannot confirm the binarity of the two components via proper motion analysis, but show that the likelihood of chance alignment with a background star is very small. We find the binary components to have likely spectral types of M7–M8 and M8–M9, derived from a combined IR spectrum. Calculating bolometric luminosities using the difference in magnitudes between the components, and our CFHT photometry, we find that the secondary has a mass of 0.05-0.07 $M_{\odot}$, making it one of the lowest mass candidate members of the Serpens South star-forming region.

3

An ERIS/NIX imaging survey for young giant exoplanets using a custom filter

3.1 Introduction

Tens of giant planet and brown dwarf companions have been discovered and extensively characterised by direct imaging in recent decades (e.g. Chauvin et al., 2004; Marois et al., 2008; Lagrange et al., 2010), using instruments and techniques designed to measure the light coming directly from companions. Direct imaging is complementary to other highly successful methods, for example generally targeting wider star-planet separations than techniques such as radial velocity (RV). The newest generation of large direct imaging surveys, such as the SPHERE Infrared Survey for Exoplanets (SHINE; Desidera et al., 2021; Langlois et al., 2021; Vigan et al., 2021) and the Gemini Planet Imager Exoplanet Survey (GPIES; Macintosh et al., 2015; Nielsen et al., 2019), are nearing the end of observations, and are beginning to shed light on the details of planet populations through their early statistical results (Nielsen et al., 2019; Vigan et al., 2021). Large direct imaging surveys of hundreds of targets can tell us about many aspects of exoplanet formation and evolution, including: the frequency of giant planets, brown dwarfs and binary systems (e.g. Montet et al., 2014; Lannier et al., 2016; Reggiani et al., 2016; Meyer et al., 2018; Baron et al., 2019; Fulton et al., 2021; Bonavita et al., 2021); the viability of disk and planet formation models (e.g. Janson et al., 2011, 2012; Rameau et al., 2013a; Vigan et al., 2017; Nielsen et al., 2019; Vigan et al., 2021), and orbital dynamics of multi-planet systems (e.g. Konopacky et al., 2016; Wang et al., 2018; Nielsen et al., 2020). Successfully discovering new giant planets and brown dwarfs that are suitable targets for these kinds of studies requires a solid understanding of where to look: which host stars to target and what contrasts and sensitivities are necessary. To know this in turn requires a firm understanding of the underlying populations of planets

The first direct imaging surveys targeting large samples of stars were informed by planet populations derived from radial velocity results. Radial velocity surveys generally target a different part of parameter space to direct imaging, being most sensitive to high mass planets close to their host stars. Early studies of the first populations of objects discovered via radial velocity found that the planet occurrence rate was best fit by a rising power law in mass and orbital period (e.g. Cumming et al., 2008). Due to the lack of giant planet detections at wider separations, these fits had to be extrapolated to inform direct imaging surveys. The number of planets was predicted to continue to increase with wider separations, implying that surveys targeting this parameter space would report many giant planet detections. Many of this generation of direct imaging surveys (e.g. Desidera et al., 2015; Chauvin et al., 2015; Biller et al., 2013, among others) ultimately reported null or fewer than expected detections, raising questions about the true underlying planet population. These results began to confirm what was suspected prior to the surveys: there are far fewer planets at wide separations than the original RV power law extension predicts.

Despite this, the most recent large direct imaging surveys, SPHERE-SHINE (Chauvin et al., 2017) and Gemini-GPIES (Macintosh et al., 2015; Nielsen et al., 2019) have each reported a handful of new detections, with detected planets and brown dwarfs covering a range of masses and separations (e.g. 51 Eri b, Macintosh et al., 2015; HIP 65426b, Chauvin et al., 2017; PDS 70b, Keppler et al., 2018). We can use these results to begin to inform the next generation of surveys. At the time of their design, the extension of the distribution of RV-detected planets to predict survey yields remained the only available assumption. New studies (e.g. Fernandes et al., 2019; Fulton et al., 2021) have in fact found a turn-over in giant planet frequency between ∼2 and 4 AU (the approximate location of the snow line, where an abundance of planet-forming material is located), with giant planets appearing scarce at wide separations. In particular, Fulton et al. (2021) find giant planet occurrences consistent with initial occurrence results from GPIES (Nielsen et al., 2019), implying that these may be the most accurate results to date for informing new imaging surveys.

Another factor that should be carefully considered when planning a new direct imaging survey is the likely brightness of the targets that we are aiming to detect, and at what point they become too faint for our instruments. The initial luminosity of a giant planet is dictated by its entropy, which is in turn influenced by its formation mechanism (Marley et al., 2007) - consequently, luminosity estimates of young objects are very dependent on our understanding and modelling of planet formation. When attempting to predict the luminosities of young giant planets, there are two main groups of available models, which either assume 'hot-start' or 'cold-start' initial conditions. Hot-start models (Burrows et al., 1997; Baraffe et al., 2003; Saumon & Marley, 2008) assume that planets form via gravitational instability, and cold-start models (Marley et al., 2007; Fortney et al., 2008) intend to replicate the process of core accretion. The two suites of models can predict significantly different initial luminosities for very young planets, that can be reflected as a difference of up to 7 magnitudes in the near infrared (for a 1 Myr, 10 M_J planet; Spiegel & Burrows, 2012).

These state-of-the-art investigations into the properties of young planets, and the predicted values and distributions of certain planet properties, show that understanding and correctly using the predictions for where we might find detectable planets should be a key consideration when designing a survey.

In this work, we consider optimal survey designs for the upcoming Enhanced Resolution Imager and Spectrograph (ERIS; Davies et al., 2018) at the Very Large Telescope (VLT). ERIS was designed as a dual replacement/upgrade of

SINFONI (Eisenhauer et al., 2003; Bonnet et al., 2004) and NACO (Rousset et al., 2003; Lenzen et al., 1998), which have been providing near-IR adaptive optics (AO) capability on the VLT for over a decade. Composed of the SPIFFIER spectrograph and the NIX imager, ERIS will be a key instrument for the next generation of large-scale direct imaging surveys. NIX is a near- and mid-IR AO enabled imager, with a grating vector apodised phase plate (gvAPP) coronagraph (Otten et al., 2017; Boehle et al., 2018; Kenworthy et al., 2018), which operates from 2-5µm. NIX will be complementary to observations undertaken with SPHERE and GPI (which operate in the near-IR): $L-$ and $M-$band follow-up can be combined with J, H, K detections to better distinguish between equilibrium and non-equilibrium chemistry models. Additionally, older, cooler planets and brown dwarf companions have typically been detected in the longer wavelength L-band (e.g. Vigan et al., 2015; Stone et al., 2018; Launhardt et al., 2020), which is also very competitive for detecting young protoplanets still embedded in circumplanetary material (e.g. Reggiani et al., 2014; Keppler et al., 2018; Launhardt et al., 2020; Jorquera et al., 2021) that is very bright at wavelengths longer than 3μm (e.g. Eisner, 2015; Szulágyi et al., 2019).

We designed the K-peak filter, a 6% width custom filter at 2.2µm, specifically for the detection of YPMOs via their 'spectral shape'. The K-peak filter has been installed in the NIX imager, and can be used with the coronagraphic capabilities of the instrument for near-IR imaging. The design of our custom filter was informed by the spectral shape of very low-mass objects in the K-band, which is significantly different to the spectral shape of earlier type objects in the same wavelength range. By using a specific combination of filters (K-peak, IB2.42 and $H2$-cont), we can trace the spectral shape of an object, and use the calculated colours to efficiently photometrically characterise an observed object.

Candidate companions detected over the course of large direct imaging surveys require multiple observations over several epochs for confirmation, as it must be shown that the candidate companion shares common proper motion and is actually bound to the target star, as opposed to being a background interloper. This significantly increases the amount of telescope time necessary to fully complete a direct imaging survey and makes it difficult to confirm companions around stars with very low proper motions. Additionally, the most crowded fields located in the Galactic plane can often have hundreds of candidate companions identified around a single host star (e.g. Vigan et al., 2021). Again, refuting or confirming each of these based on their proper motion is extremely observationally intensive. An alternative option, obtaining spectroscopy for every candidate to check for an appropriate young planetary-mass object (YPMO) spectrum as opposed to a background M star, is similarly unrealistic in scope.

The custom K-peak filter and spectral shape technique offer an option for drastically narrowing the number of candidate companions of interest in each field without proper motion follow-up, by providing a robust way of determining if a candidate companion is a bonafide very low-mass object or a background contaminant. Previous surveys (e.g. SHINE) have used a similar approach, with specific combinations of photometric filters used to aid characterisation. Our technique builds on the same ideas, and in many cases could be used in combination with photometry from previous surveys to allow more robust characterisation than previously possible.

We expect that our custom K-peak filter and spectral shape technique could be used to carry out a large survey for planetary-mass companions, observing $>$100 targets. As previous surveys have demonstrated, careful target selection is crucial to maximise resulting yields. We can learn from the model assumptions and target selection criteria of the SHINE and GPIES surveys, and also from the wealth of survey data that has been published since. This Chapter covers the design and target selection process for such a future survey. In Section 3.2, we demonstrate the need for the spectral shape technique, by examining archival data. In Section 3.3, we discuss the design of the custom K-peak filter and show the diagnostic capabilities of the spectral shape technique. In Section 3.4, we present multiple survey design options, and in Section 3.5 we weigh the advantages and disadvantages of each observational approach, using the latest planet population models.

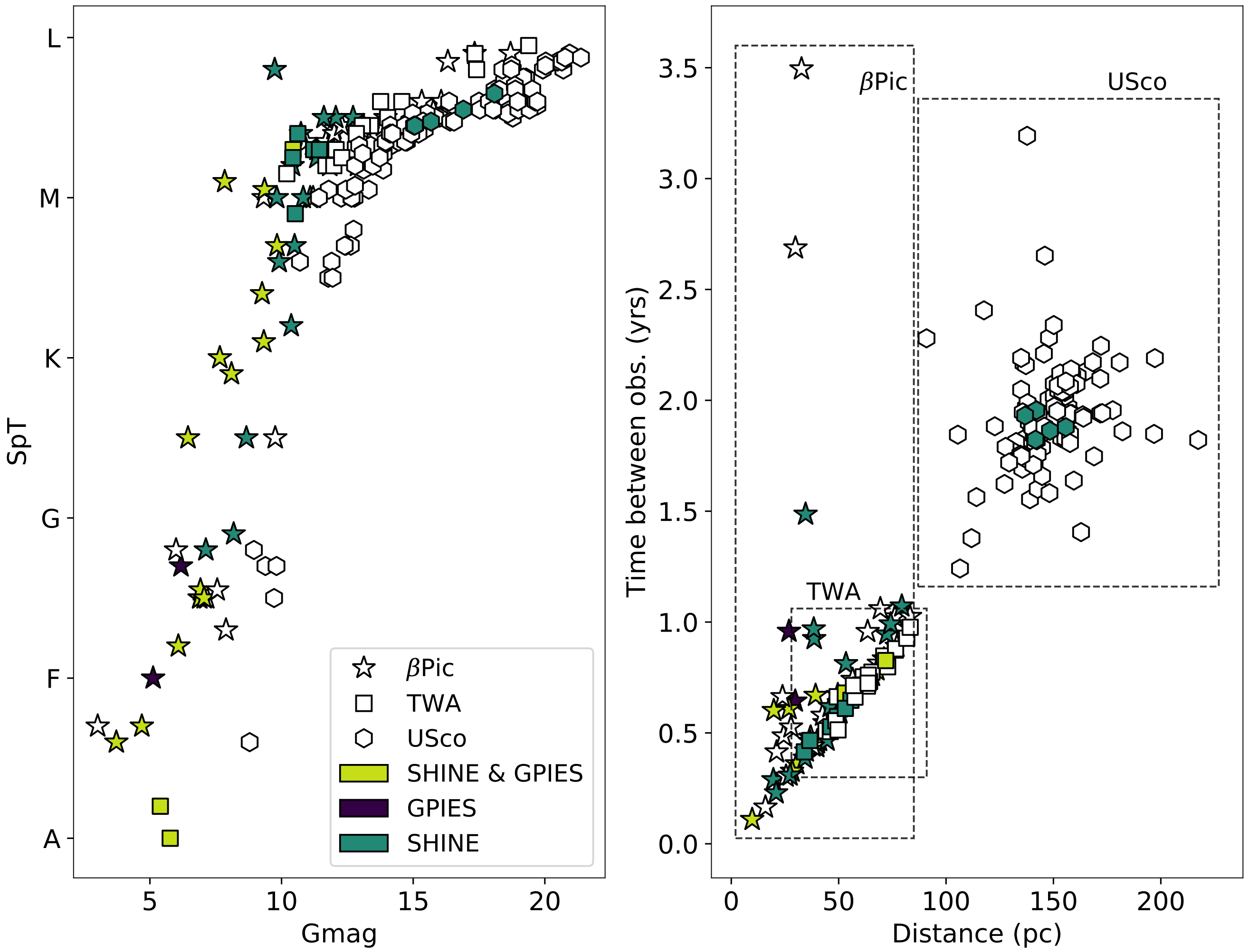

Figure 3.1 *Left: G-magnitude vs Spectral Type for objects in the Upper Scorpius (hexagons), β Pictoris (stars) and TW Hya (squares) membership lists, colour-coded based on archival imaging data. Objects with SPHERE/SHINE observations are highlighted in blue, objects with GPIES observations are highlighted in purple, and objects previously targeted by both surveys are highlighted in green. Right: Time required between observations to measure an on-sky movement of 50mas, as a function of distance to target star. Clustering of each region is identified by dashed boxes.*

3.2 Previous Surveys and the Proper Motion Problem

3.2.1 Archival Imaging from Previous Surveys

When planning a new survey of any kind, one must consider the previous archival coverage of various regions, and which have been most frequently targeted. There are two arguments to be made here. Firstly, archival imaging data can be extremely useful for increasing the observational baseline for a specific object. As a result, targeting regions that have been routinely observed in the past can actually prove very useful for confirming candidates. Secondly however, one should consider the likely remaining yield in a region if it has already been observed many times. It is highly unlikely that the most extensively surveyed have no planetary companions left to be discovered, but equally, the likelihood of discovering something new is somewhat reduced, as most remaining companions are likely below our current mass sensitivity.

Large-scale direct imaging surveys have been underway for the last two decades. As such, the scope of archival imaging data is broad. In this work, when considering possible observational approaches for a survey using NIX, we will focus primarily on star-forming regions and nearby young moving groups as example targets. Young, nearby moving groups are youthful associations of stars, usually no more than a couple of hundred parsecs from the sun. Young star-forming regions are similar in many respects, usually further away but younger - the distinguishing factor being that they contain signs of very recent or ongoing star-formation (such as nebulosity and high-mass OB stars). Youth is a key selection criteria in direct imaging surveys that operate in the infrared (IR), as directly imaged planets cool and dim with age: it is easiest to detect them when they are young and at their brightest. There has been an historic favouring of some regions over others: the earliest imaging surveys all targeted the closest stars (e.g. Chauvin et al., 2003; Masciadri et al., 2005; Biller et al., 2007, among others), due to the limited instrumental capabilities. These were followed by many thorough surveys of nearby young moving groups (e.g. Chauvin et al., 2010; Biller et al., 2013; Brandt et al., 2014), and there was generally far less focus on more distant star-forming regions. In this work, we will consider both moving groups and star-forming regions as potential targets for NIX.

In Section 3.4, we will present results for possible surveys of the Upper Scorpius star-forming region. Upper Scorpius is a representative example of the types of star-forming regions that we could image with NIX. Part of the Scorpius-Centaurus Association (the closest OB association to the sun), it is located at 145 pc (De Bruijne et al., 1997), and is thought to have an age of 5-10 Myr (Pecaut et al., 2012; Pecaut & Mamajek, 2016; David et al., 2019). It is the youngest of the three subgroups of Scorpius Centaurus (comprised of Upper Scorpius, Upper Centaurus–Lupus and Lower Centaurus–Crux) and is thought to contain ~ 2500 members, 75% of which have masses $\lesssim 0.6$ $M_{\odot}$ (Preibisch & Mamajek, 2008). The low-mass population in Upper Scorpius has been well explored in recent years, with the mass function below the stellar/substellar limit reasonably well-defined (Luhman & Esplin, 2020). Many other star-forming regions would be similarly suitable targets for a NIX survey, including Ophiuchus (∼130 pc; Ortiz-León et al., 2018b; Cánovas et al., 2019), Chamaeleon (∼180–200 pc; Voirin et al., 2018; Roccatagliata et al., 2018) and Lupus (∼150–200 pc; Comerón, 2008; Gaia Collaboration et al., 2018).

To obtain a list of likely Upper Scorpius members and their properties, we used the compilation presented in Luhman et al. (2018), who reviewed the previous member lists in the literature and also obtained new spectroscopic observations to characterise hundreds of Upper Scorpius members. Starting from this list, we applied a magnitude cut based on the predicted performance of the NIX imager. According to a preliminary version of the ERIS manual, the limiting magnitude in R-band (the wavelength of operation for the wavefront sensing system) will be approximately 14 mags. We used a cautious lower limit of R=12 to allow for all degrees of observational conditions, and applied this cut to the Upper Scorpius member list, leaving us with a sample of 141 targets suitable for NIX observations.

Additionally, we will consider two moving groups as potential NIX targets in this work, TW Hya and β Pictoris. A recent summary of young moving groups is given in Gagné et al. (2018), who detail compilations of members identified using GAIA-Tycho data (Høg et al., 2000; Gaia Collaboration et al., 2016b,a). For specific member lists, we used the more recent work of Carter et al. (2021), who present detailed compilations of the β Pictoris and TW Hya moving groups, based on Gagné et al. (2018). As discussed in detail in Carter et al. (2021), these moving groups are ideal targets for a general direct-imaging survey. β Pictoris is located at $\approx$ 35 pc from the sun, and has an estimated age of 24±3 Myr (Bell et al., 2015). The closest young group to the sun, it is an optimal target for an NIX survey: the young age corresponds to very bright young giant planets and brown dwarfs, reducing the contrast required for successful observations, and the close distance allows for detections of companions at closer separations to their target stars, a variable dictated entirely by the inner working angle of the instrument. Furthermore, moving groups in general have better defined age estimates than unassociated nearby stars, allowing for more precise mass estimates of detected companions. The second young moving group that we use as an example for NIX is the TW Hya association (Kastner et al., 1997; Gagné et al., 2018). It is located at a slightly larger distance than β Pictoris, at $\approx$ 60 pc, but is younger with an estimated age of 10±3 Myr (Bell et al., 2015). Consequently, TW Hya presents the same observational advantages as β Pictoris for a direct-imaging survey: being even younger, we expect lower mass planets to have sufficient luminosities for detection (due to their more recent formation), although at slightly larger separations due to the larger distance to TW Hya. While we focus on these two moving groups in this work, many others, including Octans, Columba and Carina (Gagné et al., 2018), would be similarly suitable for a NIX survey.

Using these three target lists, we investigated the scope of archival imaging data. We first queried the ESO and Gemini archives looking for SHINE and GPIES data, respectively. We then broadened the ESO archive search to look for matches with any previous direct imaging survey.

Figure 3.1 summarises the results of our archive search for SHINE and GPIES data, highlighting which host stars in our target lists have been observed previously. In Upper Scorpius, only 4.2% of objects in our target list have SHINE observations, either published in the F150 sample papers (Vigan et al., 2021; Desidera et al., 2021; Langlois et al., 2021) or observed in the remainder of survey time. None of the host stars in the list have been observed by GPIES. As expected, the coverage in the two moving groups is much higher. In particular, 53% of objects in our β Pictoris compilation have SHINE observations, and 27% have been targeted by GPIES. 33% of TW Hya objects have SHINE observations, and 10% have been observed by GPIES.

Figure 3.1 shows the distribution of host stars in our samples in magnitude-spectral type space. We plot G-band magnitude, as the majority of stars have a detected magnitude in this filter, and colour-code based on available archival observations (SHINE only, GPIES only, both or neither). The shape of the markers also indicates the membership of each object. In this distribution, we can see a clear bias in the target selection of these large surveys. While they have sampled a large range of spectral types, from early A to late M, the focus has clearly been on the brightest stars in each region. This is a consequence of instrument sensitivity and performance, and it is likely that NIX will be able to target some of the fainter objects plotted here (see Section 3.4). As mentioned previously, the emphasis of surveys to date has been on young moving group stars: the majority of Upper Scorpius targets points are unfilled.

Considering all archival image data that is presented in the ESO archive (including all observations categorised as 'imaging', which includes historic data that may not be high contrast or coronagraphic), we see a similar overall picture. The Upper Scorpius targets have the lowest coverage in terms of archival data: but still at the 64% level, meaning there could well be an existing long baseline of observations for any stars that are targeted in the future. The β Pictoris and TW Hya moving group targets have 92% and 100% coverage in the ESO archive, respectively, again demonstrating the bias towards moving group members in previous surveys.

Beyond the SHINE and GPIES surveys, state-of-the-art instruments are currently being used for numerous, slightly smaller direct imaging surveys (e.g. Launhardt et al., 2020), often targeting specific regions. Some of these have targeted Upper Scorpius, or the larger Scorpius-Centaurus (Sco-Cen) region in which it sits. BEAST (Janson et al., 2021), one such survey using SPHERE, is observing 85 B-type stars in Sco-Cen, 11 of which are located in Upper Scorpius. First results from this survey have proven successful, with 6 previously unknown stellar companions detected. Another ongoing Sco-Cen SPHERE survey, YSES (Bohn et al., 2020a), aims to find planetary companions to 70 K-type stars in Lower Centaurus Crux (LCC). Two planetary systems have been discovered to date by the ongoing survey (Bohn et al., 2020a,b, 2021). The current success of surveys focused on Sco-Cen subgroups is a promising sign for a future NIX survey of Upper Scorpius, and indicates that there are likely many planetary companions still to be found.

The first large L' surveys have also been undertaken in recent years ($\gtrsim 100$ targets), and can give us an insight into the potential results of a NIX survey in L'. Stone et al. (2018) present the LEECH survey, a large L' survey that observed 98 nearby B–M type stars. They report one new low-mass companion, and are also able to place tight constraints of giant planet frequencies. The NACO-ISPY survey (Launhardt et al., 2020) is observing 200 young stars, selected because they host debris or protoplanetary disks. Results from the first 2.5 years of ISPY have been released, with multiple new low-mass stellar companions reported (Cugno et al., 2019; Launhardt et al., 2020), and imaging of multiple disks in L' for the first time. The process of target selection for this survey differs from how we would approach a NIX L' survey, but it demonstrates the potential of L' observations and the advantages of using longer wavelengths to image giant planets. Following the same trend seen when looking at most of the available archival data, there is no coverage of the targets in our Upper Scorpius list by these two L' surveys. There is also minimal coverage of the TW Hya and β Pictoris moving groups, likely because the target choice in these cases is motivated by factors other than proximity. These studies, along with earlier surveys targeting fewer host stars (e.g. Heinze et al., 2010, 54 nearby Sun-like stars), demonstrate that longer-wavelength direct imaging surveys are just as valuable as the more common J, H, K studies, and that instruments such as NIX, that offer L' capabilities, ought to be extensively utilised.

3.2.2 Proper motion considerations

As discussed in Section 3.1, a major goal of the K-peak filter and spectral shape technique is to reduce the amount of observing time required to confirm or refute candidate companions via their common proper motion. The right panel of Figure 3.1 demonstrates the population of targets for which our technique could prove very useful. Shown here is the distance to each host star target in the three membership lists considered in this Chapter, plotted against the time (in years) required between observations to confirm common proper motion. This was calculated based on the total proper motion of each star, and the assumption that a minimum of 50 mas of on-sky movement would be required to confidently confirm or refute a candidate companion. As expected, the different regions (located at distinct distance ranges) are obvious from the clustering in

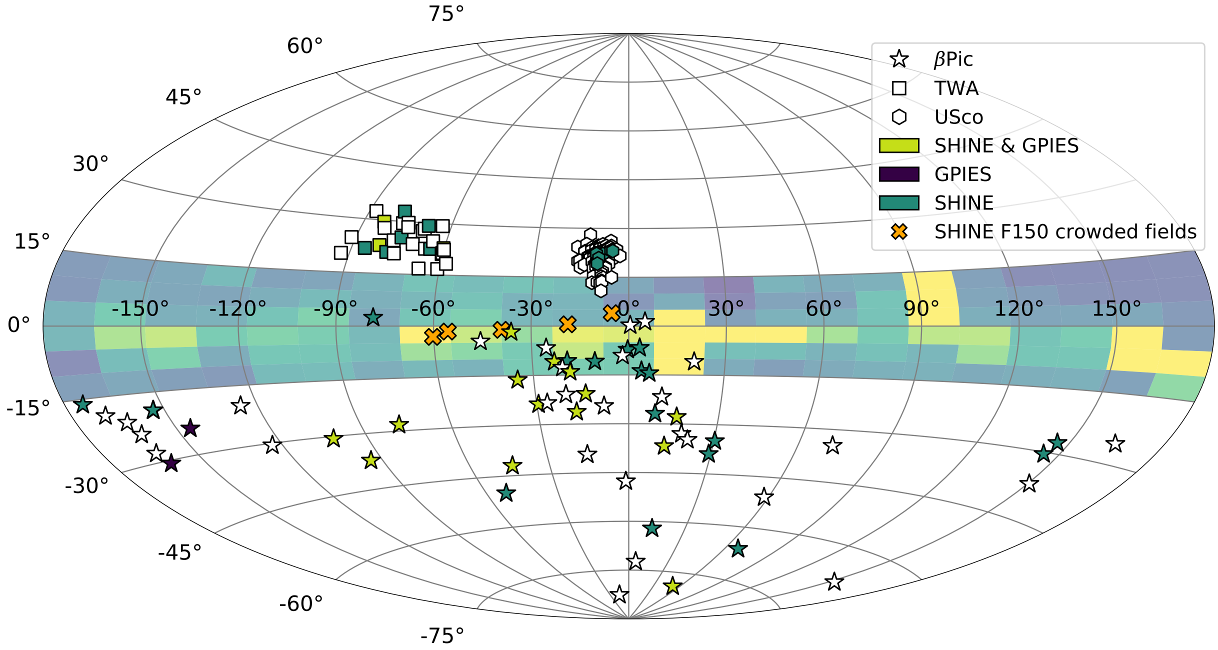

Figure 3.2 *Sky positions of Upper Scorpius, β Pictoris and TW Hya targets, projected onto a Galactic coordinate grid. Colour-coded based on archival imaging data: objects with SPHERE/SHINE observations are highlighted in blue, objects with GPIES observations are highlighted in purple, and objects previously targeted by both surveys are highlighted in green. The density of sources in the Galactic plane (±15°) is also shown, with yellow corresponding to the highest density of sources and purple to the lowest. The orange crosses indicate the five crowded fields that dominate the remaining unconfirmed SHINE F150 candidate companions (Vigan et al., 2021)*

the diagram (and shown explicitly by the black dashed boxes). Again, the colour of the markers indicates objects with SHINE or GPIES archival data.

Figure 3.1 directly demonstrates the difficulties with common proper motion follow-up. Previous surveys have tended to focus on the closest young moving groups, which require a shorter time baseline to confirm any candidate companions - this can clearly be seen by the clustering of coloured points in the lower left of parameter space. In crowded, distant fields where many candidate companions are identified by current techniques and filter sets, follow-up surveys could be lengthy if a baseline of 3 years is required between observations. With the improved diagnostic capabilities of the K-peak filter and spectral shape technique (see Section 3.3), we aim to reject far more candidate companions using just a single epoch of photometry. We could focus on a more distant region, such as Upper Scorpius, and reject enough contaminant objects with our spectral shape method that a 2-3 year baseline between observations would become a more achievable goal for a drastically smaller number of candidates.

3.2.3 Crowded Fields

A final consideration when picking a region to target for a survey is its position in the sky with respect to the Galactic plane, bulge and other crowded areas. Figure 3.2 shows the sky positions of the members of the three regions we consider in this work, with the same colour coding as used in the previous section. The clustering and small spatial extent of Upper Scorpius is clear here, due to its large distance. The contrast between the moving group targets is also striking - members of β Pictoris are located across the sky, whereas TW Hya is more compact. A key detail to consider here is the location of the Galactic plane in Figure 3.2 (Galactic latitudes ±15°). The low-resolution map covering these coordinates shows the source density across a grid of lines of sight in the Galactic plane and bulge (obtained using Simbad source counts), where yellow indicates the regions with the highest source density, and purple the lowest. The crowded bulge region is obvious around 0°, and the source density elsewhere in the plane is comparatively low, but will still be far higher than areas of sky outside the Galactic plane.

We can see that many possible Upper Scorpius targets overlap with the upper

Galactic plane, meaning any observations of host stars would require imaging of very crowded fields. Upper Scorpius targets that have been imaged by the SHINE campaign (blue hexagons) lie outside the Galactic plane area, likely for this very reason. The orange crosses in Figure 3.2 indicate the five crowded fields that dominate the remaining unconfirmed SHINE F150 candidate companions (Vigan et al., 2021), discussed further in Section 3.4.1.1. The lack of follow-up characterisation of so many companions is explained by their location, all being in the centre of the Galactic plane. Furthermore, the Galactic bulge extends beyond the plane shown here, and is far brighter and more densely crowded than any other part of the sky - this further explains why the majority of Upper Scorpius targets are lacking follow-up. By increasing our ability to remove numerous candidate companions before follow-up is needed, the spectral shape technique could be used to target Upper Scorpius members that lie along the Galactic plane line-of-sight.

3.3 K-peak custom filter

3.3.1 Filter Motivation

In the previous sections, we have shown the difficulty in balancing follow-up time with large numbers of unconfirmed candidates companions from single-epoch photometry. This dilemma was the motivation for designing the K-peak filter: can we optimise the observing time required to determine the nature of a target? One answer is to use a carefully chosen combination of photometric filters. Using only photometry, we can calculate colours that contain information about the type of object being observed, allowing approximate characterisation without further follow-up. Past works (e.g. Najita et al., 2000; Allers & Liu, 2020) have shown that custom photometric filters can be used to greatly improve the confirmation rate of photometrically selected candidate low-mass brown dwarfs. In previous work (Allers & Liu, 2020; Jose et al., 2020; Dubber et al., 2021), we used a custom filter centred on the deep 1.45µm feature present in YPMOs to distinguish between them and background sources. In the 2-5µm range covered by NIX, such water features are far less dominant, and there are strong telluric features across some of this range that would make a similar ‘water’ technique difficult to use. Instead, we use the differing spectral shape in K-band of very low-mass brown

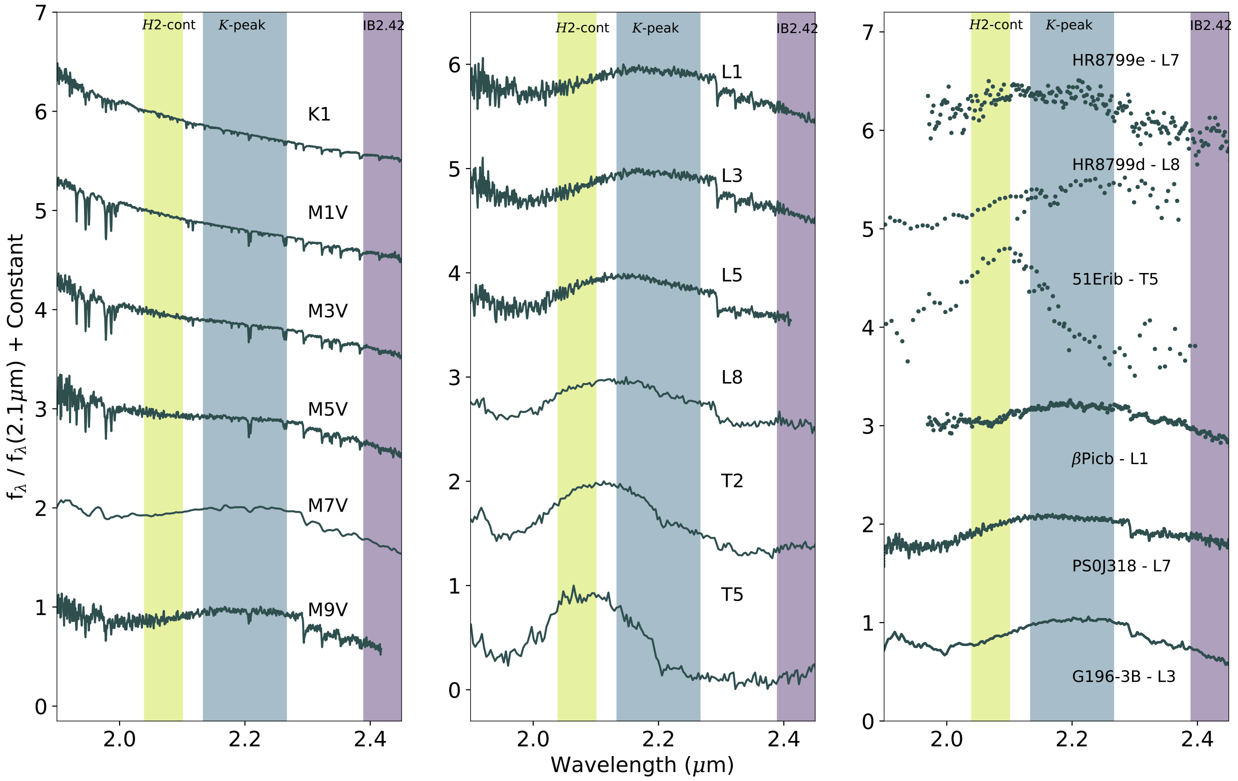

Figure 3.3 *Left and Centre: Spectral sequence for K-T spectral templates, showing the change in the spectral shape across the K-band. The three filters used for the spectral shape technique are highlighted: H2-cont (green), K-peak (blue) and IB2.42 (purple). Right: K-band spectral of well-known directly imaged exoplanets and brown dwarfs. References for spectral data: G196-3B, Burgasser (2014) (SpeX prism library); PS0J 318, Liu et al. (2013); β Pictoris b, Gravity Collaboration et al. (2020); 51 Eri b, Rajan et al. (2017); HR 8799 d, Greenbaum et al. (2018); HR 8799 e, Gravity Collaboration et al. (2019).*

dwarfs when compared to earlier spectral type stars. This can be seen in the sample of spectra shown in Figure 3.3. By locating filters at key spectral points for defining the overall shape of the spectra, the extracted colour information can be used for direct characterisation. Also shown in Figure 3.3 are spectra of well-studied brown dwarfs and exoplanets, discovered via direct imaging: 51 Eri b (Macintosh et al., 2015), β Pictoris b (Lagrange et al., 2010), PSOJ-318 (Liu et al., 2013), G196-3B (Rebolo et al., 1998) and HR 8799d and e (Marois et al., 2008, 2010). References for the spectral data are given in the caption of Figure 3.3. These spectra demonstrate the general variety in the spectral shapes of objects that have been detected via direct imaging previously, but also the similar features in the highlighted filter windows.

3.3.2 Filter Design and Diagnostic Properties

The choice of waveband was the first consideration when designing the custom filter. The wavelength coverage of NIX (2-5µm) allows either K- or L- band as the two possible options for a custom filter. Objects of interest (YPMOs) tend to be brighter in L' than K, but the background level is also much higher, a crucial consideration for imaging companions. Additionally, the spectra of objects tend to be flatter and more featureless in L' than K. Based on these factors, the K-band was chosen as the optimal band for our NIX custom filter.

Next, we considered the question of width and positioning of the filter. One certainty dictated by the design of the instrument is that the coronagraph should not be used with wide filters. Doing so would lead to spectra rather than point source images due to the high spatial spread of the light. Consequently, we considered medium width filters centred at different wavelengths in K-band, in combination with the standard $H2$-cont, IB2.42 and IB2.48 filters installed in NIX. The $H2$-cont filter has a central wavelength of 2.07μm, and a width of $\Delta\lambda/\lambda \approx 3\%$. The IB2.42 filter has a central wavelength of 2.42μm, and a width of $\approx 2.5\%$.

The properties of our final custom filter, as well as the standard IB2.42 and $H2$-cont filters, are shown in Figure 3.3. The left and middle panels of Figure 3.3 also show a sequence of K-band spectra, starting with background stars (K1-M5) and moving through to ultracool brown dwarfs/ YPMOs (M7-T5). The variation in spectral shape with spectral type is clear in this wavelength range, with earlier spectral type objects having overall flatter spectra than the late-M - mid-T objects, and a downward slope across the full K-band. Later-type objects have complex spectral gradients and features, echoed in the spectra of direct imaging detected planets and brown dwarfs (right panel). This was the basis for the spectral shape technique and custom filter design. Using two standard narrowband filters also in the K-band, $H2$-cont and IB2.42 (highlighted in green and purple in Figure 3.3), we considered different custom filter designs that would allow us to calculate colours that trace the evolving shape of the spectrum. To judge the effectiveness in distinguishing between populations of each possible filter design, we plotted colour-colour diagram for a range of possible colours and for a range of simulated object spectra, with [custom] - IB2.42 vs $H2$-cont - IB2.42 in each case. Through this iterative process, we chose the final custom filter characteristics that best distinguished between late spectral type objects (planets and brown dwarfs) and reddened earlier spectral type interlopers. Figure 3.4 shows the colour-colour diagram for the final design.

Plotted in Figure 3.4 are three datasets: first, in a gradient of orange squares, a sample of simulated stellar photometry with spectral types encompassing the spectral types expected in the field, from F0–M2. This population is reddened by $A_{\mathrm{V}} = 0, 5, 10, 15$ and 20. We used spectral standards with these spectral types taken from the IRTF Spectral Library (Rayner et al., 2009), and performed synthetic photometry on each reddened spectra in the K-peak, IB2.42 and $H2$-cont filters. We fit a best-fit line to this distribution, and show the 3σ spread as dashed lines in Figure 3.4.

We then simulated a realistic background field population using the Trilegal Galactic models (Girardi et al., 2012). This simulation required a possible line-of-sight for the NIX survey. We chose β Pictoris as the target line of sight, a stellar member of the β Pictoris moving group (Zuckerman et al., 2001; Gagné et al., 2018). We simulated a field of 1×1 arcmin (the approximate field of view of NIX), centred on RA = 86.8°, Dec = -51.1°. We used the Kroupa initial mass function (IMF) (Kroupa, 2001), including binaries, which results in a population of ~26,000 objects along the β Pictoris line-of-sight. Each model object returned by the Trilegal model has an associated effective temperature. We converted these to spectral types using Mamajek's 'Modern Mean Dwarf Stellar Color and

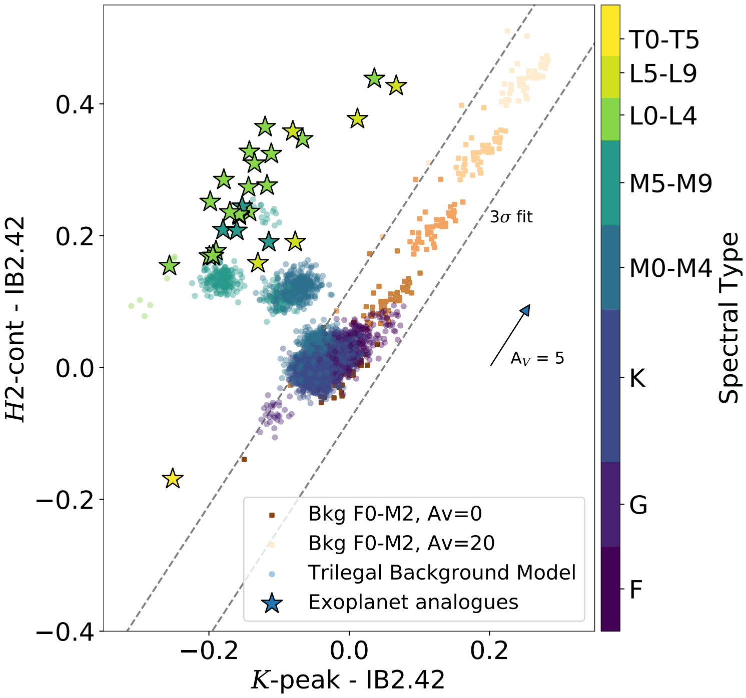

Figure 3.4 *Colour-colour diagram for 3-filter spectral shape method. NIX filters H2-cont, K-peak and IB2.42 are used to characterise young, late-type exoplanet analogues (stars) from background population (circles and squares). Objects in Trilegal Galactic model along the β Pictoris line-of-sight are plotted (circles), with the point colour indicating the spectral type of each object. Also shown is a reddened sequence of F0-M2 standard stars (coloured squares), with A_V ranging from 0-20, in increments of A_V=5. Dashed lines show a 3σ fit to this F0-M2 sequence. The arrow plotted shows the $A_V = 5$ extinction vector.*

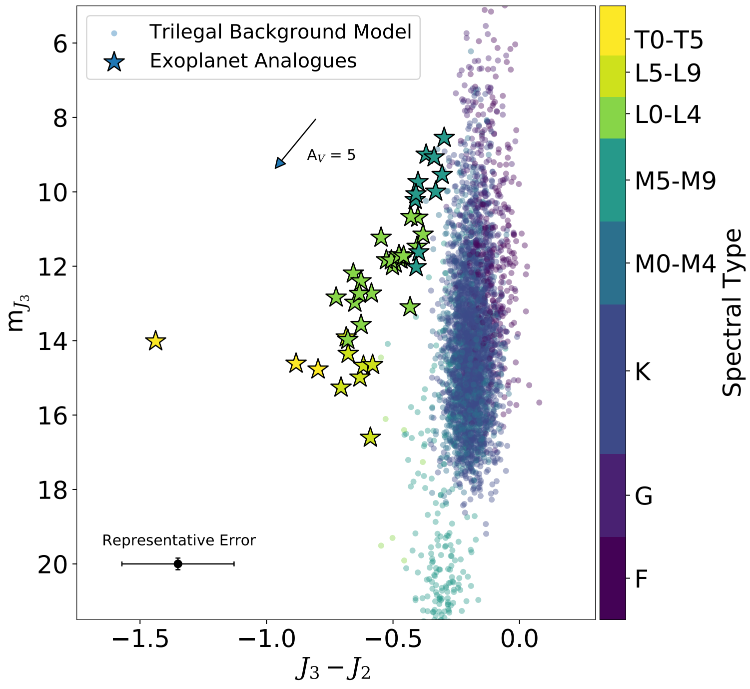

Figure 3.5 *$J_3 - J_2$ vs m_{J_3} colour-magnitude diagram. Young, late-type exoplanet analogues (stars) are plotted, as well objects returned for Trilegal Galactic model along the β Pictoris line-of-sight are plotted (circles), with the point colour indicating the spectral type of each object. Representative error bar from SHINE F150 shown in bottom left. The arrow plotted shows the $A_V = 5$ extinction vector.*

Effective Temperature Sequence' [1] (described in part in Pecaut & Mamajek, 2013). With a spectral type for each model object, we could then associate it to a spectral standard (using template with the same spectral types from the IRTF spectral library), and perform synthetic photometry in the three filters. The resulting population is plotted as the coloured circles in Figure 3.4, with the colour bar showing the spectral type of each object. As expected, objects with earlier spectral types occupy the same position as the simplified field model described above, but the Trilegal population also shows us the location of field mid-M and L objects on the colour-colour diagram, which are distinct from the earlier type objects.

The final population plotted on Figure 3.4 is a selection of young exoplanet analogues. These range in spectral type from M5–T5.5, and are all free floating objects that have been spectroscopically characterised. The sample of objects is described in detail in Bonnefoy et al. (2018). Synthetic photometry was performed on the spectral data in the same way as above, and the colour bar in Figure 3.4 again corresponds to the spectral type of these targets.

We can see a clear distinction between the reddened, background F0–M2 stars and the young exoplanet analogues on this colour-colour diagram. The optimal custom filter design is motivated by this: the young exoplanet analogues that would be targets of a direct imaging survey lie in a (mostly) unique part of this parameter space, with a clear colour offset when compared to the F0–M2 background sequence. With this combination of filters, there is a still small amount of cross-over in the parameter space covered by field-age and young objects of the latest spectral types. Despite this, the K-peak filter will allow us to obtain a better understanding of the spectral type of many targets from the colours alone. Through simulated photometry, we calculate that a colour offset measured to 0.1 mag or better will be able to robustly distinguish young planetary-mass objects from background contaminants. Simulations of on-sky performance indicate that this photometric precision should be very achievable with the NIX imager. Additionally, typical errors for SPHERE SHINE colours are on the order of 0.15-0.2 mag in the near-IR (see Section 3.4.1.1), further evidence that this level of accuracy is a reasonable assumption for NIX.

---

[1] https: //www.pas.rochester.edu/ emamajek/EEM_dwarf_UBVIJHK_colors_Teff.txt, accessed June 2021

As a result of this analysis, the final K-peak filter was manufactured with a central wavelength of 2.2μm and a width of 6%.

3.4 Possible Observing Strategies

Our custom K-peak filter has the potential to be a powerful tool for identifying very low-mass candidate objects in imaging data. In this next section, we will demonstrate the capabilities of a NIX direct imaging survey. We consider multiple survey approaches, and discuss the potential performance of NIX in each case. We do not present fully-formed survey designs, as instrument commissioning is planned for 2022, and actual instrument performance will not be known until after commissioning

We consider two categories of observational strategies: ‘targeted’ and ‘regional’ surveys. The targeted approaches we consider below involve selecting specific host stars, based on prior knowledge of possible companions from other survey data. Conversely, a regional survey approach would target all host stars that meet certain selection criteria, and are members of a chosen region, such as a specific moving group. We will discuss the pros and cons of each observational strategy in Section 3.5.

3.4.1 Targeted Surveys

3.4.1.1 Following up low-proper motion and crowded fields from the SHINE survey

As discussed in Section 3.1, the first results from the ongoing SPHERE-SHINE direct imaging survey have recently been published (Vigan et al., 2021; Langlois et al., 2021; Desidera et al., 2021). In Langlois et al. (2021), candidate companions are identified using their proximity to their host star, and then plotted on colour-magnitude diagrams using the various SPHERE filters (across $J-$,$H-$ and $K-$ bands). Where they lie in these colour magnitude diagrams can be used as an indicator of whether they are a low-mass companion to the imaged host star, or an interloping background contaminant. In Figure 3.5, we replicate one such colour-magnitude diagram using the $J2$, $J3$ dual filter. The two populations of objects shown are those described in Section 3.3.2 and plotted on Figure 3.4: an average distribution of contaminant background objects from the Trilegal Galactic model of β Pictoris, and the group of young exoplanet analogue objects described in Bonnefoy et al. (2018), which have spectral types ranging from mid-M to mid-T. We can compare Figure 3.5 directly to Figure 3.4 to assess the diagnostic capabilities of the two filter sets, which both use the spectral shape of the targets to characterise them.

In Figure 3.5, the background sequence lies on a well defined colour locus. The exoplanet analogue population begins to merge with this background sequence for the brightest objects, which includes some mid-late young Ms. In general the young L- and T- type objects are distinct from the background, with a few exceptions that might prove difficult to characterise if poor conditions lead to large photometric errors. A typical errorbar for the SHINE F150 sample is shown in the bottom right. This was calculated by obtaining the measured $J2$ and $J3$ errors in the published catalogue of SHINE F150 observations (Langlois et al., 2021), and taking the peak values of the full distributions of these errors. We then added these errors in quadrature to find the overall $J2$–$J3$ error. It should be noted that this error is likely an overestimation, as $J2$, $J3$ is a dual filter, with photometric observations obtained simultaneously. If we consider these representative errors for the young exoplanet analogues, we can see that it may not be possible to robustly distinguish M–L type objects from the background locus for some cases using only SPHERE photometry. Considering instead the colour-colour diagram shown in Figure 3.4, the distribution of exoplanet analogues is very spatially distinct when compared to the F–M background sequence, even if large photometric errors are considered (3σ region indicated by dashed lines). As in the SPHERE colour-magnitude diagram, there are regions of overlap, but for populations of different ages rather than mixing of early and late type objects.

The NIX spectral shape technique will critically confirm or refute candidate companions found previously in other imaging surveys, that are yet to be characterised. By considering the positions of targets in both the $J2$, $J3$ colour-magnitude diagram and the NIX colour-colour diagram, we will be able to estimate spectral types for previously observed objects with just further photometric observations, rejecting background K–M stars while dramatically reducing the intensiveness of follow-up time.

In order to estimate the value of this approach, we must quantify the number of candidate companions that have been observed by, and will remain unconfirmed at the end of, large-scale direct imaging surveys. Again focusing on the SPHERE-SHINE campaign as a benchmark example, we can extrapolate from the F150 sample, the first 150 stars to be observed by the survey (Vigan et al., 2021; Desidera et al., 2021; Langlois et al., 2021). According to Vigan et al. (2021), 304 candidate companions remain unconfirmed from the SHINE F150 sample. The majority of these were detected around a handful of stars in very crowded fields, which we indicate in Figure 3.2 (see Appendix 1 of Vigan et al., 2021). Observing such fields with NIX and the spectral shape technique could supply additional diagnostic information that could confirm additional candidate objects and refute many background contaminants, where SPHERE photometry alone was insufficient. This could result in a very high yield of confirmed companions using NIX with the spectral shape technique, from a small number of observations. Considering also host stars that are not in in crowded fields, one can approximate that between 60–70 candidate companions remain around other stars. Extrapolating this to the full SHINE survey (assuming similar results for the remainder of observations, and again not including other possible crowded fields) implies that upwards of an additional ∼200 unconfirmed candidate companions may remain after the SHINE survey is complete. This could lead to a plethora of targets for a NIX survey focused on SHINE follow-up.

3.4.1.2 Confirming $\Delta\mu$ selected candidates

Another possible observing strategy is to target host stars displaying anomalous proper motion trends. Expansive astrometric catalogues covering long time baselines allow us to examine the proper motions of millions of stars (e.g. Gaia Collaboration et al., 2021; Van Leeuwen, 2007). Stars showing a discrepancy in proper motion between catalogues can be an indication of a hidden perturber affecting their motion, possibly a planetary companion. This technique facilitates a more informed choice of host stars to target: when they would usually be chosen based on mass, age, brightness etc, we can add the additional information of the possible presence of a companion, before any observations are undertaken. Multiple low-mass companions have been detected using this method (e.g. Kervella et al., 2019; Currie et al., 2021).

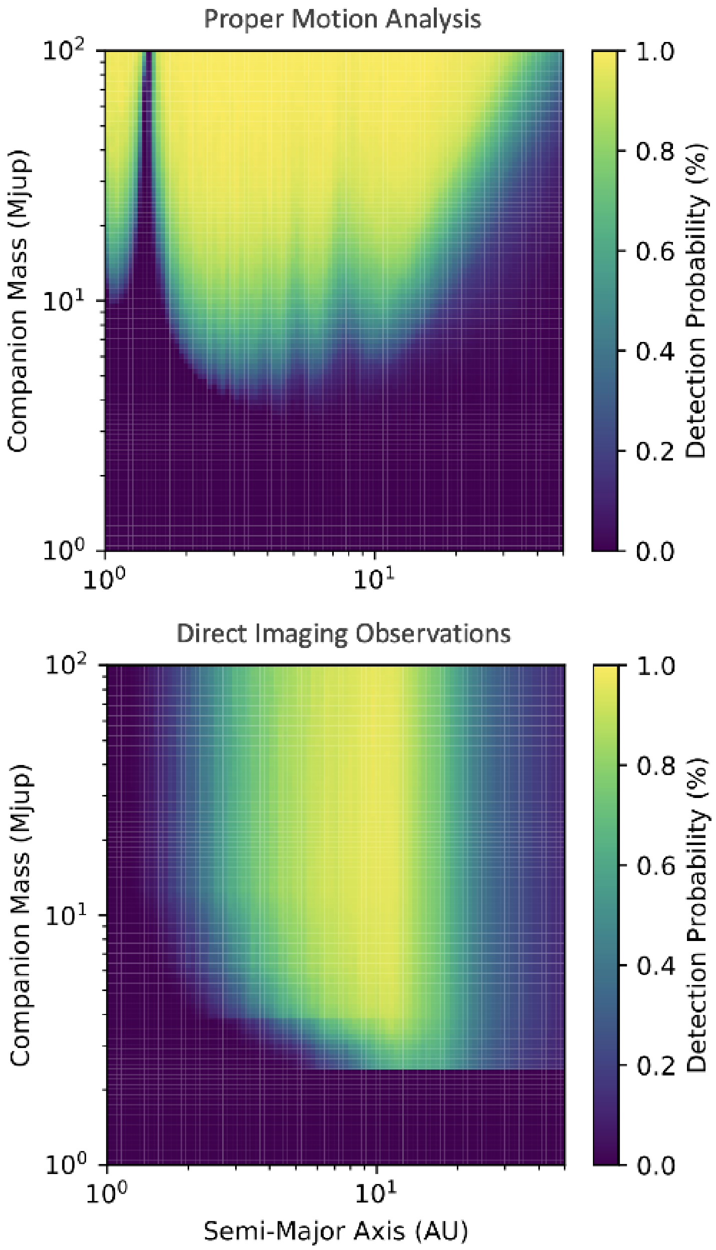

Figure 3.6 *COPAINS simulation results for a 1* $M_\odot$ *star in the* β *Pictoris moving group. Top: Fraction of simulated systems that would be selected for observations by COPAINS, in planet mass–semi-major axis space. Colourbar shows fraction of systems at each grid point with* $\geq 3\sigma$ *significance in TGAS-Gaia DR2* $\Delta\mu$*. The peak of 0% astrometric detections at small separations corresponds to systems with orbital periods comparable to the timescale of Gaia DR2, which thus have ∼null simulated* $\Delta\mu$ *values. Bottom: Completeness in direct imaging observations of the same simulated systems with NIX. Colourbar shows the fraction companions in the drawn systems at each grid point that fall above the adopted sensitivity threshold for NIX for observations in 2022.*

COPAINS (Code for Orbital Parametrisation of Astrometrically Inferred New Systems; Fontanive et al., 2019) is an innovative tool developed to use this technique, and identify previously undiscovered companions detectable via direct imaging, based on changes in stellar proper motions across multiple astrometric catalogues. We used COPAINS to estimate the range of systems that could be selected for their proper motion anomalies and be detectable with NIX ($\Delta\mu$ systems, where $\Delta\mu$ is the difference between the instantaneous velocity of a target and its true barycentric motion). We consider $\Delta\mu$ measurements between long-term proper motions from the Tycho-Gaia Astrometric Solution (TGAS; Michalik et al., 2015) subset of the Gaia Data Release 1 catalogue (Gaia Collaboration et al., 2016a,b), and short-term measurements from Gaia DR2 (Gaia Collaboration et al., 2018).

Figure 3.6 shows the results of the $\Delta\mu$ analysis from COPAINS for a typical target of a direct imaging survey, a 1-$M_\odot$ star in the β Pictoris moving group, with a parallax of 50 mas (distance of 20 pc) and proper motion of $\mu_\alpha = 5\ \mathrm{mas\,yr^{-1}}$ and $\mu_\delta = 80\ \mathrm{mas\,yr^{-1}}$, at an age of 24 ± 3 Myr (Bell et al., 2015). The left panel shows the positions in the planet mass–semi-major axis space of companions that would show a significant change in proper motion between TGAS and Gaia DR2, and would thus be selected with the COPAINS tool (Fontanive et al., 2019). For each cell in the grid, 10^4 random orbits were generated, adopting a uniform eccentricity distribution and drawing random inclinations and orbital phases, and the expected difference in proper motion between these two catalogues was calculated. The colourbar shows the fraction of these simulated systems in each point in the grid that have a $\Delta\mu$ significance of at least 3σ between the TGAS and Gaia DR2 catalogues, assuming combined uncertainties of 0.2 mas/yr in the proper motions. The right panel shows the completeness in direct imaging observations with NIX, using a predicted contrast curve. As NIX is yet to be commissioned on the VLT, there is no measured contrast curve from this specific instrument that can be used. Instead, we made use of the 3.9μm (L'-band) 5σ contrast curve presented in Otten et al. (2017). This contrast curve describes the on-sky performance of the vector apodising phase plate (vAPP, Snik et al., 2012; Otten et al., 2014) coronagraph installed on MagAO/Clio2 (Close et al., 2010, 2013; Sivanandam et al., 2006; Morzinski et al., 2014) at the *Magellan*/Clay telescope. Similar in design to the NIX grating vector apodising phase plate (gvAPP) coronagraph, it is the most up-to-date measured contrast curve suitable for synthetic NIX observations, before the commissioning of NIX on the VLT. As this contrast curve is calculated for a specific L'-band wavelength, it was scaled for use with the custom K-peak filter. The contrast actually achieved with NIX is likely to be comparable or better than the measured MagAO contrast curve. Most likely, scaling this contrast curve for use with the K-peak filter will be underestimating the contrast that will be measured with NIX, meaning the predictions reported in this Chapter are likely to be conservative. The predicted contrast curve was then converted into a mass limit using the AMES Cond evolutionary models (Allard et al., 2001) for the VLT/NaCo K_S band, at the adopted distance and age for our typical 1 $M_\odot$ β Pictoris moving group star.

Using the same simulated systems as in the left panel of Figure 3.6, we calculated the projected separation that would be observed at UT date 2022.0 for each companion, and checked whether it was detectable given the sensitivity limit. The colourbar again indicates the fraction of companions in each cell of the grid that falls above the estimated contrast curve. Systems which would be selected with COPAINS and that would be detectable with ERIS correspond to the regions of high probabilities in both panels: at separations of $\sim$3$-$15 AU with masses above $\sim$7$-$10 M_J. We compare this predicted performance to the other observing strategies in Section 3.5.

3.4.2 Regional surveys

3.4.2.1 Young Star-forming regions

Next, we consider a survey approach that would focus on members of young star-forming regions. Such regions can contain very young stars, and the active star formation increases the possibility of observing planets and brown dwarfs either during or just after formation i.e. at their brightest. As discussed in Section 3.2.1, star-forming regions have typically been less favourable targets in previous imaging surveys, primarily due to their distance and the resulting observational baseline required to confirm candidate companions via their proper motion.

To analyse the suitability of stars within such a region for a NIX imaging survey, we can consider the sensitivity achievable for a specific survey. Exo-DMC (Bonavita, 2020) is the latest (and first `python`) rendition of MESS (Multi-

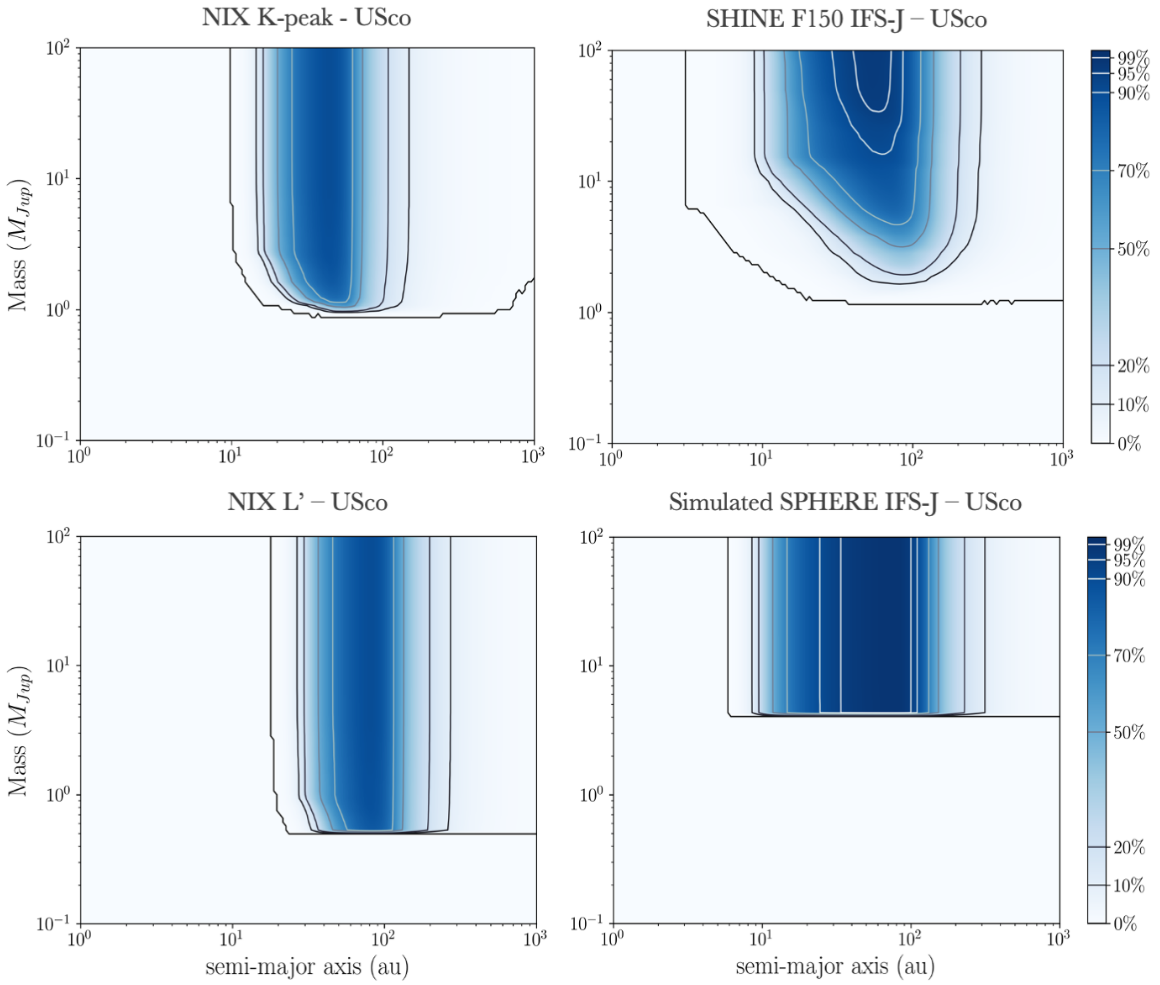
NIX K-peak - USco

SHINE F150 IFS-J – USco

NIX L’ – USco

Simulated SPHERE IFS-J – USco

Figure 3.7 *Median sensitivity maps for Upper Scorpius. Left: results from Exo-DMC simulations for the NIX K-peak (top) and L' (bottom) filters. Right: comparable results for the SPHERE imager, using the same synthetic target list (bottom), and the real SHINE F150 Upper Scorpius targets (top). Colour indicates the percentage of companions detected with the corresponding mass and semi major axis. The contour levels are indicated in the colour-bar.*

purpose Exoplanet Simulation System, Bonavita et al., 2012), a Monte Carlo tool for the statistical analysis of direct imaging survey results. In a similar fashion to its predecessors, the DMC combines information on the target stars with the instrument detection limits to estimate the probability of detection of a given synthetic planet population, ultimately generating detection probability maps.

For each star in a supplied sample, the DMC produces a grid of masses and physical separations of synthetic companions, then estimates the probability of detection given the provided detection limits. The default setup uses a flat distribution in log space for both the mass and semi-major axis but, similar to its predecessors, the DMC allows for a high level of flexibility in terms of possible assumptions on the synthetic planet population to be used for the determination of the detection probability. For each point in the mass/semi-major axis grid the DMC generates a fixed number of sets of orbital parameters. By default all the orbital parameters are uniformly distributed except for the eccentricity, which is generated using a Gaussian eccentricity distribution centred at $\mu = 0$ with a width of $\sigma = 0.3$ (for positive values of eccentricity), following the approach of Hogg et al. (2010) (see Bonavita et al., 2013, for details). This allows for proper consideration of the effects of projection when estimating the detection probability using the contrast limits. The DMC in fact calculates the projected separations corresponding to each orbital set for all the values of the semi-major axis in the grid (see Bonavita et al., 2012, for a detailed description of the method used for the projection). This enables the estimation of the probability of each synthetic companion truly being in the instrument FoV and therefore being detected, given that the value of the mass is higher than the corresponding limiting mass.

Figure 3.7 shows the results of the Exo-DMC simulations for the Upper Scorpius star-forming region. Upper Scorpius is an ideal target for the NIX imager. In Section 3.2.1, we described an Upper Scorpius member list derived from the compilation presented in Luhman et al. (2018). We use this for the remainder of the Upper Scorpius analysis, with the additional assumptions of a common age of 10 Myr (Pecaut & Mamajek, 2016) and a common distance of 145 pc (Preibisch & Mamajek, 2008) for all Upper Scorpius members in our final list (141 targets).

Figure 3.7 shows median-combined sensitivity plots for the K-peak filter (top-left), the standard L'-band (bottom-left) and, for comparison, SPHERE-SHINE (right). Two results are shown for SPHERE-SHINE: a synthetic sensitivity map (bottom-right), created using the target list above, and the SPHERE IFS *J*-band, and the sensitivity of real IFS *J*-band observations of Upper Scorpius in the SHINE F150 sample (top-right, Vigan et al., 2021). Contour levels are indicated in the colourbar, with the minimum contour being 0% in each case. In the following analyses, we will consider the best-case mass depths as dictated by the 10% contour.

The top- and bottom-left panels indicate that our NIX sensitivity is comparable in both filters for targets in Upper Scorpius, in both cases suggesting we will be most sensitive to planets from ∼30–100 AU, with the *K*-peak filter reaching masses of $\sim1\mathrm{M_J}$, and L' likely able to detect less massive planets down to $\sim0.5\mathrm{M_J}$, but at typically wider separations. Comparing this to the sensitivity of the SPHERE-SHINE IFS *J*-band (upper-right), we can clearly see that the performance of NIX will be a improvement in a similar part of semi major axis/mass parameter space. The NIX filters offer a slightly narrower coverage in semi major axis, but far deeper coverage in mass: NIX observations of the same targets in Upper Scorpius would be sensitive down to $\approx1\mathrm{M_J}$, whereas SPHERE-SHINE is generally most sensitive to planets $>3\mathrm{M_J}$. The SHINE F150 sensitivity map is, as expected, similar to the modelled map for the IFS *J*-band - but suggests a better mass sensitivity for some of the semi-major axis space covered. For the remaining regions we discuss in the work, we will only present the real SHINE F150 sensitivities. Despite these being derived from different target lists to the NIX results, they are a more meaningful comparison, as they demonstrate the true, achieved sensitivities of the SHINE survey in each region.

3.4.2.2 Young moving group members

As discussed in Section 3.2.1, large direct imaging surveys have often targeted samples of stars belonging to nearby young moving groups, due to both their proximity and youth. Observations of moving groups dominate the archival catalogue of imaging data when compared to the previously discussed star-forming regions for this reason. In Section 3.2.1, we presented two lists of moving group members, for the β Pictoris and TW Hya moving groups (Gagné et al., 2018; Carter et al., 2021). We will use these member lists for the remainder of this analysis.

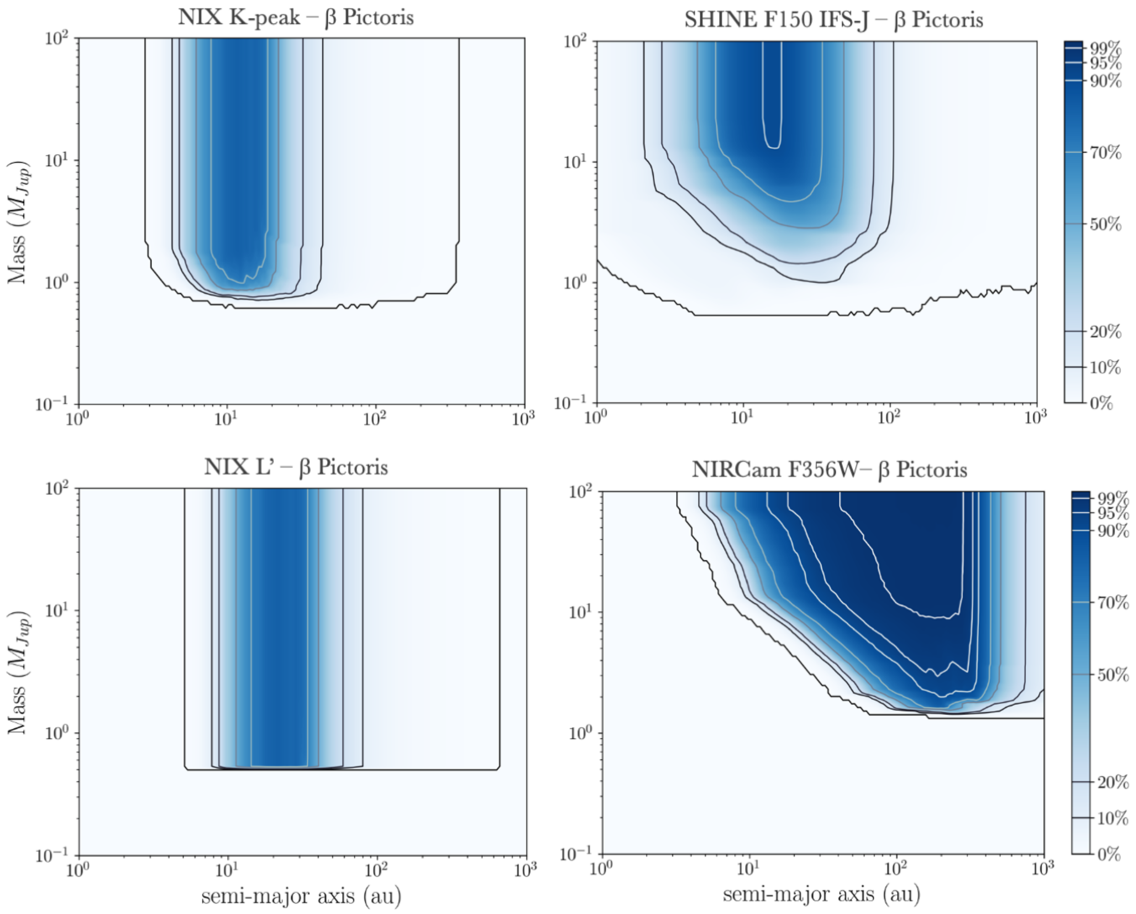

Figure 3.8 *Median sensitivity maps for the β Pictoris moving group. Left: results from Exo-DMC simulations for the NIX K-peak (top) and L′ (bottom) filters. Right: β Pictoris sensitivity results using real SHINE F150 targets (top) and simulated JWST F356W results (bottom Carter et al., 2021). Colour indicates the percentage of companions detected with the corresponding mass and semi major axis. The contour levels are indicated in the colour-bar.*

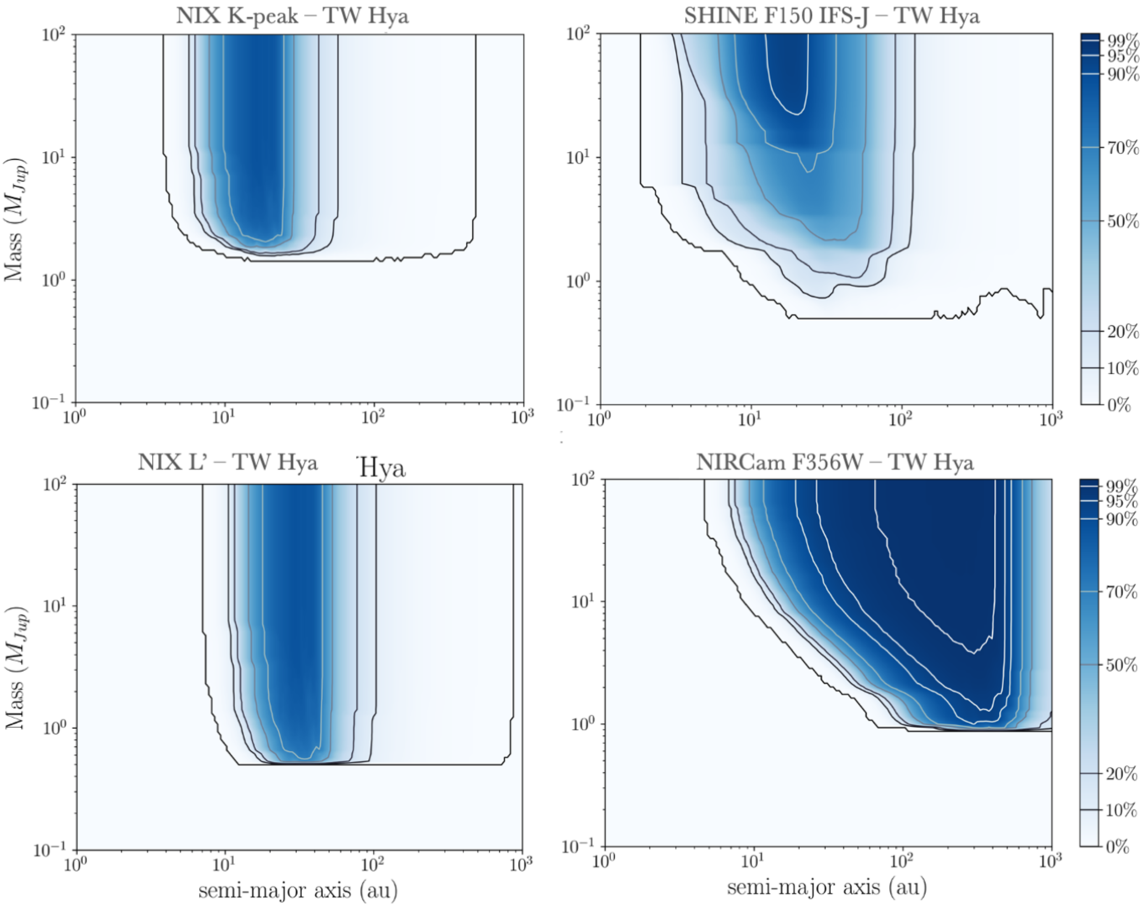

Figure 3.9 *Median sensitivity maps for the TW Hya moving group. Left: results from Exo-DMC simulations for the NIX K-peak (top) and L′ (bottom) filters. Right: TW Hya sensitivity results using real SHINE F150 targets (top) and simulated JWST F356W results (bottom Carter et al., 2021). Colour indicates the percentage of companions detected with the corresponding mass and semi major axis. The contour levels are indicated in the colour-bar.*

Exo-DMC simulations (as described above) were performed for the compilation of β Pictoris members taken from Carter et al. (2021), with results shown in Figure 3.8. The sensitivities for the individual stars were again median combined. The SPHERE sensitivities shown here are again the real results for β Pictoris members observed in the SHINE F150 sample. For β Pictoris moving group stars, the sensitivity in semi-major axis across the two NIX filters is ∼5-50 AU, reaching closer into the target stars than observations of Upper Scorpius (Figure 3.7). In terms of potential mass depth that could be achieved by targeting stars in β Pictoris with NIX, planetary companions with masses $\sim 1\mathrm{M_J}$ could be detected in both the K-peak and L' filters. Comparing this predicted performance to the actual performance of SHINE F150 IFS J-band in β Pictoris, we can see that NIX will be sensitive to slightly less massive planets in both filters, but at similar separations to those probed by SPHERE.

Figure 3.9 also shows the results from Exo-DMC simulations for the TW Hya members taken from Carter et al. (2021). Comparing these sensitivity maps to Figure 3.8, the performance of NIX and SPHERE for the two moving groups is clearly very similar, as expected due to their comparable ages and distances. There are some notable distinctions: the most sensitive area of parameter space is shifted to slightly wider separations for TW Hya members when compared to β Pictoris, because of its slightly increased distance. Additionally, the minimum detectable mass in K-peak is higher in TW Hya, reaching a depth of $\sim 2\mathrm{M_J}$, while the potential mass sensitivity in L' is essentially the same. Comparing the potential performance of NIX to SPHERE for TW Hya, we again see a similar result in mass sensitivity in the K-peak filter, and a considerable improvement for observations using the longer wavelength L' band.

Having extensively compared the predicted performance of NIX to SPHERE, we are also interested in its potential when compared to another future tool that will likely prove very successful in the field of exoplanet science. In both Figures 3.8 and 3.9, we present a fourth panel, which compares the sensitivity performances of NIX and SPHERE for each moving group to the upcoming James Webb Space Telescopeio; (JWST; Gardner et al., 2006). The instrument chosen for comparison is the Near-InfraRed Camera (NIRCam; Rieke et al., 2005), which has a similar long-wavelength capability (0.6–5μm) and angular resolution as NIX. Although not primarily designed as a coronagraphic imaging instrument, NIRCam will regardless be used for giant planet coronagraphic imaging, and the F356W filter is directly comparable to the NIX L'-band.

In the bottom-right panels of Figures 3.8 and 3.9, we present median sensitivity maps for β Pictoris and TW Hya in the NIRCam F356W filter. These use the results of Carter et al. (2021), who simulate the mass sensitivity limits of JWST coronagraphy for four NIRCam and MIRI filters. Carter et al. (2021) use the MASK335R round coronagraphic mask for all of their simulations. For both moving groups, NIRCam F356W is most sensitive to planets at wider separations that the NIX or SPHERE results, reaching the lowest depth in mass (approximately $1\mathrm{M_J}$) from ∼100 AU onwards.

3.5 Discussion

3.5.1 Merits of each survey approach

In this work, we have presented four possible approaches for a future large-scale imaging survey with ERIS NIX. The focus of the design of these options was to maximise the unique capabilities of the custom K-peak filter and the long wavelength options of NIX. In summary, these survey approaches are:

1. Targeting host stars with unconfirmed candidate companions or in very crowded fields that were previously observed in the SPHERE-SHINE campaign. Combining NIX data with existing SPHERE photometry could provide the additional information necessary to characterise and confirm (or refute) previously identified candidates.

2. Using the COPAINS tool to choose imaging targets based on $\Delta\mu$ trends between different astrometric surveys. The spectral shape technique would be useful for characterisation, and the target list would be informed by COPAINS results.

3. A survey of nearby young star-forming regions. This approach is similar to what has been done by previous collaborations - using a target list informed by likely membership of a region, which itself is chosen using distance and age. The unique aspect of such a survey with NIX is that the custom K-peak filter can rule out significant numbers of background interlopers without the

necessity of time-consuming proper-motion follow-up observations, opening up the possibility of surveying more distant star-forming regions that have been relatively neglected. Additionally, the deep sensitivity of L' will likely prove very useful in extending our sensitivity to considerably lower planet masses in such regions, and allow for studies of protoplanets in circumstellar disks.

4. A survey of young moving group stars. As with the above approach, this option is similar to past surveys, as young moving groups have been extensively targeted by direct imaging . Here, the custom K-peak filter is less uniquely useful, since proper motion follow-up is not as time intensive. Instead, the long wavelength capabilities of NIX could lead to new detections in unexplored parts of parameter space.

It is clear that the K-peak filter is specifically useful for most of the survey designs that we have explored in this work, and also that the L' capability of NIX will be extremely valuable. Figure 3.10 compares the regions of semi-major axis/ planet-mass space probed by three of the approaches discussed above. In this Figure we show the sensitivities of each approach in either K-peak only, or K-peak and L'. We also plot a catalogue of known companions, including any planets and brown dwarfs with constrained planet masses and semi-major axes that are labelled as direct imaging detections[2].

First, we consider the planet mass–semi-major axis sensitivity predicted by the COPAINS simulations, for a typical β Pictoris moving group star. In Section 3.4.1.2, we presented a sensitivity map generated using an approximate contrast curve for K-peak (K-peak results in Figure 3.10 are indicated by a cross-hatched shading). This showed that the highest probability region for selection by COPAINS and detection by NIX is 3–15 AU and 7–100 $\mathrm{M_J}$ (the highest mass considered), highlighted in lime green in Figure 3.10. The planets we would be sensitive to using target selection informed by COPAINS for the nearby β Pictoris moving group populate the closest semi-major axes of any of the survey approaches considered here, and reach into an area of parameter space where very few planets have thus-far been discovered via direct imaging. Furthermore, with all subsequent GAIA data releases, the sensitivity of this technique will continue to improve.

---

[2] Taken from exoplanet.eu, accessed June 2021

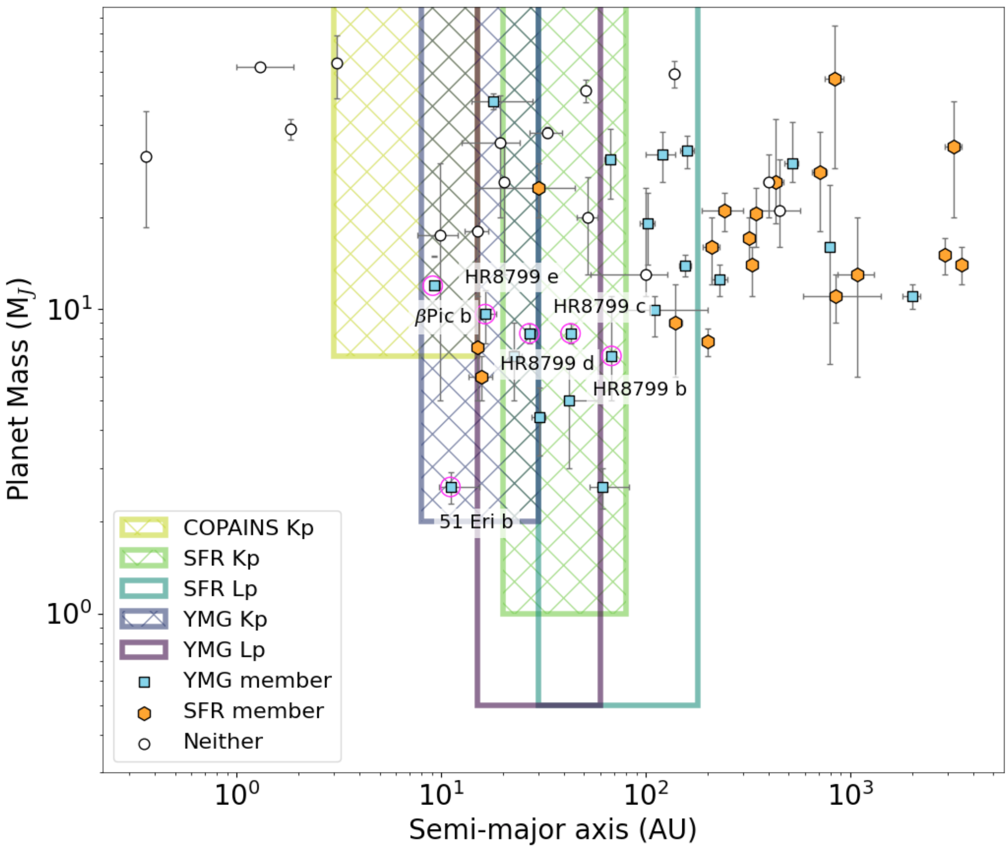

Figure 3.10 *Planet mass vs semi-major axis. Plotted are planets and brown dwarfs detected using direct imaging (exoplanet.eu). Colour-coding of points indicates members of young moving groups (blue) or star-forming regions (orange). Rectangular regions show the possible sensitivities for each survey approach. Cross-hatched areas indicate NIX simulations using the K-peak filter, areas with no fill are NIX simulations using the L' filter.*

Next, we consider targeting young, nearby star-forming regions, or young moving group stars. We explored Upper Scorpius as a possible star-forming region to target with a direct imaging survey. Exo-DMC simulation results for Upper Scorpius indicate comparable sensitivity in K-peak and L' - with the most sensitive region being for planets between 20–80 AU for K-peak and 30–180 AU in L'. The K-peak and L' sensitivities are highlighted in Figure 3.10. In K-peak we reach planet masses of $\gtrsim$1 $\mathrm{M_J}$, but the predicted performance in L' is extremely encouraging, suggesting that masses down to $\sim$0.5 $\mathrm{M_J}$ could be reached - the deepest mass limit of any of the survey approaches considered in this work. It should be noted that $\sim$0.5 $\mathrm{M_J}$ is the lowest mass covered by the evolutionary models used in Exo-DMC, which therefore impose an artificial mass cut-off.

We also ran simulations of observations for two possible moving group targets: β Pictoris (multiple lines of sight, compared to a singular target for the $\Delta\mu$ analysis in Section 3.4.1.2) and TW Hya, as discussed in Section 3.4.2.2. We present the regions of high detection probability for the TW Hya moving group in Figure 3.10, to allow comparison between a moving group target and a young star-forming region. Here we can see that the K-peak sensitivity (again indicated by the cross-hatched area), probes closer semi-major axes than the results for Upper Scorpius (8–30 AU), but does not reach as deep in mass, with the minimum likely detectable mass $\approx$2 $\mathrm{M_J}$. In contrast, the result for L' sensitivity for TW Hya moving group stars are very similar to the performance predicted for Upper Scorpius targets, again reaching a minimum detectable mass of $\sim$0.5 $\mathrm{M_J}$. A survey approach using the L' filter to survey TW Hya, or both K-peak and L' to explore Upper Scorpius, would likely be sensitive to companions with masses <2 $\mathrm{M_J}$, where very few directly-imaged planets have been discovered to date. Current understanding of the distribution of giant planet masses suggests that frequency increases with decreasing giant planet mass (i.e. in the range $\sim 0.1-10$ $\mathrm{M_J}$), suggesting that, for example, 1 $\mathrm{M_J}$ planets should be more prevalent than 2 $\mathrm{M_J}$ planets (e.g. Adams et al., 2021). Consequently, in order to maximise the yield of a NIX survey, it could be deemed most appropriate to chose the selection method that is sensitive to the lowest mass planets.

The conclusions that we can draw from Figure 3.10 are three-fold: first, independent of the survey approach chosen, NIX will be the most sensitive to both areas of parameter space where many planets have been directly imaged previously, and areas where little is known about the true direct imaging planet population. Secondly, using the COPAINS tool to inform a target list could allow us to probe a sparsely populated region of parameter space, with planetary companions close to their host stars. Thirdly, targeting more distant star-forming regions in general will likely lead to better depth in planet-mass than observing nearby young moving group stars, with the notable exception of an L'-specific survey of a nearby young moving group.

3.5.2 Planet Populations

In the previous section, we investigated the potential performance of a NIX survey, using the current population of direct-imaging discovered planets as a guide for what we might find. This approach does not give us the full picture: as we show in Figure 3.10, survey detection space is limited by instrument design and performance. Consequently, the planets that have been discovered to date do not represent the distribution of planets as a whole. To understand the full distribution of planets in the semi-major axis-planet mass parameter space, we must use planet population models.

As discussed in Section 3.1, our understanding of the underlying planet population has evolved dramatically in recent years. Prior to the publication of recent results from the latest generation of surveys (Nielsen et al., 2019; Vigan et al., 2021; Desidera et al., 2021; Langlois et al., 2021), direct imaging searches were informed by predicted detection yields derived from the distribution of radial velocity planets. Studies such as Cumming et al. (2008) found that the detected radial velocity planets (typically at $\lesssim$3 AU) followed a rising power law in mass and orbital period, thus predicting many giant planets at wide separations from their host stars. Many direct imaging surveys (including Lafrenière et al., 2007b; Heinze et al., 2010; Macintosh et al., 2014) were planned and interpreted using this assumption, as it was the best available at the time. Lower than expected yields from many such surveys confirmed suspicions that simply extending the RV power law did not accurately describe the giant planet population at wide separations.

We now have a better understanding of where we expect to find planets in a direct imaging survey. Fernandes et al. (2019) published a ground breaking study, using planets discovered by the *Kepler* telescope and radial velocity instruments (Mayor et al., 2011) to derive a turn-over in planet occurrence rates at 2–3 AU. This model agreed with data from previous surveys (e.g. Bowler, 2016; Galicher et al., 2016), suggesting that giant planets on wide orbits were rarer than previously thought. However, the occurrence of planets beyond 3 AU was not well constrained by this study, as RV and transit data doesn't typically extend to long enough orbital periods to cover these separations. The work of Fulton et al. (2021) addressed this challenge, using data from the California Legacy Survey (Rosenthal et al., 2021), which has been observing the same sample of 719 nearby stars stars for ∼30 years. This long observational baseline allowed them to constrain the giant planet occurrence rate, finding a turnover at ∼3.6 AU, and a well constrained downward slope out to ∼10 AU.

Figure 3.11 uses the planet populations predicted by Fulton et al. (2021) to assess the sensitivity of a NIX survey targeting the two young moving groups discussed here (β Pictoris and TW Hya, left and right panels, respectively) in the context of the predicted distribution of planets across the full parameter space. The distribution plotted as blue squares are the planets predicted by the Fulton et al. (2021) planet population between $0.1\mathrm{M_J} \leq M_\mathrm{P} \leq 100\mathrm{M_J}$ and $0.1\mathrm{AU} \leq a \leq 1000\mathrm{AU}$. Overlayed are the detection maps for β Pictoris (left) and TW Hya (right) in the NIX L'-band and JWST F356W filter, taken from the plots shown in Figures 3.8 and 3.9. The labelled contours indicate varying levels of sensitivities.

As we discussed in Section 3.4, Figure 3.11 demonstrates that in the L-band wavelength range, NIRCam and NIX will be sensitive to essentially the same planet star separations, but NIX will be able to go deeper in mass at closer planet-star separations for both β Pictoris and TW Hya. Based on the results of Fulton et al. (2021), neither instrument is likely to be sampling the peak of the planet populations (at around 4AU) in L-band, but NIX will push closer to the peak for all planet masses considered here around stars in β Pictoris. Regardless of the exact location of the peak of the distribution, there are many objects predicted in the tail of wider separation objects that both NIX and NIRCam will be sensitive to in L-band. It is also important to note that a comparison between NIX and JWST is only relevant up to L-band, and JWST also has longer wavelength capabilities where it is predicted to offer unrivalled sensitivity for coronagraphic observations (Carter et al., 2021).

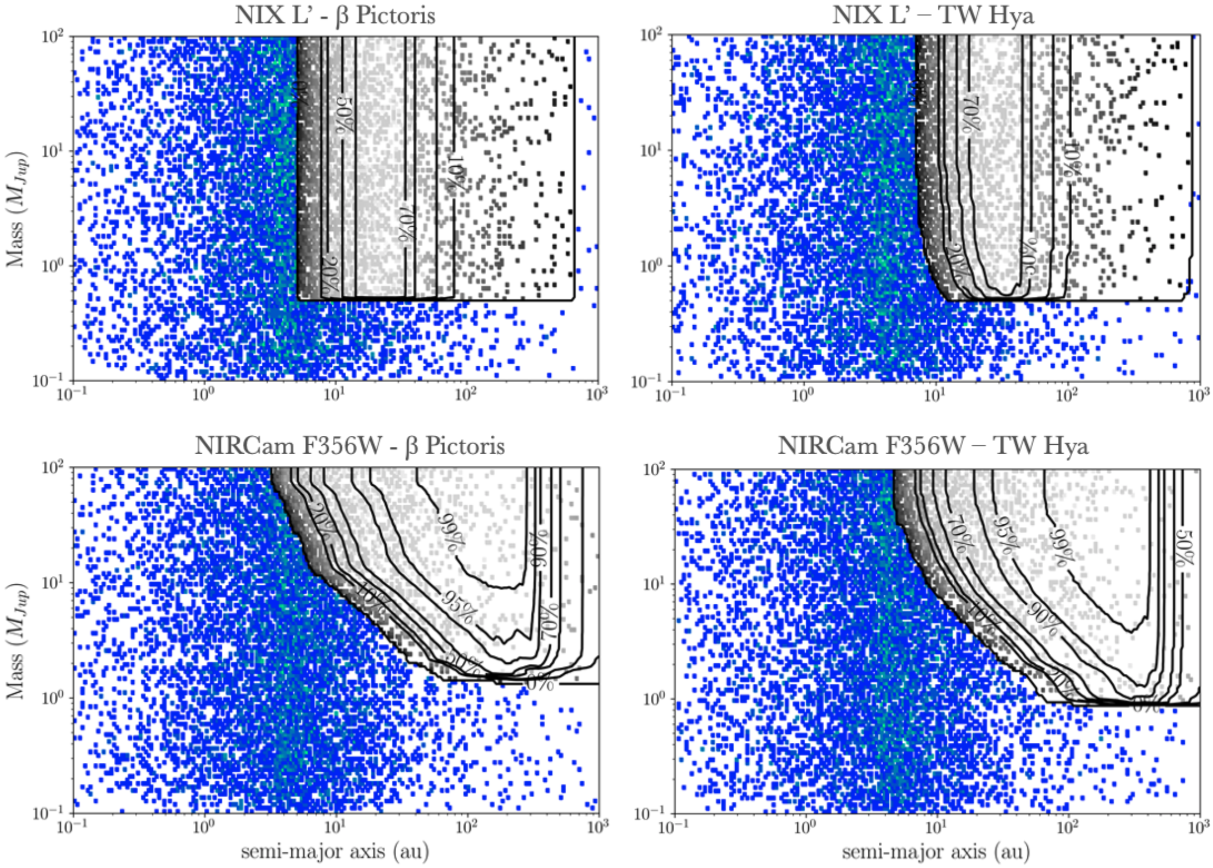

Figure 3.11 *Instrument sensitivity comparison with a modelled planet population. Blue squares show the distribution of planets returned by the model described in Fulton et al. (2021). In each panel, yellow/green overlay shows the sensitive area of parameter space for each instrument and region. Left: results for a survey β Pictoris. Right: results for a survey of TW Hya. In both cases, using: NIX L' (top) and NIRCam F356W (bottom, limits from Carter et al., 2021)*

3.6 Conclusions

We have presented the first details of the custom 2.2µm $K-$peak filter, that will be available on the NIX imager at the VLT. We aim to use this custom filter, and the spectral shape technique, to optimise a direct imaging survey for giant planets and brown dwarfs. We have also described four possible survey approaches, that aim to optimise survey yield and follow-up time requirements. The main takeaways from this analysis of observing strategies are:

- NIX will be able to efficiently follow-up the remaining candidates left at the end of the SPHERE-SHINE survey.
- A survey informed by anomalous proper motion trends using the K-peak filter could prove fruitful in exploring the small projected separation part of parameter space.
- A survey targeting a young star-forming region, such as Upper Scorpius, will likely result in a higher yield than a survey focusing on young moving groups. Firstly, moving groups have already been extensively surveyed, and for the two examples considered in this work the likely NIX contrasts are not better than those achieved by SPHERE. Secondly, we reach better mass sensitivity for star-forming regions with NIX than SPHERE, and with the K-peak filter, we are less dependent on common proper motion confirmation follow-up to confirm (or reject) candidate companions.

When operational, NIX will be a competitive instrument for direct imaging surveys. By considering possible observing strategies in advance, we aim to identify the optimal approach to maximise observing time efficiency and survey yield. The numerous large-scale imaging surveys that have been completed to date or are currently underway are invaluable when planning future observations, as are analyses of planet populations. We aim to use the wealth of knowledge from recent years of direct imaging research to design a successful survey that will optimise both the detection and confirmation of candidate exoplanet companions.

4

Investigating the Initial Mass Function in Taurus using W-band and Gaia Photometry

4.1 Introduction

The Initial Mass Function (IMF) describes the mass distribution of stars at the point of formation. While the IMF is an aspect of star-formation that has been studied for decades, the IMF for stars with masses $\gtrsim 0.5$ $M_{\odot}$ is generally better constrained than the IMF for lower mass stars and brown dwarfs. Such low-mass objects are faint and hard to detect, and a statistically significant population is needed to place constraints on the IMF.

The IMF is often assumed to take the same form across the universe, regardless of local conditions - the 'universal' assumption. In most instances, this 'universal' IMF is assumed to follow either a broken power law (BPL) or a log-normal (LN) function. A broken power law is comprised of multiple distinct sections, with different slopes depending on the mass range in question. The most commonly-used broken power law parameterisation is the Kroupa (2001) IMF. A log-normal power law is a more complex function composed of a power law and exponentials, the most commonly-used being the Chabrier (2003) IMF. All of the commonly-used functional forms of the IMF agree at masses $>1\mathrm{M}_{\odot}$, predicting the same numbers of high-mass stars (Salpeter, 1955; Miller & Scalo, 1979; Kroupa, 2001; Chabrier, 2003). There is less agreement for masses below $1\mathrm{M}_{\odot}$.

In order to confirm or refute the universality of the IMF, and to constrain its functional form at the lowest masses, a common approach is to survey specific regions, with the aim of detecting the lowest-mass objects populating this section of the universe. Densely populated star-forming regions are excellent targets for such IMF studies, as they are likely to contain plenty of members with $m < 1\mathrm{M}_{\odot}$. Such studies either make use of existing literature membership catalogues for a region, or perform a photometric survey from which they can identify their own compilation of low-mass members (e.g. Alves de Oliveira et al., 2013; Esplin & Luhman, 2019). Using a specific combinations of broadband filters, it is possible can differentiate between members of the star-forming region and foreground/background interlopers (e.g. Briceño et al., 2002; Lodieu et al., 2009; Robberto et al., 2020; Gennaro & Robberto, 2020).

In this work, I will use the latter approach of using a new photometric catalogue to identify likely members of the Taurus star-forming region, and find the best-fit parameters of the IMF using this population. The Taurus star-forming region is nearby ($\approx$ 140pc), young ($\approx 1-10$ Myr), and contains numerous low-mass stars. In Biller et al. (in prep.), we will present a new compilation of Taurus members, identified using the novel W-band custom photometric filter. This technique has already been applied to smaller clusters (Allers & Liu, 2020; Jose et al., 2020; Dubber et al., 2021), and has also proven successful in Taurus. Using G-band from Gaia eDR3 (Gaia Collaboration et al., 2021) and infrared (J, H and W) photometry from our W-band catalogue, we can identify different populations of objects in the Taurus line-of-sight, and isolate likely cluster members. This compilation of members can then be used to investigate the form of the IMF in Taurus.

In Section 4.2, I introduce the Taurus star-forming region as a target for IMF studies, and discuss the results of previous studies. In Section 4.3, I present the W-band catalogue of Taurus. In Section 4.4, I describe the process used to identify likely Taurus members in the catalogue, and explain the modelling procedure used to obtain best-fit IMF parameters using this data. In Sections 4.5 and 4.6, I outline the results from this investigation, for a variety of input conditions and differing functional forms.

4.2 Previous IMF studies

4.2.1 Taurus

In this work, I will build a tool to model the IMF of a cluster using photometric data, and apply it to the Taurus star-forming region. In future, I hope to perform this same analysis on the multiple other regions covered by the W-band survey. Taurus was chosen as a starting point for a number of important factors:

- It is nearby. When studying a nearby cluster, we can use the common proper motion between candidate members and known cluster members to confirm or refute their cluster membership. The more distant a cluster, the longer the baseline required to measure the necessary proper motion. Thus, for the most distant clusters, we cannot use this technique to assess membership.
- It is relatively young. The youth of the cluster is key when searching for young populations of objects: brown dwarfs cool with age, making the lowest mass easiest to detect when they are newly formed.
- It has generally low values of dust extinction. Dust extinction alters the infrared colour of targets, by preferentially absorbing at blue wavelengths and thus causing an overall reddening of object colours. When we use

colour-magnitude diagrams as the main tool for characterisation, high levels of extinction can introduce additional errors and blending of populations. For this reason, a low extinction cluster increases the likelihood of accurately isolating the cluster population.

- Taurus has a large stellar population, with a comparatively low stellar density. When considering the form of the IMF, a statistically significant sample size is required for the resulting constraints to have any meaningful implications. Thus we require a region with a large number of stellar members. The stellar density is less crucial than the size of the population for obtaining meaningful results, but in the case of Taurus, it may allow for an interesting comparison. As the local stellar density of Taurus is low when compared with other star-forming regions, any variation in the form of the IMF could point to environmental dependency.

Taurus has been a popular target for general population studies, and investigations of the IMF, for decades. The earliest surveys showed that the population of pre-main sequence stars and brown dwarfs in Taurus totalled a few hundred objects (see Kenyon et al., 2008, for a detailed list of papers that investigate this). Taurus appeared to have a deficit of low-mass stars, compared to the numbers predicted by a universal IMF. Briceño et al. (2002) combined deep imaging data and follow-up spectroscopy to perform an 8 deg^2 survey of Taurus, complete to 0.02 $M_\odot$. Their resulting IMF was in agreement with smaller surveys of the region, finding a stronger low-mass peak in Taurus when compared with the Trapezium cluster (Luhman et al., 2000), and a more dramatic drop-off below 0.8 $M_\odot$. Luhman (2004) also found a brown-dwarf deficit, but with a lower statistical significance when compared to other star-forming regions.

To explain this deficit, Goodwin et al. (2004) performed hydrodynamic simulations of the Taurus cloud, and concluded that the unusual IMF could be due to unusual properties of the molecular cores in which the stars formed. Guieu et al. (2006) suggested that the deficit found by previous studies was due to their focus on the highest density regions of Taurus. They performed a 28 deg^2 survey encompassing parts of the region with differing densities, discovering 17 new very low-mass members and deriving an IMF in better agreement with measurements from other clusters.

In recent years, the initial membership catalogues of Taurus have been refined and expanded (e.g. Esplin & Luhman, 2017; Luhman et al., 2017; Zhang et al., 2018). Esplin & Luhman (2019) offer a detailed compilation of Taurus members, totalling 519 likely members with masses ranging from stellar to planetary. This work builds directly on their previous Taurus studies (Luhman et al., 2017; Esplin & Luhman, 2017; Luhman et al., 2018). Using a combination of photometry, astrometry and spectroscopy, they vet every detection for signs of Taurus membership. With their final sample, they perform a rudimentary analysis of the form of the IMF in Taurus, using spectral type and dereddened K-mags as observational proxies for mass. They find an IMF consistent with other dense clusters (e.g. Da Rio et al., 2012; Hillenbrand et al., 2013), but with a shallower slope than that predicted by Chabrier (2005).

4.2.2 Other Star-forming Regions

Taurus is one of many star-forming regions where the IMF has been studied and debated. As mentioned above, a major motivating factor for studying the form of the IMF in different star-forming regions is to investigate a possible environmental dependence. Star-forming regions can have drastically varying stellar densities, which could be related to variations in the initial mass function.

The Chamaeleon I star-forming region is an example of another region with a comparatively low stellar density but many low-mass objects. It is also nearby and well-isolated from other young stellar populations. Consequently, it has been another popular target for low-mass studies of the IMF (e.g. Luhman, 2008). New members are still being identified: most recently, Kubiak et al. (2021) increased the census of known members by 40%, and determined the IMF slope to be consistent with other young clusters.

Upper Scorpius is another ideal target for IMF studies, as it has no ongoing star-formation (Preibisch & Mamajek, 2008), and is a young region (≈ 5 Myr Pecaut et al., 2012; Pecaut & Mamajek, 2016; David et al., 2019), so all stars that initially formed should still be present (an important for factor for measuring the high-mass IMF). Essentially, the current mass function in Upper Scorpius is equivalent to the initial mass function. Preibisch et al. (2002) fit the IMF of Upper Scorpius, and found that within the uncertainties, the general shape of its

IMF was consistent with IMFs of other young clusters (Kroupa & Boily, 2002). More recent surveys have continued to find results consistent the with the IMFs of either other young clusters or Galactic field values (e.g. Cook et al., 2017; Luhman & Esplin, 2020).

The Orion Nebular Cluster (ONC) is one of the most frequently observed nearby star-forming regions (Muench et al., 2008). It is young (1–3 Myr, Jeffries et al., 2011), nearby (∼430 pc, Kuhn et al., 2019), and has thousands of known members that span the full range of spectral types. Robberto et al. (2020) and Gennaro & Robberto (2020) surveyed the ONC using the Hubble Space Telescope (HST), and investigated the local form of the IMF. They used the F130N and F139M HST filters to construct a colour-magnitude diagram and identify likely ONC cluster members. They then found best-fitting IMF parameters by considering both BPL and LN forms. The analysis that is detailed in this Chapter follows a similar procedure to this study. Overall, they found general agreement with both Kroupa (2001) and Chabrier (2003), particularly for higher-mass objects.

From these example studies, the IMF appears to be generally consistent between different star-forming regions, but with large uncertainties. Reducing these uncertainties will only be possible as more members of each region are detected.

4.3 W-band Photometric Survey

The W-band consortium observed the Taurus star-forming region between 2015 and 2017, using WIRCam on the Canada France Hawaii Telescope (CFHT; Puget et al., 2004). 243 WIRCam pointings were taken in three bands (J,W,H), totalling an approximate survey area of 27 sq. deg. In 2015 and 2016, the consortium obtained 4 dither positions per stack; in 2017 this was increased to 6 dither positions per stack, yielding better cosmetics. The data reduction process is described in detail in Biller et al. (in prep.).

Figure 4.1 shows the spatial distribution of detections in the CFHT catalogue, and also indicates the coverage of the cluster achieved by our imaging. Source density is indicated by colour, with brighter areas representing more densely populated parts of the cluster. In total, the full CFHT catalogue of Taurus contains 669,700 detections. The slight overlap between the fields of view of different pointings

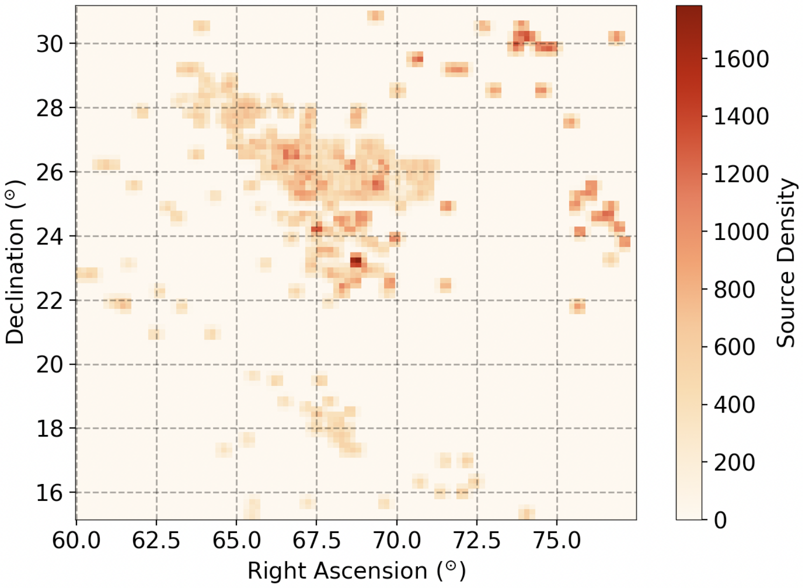

Figure 4.1 *Source density for the CFHT catalogue of Taurus. On-sky area is binned into areas of* $0.15 \times 0.15°$*, and the source density in each bin is indicated by the colour-bar.*

means that these are not necessarily unique detections, as some objects may appear in multiple frames. A catalogue of unique detections from this survey will be presented in Biller et al. (in prep.). Also described in Biller et al. (in prep.) are some issues discovered retrospectively in the photometry. The first exposures taken as part of the survey used 4 dithers, which was later found to be insufficient, causing issues with photometry for objects detected on only 1 or 2 of the dithered sub-images. This was later corrected for data obtained in 2017, by increasing to 6 dithers, thus ensuring that any given object detected in a stack was detected on at least 3 dithered sub-images. Consequently, for the remainder of the analysis presented here, I will use a subsection of the Taurus catalogue containing only photometry obtained during the 2017 observing season. This contains a total of 324,729 detections.

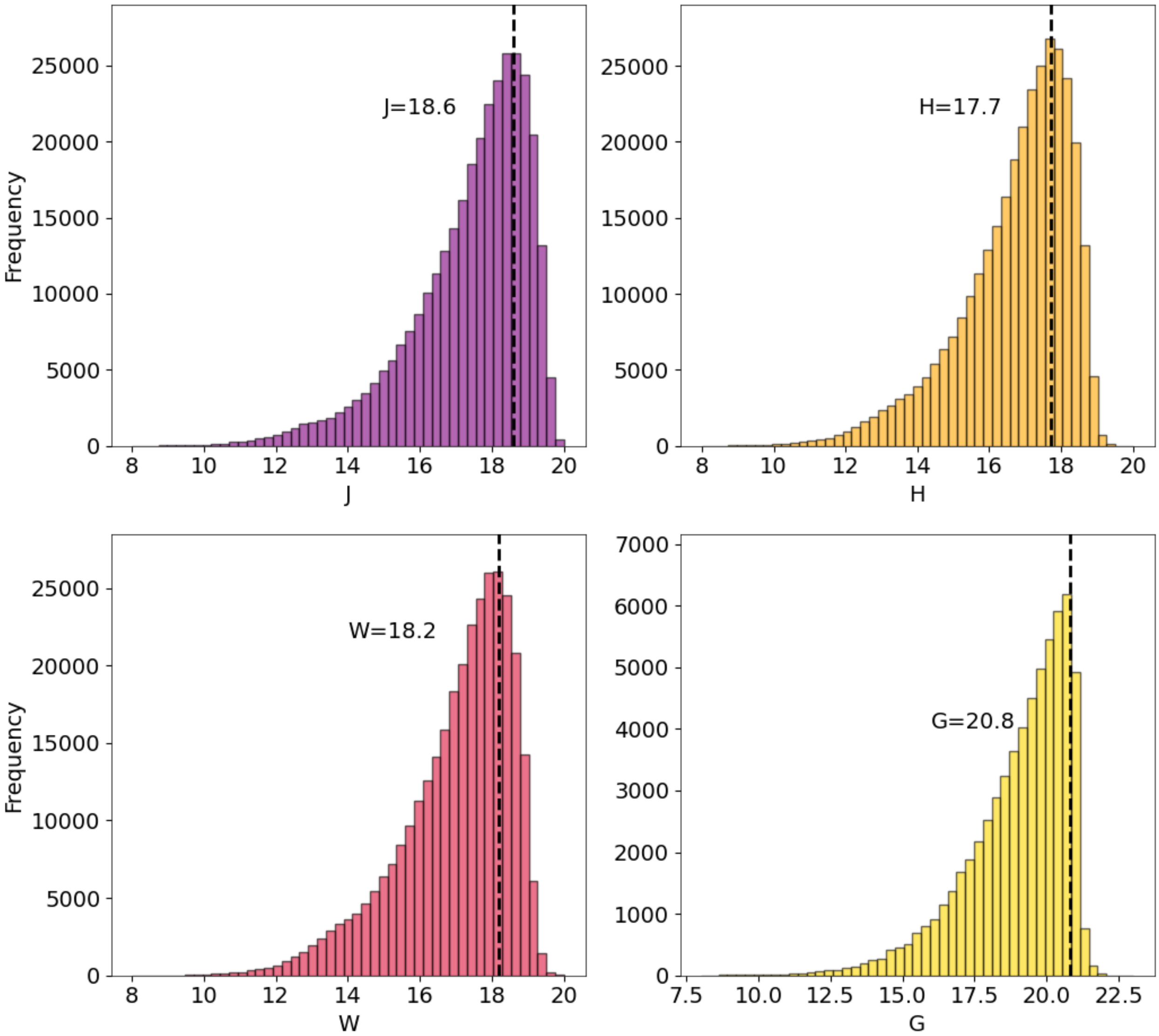

Figure 4.2 *Magnitude distributions for sources in the Taurus CFHT catalogue. Top left: CFHT J-band distribution, with limiting magnitude $J = 18.6$ indicated. Top right: CFHT H-band distribution, with limiting magnitude $H = 17.7$ indicated. Bottom left: CFHT W-band distribution, with limiting magnitude $W = 18.2$ indicated. Bottom right: Gaia eDR3 G-band distribution (cross-matched with CFHT catalogue), with limiting magnitude $G = 20.8$.*

4.4 Modelling the IMF

4.4.1 Initial Considerations

4.4.1.1 Gaia photometry

Gaia is an all-sky catalogue (Gaia Collaboration et al., 2016b,a, 2018, 2021) that has generally high completeness to faint magnitudes [1]. It is an ideal catalogue for cross-matching as most stars detected in other surveys (down to the Gaia completeness limit) will have a corresponding Gaia detection. Krolikowski et al. (2021) have shown that combining a Gaia magnitude with an infrared broad-band magnitude is highly effective in separating field populations from the members of young nearby clusters. This is especially crucial when considering the lowest mass objects. Often, background interlopers can have very similar colours to low-mass objects. By combining Gaia G-band with WIRCam J-band, it is possible to accurately separate objects into populations with differing ages.

As discussed above, the Taurus catalogue contains 324,749 detections and 62,596 of these have corresponding Gaia detections in eDR3. (Gaia Collaboration et al., 2021). Figure 4.2 shows the magnitude distributions of all objects in the cross-matched catalogue, in CFHT J-, H- and W-bands, and Gaia G-band, with limiting magnitudes indicated.

4.4.1.2 Line-of-sight Field Population

To isolate the objects in the CFHT catalogue that are likely Taurus cluster members, I constructed a colour-magnitude diagram (CMD) using G- and J-band. To assess the area of this parameter space that contains only Taurus cluster members, and to confirm that there are few field contaminants, I used the Trilegal Galactic model (Girardi et al., 2012) to obtain a line-of-sight field population for the Taurus cluster.

I ran a number of Trilegal models, each time varying the IMF used to generate

---

[1] See Gaia docs: https://gea.esac.esa.int/archive/documentation/GEDR3

data. I used each individual IMF available on the Trilegal webform [2], keeping all other input parameters the same between runs. Each time, I centred the model on RA = 68.7° and Dec = 23.2°, with a total field area of 1 $\deg^2$. This matches the central coordinates of our CFHT Taurus observations, but is a smaller field size - this choice was made purely to keep the run-times of the Galactic models at a reasonable level. I used the Gaia DR2 + Tycho + 2MASS photometric system, with the limiting magnitude set to the maximum 32 mag. All other parameters were left as their default values. I generated six populations, one for each of the IMF options, and compared their distribution in $G - J$ vs G. There was little overall variation between the different IMFs, with the resulting populations falling in the same general areas of the colour-magnitude diagram

Figure 4.3 shows a representative Trilegal population (white points) compared with the full Taurus catalogue. The field model is very clustered and coincides with a well-defined section of the full cross-matched Taurus catalogue. This Trilegal population is nominally field main sequence stars - the potential cluster population are objects brighter than the field sequence - in other words, likely pre-main sequence stars which are still above the main-sequence.

4.4.1.3 Isolating the young cluster population

To isolate the cluster population, I compared the CMD positions of model isochrones and known Taurus members with the Trilegal field population model.

My aim was to define an area of parameter space with minimal contamination from background and foreground sources, thus likely to contain a pure sample of Taurus cluster members. From the Trilegal field population model, we can see that it is possible to identify an area of parameter space solely occupied by field objects, for $G \geq 13 - 14$. At brighter magnitudes, the field objects mix with young isochrones (taken from Baraffe et al., 2015), making it difficult to disentangle differently-aged populations. Consequently, when identifying a cluster-dominated section of parameter space, I will only consider magnitudes of $G \geq 14$ mag.

At bright magnitudes, photometric catalogues can be limited by detector

---

[2] http://stev.oapd.inaf.it/cgi-bin/trilegal

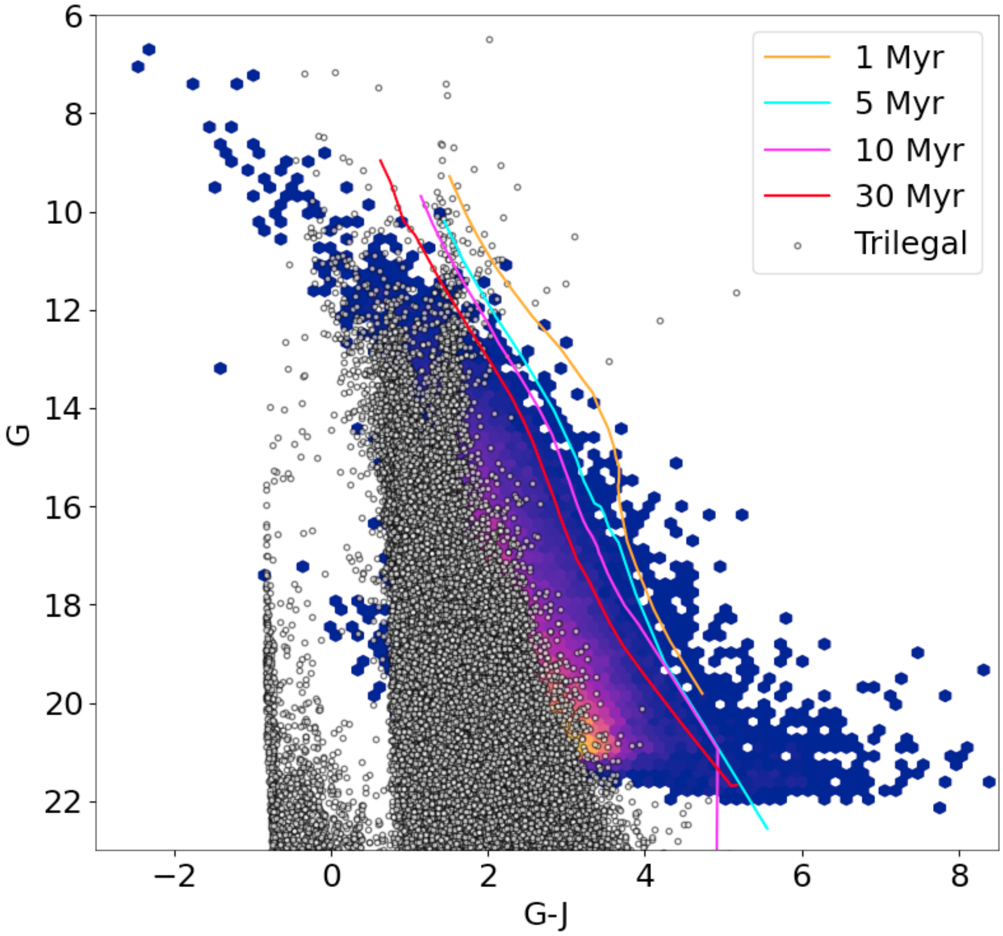

Figure 4.3 *G-J vs G colour-magnitude diagram demonstrating the location of a representative field model compared to the Taurus cluster population. Trilegal field model plotted as white points, CFHT Taurus catalogue plotted as coloured hexbin distribution. Also shown are four isochrones from Baraffe et al. (2015): 1 Myr, 5 Myr, 10 Myr and 30 Myr.*

saturation. This is not an issue for Gaia G-band, which has a saturation limit around 6 mag, far brighter than the magnitudes considered here. However, for the ground-based, infrared CFHT J-band, the saturation limit must be considered. In Biller et al. (in prep), the limit in J-band for a meaningful detection in our Taurus catalogue is found to be approximately $J = 13 - 14$. Removing all objects brighter than this limit would severely deplete the cluster sample. As a result, I instead check the brightness of every object in J, and if it is brighter than $J = 14$, I cross-match with the Two Micron All Sky Survey (2MASS; Skrutskie et al., 2006) to obtain a non-saturated J-band detection.

In Figure 4.3, I show four different isochrones: 1 Myr, 5 Myr, 10 Myr and 30 Myr (Baraffe et al., 2015). All four are clearly distinct from the model of field objects for magnitudes fainter than $G = 14$. As will be discussed further in Section 4.4.3.4, the age limit I will consider for Taurus members in this work is 10 Myr (Krolikowski et al., 2021). Consequently, I use the 10 Myr isochrone to define the edge of the 'cluster region' (the area of parameter space likely to contain primarily Taurus members). This region is bounded by $G = 14$ mag, $G - J = 10$ and the 10 Myr isochrone. In addition to the requirements imposed on the G and J magnitudes, I use the unique information provided by the W-band survey to further 'clean' the sample. After removing contaminants from the catalogue using G and J, I considered the reddening-sensitive index, Q, of the remaining detections. Q is calculated by combining J, H and W photometry, as detailed in Equation 2.1 (Chapter 2). From previous W-band studies (see e.g. Jose et al., 2020; Dubber et al., 2021), we know that extremely negative values of Q are unphysical, and are caused by large photometric uncertainties. Similarly, we expect the error on Q for clean detection to be $Q_{\mathrm{ERR}} \leq 0.1$. The magnitude limit of $G = 14$ corresponds to ≈ 0.5 $\mathrm{M}_{\odot}$ in Taurus (assuming no extinction). Through the W-band survey, we have mapped the Q-index to stellar mass, and found that detections with $Q > 1.0$ are highly likely to be stars with masses > 0.5 $\mathrm{M}_{\odot}$. Thus, if detections with $Q > 1.0$ are present in our isolated cluster sample, they are likely to be caused by spurious photometry, and I remove them from the sample. Figure 4.4 shows J vs Q index for the full W-band Taurus data, the sample of objects that are selected as they meet the selection criteria applied to Q and Q_{ERR}, and the final population identified as likely Taurus members

To summarise, to be selected as part of the isolated cluster population, a detection must have: $G > 14$, $G - J = 10$, $-3.0 < Q < 1.0$ and $Q_{\mathrm{ERR}} \leq 0.1$, and be located

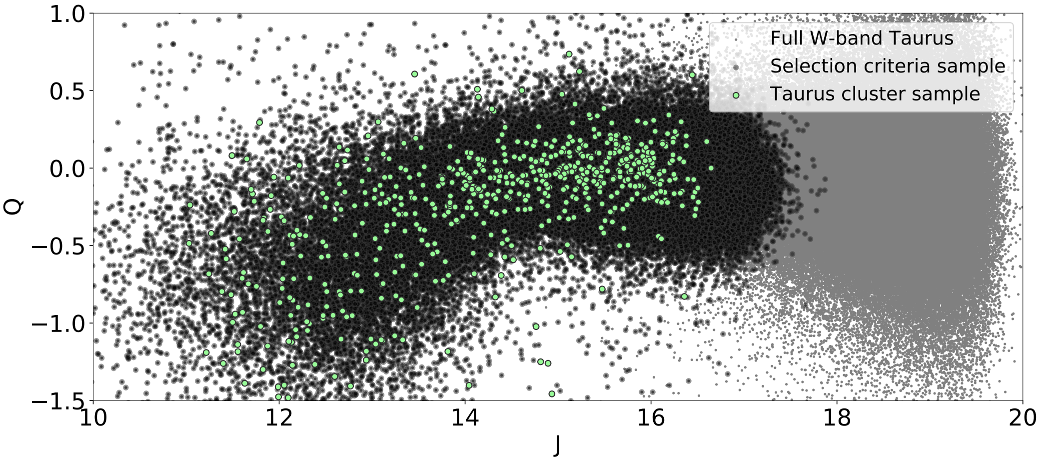

Figure 4.4 *Q-index vs J-band magnitude for various samples from the 2017 W-band Taurus catalogue. Grey (small) points show all sources in the catalogue, 324,729 in total. Black points show all sources that meet the Q-index selection criteria described in Section 4.4.1.3, 92,459 in total. Green points show sources included in the Taurus cluster sample (using limits of G = 15 and age ≤10 Myr), 651 in total.*

to the right of the 10 Myr isochrone. Figure 4.5 shows the resulting population of objects from the cross-matched catalogue that lie within the cluster region and satisfy the Q-index criteria. Also shown are Taurus members from a recent compilation published by Esplin & Luhman (2019). This population suggests that the cluster region defined is a reasonable approximation, as the vast majority of these detected Taurus members lie within it. A full comparison between the isolated cluster population and the Esplin & Luhman (2019) sample would not be particularly meaningful, as due to the necessary restriction of the W-band sample to data taken in 2017, there is only a small amount of overlap between the observed fields.

4.4.2 Choice of IMF

In this work, I consider two parameterisations of the IMF (as discussed in Section 4.1): a broken power law (BPL) and a log-normal power law (LN). Specifically, I will compare to the results found by Kroupa (2001) and Chabrier (2003), two of the most-used investigations of these functional forms.

When using the BPL IMF model, there are three indices that are sampled and

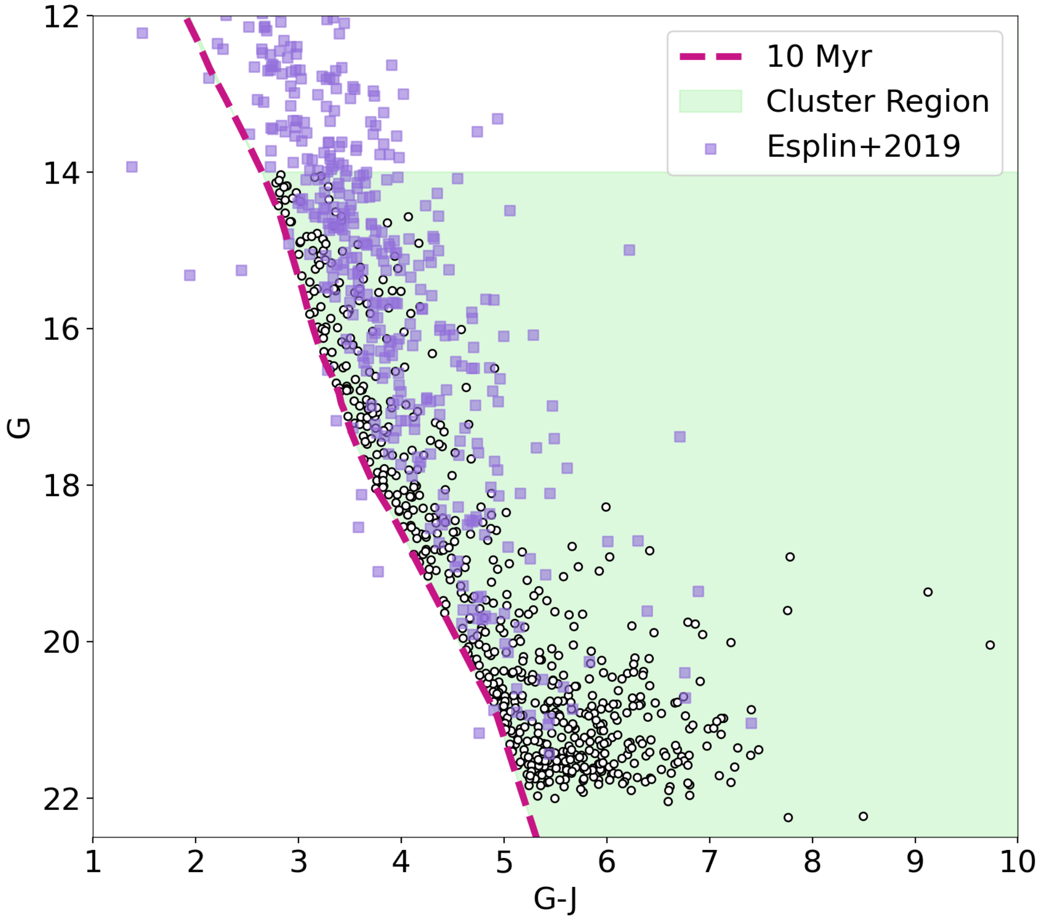

Figure 4.5 *$G - J$ vs G colour-magnitude diagram for the isolated objects that are likely to be Taurus members. The pink squares show a recent compilation of confirmed Taurus members from Esplin & Luhman (2019). The pink dashed line shows the 10 Myr isochrone from Baraffe et al. (2015). Green highlight identifies the area defined as the 'cluster region', which will be used in the MCMC modelling. For objects with $J < 14$, 2MASS J magnitudes are used instead of the likely-saturated CFHT measurements.*

optimised by a model designed to find a best-fit IMF, α_0, α_1 and α_2:

$$
\begin{aligned}
p(m|\alpha_0, \alpha_1, \alpha_2, m_{0,1}, m_{0,2}) \; &\propto m^{\alpha_2},\ m \geq m_{12} \\
&\quad k_{12}\, m^{\alpha_1},\ m_{01} \leq m < m_{12} \\
&\quad k_{01}\, m^{\alpha_0},\ m < m_{01} \\
\text{where :}& \\
&\quad k_{12} = m_{12}^{\alpha_2\,-\,\alpha_1} \\
&\quad k_{01} = k_{12}\, m_{01}^{\alpha_1\,-\,\alpha_0}
\end{aligned}
\tag{4.1}
$$

Each α describes the slope of one of the broken segments. There are two additional parameters, m_{01} and m_{12}: these describe the transition masses between each of the segments of the curve (in solar masses). In order to simplify the model, and keep the required computational time to a minimum, I do not fit for m_{01} and m_{12}, and instead assume them to be consistent with the values predicted by Kroupa (2001): m_{01} = 0.08 M$_\odot$ and m_{12} = 0.5 M$_\odot$. For reference, the values predicted by Kroupa (2001) for each of the slope parameters are: α_0 = -0.3,α_1 = -1.3 and α_2 = -2.3.

The LN IMF model has four fittable parameters, two of which I will sample and optimise in my model, m_c and σ:

$$
\begin{aligned}
p(m|m_c, \sigma, m_H, \alpha_H) \; &\propto m^{\alpha_H},\ m > m_H \\
&\quad k\frac{1}{m}e^{0.5\,\frac{log(m)-log(m_c)}{\sigma}^{2}},\ m < m_H \\
\text{where:}& \\
&\quad k = m_H^{\alpha_H+1}e^{0.5\,\frac{log(m_H)-log(m_c)}{\sigma}^{2}}
\end{aligned}
\tag{4.2}
$$

m_c is the characteristic mass (in solar masses), which is the peak in logarithmic space. σ is the width of the log-normal function. In equation 4.2, m_H and α_H are parameters related to the high-mass regime, which is described using a broken power: where m_H is the transition mass to this regime, and α_H is the power law slope. I do not fit for the high-mass parameters, and instead fix them to the values predicted by Chabrier (2003): m_H = 1.0 M$_\odot$ and $\alpha_H = -2.35$. This is done because none of the objects that I will generate in my model populations will have masses > 1.0 M$_\odot$, due to the upper limit of $G = 14$. For reference, the

Chabrier (2003) system IMF predicts values of $m_c = 0.22$ and $\sigma = 0.57$.

4.4.3 Using a Markov Chain Monte Carlo model

In order to quantify the best-fit IMF parameters for the Taurus cluster population, it is necessary to explore the full parameter space and the 'goodness of fit' between a modelled population and the observed cluster data. To do this, I perform a Markov Chain Monte Carlo (MCMC) parameter estimation, using `emcee` (Foreman-Mackey et al., 2013). The procedure followed at each step in the process is as follows:

1. Read in data table of likely cluster members (identified by their CMD positions) from the Gaia-crossmatched Taurus W-band catalogue.
2. Using the emcee IMF parameters, generate a BPL or LN IMF, and pick N model objects.
3. Using a reddening map of Taurus, assign each object a randomly-drawn extinction.
4. Similarly, assign each object a random distance, based on a distance distribution of Taurus members.
5. Generate synthetic $G-$ and $J-$band photometry for each object using isochrones from Baraffe et al. (2015).
6. Calculate a random error to add to each magnitude, to emulate the real spread in the catalogue data.
7. Adjust the total model population for completeness, using the measured Gaia completeness function.
8. Generate histograms of Gaia G-mag for both the real cluster data and the model population.
9. Calculate the log likelihood of the model compared with the data, using Poisson statistics.
10. Cycle the emcee until convergence is reached.

4.4.3.1 Populating the model from the IMF

If working with the BPL functional form, the MCMC is initialised with the power law parameter values predicted by Kroupa (2001): α_0 = -0.3, α_1 = -1.3 and α_2 = -2.3. I set up an initial bubble such that a small range around these initial values is sampled. Subsequently, at each step of the MCMC chain, new values are sampled for each of the three α parameters. Using these values, an IMF is constructed and the probabilities of a grid of masses is stored. I then sample randomly from this mass grid to populate a model cluster of N objects, where $\mathrm{N_{objects}}$ is a fitted parameter in the MCMC.

I use a similar process when modelling a LN IMF. The MCMC is initialised with $m_c = 0.22$ and $\sigma = 0.57$, the values predicted by Chabrier (2003) for their system IMF, which accounts for the existence of binary systems. Again, new values are sampled for both parameters at each step of the MCMC chain, and an IMF is constructed using the LN parameterisation. A model population of N objects with masses sampled from this IMF is stored.

4.4.3.2 Reddening map of Taurus

Having generated a population of objects with masses informed by the IMF, I next produce additional physical parameters of each cluster member. In order to compute synthetic magnitudes, one must consider the dust extinction that objects in the Taurus cluster would experience. To do so, I make use of the Galactic extinction maps created by Dobashi (2011). Using the extinction map based on the 2MASS Point Source Catalogue, I queried a region of sky matching our photometric observations of the Taurus Cloud (centred on RA = 68.7° and Dec = 23.2°). This returns a value of extinction for a grid of points on sky. Figure 4.1 demonstrates that the fields observed during the CFHT campaign do not uniformly cover this area, and instead focus on regions of Taurus where many members have previously been discovered. As a result, we extract an extinction distribution from a zoomed map of just the central core of Taurus (centred on RA = 69.8° and Dec = 27.8°).

The upper panel of Figure 4.6 shows a histogram of the resulting extinction distribution of the Taurus core, based on the 2MASS Point Source Catalogue.

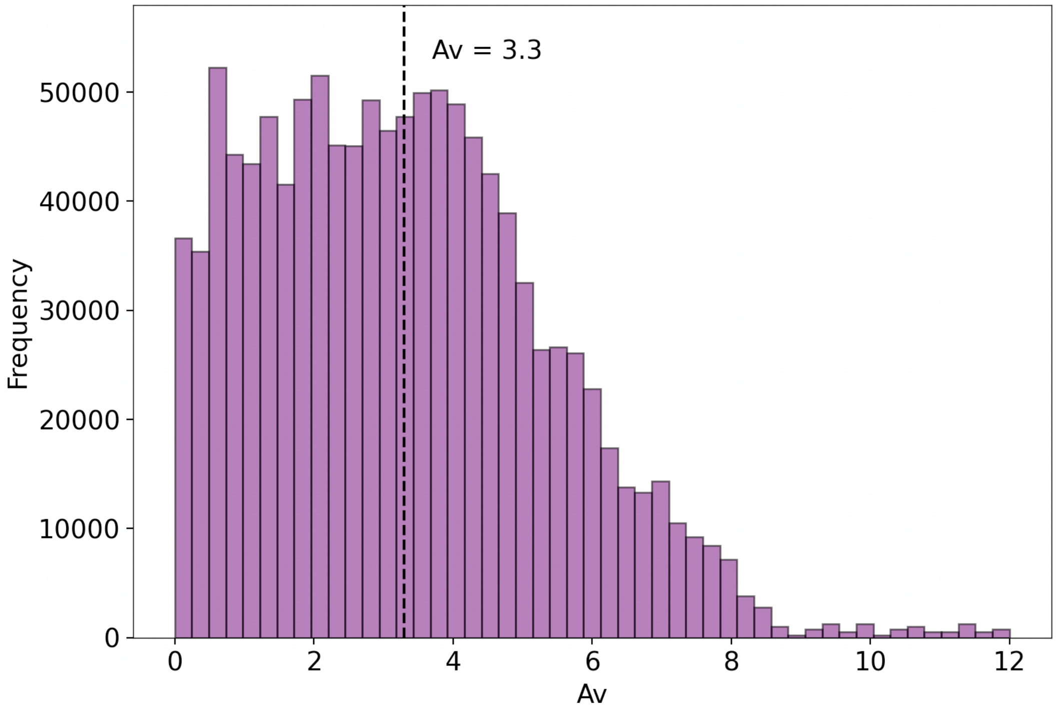

Figure 4.6 *A_V distribution for Taurus from Dobashi (2011), with mean value indicated by dashed line*

Generally, objects in the centre of Taurus cloud will experience somewhat low visual extinction, with an mean value of $A_{\rm V} = 3.3$, but higher visual extinction values are also common, up to a maximum of $A_{\rm V} = 11.9$.

Each randomly generated model object created in Section 4.4.3.1 is assigned a random visual extinction, using the distribution shown in Figure 4.6. It is converted into a probability distribution, and then used to make a random weighted choice of extinction values. Consequently, the resulting distribution of model extinctions should resemble those predicted by Dobashi (2011) for the Taurus cluster.

4.4.3.3 Distances

In order to encapsulate the 3D structure of the Taurus cloud, I assign each model object a randomly generated distance. The distribution of distances that is sampled is informed by various recent works that have mapped the structure of Taurus. Roccatagliata et al. (2020) use Gaia DR2 (Gaia Collaboration et al.,

2018) and the Taurus membership catalogue presented by Esplin & Luhman (2019), to define six distinct populations within the Taurus cloud. Each have distinct parallaxes and proper motions, allowing for individual estimations of distance. Roccatagliata et al. (2020) find that the best-fit distances for these groups range from 130–160 pc. When comparing this result to previous studies of Taurus subgroups by Galli et al. (2019) and Luhman et al. (2018), they find some agreement between the groups defined in each case, and good agreement for the approximate depth of the cloud.

Based on these analyses, I adopt a distance range of 130–160 pc for the modelled population. I assume a uniform distribution within this range, and randomly sample a distance for each of model object.

4.4.3.4 Photometry from Isochrones

After assigning random distances and extinctions to every model cluster member, I use these parameters and the object masses to generate synthetic photometry in $G-$ and $J-$bands.

The results of Krolikowski et al. (2021) indicate that Taurus is comprised of multiple subgroups, with varying ages. They conclude that the star-formation history of the region is complicated, with ‘at least two epochs of star-formation’ having occurred. As the full star-formation history of Taurus remains relatively unconstrained, I have used the spread in ages of the subgroups described in Krolikowski et al. (2021) to inform the ages of my model cluster population. Figure 12 of Krolikowski et al. (2021) shows the posterior age distributions of 15 Taurus subgroups. From this Figure, I can infer that using a range of ages from 1–10 Myr, assuming a constant star-formation history (SFH) in this range, should encompass the variation seen in the cluster. Consequently, I used the Baraffe et al. (2015) isochrones covering 1–10 Myr to generate synthetic photometry for a cluster population. These isochrones provide both Gaia and CFHT synthetic photometry[3].

For each model object, I manipulate the isochrones using the objects extinction and distance determined above. I then randomly choose one of isochrone

---

[3] http://perso.ens-lyon.fr/isabelle.baraffe/, accessed Nov 21

(assigning this age to the model object) and interpolate it to match the mass grid used when sampling from the IMF. I can then store the extincted, Taurus-distance G magnitude that corresponds to the mass of the object. This results in a population of model cluster objects, simulated to be as similar as possible to Taurus.

4.4.3.5 Modelling the errors

Until now, I have introduced variation in magnitudes only through quantifiable parameters such as distance and visual extinction. We must also consider the typical errors that the magnitudes in our observed catalogue have, and adjust our model population to reproduce a level of scatter similar to the data.

I considered the distribution of errors of the Taurus cluster data, in magnitude bins of unitary width, between $G = 15 - 23$. The distribution of errors is very similar for all bins less than $\approx G = 18$, but has a larger spread and a higher median value for magnitudes fainter than this. I stored the distributions corresponding to each unitary bin, and used these when generating my model population. For each object, I randomly sampled the error distribution corresponding to the magnitude bin that it fell within, and thus stored a random error suitable for an object of that brightness.

4.4.3.6 Completeness

The size of the model sample is the third parameter of the MCMC simulation. We can estimate this based on the number of targets in the catalogue that describes the Taurus cluster, but the real number of objects needed to replicate this population is an unknown. Photometric surveys are typically complete to specific magnitudes in each bandpass. In section 4.3, I presented the completeness limits of the 3 filters used for CFHT W-band observations: $J = 18.2$, $H = 17.6$ and $W = 17.8$. Qualitatively, this indicates that it is unlikely I am missing any objects that are brighter than these magnitudes, but will only detect a certain fraction of objects that are fainter, with this fraction decreasing as the magnitude increases. The same is true of the Gaia mission. Boubert & Everall (2020) have performed an extensive analysis of Gaia DR2 completeness. For simplicity, I assume that eDR3 achieves at least this level, and use the same models. The authors present a python package `selectionfunctions` that allows for easy access to their selection functions, which can be used to quantify completeness.

I used `selectionfunctions` to estimate the completeness of the Gaia G-band for the Taurus star-forming region. I created a grid of coordinates covering our survey area, and a list of G-mags covering the full magnitude range detected in the Taurus cluster catalogue. For each magnitude, I used `selectionfunctions` to query the probability of selection of an object of that magnitude to be detected at each point in the coordinate grid. I then took the mean value of this list, and stored it as the completeness at G-band in Taurus for an object of this magnitude. After iterating over all magnitudes, this gave a completeness function showing the probability of detection for the full range of G-band magnitudes in Taurus. This remains at essentially 100% for $G > 20.5$, and then drops steeply to ~ 0 for objects fainter than $G = 21.5$.

In the MCMC simulation, this completeness curve is used to reduce the model population to a size comparable to the real catalogue, by considering which model objects would actually be detected. After adjusting for completeness, I am left with the final model population.

4.4.3.7 Likelihood

After generating a model cluster population, the final step is to determine how well the model fits the cluster data. To do so, I make use of the luminosity function in $G-$band. I generate a 1-D histogram of magnitudes for both the model and the data. I initially considered a 2-D approach, but established that there are not enough objects in the cluster catalogue to fully sample a colour-magnitude diagram. Similarly, the size of my cluster population dictates how I compare the two histograms. Typically, the chi-squared statistic is used to compare the model to the data in an MCMC model. This uses Gaussian statistics, which requires a sufficiently large sample. In theory, the cluster population of ≈ 500 objects should be sufficient for this statistical approach. However, as I am using histogram distributions as the comparison metric, the number of objects in each bin is the quantity being compared between the model and the data. In this case, I often deal with low counts in some of the $G-$band bins (particularly at the extremes of the magnitude range), meaning Gaussian statistics are no longer suitable.

Instead, I make use of Poisson statistics. I calculate the likelihood of the model compared to the data using the following equation:

$$L(n_{\mathrm{obs}}|\theta) \propto \prod_{j=1}^{N} e^{-n_{\mathrm{mod}}} \frac{1}{n_{\mathrm{obs}}!} n_{\mathrm{mod}}^{n_{\mathrm{obs}}} \tag{4.3}$$

where θ describes the full set of fitting parameters in the MCMC model, n_{obs} is the bin count of the G mag histogram of observed cluster data, n_{mod} is the bin count of the G mag histogram of the model data, and N is the number of bins.

The MCMC chains will move to a new combination of IMF parameters based on the logarithm of this likelihood value, and will ultimately converge on the combination of parameter values that minimise the log likelihood.

4.5 Results

In this section I present posterior probability distributions and optimised parameters for MCMC runs using both the BPL and LN IMF parameterisations.

The models adopted per run vary in two ways: the star-formation history that is used, and the limiting magnitude in G-band. As discussed in Section 4.4.3.4, I based my modelling of the age of the Taurus population on work presented by Krolikowski et al. (2021). When describing the method used to isolate the likely cluster members in Section 4.4.1.3, I used an age of 10 Myr to limit the population. Consequently, one of the star-formation histories that I will assume when modelling is a constant period of formation from 1–10 Myr. However, Figure 12 of Krolikowski et al. (2021) also shows that for subgroups with ages $\gtrapprox$ 5 Myr, the age is significantly less constrained. As a result, I included another possible star-formation history when modelling: a period of constant formation from 1–5 Myr, that better reflects the most constrained ages for Taurus subgroups.

The second variation between models is the limiting G-band magnitude. In Section 4.4.1.3, I showed that it is necessary to limit the cluster population to $G > 14$ mag, because of contamination by the field population at brighter magnitudes. However, in doing this, I have removed a large chunk of the population described by the third power law parameter of the BPL IMF, α_2: i.e. objects with $m \geq 0.5$ $M_{\odot}$. As a result, the best-fit values for this parameter may not be reliable. Therefore, I also implemented a limiting magnitude of $G = 15$, enabling a model of the BPL IMF with only two power law components, α_0 and α_1.

Due to two options for both star-formation history and limiting magnitude, I used four separate MCMC runs to investigate the BPL IMF. For the LN IMF, the population is described by a continuous function up to 1 $M_{\odot}$, and I do not include any objects this massive in my model populations. As a result, I only consider a limiting magnitude of $G = 14$ for the LN parameterisation, and star-formation histories of 1–5 and 1–10 Myr, two MCMC runs in total. For each MCMC run, a burn-in stage of 1,500 steps was used (discussed further in Section 4.5.2.3), and convergence was judged by examining the log likelihood chains.

4.5.1 Removal of contaminant objects

A core assumption of the results presented in this Section is that the W-band Taurus cluster sample is a 'pure' sample, containing minimal background contaminants. To check the extent of remaining contamination and clean each Taurus cluster sample as effectively as possible, I applied a parallax and proper motion cut prior to MCMC modelling, using lower and upper bounds of: 5.5 and 8.5 for parallax, 0 and 16 for RA proper motion, and -5 and -30 for Dec proper motion (typical ranges for Taurus members, taken from Roccatagliata et al., 2020). After applying a parallax cut to the 10 Myr, $G = 14$ limited sample, for example, the number of sources retained is reduced from 651 to 587. Additionally applying the proper motion cut reduces the total number of sources in this likely Taurus member sample to 569. Whilst this is a reasonably small reduction, it is also a non-negligible fraction of likely contaminant sources and thus a crucial step, as these non-Taurus members would have effected the accuracy of my IMF analysis.

Table 4.1 *Best-fit results for the BPL models, run with varying star-formation histories and limiting magnitudes*

SFH	Limiting Magnitude	α_0	α_1	α_2	N_{objects}
1–5 Myr	$G = 15$	$0.558^{+0.177}_{-0.066}$	$1.510^{+0.308}_{-0.288}$	-	604^{+170}_{-125}
	$G = 14$	$0.772^{+0.163}_{-0.195}$	$1.600^{+0.348}_{-0.279}$	$2.526^{+0.432}_{-0.452}$	849^{+187}_{-186}
1–10 Myr	$G = 15$	$0.223^{+0.095}_{-0.040}$	$1.492^{+0.234}_{-0.219}$	-	603^{+157}_{97}
	$G = 14$	$0.528^{+0.11}_{-0.053}$	$1.547^{+0.348}_{-0.259}$	$2.519^{+0.453}_{-0.395}$	801^{+170}_{-138}

4.5.2 BPL IMF

I impose minimal priors on the IMF parameters used for the broken power law fit. I require that $\alpha_0 < \alpha_1$ and $\alpha_1 < \alpha_2$, to ensure that the slope becomes more positive/shallower for lower-mass intervals. I also limit the maximum number of objects included in the model, $N_{\text{objects}} < 1500$. This is implemented to avoid the generation of very large population models that have far more members than the sample cluster population, which would be an unnecessary use of computational power. For each run detailed in Table 4.1, I used 500 walkers and 20,000 steps in the MCMC, having established that this was sufficient to achieve convergence in all of the chains. Table 4.1 details the resulting best-fit values for each fitting parameter, for each model run.

4.5.2.1 1–5 Myr, 2-component BPL

First, I consider a constant star-formation history from 1–5 Myr, and a limiting G-band magnitude of 15, resulting in a 2-component broken power law IMF. The posterior distributions for the three MCMC fit parameters are shown in the upper panel of Figure 4.7. It is clear from these distributions this model produces a reasonable fit to the data, with clearly peaked, symmetrical distributions of N_{objects}, α_0 and α_1. The best-fit values for the power law parameters are $\alpha_0 = 0.558^{+0.177}_{-0.066}$ and $\alpha_1 = 1.51^{+0.308}_{-0.288}$, with errors calculated using the 16th, 50th and 84th percentiles of the marginalised posterior distributions (values indicated by dashed lines in the 1D histograms).

The MCMC model favours a population with a total of $N_{\text{objects}} = 604^{+170}_{-125}$, more than the 441 included in the Taurus cluster population for this limiting age and magnitude. This overestimation when comparing the catalogue size to the 'true' number of objects is expected, as a many of these model objects are removed when considering completeness and synthetic errors. In the bottom panels of Figure 4.7, I compare the observed data to the best-fit model population in colour-magnitude space, and show the best-fit IMF. The left panel indicates that the cluster population is reasonably well reproduced, except for both very bright and very faint objects - the model under-predicts the numbers of objects at these extremes. The constraints on the low-mass power law index are indicated by the shaded region in the lower right panel of 4.7 - with the upper limit predicting ~ 6 times as many objects as the lower limit, an indication that the low-mass fit could be improved.

4.5.2.2 1–5 Myr, 3-component BPL

The results for a model including objects with $14 < G < 15$ in the MCMC fit, again with a 1–5 Myr SFH, are shown in Figure 4.8. The model converges to a well-defined solution for the higher-mass power law components α_1 and α_2, but is insufficient when attempting to replicate the distribution of the lowest mass objects, with the posterior tending to much higher power law values that those determined by Kroupa (2001). The best-fit values for the power law parameters are $\alpha_0 = 0.772^{+0.163}_{-0.195}$, $\alpha_1 = 1.600^{+0.348}_{-0.279}$ and $\alpha_2 = 2.526^{+0.432}_{-0.452}$, with $N_{\text{objects}} = 849^{+187}_{-186}$. From the lower left panel of Figure 4.8, we can see that the model-generated young population does not provide a good by-eye fit to the Taurus data, particularly for the brightest magnitudes, and is found to have a much lower likelihood than the $G = 15$ limited case (shown in the legend of the lower left panel of each Figure in this Section).

4.5.2.3 1–10 Myr, 2-component BPL

Next, I consider instead a constant star-formation history from 1–10 Myr. Figure 4.9 shows the results when considering a 1–10 Myr SFH with a limiting magnitude of $G = 15$ (a 2-component BPL). The posterior distributions for all parameters show clear best-fit solutions, with well-defined sharp peaks. The best-fit values are $\alpha_0 = 0.223^{+0.096}_{-0.040}$, $\alpha_1 = 1.492^{+0.234}_{-0.219}$, and $N_{\text{objects}} = 603^{+157}_{-97}$. These power law

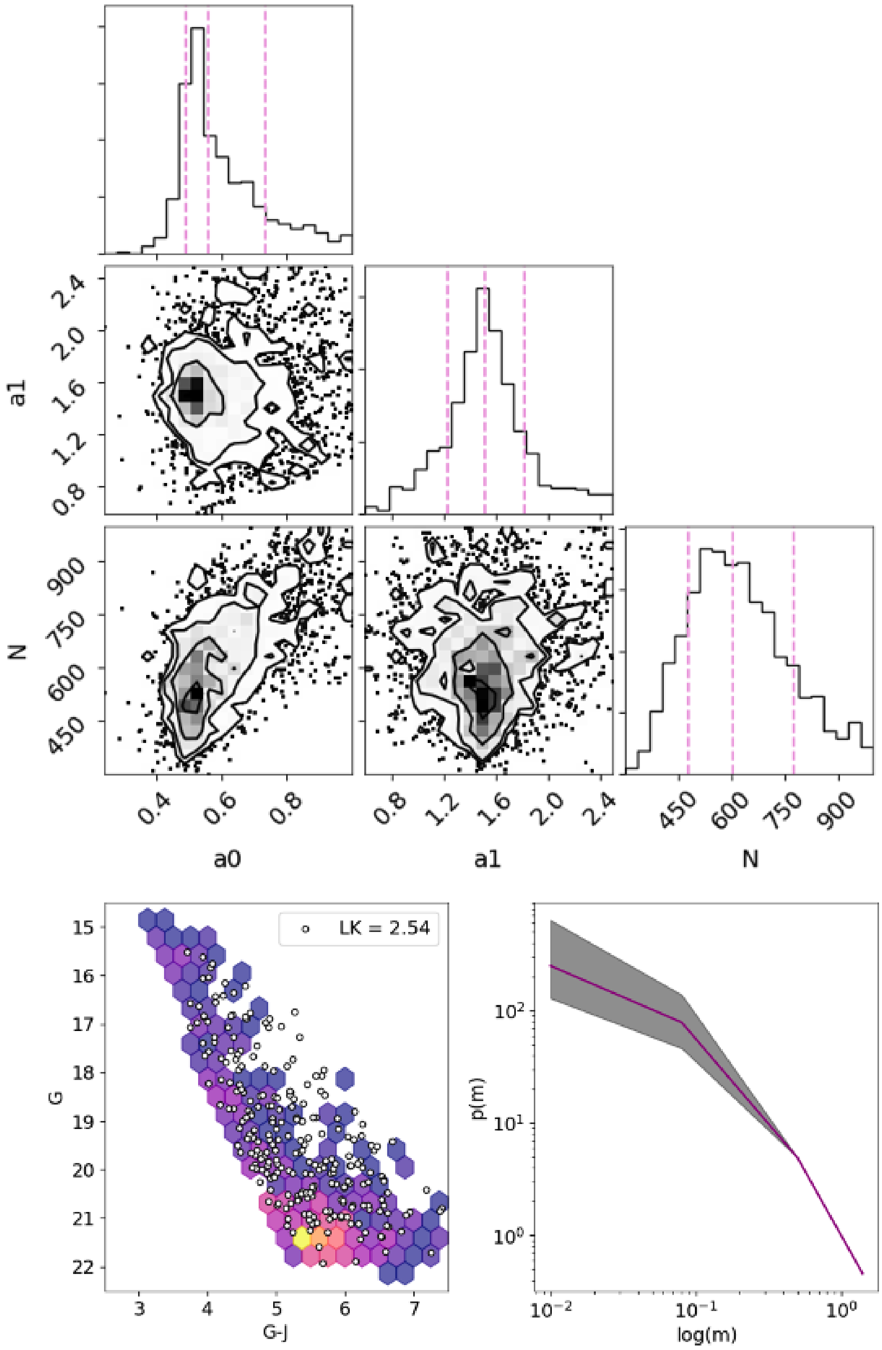

Figure 4.7 *Top: Posterior distributions of the MCMC fit parameters for the broken power law IMF. 1–5 Myr star-formation history was used, with a limiting magnitude of G = 15 mag. Bottom: G-J vs G colour magnitude diagram (left), comparing Taurus data (hexbin) to the best-fit model population (white points). Right: the best-fit IMF found by the 1–5 Myr, 2-component BPL fit, with 1σ errors indicated by the shaded region.*

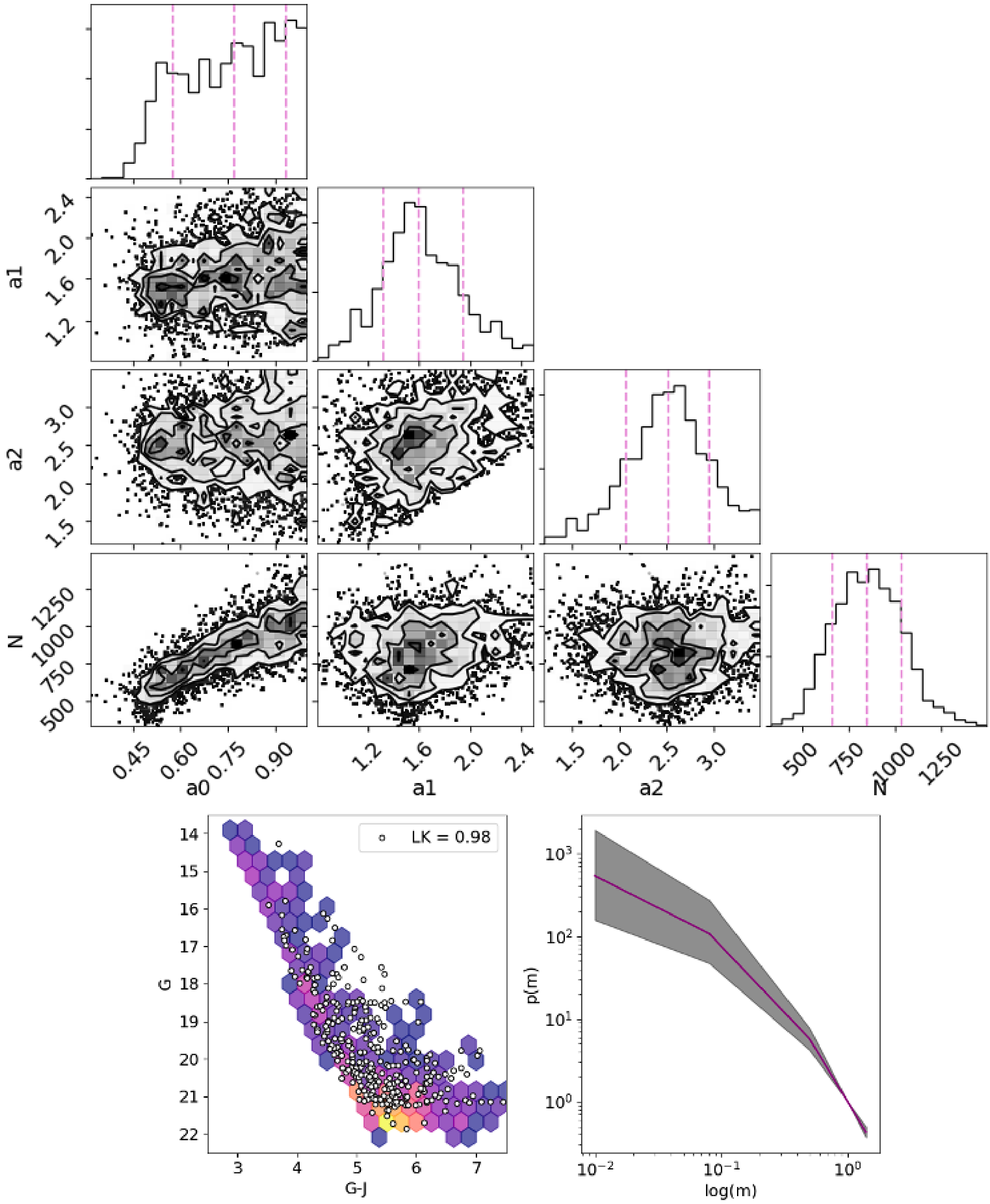

Figure 4.8 *Top: Posterior distributions of the MCMC fit parameters for the broken power law IMF. 1–5 Myr star-formation history was used, with a limiting magnitude of G = 14 mag. Bottom: G-J vs G colour magnitude diagram (left), comparing Taurus data (hexbin) to the best-fit model population (white points). Right: the best-fit IMF found by the 1–5 Myr, 3-component BPL fit, with 1σ errors indicated by the shaded region.*

index values are close to those predicted by Kroupa (2001) - implying that I may not be effectively correcting for the bias introduced by the values used for the small initial bubble (a process known as 'removing the burn-in'). I removed varying numbers of initial steps from the chains to investigate the length of the burn in, and found minimal changes in the final best-fit parameter values by varying this amount from 500-3000 steps. This implies that the burn-in has been effectively removed, and these best-fit values are accurate for this dataset and model.

The lower left panel of Figure 4.9 again compares the model population to the observed Taurus cluster data, and the lower right shows the resulting IMF and uncertainty. Comparing these plots directly to Figure 4.7, the 1–5 Myr case, there are two noticeable improvements: firstly, the model distribution in colour-magnitude better replicates the observed cluster distribution at bright magnitudes. Secondly, the constraints on both the low- and intermediate-mass power law indices are significantly tighter than for the 1–5 Myr fit. Both factors suggest that a 1–10 Myr star-formation history could be more suitable assumption for the Taurus cluster. However, if we compare the likelihood values of each model fit, the 1–5 Myr SFH model is found to have a higher likelihood than the 1–10 Myr SFH model.

4.5.2.4 1–10 Myr, 3-component BPL

I also consider a BPL MCMC run that uses a constant SFH from 1–10 Myr, and a limiting magnitude of $G = 14$. The posterior distributions shown in Figure 4.10 for this run are significantly broader and messier than in the 1–10 Myr, $G = 15$ case. As discussed in Section 4.5, this is likely because the high-mass index describes a large range of masses and magnitudes (everything with $m > 0.5$ M$_{\odot}$), but the magnitude limit of $G = 14$ that I impose means that the value of this index is determined only by objects in the range $G = 14-15$. In other words, a fraction of the total objects described by this section of the IMF actually contribute to the fit. Despite this, the posterior distributions for all three power-law indices are reasonably well constrained, with values of $\alpha_0 = 0.528^{+0.11}_{-0.053}$, $\alpha_1 = 1.547^{+0.348}_{-0.259}$ and $\alpha_2 = 2.519^{+0.453}_{-0.395}$. The best-fit number of model objects is $N_{\rm objects} = 801^{+170}_{-138}$. From the lower right panel of Figure 4.10, it is clear that constraints for the power law parameters are worse when considering a limiting magnitude of $G = 14$ instead of

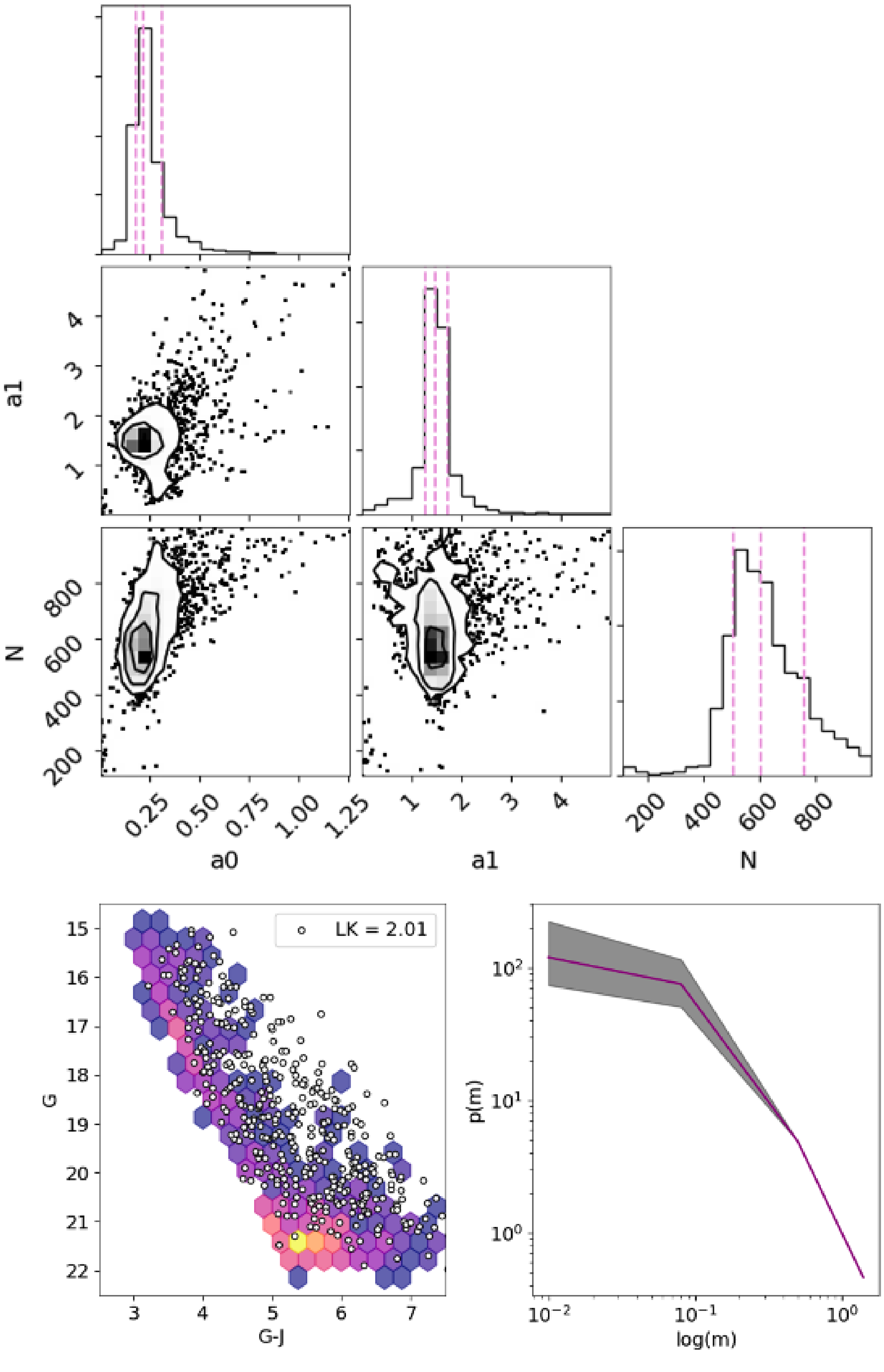

Figure 4.9 *Top: Posterior distributions of the MCMC fit parameters for the broken power law IMF. 1–10 Myr star-formation history was used, with a limiting magnitude of G = 15 mag. Bottom: G-J vs G colour magnitude diagram (left), comparing Taurus data (hexbin) to the best-fit model population (white points). Right: the best-fit IMF found by the 1–10 Myr, 2-component BPL fit, with 1σ errors indicated by the shaded region.*

Table 4.2 *Best-fit results for the LN models, run with varying star-formation histories.*

SFH	Limiting Magnitude	m_c	σ	N_{object}
1–5 Myr	$G = 14$	$0.078^{+0.046}_{-0.020}$	$0.702^{+0.123}_{-0.142}$	321^{+108}_{-76}
1–10 Myr	$G = 14$	$0.091^{+0.055}_{-0.031}$	$0.732^{+0.281}_{-0.182}$	501^{+130}_{-164}

$G = 15$, predicting a factor of ten difference in the number of low-mass objects, as informed by the upper and lower limits on the power law index.

4.5.3 LN IMF

The log-normal IMF function that I use for generating a model population has two variable parameters, m_c and σ, which are included as fitted parameters in the MCMC runs along with the true number of objects, N_{objects}. As with the BPL IMF runs, I avoid any tight priors, simply requiring that that $N_{\mathrm{objects}} < 1500$, to limit computation time, and that the IMF parameters are both > 0. Table 4.2 gives the best-fit values for each fitting parameter, for each model run using the LN IMF. For each run, I again used 500 walkers and 20,000 steps in the MCMC.

4.5.3.1 1–5 Myr

Figure 4.11 shows the MCMC results for the 1–5 Myr SFH, log-normal IMF run, as well as visualisations of the best-fit parameters. When initially discussing the Chabrier (2003) IMF in Section 4.4.3.1, I planned to start the MCMC run from the best-fit parameters found for their *system* IMF: a seemingly valid assumption as this IMF solution accounts for the presence of binaries in the sample. However, when running initial tests of the log-normal IMF, it became clear the the critical mass parameter, m_c, favoured smaller values more in agreement with the single object IMF presented by Chabrier (2003). Consequently, the initial bubble for the following MCMC runs was set up at $m_c = 0.079$ and $\sigma = 0.69$. Examining the results shown in Figure 4.11, it is clear that the log-normal IMF produces a reasonable model of the Taurus data. The best-fit parameter values are given in Table 4.2. The two IMF parameters have optimised values of $m_c = 0.078$ and $\sigma = 0.702$, concerningly close to the values found by Chabrier (2003). We

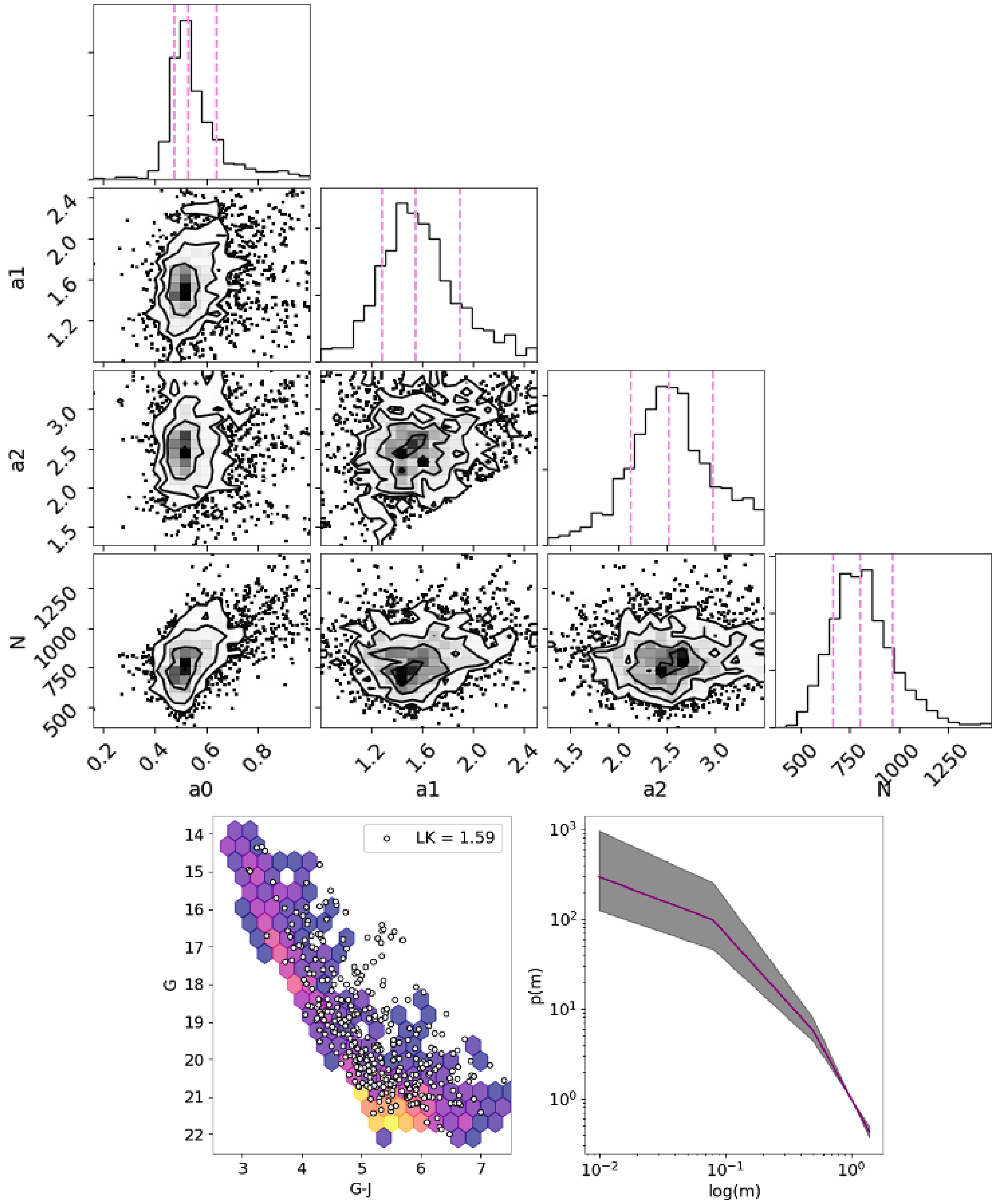

Figure 4.10 *Top: Posterior distributions of the MCMC fit parameters for the broken power law IMF. 1–10 Myr star-formation history was used, with a limiting magnitude of G = 14 mag. Bottom: G-J vs G colour magnitude diagram (left), comparing Taurus data (hexbin) to the best-fit model population (white points). Right: the best-fit IMF found by the 1–10 Myr, 3-component BPL fit, with 1σ errors indicated by the shaded region.*

performed the same tests described above for the 1–10 Myr, 2-component BPL fit, and confirmed that our optimised parameter results are not affected by the location of the initial bubble. The number of model objects in the best fit, $N_{\text{objects}} = 321$, is considerably lower than the known number of objects in the sample.

Considering the lower panels of Figure 4.11, we can see that the best-fit IMF does reasonably well at reproducing the observed Taurus data, but the low number of objects is clear. The resulting IMF shown in the right panel of Figure 4.11 predicts a factor of ∼5 difference in the number of low-mass objects, within the upper and lower limits, a similar level of constraint to the 1–5 Myr, 2-component BPL fit.

4.5.3.2 1–10 Myr

The final MCMC run combines a 1–10 Myr SHF with a log-normal IMF. The results for this are shown in Figure 4.12 and Table 4.2. The derived constraints on the IMF shown in the lower-right panel of Figure 4.12 are tight for the IMF parameters, but the distribution of N_{objects} is very broad. The best-fit parameter values are $m_c = 0.091^{+0.055}_{-0.031}$, $\sigma = 0.732^{+0.281}_{-0.182}$ and $N_{\text{objects}} = 501^{+130}_{-164}$. The likelihood values for both the 1–5 and 1–10 Myr LN models (see legends of Figures 4.11 and 4.12) are significantly lower than those found for the BPL fits, suggesting that this IMF parameterisation may be generally less well suited for modelling the Taurus IMF.

4.5.4 Additional Considerations

When considering the results presented above, it is clear that in some instances the models that I have developed do not provide a good fit to the data. This could be resolved with some additional extensions to the work, which are discussed further in Section 4.6, but is also likely due to some known issues with the above analysis. An assumption made in the models presented is that the sources in our Taurus cluster sample are single systems, without disks, and are not actively accreting. In reality, Taurus is a young region, meaning many of its members are likely disk-hosting, and could still be actively accreting. Additionally, we know

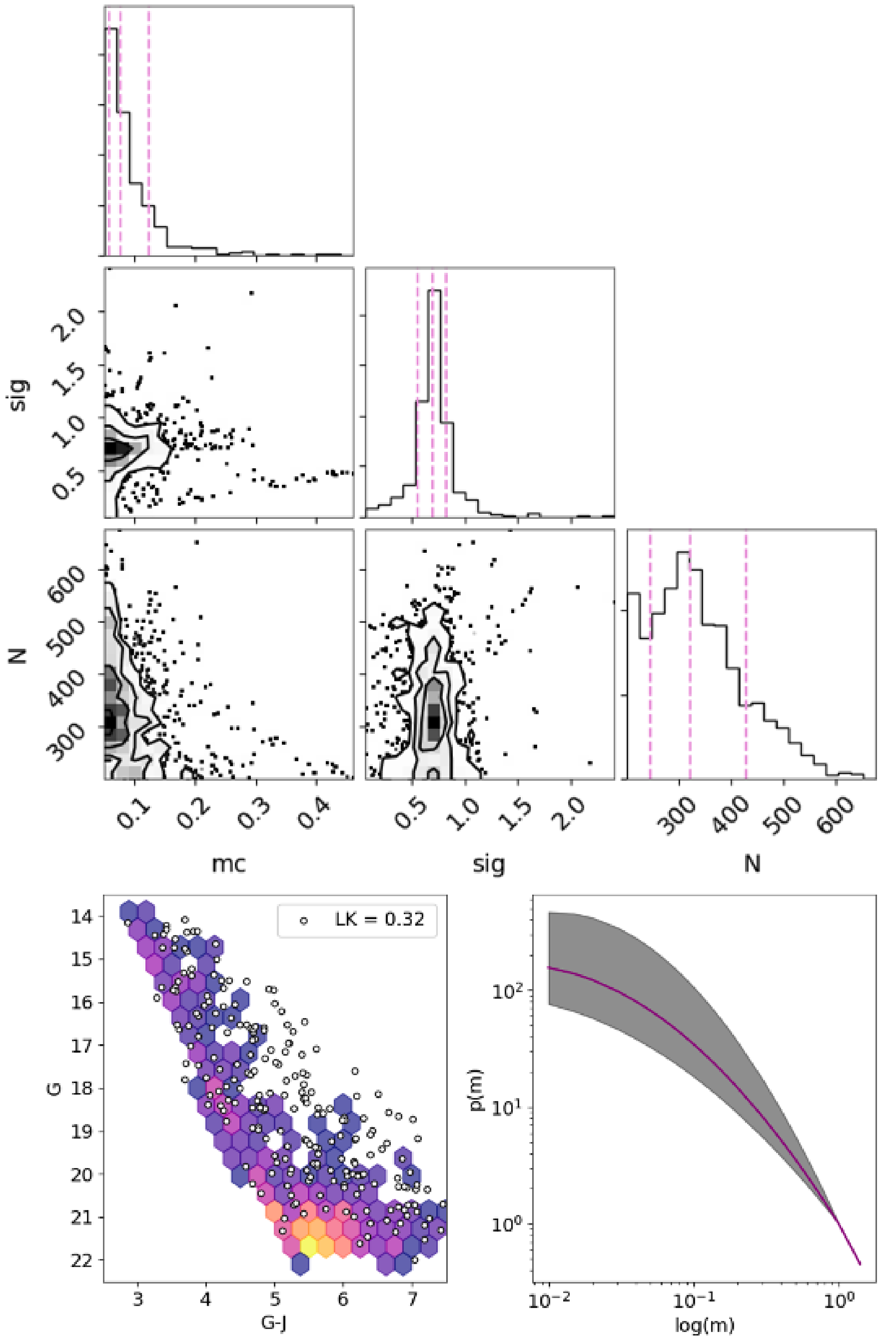

Figure 4.11 *Top: Posterior distributions of the MCMC fit parameters for the log-normal IMF. 1–5 Myr star-formation history was used, with a limiting magnitude of G = 14 mag. Bottom: G-J vs G colour magnitude diagram (left), comparing Taurus data (hexbin) to the best-fit model population (white points). Right: the best-fit IMF found by the 1–5 Myr, LN fit, with 1σ errors indicated by the shaded region.*

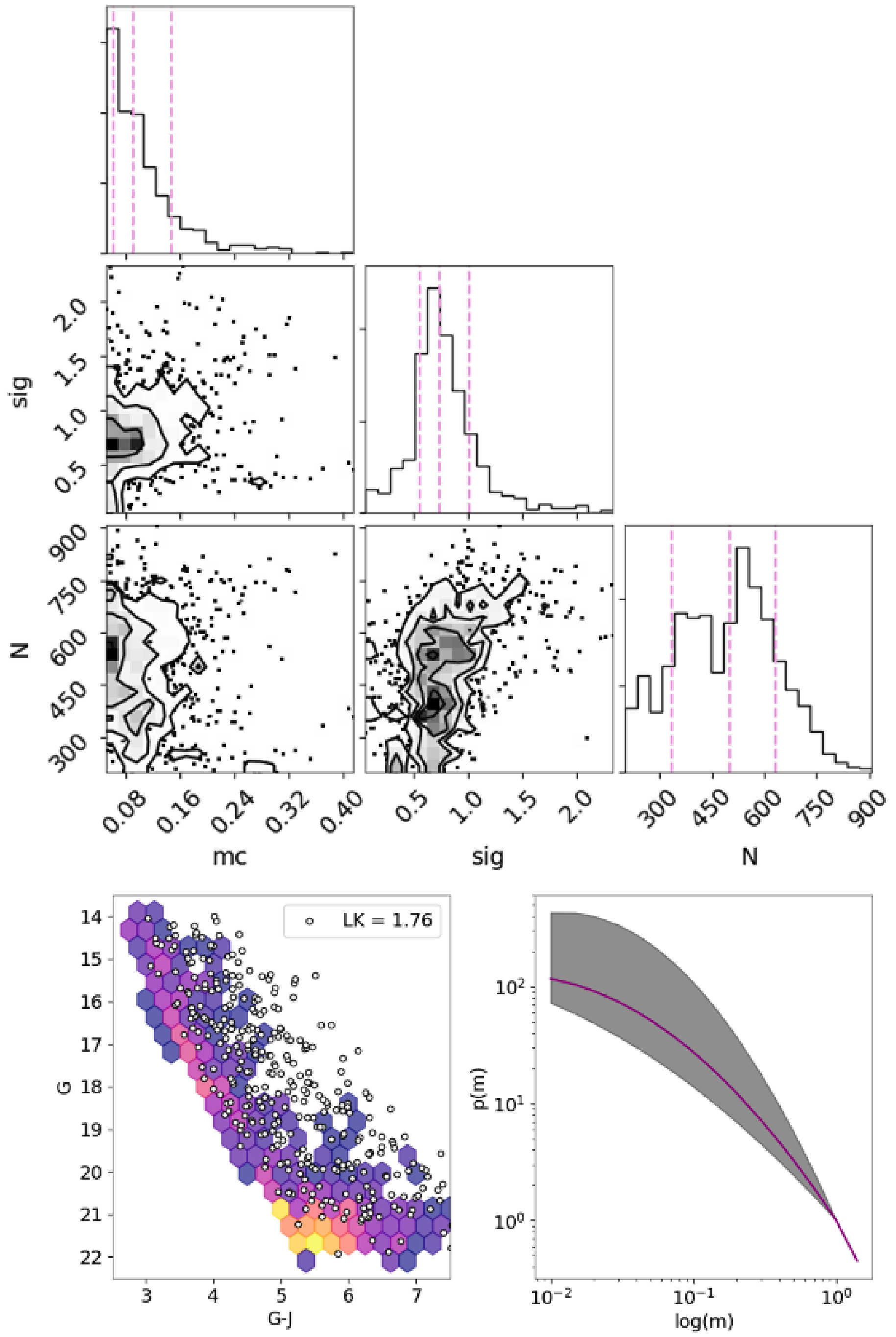

Figure 4.12 *Top: Posterior distributions of the MCMC fit parameters for the log-normal IMF. 1–10 Myr star-formation history was used, with a limiting magnitude of G = 14 mag. Bottom: G-J vs G colour magnitude diagram (left), comparing Taurus data (hexbin) to the best-fit model population (white points). Right: the best-fit IMF found by the 1–10 Myr, LN fit, with 1σ errors indicated by the shaded region.*

that binary systems are common, and will be present in our catalogue. Disk-hosting young stars display infrared excesses, which would affect their position on the $G - J$ vs G colour magnitude diagram, as would any ongoing accretion, which would impact the measured G-band magnitude. These possible characteristics of sources in our catalogue need to be factored into the IMF modelling, but will dramatically increase the complexity of the problem, and thus will be carefully considered in a future version.

4.6 Discussion

Firstly, the MCMC results discussed in Section 4.5 show a broken power law IMF generally produces slightly better best-fit model populations for the likely Taurus cluster data, specifically when limiting the population to objects with $G < 15$. Secondly, it is crucial to bear in mind the limitations of this analysis, including the lack of treatment of the phenomena discussed in the previous section, and the restriction of the data to only include fields observed in 2017. This results in incomplete spatial coverage of the Taurus cluster, meaning that there are known cluster members that are definitely not included in our sample.

Regardless, it is still possible to use the above results to draw conclusions about the ability of the MCMC tool presented in this work to model the IMF of Taurus and other young clusters. To compare the four BPL IMFs that can be constructed with each set of best-fit parameters, I have plotted each result in the left panel of Figure 4.13. Also plotted is the IMF reported by Kroupa (2001), with maximum and minimum parameter values indicated by the shaded region.

From Figure 4.13, we can see than none of the model runs strongly disagree with the Galactic IMF derived by Kroupa (2001). We can also compare the constraints on each of the final best-fits. The worst constrained IMF parameters are for the 1–5 Myr, 3-component BPL fit, with an upper limit that goes far beyond the possible range of Kroupa (2001) for the lowest masses. The other BPL IMFs have similar properties, the best-constrained being the 1–5 Myr and 1–10 Myr, 2-component BPL fits, with the 1–10 Myr case predicting very similar IMF parameters to Kroupa (2001), and having the overall best constrained power law indicies. This, and the fact that the 1–10 Myr 3-component fit performs significantly better than the 1–5 Myr 3-component case, could be taken as tentative support that including objects with ages up to 10 Myr is a necessary step for modelling Taurus data.

In the right panel of Figure 4.13, I show the best-fit log-normal IMFs, and compare them to the Chabrier (2003) IMFs for single stars and systems. The main result demonstrated by this Figure is both log-normal IMFs agree well with the Chabrier (2003) single functional form. Despite the investigation into the effect burn-in phase and initial bubble described above, the similarity in optimised parameter values between the Chabrier (2003) functional form and my best-fit 5 Myr model is concerning, and will be investigated further in future work.

The main takeaways from my investigation into the IMF of Taurus are that a) both the broken power law and log-normal IMFs provide a good fit to this data, b) a 1–10 Myr star-formation history is slightly more suitable than 1–5 Myr, supporting the idea of an older population of Taurus members, and c) using a 3-component broken power law model when the input data is necessarily limited to G=14 produces significantly less constrained results that the G=15 limiting case. One extension to the work presented here that should be considered is the possible variation of transition masses in the broken power law IMF. As detailed in Equation 4.1, m_{01} and m_{12} describe the masses at which the power law segments transition, and have values of $m_{01} = 0.08$ M$_{\odot}$ and $m_{12} = 0.5$ M$_{\odot}$, as predicted by Kroupa (2001). In the analysis presented here, I fix the transition masses at these values, in an attempt to simplify and optimise the modelling process. However, other studies of the local IMF in star-forming regions often find transition masses that vary somewhat from the Kroupa (2001) values (see Section 4.6.2 for examples). These works are an indication that the transition masses should be included as fit parameters in the MCMC runs - this will be investigated in future work.

4.6.1 Star-Formation History of Taurus

Krolikowski et al. (2021) use Gaia DR2 to identify spatially-distinct groups within the Taurus star-forming region, and derive isochronal ages for each group. This work supports an approximate spread of 1–6 Myr in median age for the groups considered, with some up to 10 Myr within wide error bars. This was the motivation for the two star-formation histories considered in Section 4.5.

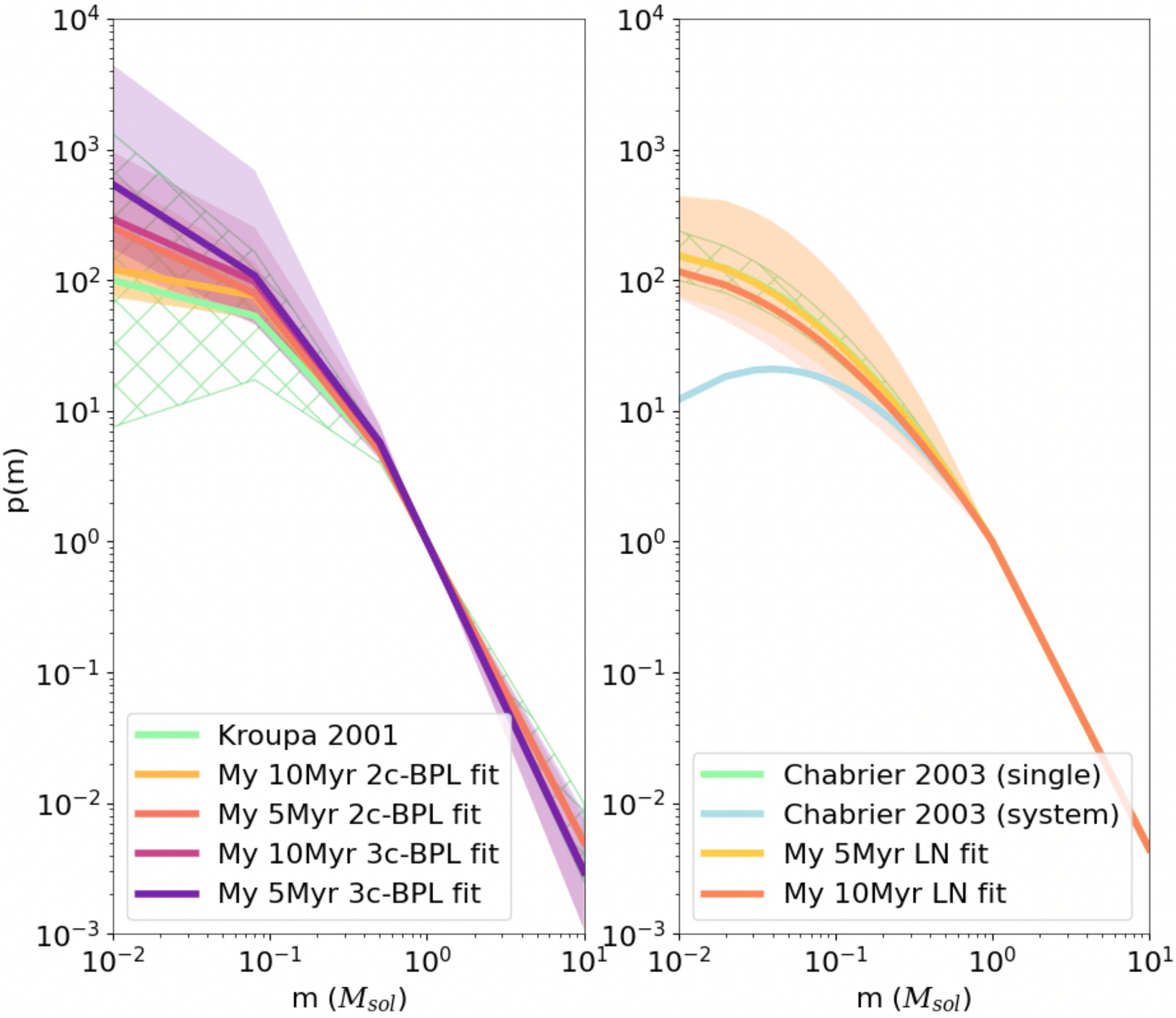

Figure 4.13 *Left: IMF results from MCMC fitting for Taurus cluster, using the broken power law functional form. IMFs constructed using best-fit parameters are shown, using each set of initial assumptions (as detailed in Table 4.1). Shaded regions indicate 1σ errors on the fit parameters in each case. Also plotted is the Kroupa (2001) and (Chabrier, 2003) IMFs for reference (green), with hatch-shaded error regions. Right: IMF results using the log-normal functional form. IMFs constructed using the best-fit parameters given in Table 4.2. Shaded regions indicate 1σ errors on the fit parameters in each case. Also plotted are (Chabrier, 2003) IMFs for reference (green and blue)*

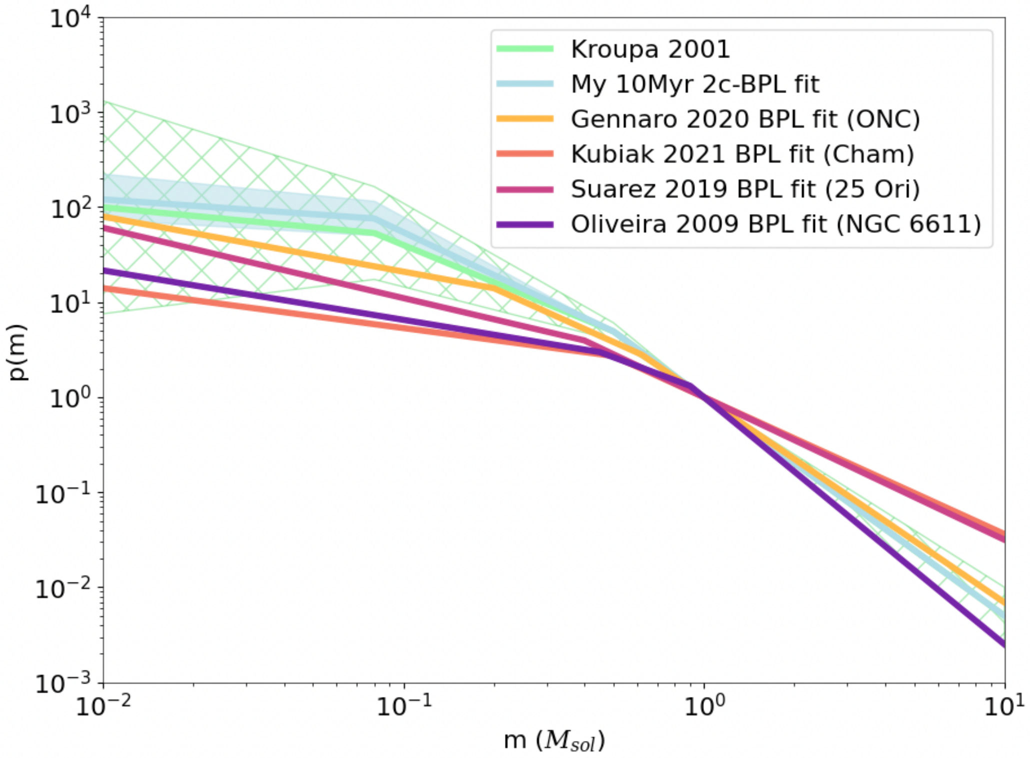

Figure 4.14 *Results from IMF studies of other star-forming regions. Plotted are the IMFs derived by Gennaro & Robberto (2020); Kubiak et al. (2021); Suárez et al. (2019); Oliveira et al. (2009) for the ONC, Chamaeleon, 25 Orionis and NGC 6111, respectively. Also plotted is the Kroupa (2001) IMF for reference (green), with hatch-shaded error regions. My 1–10 Myr, 2-component BPL IMF fit is plotted in blue for comparison.*

However, they also describe evidence of an older distributed population with ages above 10 Myr, contained within a few, low-density groups that are more dispersed within Taurus. This older population was also identified by Kraus et al. (2017), who perform a census of the Taurus region using literature data, focusing on the disk-properties of possible member objects. They derive the age of the dispersed older population to be 10–20 Myr, older than the age determined by Krolikowski et al. (2021). Both studies agree that the older members are fewer in number than the young cluster members.

In Section 4.5, I consider a maximum age of 10 Myr for objects in my model of Taurus cluster data. The studies discussed above suggest that this strict age cap may not be appropriate for Taurus, and it may in fact be necessary to consider objects with ages up to ∼20 Myr. Doing so would require a more complex approach to modelling the star-formation history than I am currently using. Simply extending the assumed uniform SFH up to 20 Myr would likely be an inappropriate technique, as the density of older objects within Taurus is likely much lower than the younger population, and as a result there are likely far fewer such objects within our catalogue. A more suitable method would be to assess the likely sub-group membership of each catalogue object, and generate the proportion of objects in each age range. This is outside the scope of this work, but would be an interesting extension of the project in the future.

4.6.2 Support for a Universal IMF

In Figure 4.14, I show best-fit IMFs from a number of different studies, of a variety of star-forming regions:

- Gennaro & Robberto (2020) present a study of the Orion Nebula Cluster. Described in Section 4.2.2, it has very similar properties to Taurus, with an age of 1–3 Myr and many stellar members. It is more distant, at ≈ 403 pc. The authors present two possible IMFs for the ONC, one using a BPL functional form and one using a LN. Their BPL results are shown in 4.14.
- Kubiak et al. (2021) derive an IMF for the Chamaeleon star-forming region, another region with comparable properties to Taurus - it also has a low stellar density but a high number of low-mass objects, and is similarly

nearby (∼ 200 pc).

- Suárez et al. (2019) investigate the mass distribution of the members of 25 Orionis, a group in Orion dense with pre-main sequence stars. It has an age of 7–10 Myr, and is at a distance of ∼ 456 pc.
- Oliveira et al. (2009) present an IMF for NGC 6611, a young massive cluster - with an age of just 2–3 Myr, it is again comparable to the local conditions of the Taurus cluster.

In Figure 4.14 I compare these results, to each other and to my best-fit BPL IMF for the Taurus CFHT catalogue. Generally, we can see that my result predicts more low-mass objects than the IMF studies described above, by as much as a factor of 10. However, my best-fit model predicts a very similar number of low-mass objects to the two Gennaro & Robberto (2020) results for the ONC. The general lack of variation in form between my result and the four example studies described here could be interpreted as tentative support for a universal IMF. The agreement between these different young clusters is clear, and the majority of the results are also comparable to the Galactic field IMF presented by Kroupa (2001). However, it should be noted that whilst these IMFs describe different, distinct regions, their properties are similar in many respects: the general environmental variation of the test subjects is likely small. In this case, one would not necessarily expect variation in the IMF, even if it was found to be environmentally-dependent. Furthermore, as discussed throughout this Chapter, a number of necessary limits were placed on the CFHT Taurus data, meaning that the dataset used in this modelling is not a full, spatially complete sample of the Taurus cluster. As a result, any conclusions drawn from this analysis should be treated as tentative, until further analysis can be performed with the full W-band catalogue.

4.7 Conclusions

In this Chapter I have investigated the form of the local initial mass function in the Taurus star-forming region, with an emphasis on low-mass objects. Using the W-band CFHT catalogue of Taurus, and the wealth of data afforded by the Gaia mission, I isolated catalogue objects that are likely to be Taurus members, based on their positions in the $G - J$ vs G colour-magnitude diagram. In order to assess the functional form and best-fit IMF parameters for this isolated cluster dataset, I produced a model population of Taurus-like objects for comparison. This was done using a set of isochrones from Baraffe et al. (2015). I considered six MCMC runs to compare the model cluster population to the observed data, each using a specific combination of IMF function, limiting G-band magnitude and star-formation history.

The main results from my population modelling can be summarised as follows:

- Both the broken power law IMF parameterisation (based on Kroupa, 2001) and the log-normal parameterisation (based on Chabrier, 2003) produce good fits to the 2017 CFHT data for the Taurus cluster.
- A uniform 1–10 Myr star-formation history results in slightly tighter constraints on the power law parameters, specifically when limiting the population to objects fainter than $G = 15$, i.e. described by the first two components of the broken power law.
- This best-fit star-formation history agrees with previous studies of Taurus which establish that the population of Taurus includes members with ages of 10 Myr or older. Objects with ages > 10 Myr should be included in a future extension of this work
- The best-fit parameter values for the best BPL fit agree within the errors with the Galactic IMF derived by Kroupa (2001), as well as a number of studies of other nearby star-forming regions, which could serve as tentative evidence of a universal IMF

In this work I have used basic photometric data to explore a fundamental aspect of the star-formation process. The simplicity of the data required will hopefully ease the extension of this study to other star-forming regions. The W-band data is particularly useful due to the additional information provided by the Q-index. In future, adding further photometric information, especially from open-access, all sky surveys such as 2MASS (Skrutskie et al., 2006) and Pan-STARRS1 (Chambers et al., 2016), could improve the IMF constraints derived, or improve the process of isolating the cluster data. The imminent release of the DR3 from the Gaia mission (expected mid-2022) will likely boost the number of cluster members included in the dataset, as more CFHT detections will have corresponding Gaia detections. The many extensions to this work will be investigated in future studies, and will continue to shed light on the local IMF in Taurus, and more generally the overall universality of the IMF.

5

Conclusions and Future Work

5.1 Summary of Results

The contents of this thesis have focused on observational survey data of nearby, young regions, with the aim of detecting and characterising new, low-mass brown dwarfs and giant exoplanets. I have described two custom filters that can be used to optimise searches for these objects, and maximise the yield of surveys undertaken with ground-based telescopes. The W-band survey has had a very high success rate in the regions surveyed to date (Jose et al., 2020; Dubber et al., 2021), highlighting the importance of maximising the information obtained during photometric observations. A future NIX survey will build on this fundamental idea, applying it to direct imaging, a technique that has typically yielded fewer discoveries than expected per survey. The 'spectral shape' technique outlined in this work, in combination with our improved understanding of exoplanet population distributions, will hopefully increase the pool of known giant exoplanets, aiding future population studies.

Beyond observations, the secondary focus of this thesis is the characterisation of objects detected via photometric and spectroscopic surveys. I have described the process of characterising photometrically-identified YPMOs, with spectroscopy and, in some cases, high-resolution imaging data. Additionally, I have shown the potential for using existing photometric catalogues to investigate the form of the initial mass function in star-forming regions.

5.1.1 Chapter 2

In Chapter 2, I presented results from a multi-technique survey of the Serpens star-forming region. By using the W-band custom filter on CFHT/WIRCam to obtain multi-band photometry and a reddening-free index, I was able to optimise our target selection for spectroscopic follow-up. I identified five low-mass candidate members of Serpens Core and Serpens South, four of which have spectral types later than M5, and masses consistent with $m \leq 0.12\mathrm{M}_{\odot}$. I also presented the discovery of a new brown-dwarf binary in Serpens South, with late-M component objects. The membership of these objects cannot be easily confirmed, due to the distance of Serpens and the time it would take to see the necessary on-sky motion. However, assuming that these objects are members, they are some of the lowest mass Serpens objects ever detected.

The Serpens star-forming region has not historically been a popular target for surveys aiming to detect low-mass objects (particularly Serpens South), as it is more distant than many other young regions, and significantly more extincted. These results therefore add to the reasonably small sample of known brown dwarfs in Serpens (although not proper-motion confirmed). They also demonstrate that it is possible to identify brown dwarfs in highly extincted regions, although the extreme levels in parts of Serpens do push the W-band technique to its limits. As is discussed throughout this thesis, increasing the numbers of known low-mass objects is crucial for robust population studies. In particular, studies of specific star-forming regions can be very illuminating when investigating environmental variation, such as in the IMF as discussed in Chapter 4.

5.1.2 Chapter 3

In Chapter 3, I described the process of designing a future direct imaging survey using the ERIS/NIX imager on the VLT. The goal of this work was to learn from previous large-scale imaging surveys, and newly-published population studies, to analyse and rank possible targets for a NIX survey. I considered both moving group and star-forming region targets, choosing representative examples to model. I showed the areas of parameters space that NIX will be sensitive to in these regions, describing the masses and separations that could be probed. I concluded that a survey of a nearby, young star-forming region will likely result in the highest yield for a NIX imaging survey, and that combining the custom $K-$peak filter with proper motion information could be very effective at probing small separations.

A time-consuming aspect of large-scale imaging surveys such as SHINE (Desidera et al., 2021; Langlois et al., 2021; Vigan et al., 2021) and GPIES (Nielsen et al., 2019) are the numerous follow-up observations required. These are necessary to confirm that a candidate object is not a chance-aligned background star, and is in fact a true low-mass companion. The spectral shape technique described in this thesis will provide more diagnostic information than typical first-epoch observations, allowing for loose characterisation and selection of highly likely companion objects for follow-up. It will also enable imaging observations of more distant regions, reducing the reliance on common proper motion follow-up to characterise candidate companions.

5.1.3 Chapter 4

In Chapter 4, I used photometric survey data to investigate the IMF of the Taurus cluster. I combined the W-band photometric catalogue of Taurus from CFHT/WIRCam with Gaia eDR3 data, and used the positions of a field population and young model isochrones in a CMD to identify objects likely to be Taurus members. I was the able to simulate a population that best-recreated the observed luminosity function of the data in Gaia $G-$band. I found that drawing object masses from either a log-normal or a 2-component broken power law IMF, and simulating a uniform star-formation history from 1–10 Myr, produced a population objects that could effectively replicate the observed catalogue.

Deriving constrains on the local IMF in specific clusters is an incredibly enlightening and important endeavour when considering the universality of the IMF. To determine an answer to this key question, it is crucial that we have a good understanding of the IMF (particularly for low-mass objects) in a wide range of environments within the Galaxy. The work I present here does not place particularly tight constraints on the form of the IMF in Taurus, but does demonstrate how we can expand the scope of IMF determinations using reasonably basic photometric data.

5.2 Future Work

5.2.1 Further Serpens Core Data

The single Serpens Core object observed spectroscopically in Chapter 2 was chosen as a test case for this sub-cluster of Serpens, observed with a large sample of Serpens South targets. Serpens Core was not initially prioritised for spectroscopic follow-up, but the robust detection of a late-type brown dwarf has encouraged the collection of further data. Using multiple successful telescope proposals, on both IRTF/SpeX and Gemini/GNIRS, I will obtain further spectroscopic follow-up of an additional 14 objects in Serpens Core. This has been completed for 10 objects bright enough to be observed with IRTF/SpeX, shown in Figure 5.1. Four fainter targets will be observed by Gemini/GNIRS in the near future.

I will characterise this new spectral data using the techniques outlined in Chapter 2, and hope to confirm many of these targets as new low-mass brown dwarfs in Serpens Core. With comparably-sized datasets for Serpens South and Serpens Core, I will then be able to compare the results for the two subclusters. With the observation of the final four targets with Gemini/GNIRS, the spectroscopic follow-up of Serpens Core based on the W-band catalogue will be complete down to $H = 17.3$ mag. With this information, I will then be able to perform a statistical analysis of Serpens Core, and investigate the IMF using my new detections.

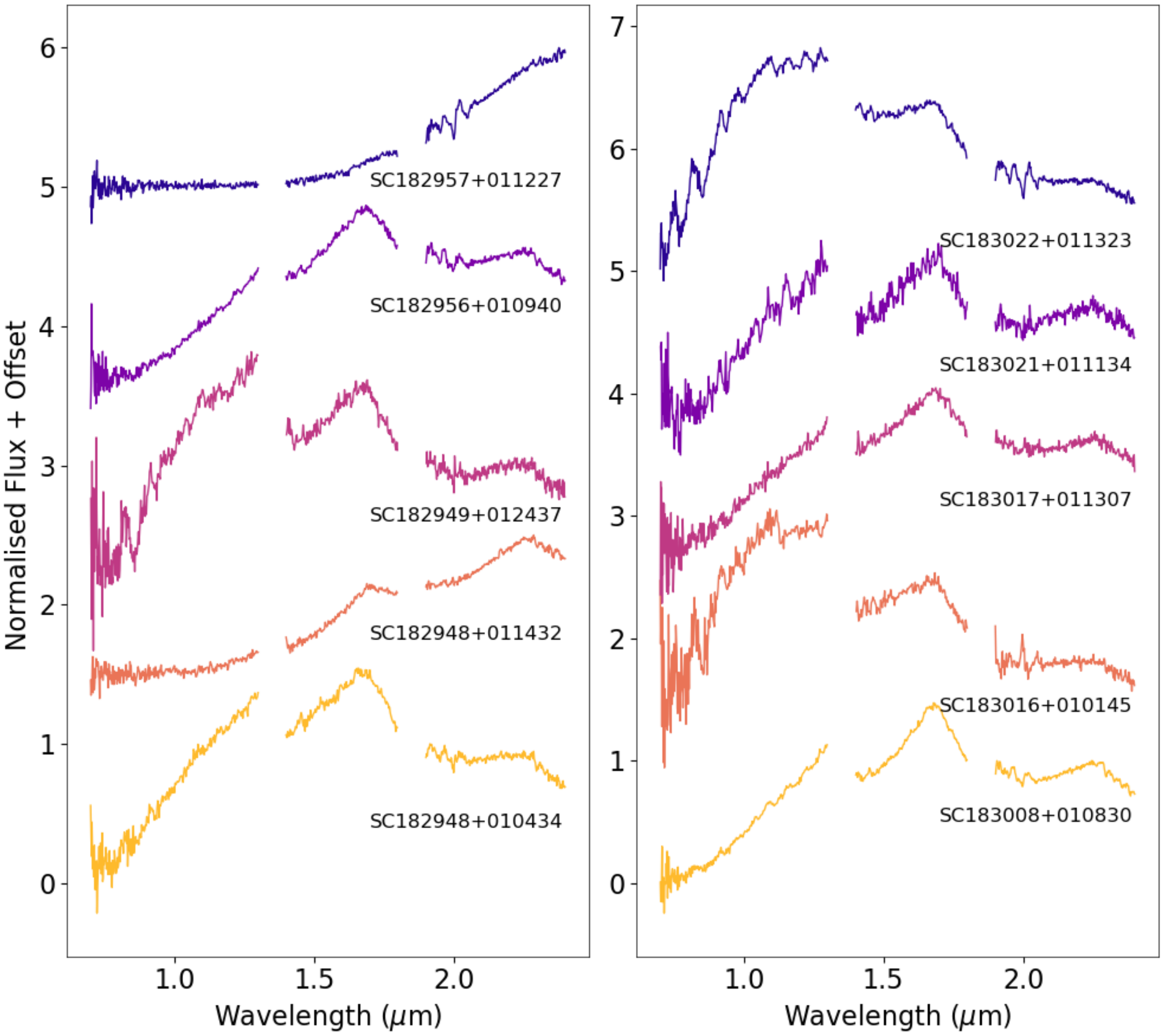

Figure 5.1 *IRTF SpeX spectra of 10 bright (H = 13.99–16.89) Serpens Core candidate members, observed during May–August 2021. $J-$, $H-$ and $K-$ bands are plotted (before dereddening), normalised to the K-band peak.*

5.2.2 Developing the IMF model for Taurus

As mentioned in Chapter 4, there are a number of possible extensions to the analysis presented of the IMF in the Taurus star-forming region. Firstly, evidence of a dispersed, older population of Taurus members has been discussed in many studies (e.g. Kraus et al., 2017; Krolikowski et al., 2021) - by limiting the population included in my model to 10 Myr, I am not recreating the full properties of Taurus members. Secondly, the classification of known Taurus members into astrometrically-defined subgroups is an ongoing process (including within the W-band collaboration, see Biller et al., in prep): it may be possible to use proper motion data for the objects in the Taurus CFHT catalogue to assign sub-cluster membership to detected objects, and compare the resulting age distribution to that found by the IMF fitting model. These additional considerations may improve or change the results for the local IMF in Taurus, and will be investigated prior to the publication of this work.

5.2.3 Investigating the IMF in other clusters

The W-band survey is expansive, covering multiple star-forming regions of various sizes, ages and distances. In Chapter 4, I applied my IMF-fitting tool to just one of these W-band catalogues. Theoretically, using it to study the mass function in other star-forming regions should be straightforward. The main caveat of this statement is the size of the photometric catalogue. Due to the use of a binned magnitude distribution for comparing models in the MCMC simulations, a large sample is crucial to efficiently populate the histograms. Another factor is the typical level of extinction across the region in question. High levels of visual extinction will affect how effectively one can separate the catalogue of objects into field and cluster populations, a step crucial for conducting the MCMC analysis.

For W-band regions with many photometric detections (at least ∼50,000 sources) and generally low extinctions ($A_{\rm V,mean} \lesssim 5$), I plan to analyse the form of the IMF using my MCMC tool, and derive best-fit parameters for the cluster populations - including an estimate of the range of ages of the member objects. A sample of these results for multiple regions could then be used for a thorough investigation into the environmental dependence of the IMF, by comparing the statistical significance of the best-fit IMF parameters.

5.3 Final Thoughts

At the time of writing, the number of known exoplanets will soon surpass 5,000. The progress that has been made to reach this milestone in the last decade must have seemed a far-fetched dream when the first detections were made in the mid-1990s. But advancement in instrumentation, theory, data reduction and analysis have made it a reality, and the detected number of brown dwarfs and exoplanets looks likely to explode over the next decade. The work presented in this thesis uses established, reliable techniques as well as innovative methods and new instruments to increase the number of known young planetary-mass objects. It is a drop in the ocean of this expansive discipline, but each drop contributes in a small way to the bigger picture. Population studies and large-scale characterisation efforts will continue to develop as the known population expands. My hope is that the work I have done on both past and future surveys will prove useful to this development, and will aid future studies of young planetary-mass objects.

Bibliography

Adams F. C., Meyer M. R., Adams A. D., 2021, A Theoretical Framework for the Mass Distribution of Gas Giant Planets Forming through the Core Accretion Paradigm, ApJ, 909, 1

Allard F., Hauschildt P. H., Alexander D. R., Tamanai A., Schweitzer A., 2001, The Limiting Effects of Dust in Brown Dwarf Model Atmospheres, ApJ, 556, 357

Allard F., Homeier D., Freytag B., Sharp C. M., 2012a, in Reylé C., Charbonnel C., Schultheis M., eds, EAS Publications Series Vol. 57, EAS Publications Series. pp 3–43 (`arXiv:1206.1021`), doi:10.1051/eas/1257001

Allard F., Homeier D., Freytag B., 2012b, Models of very-low-mass stars, brown dwarfs and exoplanets, Philosophical Transactions of the Royal Society of London Series A, 370, 2765

Allers K. N., Liu M. C., 2013, A Near-infrared Spectroscopic Study of Young Field Ultracool Dwarfs, ApJ, 772, 79

Allers K. N., Liu M. C., 2020, A Novel Survey for Young Substellar Objects with the W-band Filter. I. Filter Design and New Discoveries in Ophiuchus and Perseus, PASP, 132, 104401

Allers K. N., et al., 2007, Characterizing Young Brown Dwarfs Using Low-Resolution Near-Infrared Spectra, ApJ, 657, 511

Alves de Oliveira C., Moraux E., Bouvier J., Bouy H., Marmo C., Albert L., 2010, The low-mass population of the ρ Ophiuchi molecular cloud, A&A, 515, A75

Alves de Oliveira C., Moraux E., Bouvier J., Duchêne G., Bouy H., Maschberger T., Hudelot P., 2013, Spectroscopy of brown dwarf candidates in IC 348 and the determination of its substellar IMF down to planetary masses, A&A, 549, A123

Andrews S. M., et al., 2012, The TW Hya Disk at 870 μm: Comparison of CO and Dust Radial Structures, ApJ, 744, 162

Andrews S. M., et al., 2016, Ringed Substructure and a Gap at 1 au in the Nearest Protoplanetary Disk, ApJ, 820, L40

Audouze J., Tinsley B. M., 1976, Chemical evolution of galaxies., ARA&A, 14, 43

Bailer-Jones C. A. L., Rybizki J., Fouesneau M., Mantelet G., Andrae R., 2018, Estimating Distance from Parallaxes. IV. Distances to 1.33 Billion Stars in Gaia Data Release 2, AJ, 156, 58

Bally J., 2008, Overview of the Orion Complex. p. 459

Bally J., Walawender J., Johnstone D., Kirk H., Goodman A., 2008, The Perseus Cloud. p. 308

Baraffe I., Chabrier G., Allard F., Hauschildt P. H., 1998, Evolutionary models for solar metallicity low-mass stars: mass-magnitude relationships and color-magnitude diagrams, A&A, 337, 403

Baraffe I., Chabrier G., Barman T. S., Allard F., Hauschildt P. H., 2003, Evolutionary models for cool brown dwarfs and extrasolar giant planets. The case of HD 209458, A&A, 402, 701

Baraffe I., Homeier D., Allard F., Chabrier G., 2015, New evolutionary models for pre-main sequence and main sequence low-mass stars down to the hydrogen-burning limit, A&A, 577, A42

Barenfeld S. A., Bubar E. J., Mamajek E. E., Young P. A., 2013, A Kine-chemical Investigation of the AB Dor Moving Group "Stream", ApJ, 766, 6

Barman T. S., Macintosh B., Konopacky Q. M., Marois C., 2011, Clouds and Chemistry in the Atmosphere of Extrasolar Planet HR8799b, ApJ, 733, 65

Baron F., Lafrenière D., Artigau É., Gagné J., Rameau J., Delorme P., Naud M.-E., 2019, Constraints on the Occurrence and Distribution of 1-20 M $_{Jup}$ Companions to Stars at Separations of 5-5000 au from a Compilation of Direct Imaging Surveys, AJ, 158, 187

Basri G., Marcy G. W., Graham J. R., 1996, Lithium in Brown Dwarf Candidates: The Mass and Age of the Faintest Pleiades Stars, ApJ, 458, 600

Bastian N., Covey K. R., Meyer M. R., 2010, A Universal Stellar Initial Mass Function? A Critical Look at Variations, ARA&A, 48, 339

Bate M. R., 2012, Stellar, brown dwarf and multiple star properties from a radiation hydrodynamical simulation of star cluster formation, MNRAS, 419, 3115

Bate M. R., Bonnell I. A., Bromm V., 2002, The formation mechanism of brown dwarfs, MNRAS, 332, L65

Bayo A., et al., 2011, Spectroscopy of very low mass stars and brown dwarfs in the Lambda Orionis star forming region. I. Enlarging the census down to the planetary mass domain in Collinder 69, A&A, 536, A63

Beckers J. M., 1993, Adaptive optics for astronomy - Principles, performance, and applications, ARA&A, 31, 13

Bell C. P. M., Mamajek E. E., Naylor T., 2015, A self-consistent, absolute isochronal age scale for young moving groups in the solar neighbourhood, MNRAS, 454, 593

Bergfors C., et al., 2010, Lucky Imaging survey for southern M dwarf binaries, A&A, 520, A54

Best W. M. J., Liu M. C., Magnier E. A., Bowler B. P., Aller K. M., et al., 2017, A Search for L/T Transition Dwarfs with Pan-STARRS1 and WISE. III. Young L Dwarf Discoveries and Proper Motion Catalogs in Taurus and Scorpius-Centaurus, ApJ, 837, 95

Beuzit J.-L., Feldt M., Dohlen K., Mouillet D., Puget P., et al., 2008, in Ground-based and Airborne Instrumentation for Astronomy II. p. 701418, doi:10.1117/12.790120

Beuzit J. L., et al., 2019, SPHERE: the exoplanet imager for the Very Large Telescope, A&A, 631, A155

Biller B. A., et al., 2007, An Imaging Survey for Extrasolar Planets around 45 Close, Young Stars with the Simultaneous Differential Imager at the Very Large Telescope and MMT, ApJS, 173, 143

Biller B., Allers K., Liu M., Close L. M., Dupuy T., 2011, A Keck LGS AO Search for Brown Dwarf and Planetary Mass Companions to Upper Scorpius Brown Dwarfs, ApJ, 730, 39

Biller B. A., et al., 2013, The Gemini/NICI Planet-Finding Campaign: The Frequency of Planets around Young Moving Group Stars, ApJ, 777, 160

Biller B. A., et al., 2021, A high-contrast search for variability in HR 8799bc with VLT-SPHERE, MNRAS, 503, 743

Boccaletti A., et al., 2020, SPHERE+: Imaging young Jupiters down to the snowline, arXiv e-prints, p. arXiv:2003.05714

Boehle A., Glauser A. M., Kenworthy M. A., Snik F., Doelman D., Quanz S. P., Meyer M. R., 2018, in Ground-based and Airborne Instrumentation for Astronomy VII. p. 107023Y, doi:10.1117/12.2310108

Boeshaar P. C., Tyson J. A., 1985, New limits on the surface density of M dwarfs. I - Photographic survey and preliminary CCD data, AJ, 90, 817

Bohn A. J., et al., 2020a, The Young Suns Exoplanet Survey: Detection of a wide-orbit planetary-mass companion to a solar-type Sco-Cen member, MNRAS, 492, 431

Bohn A. J., et al., 2020b, Two Directly Imaged, Wide-orbit Giant Planets around the Young, Solar Analog TYC 8998-760-1, ApJ, 898, L16

Bohn A. J., et al., 2021, Discovery of a directly imaged planet to the young solar analog YSES 2, A&A, 648, A73

Bonavita M., 2020, Exo-DMC: Exoplanet Detection Map Calculator (ascl:2010.008)

Bonavita M., Chauvin G., Desidera S., Gratton R., Janson M., Beuzit J. L., Kasper M., Mordasini C., 2012, MESS (multi-purpose exoplanet simulation system). A Monte Carlo tool for the statistical analysis and prediction of exoplanet search results, A&A, 537, A67

Bonavita M., de Mooij E. J. W., Jayawardhana R., 2013, Quick-MESS: A Fast Statistical Tool for Exoplanet Imaging Surveys, PASP, 125, 849

Bonavita M., D'Orazi V., Mesa D., Fontanive C., Desidera S., others. 2017, Orbiting a binary. SPHERE characterisation of the HD 284149 system, A&A, 608, A106

Bonavita M., et al., 2021, New binaries from the SHINE survey, arXiv e-prints, p. arXiv:2103.13706

Bonnefoy M., et al., 2018, The GJ 504 system revisited. Combining interferometric, radial velocity, and high contrast imaging data, A&A, 618, A63

Bonnet H., et al., 2004, First light of SINFONI at the VLT, The Messenger, 117, 17

Borucki W. J., et al., 2010, Kepler Planet-Detection Mission: Introduction and First Results, Science, 327, 977

Boss A. P., 1997, Giant planet formation by gravitational instability., Science, 276, 1836

Boss A. P., 2000, Possible Rapid Gas Giant Planet Formation in the Solar Nebula and Other Protoplanetary Disks, ApJ, 536, L101

Boubert D., Everall A., 2020, Completeness of the Gaia verse II: what are the odds that a star is missing from Gaia DR2?, MNRAS, 497, 4246

Bowler B. P., 2016, Imaging Extrasolar Giant Planets, PASP, 128, 102001

Bowler B. P., Liu M. C., Shkolnik E. L., Dupuy T. J., 2013, Planets around Low-mass Stars. III. A Young Dusty L Dwarf Companion at the Deuterium-burning Limit, ApJ, 774, 55

Brandl B. R., et al., 2010, in McLean I. S., Ramsay S. K., Takami H., eds, Society of Photo-Optical Instrumentation Engineers (SPIE) Conference Series Vol. 7735, Ground-based and Airborne Instrumentation for Astronomy III. p. 77352G, doi:10.1117/12.857346

Brandl B. R., et al., 2014, in Ramsay S. K., McLean I. S., Takami H., eds, Society of Photo-Optical Instrumentation Engineers (SPIE) Conference Series Vol. 9147, Ground-based and Airborne Instrumentation for Astronomy V. p. 914721 (`arXiv:1409.3087`), doi:10.1117/12.2056468

Brandner W., et al., 2000, Timescales of Disk Evolution and Planet Formation: HST, Adaptive Optics, and ISO Observations of Weak-Line and Post-T Tauri Stars, AJ, 120, 950

Brandt T. D., et al., 2014, The Moving Group Targets of the SEEDS High-contrast Imaging Survey of Exoplanets and Disks: Results and Observations from the First Three Years, ApJ, 786, 1

Briceño C., Hartmann L., Stauffer J., Martín E., 1998, A Search for Very Low Mass Pre-Main-Sequence Stars in Taurus, AJ, 115, 2074

Briceño C., Luhman K. L., Hartmann L., Stauffer J. R., Kirkpatrick J. D., 2002, The Initial Mass Function in the Taurus Star-forming Region, ApJ, 580, 317

de Bruijne J. H. J., Hoogerwerf R., Brown A. G. A., Aguilar L. A., de Zeeuw P. T., 1997, in Bonnet R. M., et al., eds, ESA Special Publication Vol. 402, Hipparcos - Venice '97. pp 575–578 (`arXiv:astro-ph/9707090`)

Bryan M. L., et al., 2016, Statistics of Long Period Gas Giant Planets in Known Planetary Systems, ApJ, 821, 89

Burgasser A. J., 2014, in Astronomical Society of India Conference Series. (`arXiv:1406.4887`)

Burgasser A. J., McElwain M. W., 2006, Resolved Spectroscopy of M Dwarf/L Dwarf Binaries. I. DENIS J220002.05-303832.9AB, AJ, 131, 1007

Burgasser A. J., Dhital S., West A. A., 2009, Resolved Spectroscopy of M Dwarf/L Dwarf Binaries. III. The "Wide" L3.5/L4 Dwarf Binary 2Mass J15500845+1455180AB, AJ, 138, 1563

Burrows A., et al., 1997, A Nongray Theory of Extrasolar Giant Planets and Brown Dwarfs, ApJ, 491, 856

Caimmi R., 2008, The G-dwarf problem in the Galaxy, New Astron., 13, 314

Calvet N., D'Alessio P., Hartmann L., Wilner D., Walsh A., Sitko M., 2002, Evidence for a Developing Gap in a 10 Myr Old Protoplanetary Disk, ApJ, 568, 1008

Cánovas H., et al., 2019, Census of ρ Ophiuchi candidate members from Gaia Data Release 2, A&A, 626, A80

Cantat-Gaudin T., et al., 2018, A Gaia DR2 view of the open cluster population in the Milky Way, A&A, 618, A93

Cappellari M., et al., 2012, Systematic variation of the stellar initial mass function in early-type galaxies, Nature, 484, 485

Cardelli J. A., Clayton G. C., Mathis J. S., 1989, The Relationship between Infrared, Optical, and Ultraviolet Extinction, ApJ, 345, 245

Carter A. L., et al., 2021, Direct imaging of sub-Jupiter mass exoplanets with James Webb Space Telescope coronagraphy, MNRAS, 501, 1999

Chabrier G., 2003, Galactic Stellar and Substellar Initial Mass Function, PASP, 115, 763

Chabrier G., 2005, in Corbelli E., Palla F., Zinnecker H., eds, Astrophysics and Space Science Library Vol. 327, The Initial Mass Function 50 Years Later. p. 41 (`arXiv:astro-ph/0409465`), doi:10.1007/978-1-4020-3407-7_5

Chabrier G., Baraffe I., Allard F., Hauschildt P., 2000, Evolutionary Models for Very Low-Mass Stars and Brown Dwarfs with Dusty Atmospheres, ApJ, 542, 464

Chambers K. C., Magnier E. A., Metcalfe N., Flewelling H. A., Huber M. E., et al., 2016, The Pan-STARRS1 Surveys, arXiv e-prints, p. arXiv:1612.05560

Charbonneau D., Brown T. M., Noyes R. W., Gilliland R. L., 2002, Detection of an Extrasolar Planet Atmosphere, ApJ, 568, 377

Chauvin G., et al., 2003, Adaptive optics imaging survey of the Tucana-Horologium association, A&A, 404, 157

Chauvin G., Lagrange A. M., Dumas C., Zuckerman B., Mouillet D., Song I., Beuzit J. L., Lowrance P., 2004, A giant planet candidate near a young brown dwarf. Direct VLT/NACO observations using IR wavefront sensing, A&A, 425, L29

Chauvin G., et al., 2010, Deep imaging survey of young, nearby austral stars . VLT/NACO near-infrared Lyot-coronographic observations, A&A, 509, A52

Chauvin G., et al., 2015, The VLT/NaCo large program to probe the occurrence of exoplanets and brown dwarfs at wide orbits. II. Survey description, results, and performances, A&A, 573, A127

Chauvin G., Desidera S., Lagrange A.-M., Vigan A., Gratton R., et al., 2017, Discovery of a warm, dusty giant planet around HIP 65426, A&A, 605, L9

Chilcote J. K., et al., 2018, in Evans C. J., Simard L., Takami H., eds, Society of Photo-Optical Instrumentation Engineers (SPIE) Conference Series Vol. 10702, Ground-based and Airborne Instrumentation for Astronomy VII. p. 1070244 (`arXiv:1807.07145`), doi:10.1117/12.2313771

Chilcote J., et al., 2020, in Society of Photo-Optical Instrumentation Engineers (SPIE) Conference Series. p. 114471S, doi:10.1117/12.2562578

Choi J., Dotter A., Conroy C., Cantiello M., Paxton B., Johnson B. D., 2016, Mesa Isochrones and Stellar Tracks (MIST). I. Solar-scaled Models, ApJ, 823, 102

Chun M., et al., 2008, in Hubin N., Max C. E., Wizinowich P. L., eds, Society of Photo-Optical Instrumentation Engineers (SPIE) Conference Series Vol. 7015, Adaptive Optics Systems. p. 70151V (`arXiv:0809.3017`), doi:10.1117/12.787683

Cieza L. A., et al., 2016, Imaging the water snow-line during a protostellar outburst, Nature, 535, 258

Claudi R., Maire A.-L., Mesa D., Cheetham A., Fontanive C., et al., 2019, SPHERE dynamical and spectroscopic characterization of HD 142527B, A&A, 622, A96

Close L. M., Gasho V., Kopon D., Males J., Follette K. B., Brutlag K., Uomoto A., Hare T., 2010, in Ellerbroek B. L., Hart M., Hubin N., Wizinowich P. L., eds, Society of Photo-Optical Instrumentation Engineers (SPIE) Conference Series Vol. 7736, Adaptive Optics Systems II. p. 773605, doi:10.1117/12.857924

Close L. M., et al., 2012, in Ellerbroek B. L., Marchetti E., Véran J.-P., eds, Society of Photo-Optical Instrumentation Engineers (SPIE) Conference Series Vol. 8447, Adaptive Optics Systems III. p. 84470X, doi:10.1117/12.926545

Close L. M., et al., 2013, Diffraction-limited Visible Light Images of Orion Trapezium Cluster with the Magellan Adaptive Secondary Adaptive Optics System (MagAO), ApJ, 774, 94

Colman T., Teyssier R., 2020, On the origin of the peak of the stellar initial mass function: exploring the tidal screening theory, MNRAS, 492, 4727

Comerón F., 2008, The Lupus Clouds. p. 295

Cook N. J., Scholz A., Jayawardhana R., 2017, Very Low-mass Stars and Brown Dwarfs in Upper Scorpius Using Gaia DR1: Mass Function, Disks, and Kinematics, AJ, 154, 256

Cruz K. L., Kirkpatrick J. D., Burgasser A. J., 2009, Young L Dwarfs Identified in the Field: A Preliminary Low-Gravity, Optical Spectral Sequence from L0 to L5, AJ, 137, 3345

Cugno G., et al., 2019, ISPY - NaCo Imaging Survey for Planets around Young stars. A young companion candidate embedded in the R CrA cloud, A&A, 624, A29

Cumming A., Butler R. P., Marcy G. W., Vogt S. S., Wright J. T., Fischer D. A., 2008, The Keck Planet Search: Detectability and the Minimum Mass and Orbital Period Distribution of Extrasolar Planets, PASP, 120, 531

Currie T., et al., 2021, A New Type of Exoplanet Direct Imaging Search: The SCExAO/CHARIS Survey of Accelerating Stars, arXiv e-prints, p. arXiv:2109.09745

Cushing M. C., Vacca W. D., Rayner J. T., 2004, Spextool: A Spectral Extraction Package for SpeX, a 0.8-5.5 Micron Cross-Dispersed Spectrograph, PASP, 116, 362

Cushing M. C., Rayner J. T., Vacca W. D., 2005, An Infrared Spectroscopic Sequence of M, L, and T Dwarfs, ApJ, 623, 1115

Cushing M. C., et al., 2008, Atmospheric Parameters of Field L and T Dwarfs, ApJ, 678, 1372

Cushing M. C., Kirkpatrick J. D., Gelino C. R., Griffith R. L., Skrutskie M. F., et al., 2011, The Discovery of Y Dwarfs using Data from the Wide-field Infrared Survey Explorer (WISE), ApJ, 743, 50

Cutri R. M., others others 2013, VizieR Online Data Catalog: AllWISE Data Release (Cutri+ 2013), VizieR Online Data Catalog, p. II/328

D'Angelo G., Lissauer J. J., 2018, in Deeg H. J., Belmonte J. A., eds, , Handbook of Exoplanets. p. 140, doi:10.1007/978-3-319-55333-7_140

Da Rio N., Robberto M., Hillenbrand L. A., Henning T., Stassun K. G., 2012, The Initial Mass Function of the Orion Nebula Cluster across the H-burning Limit, ApJ, 748, 14

Dattilo A., et al., 2019, Identifying Exoplanets with Deep Learning. II. Two New Super-Earths Uncovered by a Neural Network in K2 Data, AJ, 157, 169

David T. J., Hillenbrand L. A., Gillen E., Cody A. M., Howell S. B., Isaacson H. T., Livingston J. H., 2019, Age Determination in Upper Scorpius with Eclipsing Binaries, ApJ, 872, 161

Davies R., Esposito S., Schmid H.-M., Taylor W., Agapito G., et al., 2018, in Ground-based and Airborne Instrumentation for Astronomy VII. p. 1070209 (`arXiv:1807.05089`), doi:10.1117/12.2311480

Deeg H. J., Alonso R., 2018, in Deeg H. J., Belmonte J. A., eds, , Handbook of Exoplanets. p. 117, doi:10.1007/978-3-319-55333-7_117

Dehnen W., Binney J. J., 1998, Local stellar kinematics from HIPPARCOS data, MNRAS, 298, 387

Desidera S., et al., 2015, The VLT/NaCo large program to probe the occurrence of exoplanets and brown dwarfs in wide orbits. I. Sample definition and characterization, A&A, 573, A126

Desidera S., et al., 2021, The SPHERE infrared survey for exoplanets (SHINE). I. Sample definition and target characterization, A&A, 651, A70

Dhital S., Burgasser A. J., Looper D. L., Stassun K. G., 2011, Resolved Spectroscopy of M Dwarf/L Dwarf Binaries. IV. Discovery of AN M9 + L6 Binary Separated by Over 100 AU, AJ, 141, 7

Di Stefano R., Berndtsson J., Urquhart R., Soria R., Kashyap V. L., Carmichael T. W., Imara N., 2021, A possible planet candidate in an external galaxy detected through X-ray transit, Nature Astronomy, 5, 1297

Dobashi K., 2011, Atlas and Catalog of Dark Clouds Based on the 2 Micron All Sky Survey, PASJ, 63, S1

van Dokkum P. G., Conroy C., 2010, A substantial population of low-mass stars in luminous elliptical galaxies, Nature, 468, 940

Dotter A., 2016, MESA Isochrones and Stellar Tracks (MIST) 0: Methods for the Construction of Stellar Isochrones, ApJS, 222, 8

Dubber S., et al., 2021, A novel survey for young substellar objects with the W-band filter III: Searching for very low-mass brown dwarfs in Serpens South and Serpens Core, MNRAS, 505, 4215

Dunham M. M., et al., 2015, Young Stellar Objects in the Gould Belt, ApJS, 220, 11

ESA 1997, in The HIPPARCOS and TYCHO catalogues. Astrometric and photometric star catalogues derived from the ESA HIPPARCOS Space Astrometry Mission.

Eiroa C., Djupvik A. A., Casali M. M., 2008, The Serpens Molecular Cloud. p. 693

Eisenhauer F., et al., 2003, in Iye M., Moorwood A. F. M., eds, Society of Photo-Optical Instrumentation Engineers (SPIE) Conference Series Vol. 4841, Instrument Design and Performance for Optical/Infrared Ground-based Telescopes. pp 1548–1561 (`arXiv:astro-ph/0306191`), doi:10.1117/12.459468

Eisner J. A., 2015, Spectral Energy Distributions of Accreting Protoplanets, ApJ, 803, L4

Elmegreen B. G., 2009, in Sheth K., Noriega-Crespo A., Ingalls J. G., Paladini R., eds, The Evolving ISM in the Milky Way and Nearby Galaxies. p. 14 (`arXiv:0803.3154`)

Esplin T. L., Luhman K. L., 2017, A Survey For Planetary-mass Brown Dwarfs in the Taurus and Perseus Star-forming Regions, AJ, 154, 134

Esplin T. L., Luhman K. L., 2019, A Survey for New Members of Taurus from Stellar to Planetary Masses, AJ, 158, 54

Faherty J. K., et al., 2020, WISE 2150-7520AB: A Very Low-mass, Wide Comoving Brown Dwarf System Discovered through the Citizen Science Project Backyard Worlds: Planet 9, ApJ, 889, 176

Feast M. W., Catchpole R. M., 1997, The Cepheid period-luminosity zero-point from HIPPARCOS trigonometrical parallaxes, MNRAS, 286, L1

Feast M., Whitelock P., 1997, Galactic kinematics of Cepheids from HIPPARCOS proper motions, MNRAS, 291, 683

Fernandes R. B., Mulders G. D., Pascucci I., Mordasini C., Emsenhuber A., 2019, Hints for a Turnover at the Snow Line in the Giant Planet Occurrence Rate, ApJ, 874, 81

Ferreras I., La Barbera F., de La Rosa I. G., Vazdekis A., de Carvalho R. R., Falcon-Barroso J., Ricciardelli E., 2013, Systematic variation of the stellar initial mass function with velocity dispersion in early-type galaxies., MNRAS, 429, L15

Filippazzo J. C., Rice E. L., Faherty J., Cruz K. L., Van Gordon M. M., Looper D. L., 2015, Fundamental Parameters and Spectral Energy Distributions of Young and Field Age Objects with Masses Spanning the Stellar to Planetary Regime, ApJ, 810, 158

Fitzpatrick E. L., 1986, An average interstellar extinction curve for the Large Magellanic Cloud., AJ, 92, 1068

Fitzpatrick E. L., 1999, Correcting for the Effects of Interstellar Extinction, PASP, 111, 63

Fontanive C., Mužić K., Bonavita M., Biller B., 2019, A new method for target selection in direct imaging programmes with COPAINS, MNRAS, 490, 1120

Fontanive C., et al., 2020, A Wide Planetary-mass Companion to a Young Low-mass Brown Dwarf in Ophiuchus, ApJ, 905, L14

Foreman-Mackey D., Hogg D. W., Lang D., Goodman J., 2013, emcee: The MCMC Hammer, PASP, 125, 306

Forgan D., Parker R. J., Rice K., 2015, The dynamical fate of self-gravitating disc fragments after tidal downsizing, MNRAS, 447, 836

Fortney J. J., Marley M. S., Saumon D., Lodders K., 2008, Synthetic Spectra and Colors of Young Giant Planet Atmospheres: Effects of Initial Conditions and Atmospheric Metallicity, ApJ, 683, 1104

Fuhrmann K., 1998, Nearby stars of the Galactic disk and halo, A&A, 338, 161

Fulton B. J., et al., 2021, The California Legacy Survey II. Occurrence of Giant Planets Beyond the Ice line, arXiv e-prints, p. arXiv:2105.11584

Gagné J., Faherty J. K., 2018, BANYAN. XIII. A First Look at Nearby Young Associations with Gaia Data Release 2, ApJ, 862, 138

Gagné J., Burgasser A. J., Faherty J. K., Lafreniére D., Doyon R., Filippazzo J. C., Bowsher E., Nicholls C. P., 2015, SDSS J111010.01+011613.1: A New Planetary-mass T Dwarf Member of the AB Doradus Moving Group, ApJ, 808, L20

Gagné J., et al., 2017, BANYAN. IX. The Initial Mass Function and Planetary-mass Object Space Density of the TW HYA Association, ApJS, 228, 18

Gagné J., Roy-Loubier O., Faherty J. K., Doyon R., Malo L., 2018, BANYAN. XII. New Members of Nearby Young Associations from GAIA-Tycho Data, ApJ, 860, 43

Gaia Collaboration et al., 2016a, The Gaia mission, A&A, 595, A1

Gaia Collaboration et al., 2016b, Gaia Data Release 1. Summary of the astrometric, photometric, and survey properties, A&A, 595, A2

Gaia Collaboration et al., 2018, Gaia Data Release 2. Summary of the contents and survey properties, A&A, 616, A1

Gaia Collaboration et al., 2021, Gaia Early Data Release 3. Summary of the contents and survey properties, A&A, 649, A1

Galicher R., et al., 2016, The International Deep Planet Survey. II. The frequency of directly imaged giant exoplanets with stellar mass, A&A, 594, A63

Galli P. A. B., et al., 2019, Structure and kinematics of the Taurus star-forming region from Gaia-DR2 and VLBI astrometry, A&A, 630, A137

Gardner J. P., et al., 2006, The James Webb Space Telescope, Space Sci. Rev., 123, 485

Gaudi B. S., 2012, Microlensing Surveys for Exoplanets, ARA&A, 50, 411

Gaudi B. S., et al., 2020, The Habitable Exoplanet Observatory (HabEx) Mission Concept Study Final Report, arXiv e-prints, p. arXiv:2001.06683

Gennaro M., Robberto M., 2020, HST Survey of the Orion Nebula Cluster in the H_2O 1.4 μm Absorption Band. II. The Substellar IMF Down to Planetary Masses, ApJ, 896, 80

Gennaro M., et al., 2018, Evidence of a Non-universal Stellar Initial Mass Function. Insights from HST Optical Imaging of Six Ultra-faint Dwarf Milky Way Satellites, ApJ, 855, 20

Getman K. V., Broos P. S., Kuhn M. A., Feigelson E. D., Richert A. J. W., Ota Y., Bate M. R., Garmire G. P., 2017, Star Formation In Nearby Clouds (SFiNCs): X-Ray and Infrared Source Catalogs and Membership, ApJS, 229, 28

Girardi L., et al., 2012, TRILEGAL, a TRIdimensional modeL of thE GALaxy: Status and Future, Astrophysics and Space Science Proceedings, 26, 165

Goldreich P., Ward W. R., 1973, The Formation of Planetesimals, ApJ, 183, 1051

Gomez Gonzalez C. A., et al., 2017, VIP: Vortex Image Processing Package for High-contrast Direct Imaging, AJ, 154, 7

Goodwin S. P., Whitworth A. P., Ward-Thompson D., 2004, An explanation for the unusual IMF in Taurus, A&A, 419, 543

Gravity Collaboration et al., 2019, First direct detection of an exoplanet by optical interferometry. Astrometry and K-band spectroscopy of HR 8799 e, A&A, 623, L11

Gravity Collaboration et al., 2020, Peering into the formation history of β Pictoris b with VLTI/GRAVITY long-baseline interferometry, A&A, 633, A110

Green G. M., Schlafly E., Zucker C., Speagle J. S., Finkbeiner D., 2019, A 3D Dust Map Based on Gaia, Pan-STARRS 1, and 2MASS, ApJ, 887, 93

Greenbaum A. Z., Pueyo L., Ruffio J.-B., Wang J. J., De Rosa R. J., et al., 2018, GPI Spectra of HR 8799 c, d, and e from 1.5 to 2.4 μm with KLIP Forward Modeling, AJ, 155, 226

Greener M. J., Merrifield M., Aragón-Salamanca A., Peterken T., Andrews B., Lane R. R., 2021, SDSS-IV MaNGA: the 'G-dwarf problem' revisited, MNRAS, 502, L95

Grunblatt S. K., et al., 2022, TESS Giants Transiting Giants II: The hottest Jupiters orbiting evolved stars, arXiv e-prints, p. arXiv:2201.04140

Guieu S., Dougados C., Monin J. L., Magnier E., Martín E. L., 2006, Seventeen new very low-mass members in Taurus. The brown dwarf deficit revisited, A&A, 446, 485

Guo K., et al., 2020, The SAMI Galaxy Survey: the contribution of different kinematic classes to the stellar mass function of nearby galaxies, MNRAS, 491, 773

Gutermuth R. A., et al., 2008, The Spitzer Gould Belt Survey of Large Nearby Interstellar Clouds: Discovery of a Dense Embedded Cluster in the Serpens-Aquila Rift, ApJ, 673, L151

Haffert S. Y., Bohn A. J., de Boer J., Snellen I. A. G., Brinchmann J., Girard J. H., Keller C. U., Bacon R., 2019, Two accreting protoplanets around the young star PDS 70, Nature Astronomy, 3, 749

Hauschildt P. H., Allard F., Baron E., 1999, The NextGen Model Atmosphere Grid for 3000¡=T$_{eff}$¡=10,000 K, ApJ, 512, 377

Hayashi C., Nakano T., 1963, Evolution of Stars of Small Masses in the Pre-Main-Sequence Stages, Progress of Theoretical Physics, 30, 460

Hayashi C., Nakazawa K., Adachi I., 1977, Long-Term Behavior of Planetesimals and the Formation of the Planets, PASJ, 29, 163

Heinze A. N., Hinz P. M., Sivanandam S., Kenworthy M., Meyer M., Miller D., 2010, Constraints on Long-period Planets from an L'- and M-band Survey of Nearby Sun-like Stars: Observations, ApJ, 714, 1551

Herbst W., 2008, Star Formation in IC 348. p. 372

Herczeg G. J., Hillenbrand L. A., 2014, An Optical Spectroscopic Study of T Tauri Stars. I. Photospheric Properties, ApJ, 786, 97

Herczeg G. J., Hillenbrand L. A., 2015, Empirical Isochrones for Low Mass Stars in Nearby Young Associations, ApJ, 808, 23

Herczeg G. J., et al., 2019, An Initial Overview of the Extent and Structure of Recent Star Formation within the Serpens Molecular Cloud Using Gaia Data Release 2, ApJ, 878, 111

Hillenbrand L. A., Carpenter J. M., 2000, Constraints on the Stellar/Substellar Mass Function in the Inner Orion Nebula Cluster, ApJ, 540, 236

Hillenbrand L. A., Hoffer A. S., Herczeg G. J., 2013, An Enhanced Spectroscopic Census of the Orion Nebula Cluster, AJ, 146, 85

Hoeijmakers H. J., et al., 2018a, Atomic iron and titanium in the atmosphere of the exoplanet KELT-9b, Nature, 560, 453

Hoeijmakers H. J., Schwarz H., Snellen I. A. G., de Kok R. J., Bonnefoy M., Chauvin G., Lagrange A. M., Girard J. H., 2018b, Medium-resolution integral-field spectroscopy for high-contrast exoplanet imaging. Molecule maps of the β Pictoris system with SINFONI, A&A, 617, A144

Høg E., et al., 2000, The Tycho-2 catalogue of the 2.5 million brightest stars, A&A, 355, L27

Hogg D. W., Myers A. D., Bovy J., 2010, Inferring the Eccentricity Distribution, ApJ, 725, 2166

Hopkins A. M., 2018, The Dawes Review 8: Measuring the Stellar Initial Mass Function, Publ. Astron. Soc. Australia, 35, e039

Hosek Matthew W. J., Lu J. R., Anderson J., Najarro F., Ghez A. M., Morris M. R., Clarkson W. I., Albers S. M., 2019, The Unusual Initial Mass Function of the Arches Cluster, ApJ, 870, 44

Janson M., Bonavita M., Klahr H., Lafrenière D., Jayawardhana R., Zinnecker H., 2011, High-contrast Imaging Search for Planets and Brown Dwarfs around the Most Massive Stars in the Solar Neighborhood, ApJ, 736, 89

Janson M., Bonavita M., Klahr H., Lafrenière D., 2012, How do Most Planets Form?—Constraints on Disk Instability from Direct Imaging, ApJ, 745, 4

Janson M., et al., 2021, BEAST begins: sample characteristics and survey performance of the B-star Exoplanet Abundance Study, A&A, 646, A164

Jeffries R. D., Littlefair S. P., Naylor T., Mayne N. J., 2011, No wide spread of stellar ages in the Orion Nebula Cluster, MNRAS, 418, 1948

Johnson S. A., Penny M., Gaudi B. S., Kerins E., Rattenbury N. J., Robin A. C., Calchi Novati S., Henderson C. B., 2020, Predictions of the Nancy Grace Roman Space Telescope Galactic Exoplanet Survey. II. Free-floating Planet Detection Rates, AJ, 160, 123

Jones J., et al., 2015, The Ages of A-Stars. I. Interferometric Observations and Age Estimates for Stars in the Ursa Major Moving Group, ApJ, 813, 58

Jorquera S., et al., 2021, A Search for Companions via Direct Imaging in the DSHARP Planet-forming Disks, AJ, 161, 146

Jose J., et al., 2020, A Novel Survey for Young Substellar Objects with the W-band Filter. II. The Coolest and Lowest Mass Members of the Serpens-South Star-forming Region, ApJ, 892, 122

Kaas A. A., 1999, K-Band Variability as a Method to Select Young Stellar Object Candidates, AJ, 118, 558

Kastner J. H., Zuckerman B., Weintraub D. A., Forveille T., 1997, X-ray and molecular emission from the nearest region of recent star formation., Science, 277, 67

Kenworthy M. A., Snik F., Keller C. U., Doelman D., Por E. H., et al., 2018, in Ground-based and Airborne Instrumentation for Astronomy VII. p. 1070246, doi:10.1117/12.2313964

Kenyon S. J., Gómez M., Whitney B. A., 2008, Low Mass Star Formation in the Taurus-Auriga Clouds. p. 405

Keppler M., et al., 2018, Discovery of a planetary-mass companion within the gap of the transition disk around PDS 70, A&A, 617, A44

Kervella P., Arenou F., Mignard F., Thévenin F., 2019, Stellar and substellar companions of nearby stars from Gaia DR2. Binarity from proper motion anomaly, A&A, 623, A72

Kirkpatrick J. D., 2005, New Spectral Types L and T, ARA&A, 43, 195

Kirkpatrick J. D., Reid I. N., Liebert J., Cutri R. M., Nelson B., et al., 1999, Dwarfs Cooler than “M”: The Definition of Spectral Type “L” Using Discoveries from the 2 Micron All-Sky Survey (2MASS), ApJ, 519, 802

Kirkpatrick J. D., Looper D. L., Burgasser A. J., Schurr S. D., Cutri R. M., et al., 2010, Discoveries from a Near-infrared Proper Motion Survey Using Multi-epoch Two Micron All-Sky Survey Data, ApJS, 190, 100

Kirkpatrick J. D., et al., 2011, The First Hundred Brown Dwarfs Discovered by the Wide-field Infrared Survey Explorer (WISE), ApJS, 197, 19

Kirkpatrick J. D., et al., 2019, Preliminary Trigonometric Parallaxes of 184 Late-T and Y Dwarfs and an Analysis of the Field Substellar Mass Function into the “Planetary” Mass Regime, ApJS, 240, 19

Klotz A., Caux E., Monin J. L., Lodieu N., 2004, Substellar objects in star formation regions: A deep near infrared study in the Serpens cloud, A&A, 425, 927

Knapp G. R., et al., 2004, Near-Infrared Photometry and Spectroscopy of L and T Dwarfs: The Effects of Temperature, Clouds, and Gravity, AJ, 127, 3553

Komiya Y., Suda T., Minaguchi H., Shigeyama T., Aoki W., Fujimoto M. Y., 2007, The Origin of Carbon Enhancement and the Initial Mass Function of Extremely Metal-poor Stars in the Galactic Halo, ApJ, 658, 367

Konopacky Q. M., Ghez A. M., Rice E. L., Duchêne G., 2007, New Very Low Mass Binaries in the Taurus Star-forming Region, ApJ, 663, 394

Konopacky Q. M., Marois C., Macintosh B. A., Galicher R., Barman T. S., Metchev S. A., Zuckerman B., 2016, Astrometric Monitoring of the HR 8799 Planets: Orbit Constraints from Self-consistent Measurements, AJ, 152, 28

Kraus A. L., Ireland M. J., Martinache F., Lloyd J. P., 2008, Mapping the Shores of the Brown Dwarf Desert. I. Upper Scorpius, ApJ, 679, 762

Kraus A. L., Herczeg G. J., Rizzuto A. C., Mann A. W., Slesnick C. L., Carpenter J. M., Hillenbrand L. A., Mamajek E. E., 2017, The Greater Taurus-Auriga Ecosystem. I. There is a Distributed Older Population, ApJ, 838, 150

Krolikowski D. M., Kraus A. L., Rizzuto A. C., 2021, Gaia EDR3 Reveals the Substructure and Complicated Star Formation History of the Greater Taurus-Auriga Star-forming Complex, AJ, 162, 110

Kroupa P., 2001, On the variation of the initial mass function, MNRAS, 322, 231

Kroupa P., Boily C. M., 2002, On the mass function of star clusters, MNRAS, 336, 1188

Kubiak K., Mužić K., Sousa I., Almendros-Abad V., Köhler R., Scholz A., 2021, New low-mass members of Chamaeleon I and Cha, A&A, 650, A48

Kuhn M. A., Hillenbrand L. A., Sills A., Feigelson E. D., Getman K. V., 2019, Kinematics in Young Star Clusters and Associations with Gaia DR2, ApJ, 870, 32

Kumar S. S., 1963, The Structure of Stars of Very Low Mass., ApJ, 137, 1121

Lacy B., Burrows A., 2020, Prospects for Directly Imaging Young Giant Planets at Optical Wavelengths, ApJ, 892, 151

Lacy B., Shlivko D., Burrows A., 2019, Characterization of Exoplanet Atmospheres with the Optical Coronagraph on WFIRST, AJ, 157, 132

Lafrenière D., Marois C., Doyon R., Nadeau D., Artigau É., 2007a, A New Algorithm for Point-Spread Function Subtraction in High-Contrast Imaging: A Demonstration with Angular Differential Imaging, ApJ, 660, 770

Lafrenière D., et al., 2007b, The Gemini Deep Planet Survey, ApJ, 670, 1367

Lafrenière D., Marois C., Doyon R., Barman T., 2009, HST/NICMOS Detection of HR 8799 b in 1998, ApJ, 694, L148

Lagrange A. M., et al., 2009, A probable giant planet imaged in the β Pictoris disk. VLT/NaCo deep L'-band imaging, A&A, 493, L21

Lagrange A. M., et al., 2010, A Giant Planet Imaged in the Disk of the Young Star β Pictoris, Science, 329, 57

Lam K. W. F., et al., 2021, GJ 367b: A dense, ultrashort-period sub-Earth planet transiting a nearby red dwarf star, Science, 374, 1271

Langlois M., et al., 2021, The SPHERE infrared survey for exoplanets (SHINE). II. Observations, data reduction and analysis, detection performances, and initial results, A&A, 651, A71

Lannier J., et al., 2016, MASSIVE: A Bayesian analysis of giant planet populations around low-mass stars, A&A, 596, A83

Larson R. B., 1992, Towards understanding the stellar initial mass function., MNRAS, 256, 641

Larson R. B., 1998, Early star formation and the evolution of the stellar initial mass function in galaxies, MNRAS, 301, 569

Launhardt R., et al., 2020, ISPY-NACO Imaging Survey for Planets around Young stars. Survey description and results from the first 2.5 years of observations, A&A, 635, A162

van Leeuwen F., 2007, Validation of the new Hipparcos reduction, A&A, 474, 653

Lenzen R., Hofmann R., Bizenberger P., Tusche A., 1998, in Fowler A. M., ed., Society of Photo-Optical Instrumentation Engineers (SPIE) Conference Series Vol. 3354, Infrared Astronomical Instrumentation. pp 606–614, doi:10.1117/12.317287

Lissauer J. J., 1993, Planet formation., ARA&A, 31, 129

Liu M. C., et al., 2013, The Extremely Red, Young L Dwarf PSO J318.5338-22.8603: A Free-floating Planetary-mass Analog to Directly Imaged Young Gas-giant Planets, ApJ, 777, L20

Lodieu N., Caux E., Monin J. L., Klotz A., 2002, Discovery of the first young brown dwarf in the Serpens cluster, A&A, 383, L15

Lodieu N., Zapatero Osorio M. R., Rebolo R., Martín E. L., Hambly N. C., 2009, A census of very-low-mass stars and brown dwarfs in the σ Orionis cluster, A&A, 505, 1115

Lodieu N., Dobbie P. D., Cross N. J. G., Hambly N. C., Read M. A., Blake R. P., Floyd D. J. E., 2013, Probing the Upper Scorpius mass function in the planetary-mass regime, MNRAS, 435, 2474

Lodieu N., Zapatero Osorio M. R., Béjar V. J. S., Peña Ramírez K., 2018, The optical + infrared L dwarf spectral sequence of young planetary-mass objects in the Upper Scorpius association, MNRAS, 473, 2020

Long F., et al., 2018, Gaps and Rings in an ALMA Survey of Disks in the Taurus Star-forming Region, ApJ, 869, 17

Lu J. R., Do T., Ghez A. M., Morris M. R., Yelda S., Matthews K., 2013, Stellar Populations in the Central 0.5 pc of the Galaxy. II. The Initial Mass Function, ApJ, 764, 155

Lucas P. W., Roche P. F., 2000, A population of very young brown dwarfs and free-floating planets in Orion, MNRAS, 314, 858

Lucatello S., Gratton R. G., Beers T. C., Carretta E., 2005, Observational Evidence for a Different Initial Mass Function in the Early Galaxy, ApJ, 625, 833

Luhman K. L., 1999, Young Low-Mass Stars and Brown Dwarfs in IC 348, ApJ, 525, 466

Luhman K. L., 2004, New Brown Dwarfs and an Updated Initial Mass Function in Taurus, ApJ, 617, 1216

Luhman K. L., 2008, Chamaeleon. p. 169

Luhman K. L., Esplin T. L., 2020, Refining the Census of the Upper Scorpius Association with Gaia, AJ, 160, 44

Luhman K. L., Rieke G. H., Young E. T., Cotera A. S., Chen H., Rieke M. J., Schneider G., Thompson R. I., 2000, The Initial Mass Function of Low-Mass Stars and Brown Dwarfs in Young Clusters, ApJ, 540, 1016

Luhman K. L., Stauffer J. R., Muench A. A., Rieke G. H., Lada E. A., Bouvier J., Lada C. J., 2003, A Census of the Young Cluster IC 348, ApJ, 593, 1093

Luhman K. L., Mamajek E. E., Allen P. R., Cruz K. L., 2009, An Infrared/X-Ray Survey for New Members of the Taurus Star-Forming Region, ApJ, 703, 399

Luhman K. L., Esplin T. L., Loutrel N. P., 2016, A Census of Young Stars and Brown Dwarfs in IC 348 and NGC 1333, ApJ, 827, 52

Luhman K. L., Mamajek E. E., Shukla S. J., Loutrel N. P., 2017, A Survey for New Members of the Taurus Star-forming Region with the Sloan Digital Sky Survey, AJ, 153, 46

Luhman K. L., Herrmann K. A., Mamajek E. E., Esplin T. L., Pecaut M. J., 2018, New Young Stars and Brown Dwarfs in the Upper Scorpius Association, AJ, 156, 76

Macintosh B., Graham J. R., Ingraham P., Konopacky Q., Marois C., et al., 2014, First light of the Gemini Planet Imager, Proceedings of the National Academy of Science, 111, 12661

Macintosh B., Graham J. R., Barman T., De Rosa R. J., Konopacky Q., et al., 2015, Discovery and spectroscopy of the young jovian planet 51 Eri b with the Gemini Planet Imager, Science, 350, 64

Mainzer A. K., McLean I. S., 2003, Using Narrowband Photometry to Detect Young Brown Dwarfs in IC 348, ApJ, 597, 555

Mainzer A. K., et al., 2003, in Melugin R. K., Roeser H.-P., eds, Society of Photo-Optical Instrumentation Engineers (SPIE) Conference Series Vol. 4857, Airborne Telescope Systems II. pp 21–28, doi:10.1117/12.458635

Mamajek E. E., Bell C. P. M., 2014, On the age of the β Pictoris moving group, MNRAS, 445, 2169

Manara C. F., et al., 2019, Observational constraints on dust disk sizes in tidally truncated protoplanetary disks in multiple systems in the Taurus region, A&A, 628, A95

Marley M. S., Fortney J. J., Hubickyj O., Bodenheimer P., Lissauer J. J., 2007, On the Luminosity of Young Jupiters, ApJ, 655, 541

Marley M. S., et al., 2021, The Sonora Brown Dwarf Atmosphere and Evolution Models. I. Model Description and Application to Cloudless Atmospheres in Rainout Chemical Equilibrium, ApJ, 920, 85

Marois C., Lafrenière D., Doyon R., Macintosh B., Nadeau D., 2006, Angular Differential Imaging: A Powerful High-Contrast Imaging Technique, ApJ, 641, 556

Marois C., Macintosh B., Barman T., Zuckerman B., Song I., et al., 2008, Direct Imaging of Multiple Planets Orbiting the Star HR 8799, Science, 322, 1348

Marois C., Zuckerman B., Konopacky Q. M., Macintosh B., Barman T., 2010, Images of a fourth planet orbiting HR 8799, Nature, 468, 1080

Masciadri E., Mundt R., Henning T., Alvarez C., Barrado y Navascués D., 2005, A Search for Hot Massive Extrasolar Planets around Nearby Young Stars with the Adaptive Optics System NACO, ApJ, 625, 1004

Matzner C. D., Levin Y., 2005, Protostellar Disks: Formation, Fragmentation, and the Brown Dwarf Desert, ApJ, 628, 817

Mayor M., Queloz D., 1995, A Jupiter-mass companion to a solar-type star, Nature, 378, 355

Mayor M., et al., 2011, The HARPS search for southern extra-solar planets XXXIV. Occurrence, mass distribution and orbital properties of super-Earths and Neptune-mass planets, arXiv e-prints, p. arXiv:1109.2497

Mennesson B., et al., 2016, in MacEwen H. A., Fazio G. G., Lystrup M., Batalha N., Siegler N., Tong E. C., eds, Society of Photo-Optical Instrumentation Engineers (SPIE) Conference Series Vol. 9904, Space Telescopes and Instrumentation 2016: Optical, Infrared, and Millimeter Wave. p. 99040L, doi:10.1117/12.2240457

Meyer M. R., Amara A., Reggiani M., Quanz S. P., 2018, M-dwarf exoplanet surface density distribution. A log-normal fit from 0.07 to 400 AU, A&A, 612, L3

Michalik D., Lindegren L., Hobbs D., 2015, The Tycho-Gaia astrometric solution . How to get 2.5 million parallaxes with less than one year of Gaia data, A&A, 574, A115

Miller G. E., Scalo J. M., 1979, The Initial Mass Function and Stellar Birthrate in the Solar Neighborhood, ApJS, 41, 513

Miret-Roig N., et al., 2021, A rich population of free-floating planets in the Upper Scorpius young stellar association, Nature Astronomy,

Montet B. T., Crepp J. R., Johnson J. A., Howard A. W., Marcy G. W., 2014, The TRENDS High-contrast Imaging Survey. IV. The Occurrence Rate of Giant Planets around M Dwarfs, ApJ, 781, 28

Morgan W. W., Keenan P. C., Kellman E., 1943, An Atlas of Stellar Spectra with an Outline of Spectral Classification. Univ. Chicago Press, Chicago, IL

Morzinski K. M., et al., 2014, in Marchetti E., Close L. M., Vran J.-P., eds, Society of Photo-Optical Instrumentation Engineers (SPIE) Conference Series Vol. 9148, Adaptive Optics Systems IV. p. 914804 (`arXiv:1407.5098`), doi:10.1117/12.2057048

Mróz P., et al., 2020, A Terrestrial-mass Rogue Planet Candidate Detected in the Shortest-timescale Microlensing Event, ApJ, 903, L11

Muench A. A., Lada C. J., Luhman K. L., Muzerolle J., Young E., 2007, A Spitzer Census of the IC 348 Nebula, AJ, 134, 411

Muench A., Getman K., Hillenbrand L., Preibisch T., 2008, Star Formation in the Orion Nebula I: Stellar Content. p. 483

Najita J. R., Tiede G. P., Carr J. S., 2000, From Stars to Superplanets: The Low-Mass Initial Mass Function in the Young Cluster IC 348, ApJ, 541, 977

Nakajima T., Oppenheimer B. R., Kulkarni S. R., Golimowski D. A., Matthews K., Durrance S. T., 1995, Discovery of a cool brown dwarf, Nature, 378, 463

Newton E. R., et al., 2021, TESS Hunt for Young and Maturing Exoplanets (THYME). IV. Three Small Planets Orbiting a 120 Myr Old Star in the Pisces-Eridanus Stream, AJ, 161, 65

Nielsen E. L., De Rosa R. J., Macintosh B., Wang J. J., Ruffio J.-B., et al., 2019, The Gemini Planet Imager Exoplanet Survey: Giant Planet and Brown Dwarf Demographics From 10-100 AU, arXiv e-prints,

Nielsen E. L., et al., 2020, The Gemini Planet Imager Exoplanet Survey: Dynamical Mass of the Exoplanet β Pictoris b from Combined Direct Imaging and Astrometry, AJ, 159, 71

Noecker M. C., Zhao F., Demers R., Trauger J., Guyon O., Jeremy Kasdin N., 2016, Coronagraph instrument for WFIRST-AFTA, Journal of Astronomical Telescopes, Instruments, and Systems, 2, 011001

Nordström B., et al., 2004, The Geneva-Copenhagen survey of the Solar neighbourhood. Ages, metallicities, and kinematic properties of $\sim$14 000 F and G dwarfs, A&A, 418, 989

Oliveira J. M., Jeffries R. D., van Loon J. T., 2009, The low-mass initial mass function in the young cluster NGC6611, MNRAS, 392, 1034

Ortega V. G., Jilinski E., de La Reza R., Bazzanella B., 2007, On the common origin of the AB Doradus moving group and the Pleiades cluster, MNRAS, 377, 441

Ortiz-León G. N., et al., 2017, The Gould's Belt Distances Survey (GOBELINS). III. The Distance to the Serpens/Aquila Molecular Complex, ApJ, 834, 143

Ortiz-León G. N., et al., 2018a, The Gould's Belt Distances Survey (GOBELINS). V. Distances and Kinematics of the Perseus Molecular Cloud, ApJ, 865, 73

Ortiz-León G. N., et al., 2018b, Gaia-DR2 Confirms VLBA Parallaxes in Ophiuchus, Serpens, and Aquila, ApJ, 869, L33

Otten G. P. P. L., Snik F., Kenworthy M. A., Miskiewicz M. N., Escuti M. J., 2014, Performance characterization of a broadband vector Apodizing Phase Plate coronagraph, Optics Express, 22, 30287

Otten G. P. P. L., Snik F., Kenworthy M. A., Keller C. U., Males J. R., et al., 2017, On-sky Performance Analysis of the Vector Apodizing Phase Plate Coronagraph on MagAO/Clio2, ApJ, 834, 175

Paxton B., Bildsten L., Dotter A., Herwig F., Lesaffre P., Timmes F., 2011, Modules for Experiments in Stellar Astrophysics (MESA), ApJS, 192, 3

Paxton B., et al., 2013, Modules for Experiments in Stellar Astrophysics (MESA): Planets, Oscillations, Rotation, and Massive Stars, ApJS, 208, 4

Paxton B., et al., 2015, Modules for Experiments in Stellar Astrophysics (MESA): Binaries, Pulsations, and Explosions, ApJS, 220, 15

Pearson K. A., Palafox L., Griffith C. A., 2018, Searching for exoplanets using artificial intelligence, MNRAS, 474, 478

Pecaut M. J., Mamajek E. E., 2013, Intrinsic Colors, Temperatures, and Bolometric Corrections of Pre-main-sequence Stars, ApJS, 208, 9

Pecaut M. J., Mamajek E. E., 2016, The star formation history and accretion-disc fraction among the K-type members of the Scorpius-Centaurus OB association, MNRAS, 461, 794

Pecaut M. J., Mamajek E. E., Bubar E. J., 2012, A Revised Age for Upper Scorpius and the Star Formation History among the F-type Members of the Scorpius-Centaurus OB Association, ApJ, 746, 154

Penny M. T., Gaudi B. S., Kerins E., Rattenbury N. J., Mao S., Robin A. C., Calchi Novati S., 2019, Predictions of the WFIRST Microlensing Survey. I. Bound Planet Detection Rates, ApJS, 241, 3

Perryman M. A. C., et al., 1997, The Hipparcos Catalogue., A&A, 500, 501

Phillips M. W., et al., 2020, A new set of atmosphere and evolution models for cool T-Y brown dwarfs and giant exoplanets, A&A, 637, A38

Poleski R., McCullough P. R., Valenti J. A., Burke C. J., Machalek P., Janes K., 2010, The XO Planetary Survey Project: Astrophysical False Positives, ApJS, 189, 134

Povich M. S., et al., 2013, The MYStIX Infrared-Excess Source Catalog, ApJS, 209, 31

Preibisch T., Mamajek E., 2008, The Nearest OB Association: Scorpius-Centaurus (Sco OB2). p. 235

Preibisch T., Brown A. G. A., Bridges T., Guenther E., Zinnecker H., 2002, Exploring the Full Stellar Population of the Upper Scorpius OB Association, AJ, 124, 404

Prevot M. L., Lequeux J., Maurice E., Prevot L., Rocca-Volmerange B., 1984, The typical interstellar extinction in the Small Magellanic Cloud., A&A, 132, 389

Puget P., et al., 2004, in Moorwood A. F. M., Iye M., eds, Proc. SPIEVol. 5492, Ground-based Instrumentation for Astronomy. pp 978–987, doi:10.1117/12.551097

Quanz S. P., Crossfield I., Meyer M. R., Schmalzl E., Held J., 2015, Direct detection of exoplanets in the 3-10 μm range with E-ELT/METIS, International Journal of Astrobiology, 14, 279

Rajan A., et al., 2017, Characterizing 51 Eri b from 1 to 5 μm: A Partly Cloudy Exoplanet, AJ, 154, 10

Rajpurohit A. S., Reylé C., Allard F., Homeier D., Schultheis M., Bessell M. S., Robin A. C., 2013, The effective temperature scale of M dwarfs, A&A, 556, A15

Rameau J., et al., 2013a, A survey of young, nearby, and dusty stars conducted to understand the formation of wide-orbit giant planets. VLT/NaCo adaptive optics thermal and angular differential imaging, A&A, 553, A60

Rameau J., et al., 2013b, Discovery of a Probable 4-5 Jupiter-mass Exoplanet to HD 95086 by Direct Imaging, ApJ, 772, L15

Rayner J. T., Toomey D. W., Onaka P. M., Denault A. J., Stahlberger W. E., et al., 2003, SpeX: A Medium-Resolution 0.8-5.5 Micron Spectrograph and Imager for the NASA Infrared Telescope Facility, PASP, 115, 362

Rayner J. T., Cushing M. C., Vacca W. D., 2009, The Infrared Telescope Facility (IRTF) Spectral Library: Cool Stars, ApJS, 185, 289

Rebolo R., Zapatero Osorio M. R., Martín E. L., 1995, Discovery of a brown dwarf in the Pleiades star cluster, Nature, 377, 129

Rebolo R., Zapatero Osorio M. R., Madruga S., Bejar V. J. S., Arribas S., Licandro J., 1998, Discovery of a Low-Mass Brown Dwarf Companion of the Young Nearby Star G 196-3, Science, 282, 1309

Rebull L. M., Padgett D. L., McCabe C.-E., Hillenbrand L. A., Stapelfeldt K. R., et al., 2010, The Taurus Spitzer Survey: New Candidate Taurus Members Selected Using Sensitive Mid-Infrared Photometry, ApJS, 186, 259

Reggiani M., et al., 2014, Discovery of a Companion Candidate in the HD 169142 Transition Disk and the Possibility of Multiple Planet Formation, ApJ, 792, L23

Reggiani M., et al., 2016, The VLT/NaCo large program to probe the occurrence of exoplanets and brown dwarfs at wide orbits . III. The frequency of brown dwarfs and giant planets as companions to solar-type stars, A&A, 586, A147

Reid I. N., et al., 1999, L Dwarfs and the Substellar Mass Function, ApJ, 521, 613

Reipurth B., Clarke C., 2001, The Formation of Brown Dwarfs as Ejected Stellar Embryos, AJ, 122, 432

Ricker G. R., et al., 2015, Transiting Exoplanet Survey Satellite (TESS), Journal of Astronomical Telescopes, Instruments, and Systems, 1, 014003

Rieke M. J., Kelly D., Horner S., 2005, in Heaney J. B., Burriesci L. G., eds, Society of Photo-Optical Instrumentation Engineers (SPIE) Conference Series Vol. 5904, Cryogenic Optical Systems and Instruments XI. pp 1–8, doi:10.1117/12.615554

Robberto M., et al., 2020, HST Survey of the Orion Nebula Cluster in the H_2O 1.4 μm Absorption Band. I. A Census of Substellar and Planetary-mass Objects, ApJ, 896, 79

Roberge A., Moustakas L. A., 2018, The Large Ultraviolet/Optical/Infrared Surveyor, Nature Astronomy, 2, 605

Roccatagliata V., Sacco G. G., Franciosini E., Randich S., 2018, The double population of Chamaeleon I detected by Gaia DR2, A&A, 617, L4

Roccatagliata V., Franciosini E., Sacco G. G., Randich S., Sicilia-Aguilar A., 2020, A 3D view of the Taurus star-forming region by Gaia and Herschel. Multiple populations related to the filamentary molecular cloud, A&A, 638, A85

Rocha-Pinto H. J., Maciel W. J., 1996, The metallicity distribution of G dwarfs in the solar neighbourhood., MNRAS, 279, 447

Rosenthal L. J., et al., 2021, The California Legacy Survey. I. A Catalog of 178 Planets from Precision Radial Velocity Monitoring of 719 Nearby Stars over Three Decades, ApJS, 255, 8

Rousset G., et al., 2003, in Wizinowich P. L., Bonaccini D., eds, Vol. 4839, Adaptive Optical System Technologies II. SPIE, pp 140 – 149, `https://doi.org/10.1117/12.459332`

Sajadian S., 2021, Sensitivity to habitable planets in the Roman microlensing survey, MNRAS, 508, 5991

Salpeter E. E., 1955, The Luminosity Function and Stellar Evolution., ApJ, 121, 161

Saumon D., Marley M. S., 2008, The Evolution of L and T Dwarfs in Color-Magnitude Diagrams, ApJ, 689, 1327

Saumon D., Marley M. S., Cushing M. C., Leggett S. K., Roellig T. L., Lodders K., Freedman R. S., 2006, Ammonia as a Tracer of Chemical Equilibrium in the T7.5 Dwarf Gliese 570D, ApJ, 647, 552

Schlieder J. E., Lépine S., Simon M., 2012, Cool Young Stars in the Northern Hemisphere: β Pictoris and AB Doradus Moving Group Candidates, AJ, 143, 80

Seo Y. M., et al., 2015, An Ammonia Spectral Map of the L1495-B218 Filaments in the Taurus Molecular Cloud. I. Physical Properties of Filaments and Dense Cores, ApJ, 805, 185

Shallue C. J., Vanderburg A., 2018, Identifying Exoplanets with Deep Learning: A Five-planet Resonant Chain around Kepler-80 and an Eighth Planet around Kepler-90, AJ, 155, 94

Sivanandam S., Hinz P. M., Heinze A. N., Freed M., Breuninger A. H., 2006, in McLean I. S., Iye M., eds, Society of Photo-Optical Instrumentation Engineers (SPIE) Conference Series Vol. 6269, Society of Photo-Optical Instrumentation Engineers (SPIE) Conference Series. p. 62690U (`arXiv:astro-ph/0606131`), doi:10.1117/12.672344

Skrutskie M. F., et al., 2006, The Two Micron All Sky Survey (2MASS), AJ, 131, 1163

Slesnick C. L., Hillenbrand L. A., Carpenter J. M., 2004, The Spectroscopically Determined Substellar Mass Function of the Orion Nebula Cluster, ApJ, 610, 1045

Slesnick C. L., Carpenter J. M., Hillenbrand L. A., 2006, A Large-Area Search for Low-Mass Objects in Upper Scorpius. I. The Photometric Campaign and New Brown Dwarfs, AJ, 131, 3016

Snik F., Otten G., Kenworthy M., Miskiewicz M., Escuti M., Packham C., Codona J., 2012, in Modern Technologies in Space- and Ground-based Telescopes and Instrumentation II. p. 84500M (`arXiv:1207.2970`), doi:10.1117/12.926222

Sonnenfeld A., Treu T., Gavazzi R., Marshall P. J., Auger M. W., Suyu S. H., Koopmans L. V. E., Bolton A. S., 2012, Evidence for Dark Matter Contraction and a Salpeter Initial Mass Function in a Massive Early-type Galaxy, ApJ, 752, 163

Soummer R., Pueyo L., Larkin J., 2012, Detection and Characterization of Exoplanets and Disks Using Projections on Karhunen-Loève Eigenimages, ApJ, 755, L28

Spezzi L., Alves de Oliveira C., Moraux E., Bouvier J., Winston E., et al., 2012, Searching for planetary-mass T-dwarfs in the core of Serpens, A&A, 545, A105

Spiegel D. S., Burrows A., 2012, Spectral and Photometric Diagnostics of Giant Planet Formation Scenarios, ApJ, 745, 174

Stone J. M., et al., 2018, The LEECH Exoplanet Imaging Survey: Limits on Planet Occurrence Rates under Conservative Assumptions, AJ, 156, 286

Suárez G., Downes J. J., Román-Zúñiga C., Cerviño M., Briceño C., Petr-Gotzens M. G., Vivas K., 2019, System initial mass function of the 25 Ori group from planetary-mass objects to intermediate/high-mass stars, MNRAS, 486, 1718

Szulágyi J., Dullemond C. P., Pohl A., Quanz S. P., 2019, Observability of forming planets and their circumplanetary discs II. - SEDs and near-infrared fluxes, MNRAS, 487, 1248

The LUVOIR Team 2019, The LUVOIR Mission Concept Study Final Report, arXiv e-prints, p. arXiv:1912.06219

Todorov K., Luhman K. L., McLeod K. K., 2010, Discovery of a Planetary-mass Companion to a Brown Dwarf in Taurus, ApJ, 714, L84

Todorov K. O., Luhman K. L., Konopacky Q. M., McLeod K. K., Apai D., Ghez A. M., Pascucci I., Robberto M., 2014, A Search for Companions to Brown Dwarfs in the Taurus and Chamaeleon Star-Forming Regions, ApJ, 788, 40

Tokuda K., et al., 2018, Warm CO Gas Generated by Possible Turbulent Shocks in a Low-mass Star-forming Dense Core in Taurus, ApJ, 862, 8

Trauger J. T., Traub W. A., 2007, A laboratory demonstration of the capability to image an Earth-like extrasolar planet, Nature, 446, 771

Treu T., Auger M. W., Koopmans L. V. E., Gavazzi R., Marshall P. J., Bolton A. S., 2010, The Initial Mass Function of Early-Type Galaxies, ApJ, 709, 1195

Tsapras Y., 2018, Microlensing Searches for Exoplanets, Geosciences, 8, 365

Vacca W. D., Cushing M. C., Rayner J. T., 2003, A Method of Correcting Near-Infrared Spectra for Telluric Absorption, PASP, 115, 389

Vigan A., Gry C., Salter G., Mesa D., Homeier D., Moutou C., Allard F., 2015, High-contrast imaging of Sirius A with VLT/SPHERE: looking for giant planets down to one astronomical unit, MNRAS, 454, 129

Vigan A., et al., 2017, The VLT/NaCo large program to probe the occurrence of exoplanets and brown dwarfs at wide orbits. IV. Gravitational instability rarely forms wide, giant planets, A&A, 603, A3

Vigan A., et al., 2021, The SPHERE infrared survey for exoplanets (SHINE). III. The demographics of young giant exoplanets below 300 au with SPHERE, A&A, 651, A72

Voirin J., Manara C. F., Prusti T., 2018, A revised estimate of the distance to the clouds in the Chamaeleon complex using the Tycho-Gaia Astrometric Solution, A&A, 610, A64

Wang J. J., et al., 2018, Dynamical Constraints on the HR 8799 Planets with GPI, AJ, 156, 192

Watkins S. J., Bhattal A. S., Boffin H. M. J., Francis N., Whitworth A. P., 1998, Numerical simulations of protostellar encounters - II. Coplanar disc-disc encounters, MNRAS, 300, 1205

Whitworth A. P., 2018, Brown Dwarf Formation: Theory. p. 95, doi:10.1007/978-3-319-55333-7_95

Whitworth A. P., Stamatellos D., 2006, The minimum mass for star formation, and the origin of binary brown dwarfs, A&A, 458, 817

Whitworth A., Bate M. R., Nordlund Å., Reipurth B., Zinnecker H., 2007, in Reipurth B., Jewitt D., Keil K., eds, Protostars and Planets V. p. 459

Wilkinson S., Merín B., Riviere-Marichalar P., 2018, New member candidates of Upper Scorpius from Gaia DR1, A&A, 618, A12

Winston E., et al., 2007, A Combined Spitzer and Chandra Survey of Young Stellar Objects in the Serpens Cloud Core, ApJ, 669, 493

Winston E., et al., 2010, The Properties of X-ray Luminous Young Stellar Objects in the NGC 1333 and Serpens Embedded Clusters, AJ, 140, 266

Winston E., Wolk S. J., Gutermuth R., Bourke T. L., 2018, Chandra Detection of an Evolved Population of Young Stars in Serpens South, AJ, 155, 241

Wolszczan A., Frail D. A., 1992, A planetary system around the millisecond pulsar PSR1257 + 12, Nature, 355, 145

Worthey G., Dorman B., Jones L. A., 1996, The G Dwarf Problem Exists in Other Galaxies, AJ, 112, 948

Wright J. T., 2018, in Deeg H. J., Belmonte J. A., eds, , Handbook of Exoplanets. p. 4, doi:10.1007/978-3-319-55333-7_4

Wright E. L., et al., 2010, The Wide-field Infrared Survey Explorer (WISE): Mission Description and Initial On-orbit Performance, AJ, 140, 1868

Zang W., et al., 2021, An Earth-mass planet in a time of COVID-19: KMT-2020-BLG-0414Lb, Research in Astronomy and Astrophysics, 21, 239

Zapatero Osorio M. R., Béjar V. J. S., Peña Ramírez K., 2017, Optical and Near-infrared Spectra of σ Orionis Isolated Planetary-mass Objects, ApJ, 842, 65

de Zeeuw P. T., Hoogerwerf R., de Bruijne J. H. J., Brown A. G. A., Blaauw A., 1999, A HIPPARCOS Census of the Nearby OB Associations, AJ, 117, 354

Zhang Z., Liu M. C., Best W. M. J., Magnier E. A., Aller K. M., et al., 2018, The Pan-STARRS1 Proper-motion Survey for Young Brown Dwarfs in Nearby Star-forming Regions. I. Taurus Discoveries and a Reddening-free Classification Method for Ultracool Dwarfs, ApJ, 858, 41

Zinnecker H., Yorke H. W., 2007, Toward Understanding Massive Star Formation, ARA&A, 45, 481

Zuckerman B., Song I., Bessell M. S., Webb R. A., 2001, The β Pictoris Moving Group, ApJ, 562, L87

Zuckerman B., Song I., Bessell M. S., 2004, The AB Doradus Moving Group, ApJ, 613, L65